Bio-inspired Sensors: from Hair-like Sensilla of Arachnids and Insects to 3D-printed Acoustic and Airflow Sensors

Samuele Martinelli

Centre of Ultrasonic Engineering

Department of Electronic and Electrical Engineering

University of Strathclyde

A thesis submitted for the degree of

Doctor of Philosophy

May 2026, Glasgow, U.K.

Declaration

This thesis is the result of the author's original research. It has been composed by the author and has not been previously submitted for examination which has led to the award of a degree.

Signed: 

Date: 05/05/2026

Abstract

Leonardo da Vinci observed that “Human subtlety will never devise an invention more beautiful, more simple or more direct than does nature because in her inventions nothing is lacking, and nothing is superfluous.” This statement remains profoundly relevant, as natural systems continue to inspire technological innovation. Among these, the hair mechanoreceptors of insects and arachnids represent highly efficient biological sensors capable of detecting airflows and low-frequency near-field sounds. Variants of these structures are hypothesized to sense acceleration, direct contact, and even thermal or chemical stimuli, suggesting an evolutionary link to olfactory and infrared sensilla. Their multifunctionality has motivated extensive research into bioinspired sensing technologies.

Historically, such sensors have been fabricated using micro-electromechanical systems (MEMS), a technology originating in the mid-20th century and widely adopted by the 1990s. MEMS enabled miniaturization and integration of sensors but remains constrained by complex, costly manufacturing processes. In contrast, additive manufacturing techniques, particularly 3D printing, offer simplified workflows, reduced costs, and greater design flexibility. Digital Light Processing (DLP), a photopolymer-based 3D-printing method, is particularly promising for producing sensor arrays and enabling batch fabrication, thereby reducing production time and improving scalability.

This thesis explores the design and fabrication of bioinspired sensors using DLP-based 3D printing. Two prototypes are presented: an acoustic sensor responsive to specific frequency bands and an airflow sensor capable of converting wind speed variations into electrical signals. While the acoustic sensor demonstrated mechanical functionality, electrical transduction

remains a challenge; its successful implementation could enable frequency-selective audio acquisition, reducing computational demands in applications such as speech recognition. The airflow sensor achieved reliable electrical output and demonstrates potential for large-scale deployment in arrays, with applications spanning fluid dynamics, autonomous navigation, biomedical monitoring, and meteorology. These findings underscore the potential of DLP-based additive manufacturing to advance bioinspired sensing through cost-effective, scalable, and versatile solutions. The PhD research work showed that it is possible to 3D-print structures bio-inspired by nature that can react to different acoustic frequency bands, and that it is possible to repurpose these structures to sense other physical phenomena, for example airflow velocity.

Acknowledgments

I would like to begin by expressing my deepest gratitude to my father, whose memory has been a source of strength throughout this journey. He passed away during the course of my PhD, and his support and encouragement continue to inspire me. He could not be there physically during my first university graduation, and unfortunately, he will not be here for this one. If not for him, I would probably not have left my little town in Italy and be here in Glasgow in the first place. I truly wished he could be here right now to see how far I've walked. I know how proud you were of me, and you will never be forgotten. I need to also thank my mom and my sister for being a point of strength throughout my whole PhD and for supporting me.

I don't think I can truly express in words how thankful I am for my supervisors, James and Andy. I could've not found better supervisors. I apologise for maybe being too annoying at times. Your guidance has been invaluable, and I will treasure it with me for the rest of my professional life.

Temi, my wife, you have been my point of balance throughout this whole PhD. We met as I was starting this journey, and I'm not joking when I say that you have been responsible for keeping me sane. You always supported me, always was there for me. There are no words to express how grateful I am, and I hope you know how important you are for me and how much I value having you in my life.

Everybody around me in the office, especially Lara and Pete, thank you very much. You made this journey more fun (and bearable). Thanks to all my friends outside of university too for helping in my time in need, or when I simply needed to chat and take my mind off things. To all the other PhD students, and everybody else in CUE or at the University of Strathclyde

thank you for helping me in this path. You are too many to name, but whether it was to rebalance myself and make sense of my ideas, or for your invaluable help during my experiments, without you it would've probably not been possible. Thanks also to all the people I met at conferences that sparked amazing conversations, albeit I doubt even a single one will read this.

To Jerome and Thomas, from Université de Tours, thank you for making me feel more welcome during my exchange in Tours. And thank you for the invaluable discussion from a biological point of view, it allowed me to shine new light on this work.

Last but not least, I would like to thank Defence Science and Technology Laboratory (DSTL) for funding this project. Truly, without them this piece of work will not exist. A special thanks goes to Jitu and Giles for being there whenever I needed help.

Contents

List of Figures

List of Tables

1

Introduction

In the past few centuries humans have taken inspiration from nature from their engineering creations. And it makes sense, as nature has millennia of evolution and improvement on their side. In particular, insects and arachnids inspire innovation for miniaturization of technology. Their sensory system is small, highly sensitive and efficient. Since the year 2000, engineers all over the world created several sensors inspired by the hair-like structures found in insects and arachnids that react, mainly, to airflow and low-frequency near-field sound [1-19]. They mainly used conventional microelectromechanical system (MEMS) manufacturing techniques, but in 2020 a research team used 3D-printing as an alternative [20]. Since the 2010s, 3D printing has grown in academia as a research topic for sensor manufacturing [21]. This technique allows faster prototyping, fewer geometric constraints, and experimentation with new emerging materials [21]. One of the main disadvantages of using 3D-printing to produce sensors is scalability. The majority of techniques cannot print in batches as their printing occurs point-by-point for each layer. This cannot compete with MEMS techniques that produce multiple sensors in batches at the same time. However, Digital Light Processing (DLP) is a 3D-printing technique that stands out as each layer is printed at the same time [22, 23]. DLP can in theory allow batch printing of sensors similarly to MEMS.

The goal of this thesis is to develop a DLP 3D-printed sensor, inspired by hair-like receptors of insects and arachnids, to react to different narrow frequency bands of sound or airflow velocities by changes in the hair structure. The acoustic sensor would allow audio signals acquisition with separated frequency bands through several hair sensors in an array, as DLP can allow easy integration of multiple sensors within one structure. Therefore, the acoustic

sensor would provide information on the frequency content of an audio signal without digital processing (e.g., Fast Fourier Transform), as the audio signal is filtered mechanically at acquisition by the sensory array. Meanwhile, the airflow sensor can allow multi-point sensing of airflow over a wide area through an array of these sensors instead of a single point measurement (as it is done nowadays). This can help autonomous vehicles, and other applications. The potential is to have low data overhead, low latency and low power consumption. Moreover, 3D printing allows for less wasteful prototyping and for easier sensor array integration.

The thesis has the following structure. Chapter 1 presents background knowledge that was used during this thesis, from the basics of sound propagation to a review of past sensors inspired by the hair-like sensilla of insects and arachnids. Chapter 2 introduces the methodology and instrumentation used throughout the thesis. Chapter 3 presents the acoustic hair sensor, the reasoning for its design and the mechanical results. By changing the hair shaft geometry, the sensor would react mechanically to different narrow frequency bands. Multiple attempts to convert the mechanical displacement in electric results were made, but the strategies adopted were not sensitive enough. Nevertheless, the chapter goes through these efforts to describe what did not work and to pave the road for future readers with the same goal. Moreover, this chapter gives context to the design of this sensor which was expanded and allowed the creation of its airflow counterpart. Chapter 4 is dedicated to the airflow sensor. The sensor showed a response to a good range of airflow velocities and, directionality in one axis. Indicating that it could be used in arrays to also give information on the direction of flow. Additionally, changing the geometry will change the range and sensitivity of the sensor. Chapter 5 describes the work conducted at the University of Tours in France, as part of a collaboration with entomologists. This chapter shows the investigation of the acoustic sensor using a particle image velocimetry.

Lastly, Chapter 6 concludes the thesis, it summarizes the content presented earlier and suggests directions for future work.

List of publications

The work from Chapter 3 and 4 has been presented in the following conferences:

- Invertebrate Sound and Vibration 2023, Lincoln, United Kingdom – poster presentation
- The Doctoral School Multidisciplinary Symposium 2023: Horizons for Humanity, Glasgow, United Kingdom – poster presentation
- IEEE Sensors 2023, Vienna, Austria – poster presentation and conference proceeding publication:
    - S. Martinelli, A. Reid, R. Domingo-Roca, and J. F. C. Windmill, "Additive Manufacturing of an Insect Bio-Inspired Hair Acoustic Sensor," in 2023 IEEE SENSORS, 29 Oct.–1 Nov. 2023, doi: 10.1109/SENSORS56945.2023.10324858.
- IOP Anglo-French Physical Acoustics Conference 2024, Loch Lomond, United Kingdom – oral presentation
- ScotCHEM Polymer and Soft Materials Conference III, 2024, Glasgow United Kingdom
- CENSIS Technology Summit 2024, Glasgow, United kingdom – poster presentation for which I won the Best Research Poster award
- 188th Meeting of the Acoustical Society of America: joint with 25th International Congress on Acoustics, New Orleans, United States of America – oral presentation

- Engineering Academics Network Congress 2025: Realising the Vision, Manchester, United Kingdom – poster presentation as one of the finalists for the Hammerman Student Award
- IEEE International Conference on Flexible and Printable Sensors and Systems (FLEPS) 2025, Singapore – oral presentation and conference proceeding publication and won the 3rd place for the Student Best Paper Award:
    - S. Martinelli, A. Reid, and J. F. C. Windmill, "Additive Manufacturing of an Airflow Sensor Inspired by the Flat Trichobothria of Scorpions," in 2025 IEEE International Conference on Flexible and Printable Sensors and Systems (FLEPS), 2025–06–22 2025: IEEE, pp. 1–4, doi: 10.1109/fleps65444.2025.11105673.

Moreover, part of chapter 4 has been published in the IEEE Sensors Journal:

- S. Martinelli, A. Reid, and J. F. C. Windmill, "3D-Printed Airflow Hair Sensor Inspired by the *Buthus occitanus* Scorpion's flat Trichobothria," IEEE Sensors Journal, vol. 2026, no. 2, pp. 1428 – 1435, 15 Jan. 2026, doi: 10.1109/JSEN.2025.3635869.

2

Literature Review

"If I have seen further it is by standing on the shoulders of giants."

Isaac Newton

This chapter firstly provides basic background theory useful for the understanding of the content in this thesis. It then proceeds by outlining the current technologies, with their advantages and limitations; from which this project is built on.

2.1 Sound propagation

Everybody is familiar with the phenomena created by dropping a stone in a lake, river, or sea. On the surface of the water, propagating outwards from the point of impact of the stone, one can notice a pattern of highs (crests) and lows (troughs), i.e., the water oscillates above and below the level of calm water. This is an example of what a wave is in technical terms, 'a wave indicates cycles of highs and lows in some quantity' [24]. Waves can be classified in two types, mechanical and electromagnetic waves. The former requires a medium to propagate, an example is sound waves. The latter does not require a medium to travel; this is out of the scope of this project, therefore it will not be described here.

When talking about propagation of sound waves, this moving 'quantity' is air ***pressure***, measured in Pascals (Pa). Sound waves are nothing but a succession of pressures higher (rarefactions) and lower (compressions) than ambient atmospheric pressure. To be more specific, in the example of an object dropped in a water body we talk of a transverse wave, that is when the wave travels horizontally; the oscillation is up and downs. While sound waves are an example of longitudinal waves; the pressure oscillates back and forth, i.e., air molecules' average travelled distance is zero. A simple graphical representation of a travelling sound wave is given in Figure 2.1.

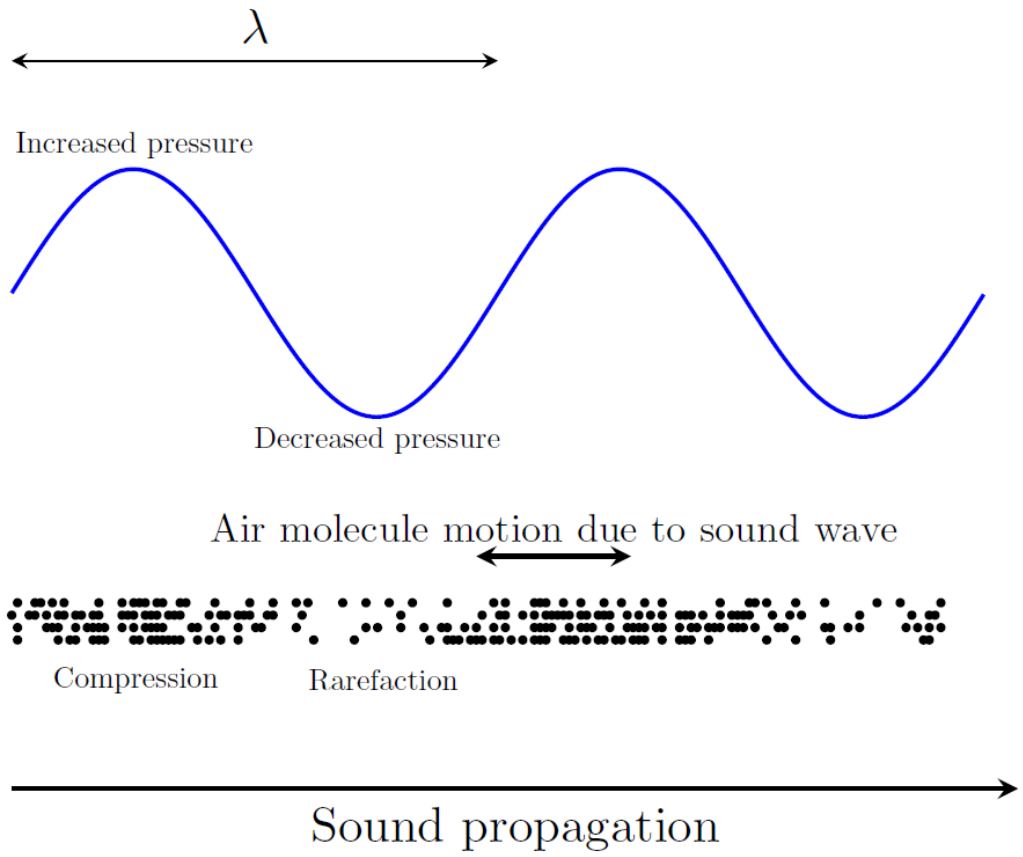

Figure 2.1: Basic representation of longitudinal sound wave propagation.

The distance between two successive points of compression (or rarefaction) is called ***wavelength***, indicated with the Greek letter λ (see Figure 2.1) and measured in length units. The number of cycles of compression and rarefaction in one second is called ***frequency***, f, measured in Hertz (Hz). The inverse of the frequency is called ***period***, T, it measures the amount of time required to complete one full cycle. The product between wavelength and frequency gives the speed of the wave. Therefore, the ***speed of sound***, c, would be evaluated as in Eq. (2.1).

$$c = \lambda f = \frac{\lambda}{T} \tag{2.1}$$

The speed of sound is strongly affected by temperature variations (±6m/s per ±10°C in air [24]) and less by other factors such as humidity and atmospheric pressure. Sound does not only

propagate in air but also in liquids and solids. Its speed depends on the medium in which the sound is travelling, for example, in air at a temperature of 20 ˚C and pressure of ~101 kPa, sound travels at ~343 m/s.

The difference between the air pressure and the pressure at its maximum point is the ***amplitude*** of the sound wave, which is related to the energy carried by the wave. The rate of energy flowing per second is called ***power***, measured in Watts (W). While the ***intensity*** of the wave is the power flowing through an area of one meter squared, therefore it is measured in W/m^2. As the sound wave moves further away from its source its amplitude and intensity diminish more and more, until the sound eventually ceases. Decrease of intensity in the wave is called ***attenuation***.

2.1.1 Attenuation

A light bulb can seem incredibly bright up close yet be barely seen if we move 10 meters away. The power emitted by the light bulb is the same in both cases, it does not depend on distance. Nevertheless, the emitted energy spreads in all directions as it propagates away from its source. The same is valid for sound waves. The dependence of the wave's intensity to the distance from the source follows the inverse square law; that is that the intensity depends on the inverse of the squared distance. For example, if the distance doubles, the intensity reduces by one quarter ($1/2^2 = 1/4$). Moreover, part of the sound waves' energy is also absorbed by the atmosphere, especially at higher frequencies (>1kHz). The higher the frequency, the higher is the energy absorbed by the atmosphere. This explains why when hearing music at great distance the sound seems dull, most of the high frequencies of the music are attenuated and what remains to hear is mainly the lower frequencies. Attenuation includes all the effects that reduce the intensity of the sound wave, including thermal and viscous dissipation and the inverse square law.

As the intensity attenuation can vary by factor of billions, to keep numbers small, the intensity ratio of a sound is measured in ***decibel*** (dB). The sound pressure level, *SPL*, in dB is measured as the base 10 logarithm of the ratio between the sound pressure in Pa, p, and the lower audible sound pressure as reference (20μPa in air for human hearing), p_0, as follows

$$SPL = 20 \log_{10} \frac{p}{p_0} \tag{2.2}$$

For example, a normal conversation is at an SPL of ~60dB, while a jet engine at 10m of distance is ~120dB [24].

2.1.2 Reflection, refraction and absorption

It is possible to see that light is reflected differently across different surfaces, for example the reflection of a mirror is different from the one of a window. Sound waves behave similarly. If the reflecting surface is smooth the wave reflects in a direction depending on the incident wave reflection (Figure 2.2). This is known as ***specular reflection***, or just ***reflection***. It is also possible to notice that rough surfaces (e.g., scratches) appear white-ish. This happens because the light reflects in all directions due to all the small irregularities on the surface. This phenomenon is called ***diffuse reflection***, or ***scattering***, and it applies also to sound waves.

When the wave is travelling between two media, part of the wave is reflected, while another part will continue to travel in the second medium. This is called ***refraction*** (Figure 2.2), and the angle of the reflected wave depends on the refractive indexes of the two media. The amount of sound wave energy that is reflected or refracted depends on the ***acoustic impedance*** of the medium, which is the product between its density and the speed of sound in it. The difference between two medium impedances gives the percentage of reflected energy, if the impedance difference is large most of the wave will be reflected. In practice, when a sound wave meets an object less than 0.01% propagates through it, almost its entirety is reflected. Refraction is of

major importance for light waves, while in sound waves occurs mostly between changes of temperature in air (as its impedance changes as well), causing the sound waves to bend.

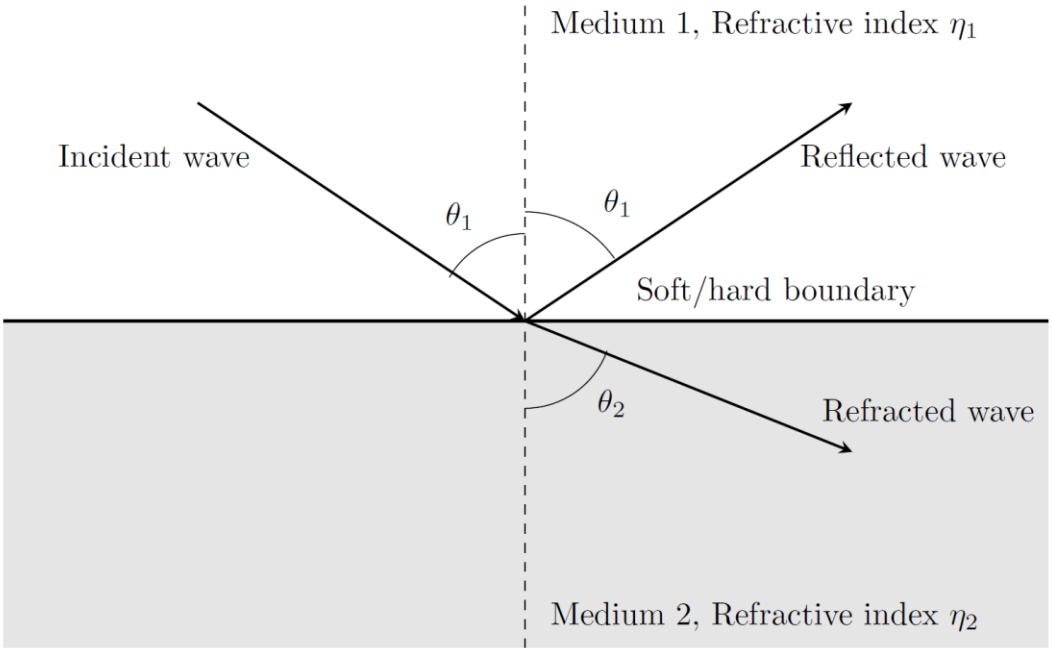

Figure 2.2: Graphic representation of reflection and refraction of a wave on a smooth surface. The angle Θ_1 of the incident wave is the same as the reflected one. The angle Θ_2 of the refracted wave is related to the incident wave via Snell's law.

In the case of sound waves, apart from reflection, scattering and/or refraction, the material may also absorb part of the sound wave too. Absorption depends on the material and texture of the object encountered by the wave. Soft textured materials (such as the ones used in recording studios) absorb more than hard smooth surfaces (like a wall). Similar to attenuation, high frequencies are the most affected by absorption, while lower frequencies are less absorbed by the material.

2.1.3 Diffraction

All waves can bend around corners, including sound waves. This is called ***diffraction***. Because of this phenomenon a small object becomes virtually invisible to the wave, as the wave will bend around it. The concept of what is small or large depends on the wavelength. The wavelength of visible light ranges from 400nm to 700nm; even a hair might appear "large"

close to a light source. On the other hand, audible sound has wavelengths ranging approximately from 17m to 17mm; even a person can look “small”. Since lower frequencies are in the order of meters, mammals that need to communicate for longer distances where multiple objects are present (e.g., a forest) will use this range. An example is elephants which under the right conditions can communicate at distances up to 10km [25]. If the communication frequencies would be higher this would pose an issue as the sound waves would interact more with trees and other objects along the way, making communication more difficult.

Diffraction also rules how sound interacts in situations where there is a barrier with an opening, like a hole in a wall. As the sound wave passes through the hole it will bend around the edges and spread out. The amount of spread depends on the size of the opening and the wavelength of the wave (Figure 2.3). When going through a large opening, like a window, the wave will spread less than when passing through a small hole. The smaller the opening, the wider the spreading angle.

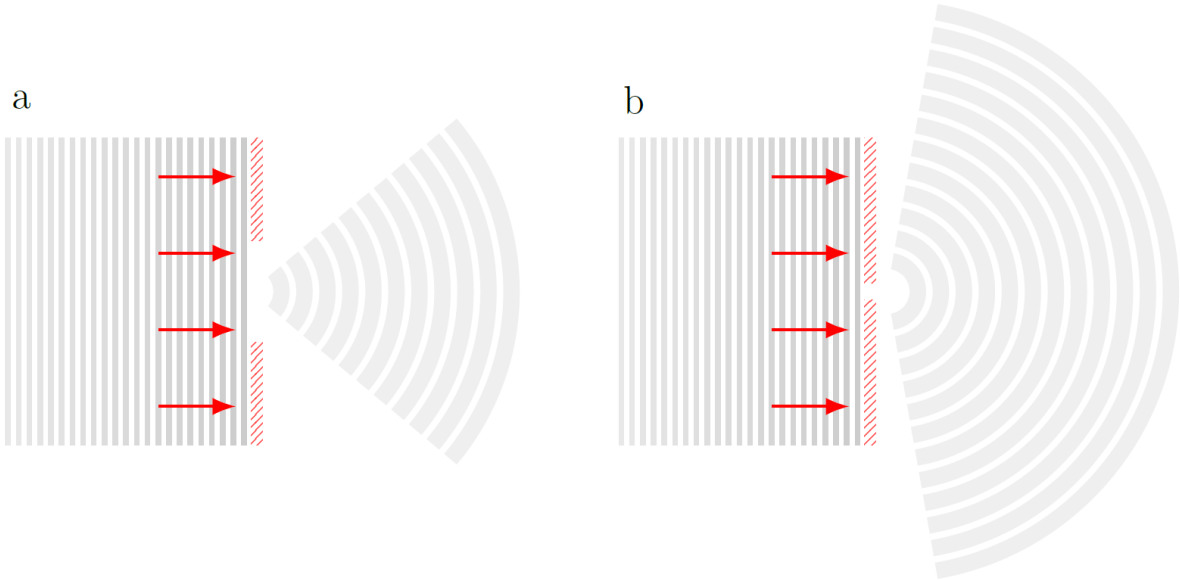

Figure 2.3: Graphical representation of diffraction through an opening. Showing the difference of bending angle between smaller (a) and wider (b) openings.

2.1.4 Interference

When two waves of the same frequency meet, we talk of ***interference***. Interferences can be *constructive* or *destructive* (Figure 2.4). At the intersection of two equal pressures, constructive interference occurs. This means that the pressure amplitude at that point is the sum of the two singular amplitudes. In Figure 2.4 black dots show constructive interference during rarefaction, while red dots during compression. Meanwhile, when the two waves meet at opposite pressure states (i.e., one wave is at compression state while the other is at rarefaction state), destructive interference occurs. This means that the resulting amplitude at that point is the difference between the amplitudes at intersection. Hence, the two waves will cancel out to some extent. In all the other regions when the waves overlap, *partial cancellation* happens.

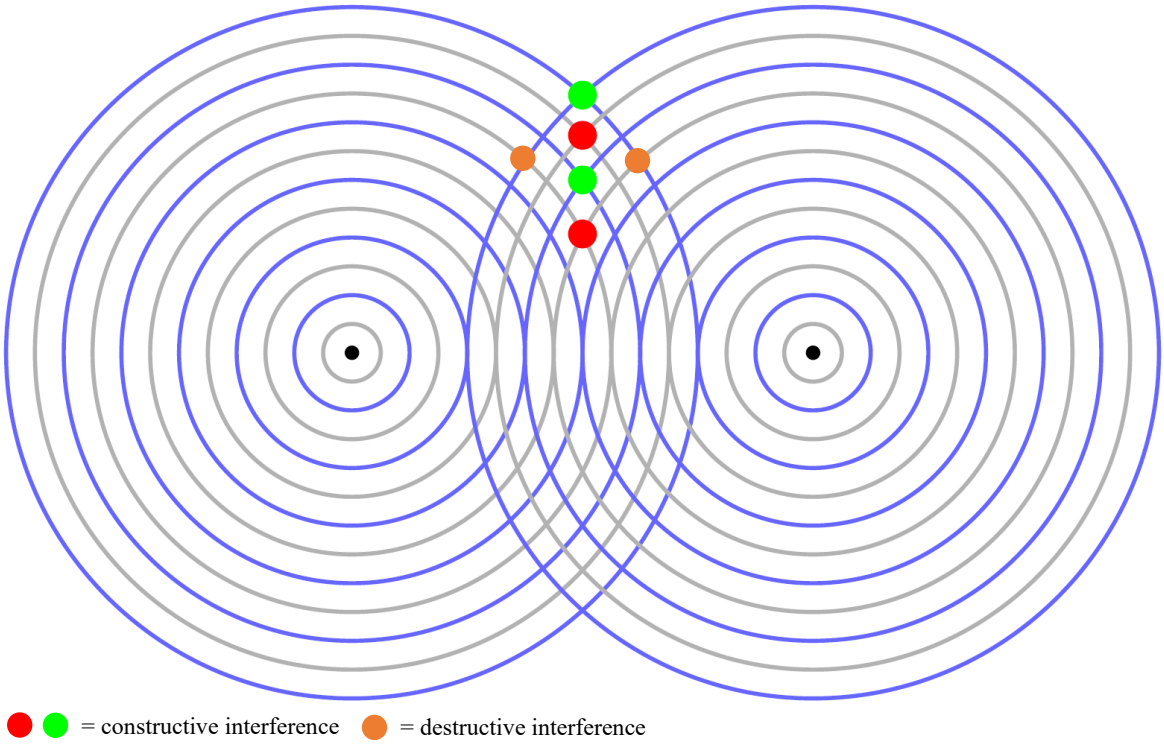

Figure 2.4: Graphical representation of two sound waves with same frequency emitted by two nearby sources. Compression is indicated by grey circles, while rarefaction by blue ones.

2.1.5 Doppler Effect

A familiar phenomenon is the one represented by the sound of the siren of an ambulance in motion. The sound produced by the siren (the source) is always the same, but its motion produces a frequency shift when perceived by a standing person (the receiver). This occurrence is called ***Doppler effect***. When the source moves towards the receiver, the perceived frequency is higher, while when the source moves away, the receiver will perceive a lower frequency. A graphical representation of the Doppler effect in this example is shown in Figure 2.5.

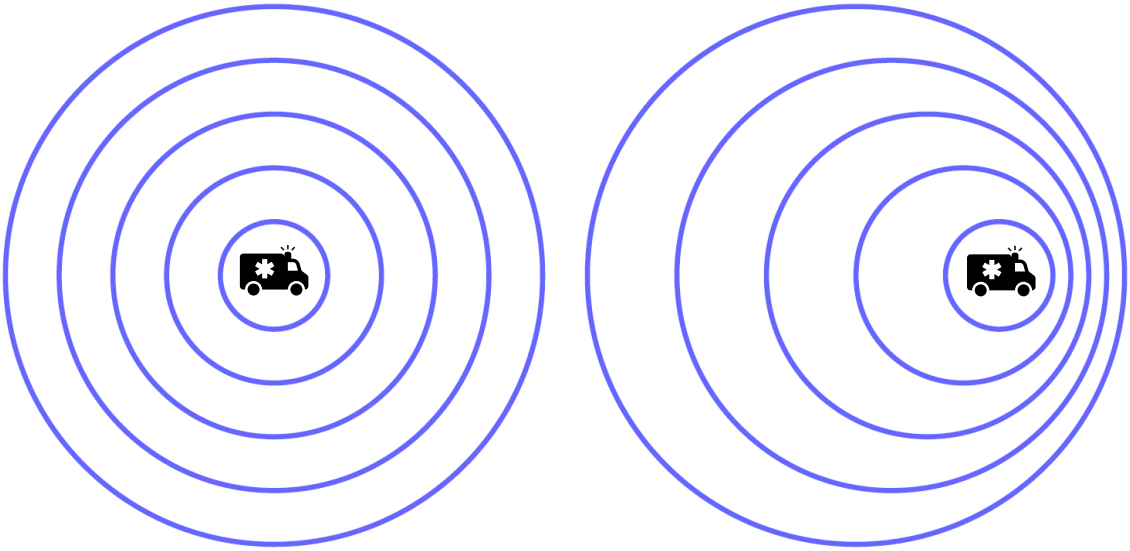

Figure 2.5: Graphical representation of the Doppler effect using the ambulance's siren as an example. When the ambulance is still (left) the perceived frequency is always the same at all locations. When the ambulance is moving (right) the Doppler effect occurs. The perceived frequency is higher when the ambulance moves towards the receiver (front of the ambulance), while it is lower when it moves away from the receiver (back of the ambulance).

2.1.6 Classification of Acoustic Sound Waves

Acoustic sound waves are usually divided into three major groups based on their frequency. **Infrasounds** refers to waves below the human audible spectrum (<20 Hz) [24]. Acoustic waves between 20 Hz and 20 kHz are part of the **audible frequency range** [24]. Lastly, sound waves above the human audible spectrum (>20 kHz) are commonly referred to as **ultrasounds** [24].

Moreover, the audible frequency range is commonly divided in three subgroups, bass, mid-range and treble. Table X shows the classification of acoustic sound waves.

Table 2.1: Classification of Acoustic Sound Waves.

Acoustic Sound wave type	**Frequency range**
Infrasounds	0-20 Hz
Audible, bass	20-250 Hz
Audible, mid-range	250-2000 Hz
Audible, treble	2-20 kHz
Ultrasounds	>20 kHz

2.2 Hearing Systems in Biology

Different animals, including humans, use sound for different purposes, for example for mating, communication or to escape predators. Different animals will hear in different frequency ranges. For example, a healthy adult human can hear approximatively in a range between 20Hz to 20kHz, some dog and cat breeds (depending on breed) can reach, respectively up to 45kHz [26] and 85kHz [27]. Insects are no different as they can detect sound for multiple reasons and on different frequency ranges; albeit some insects do not have auditory systems. This section serves as a review of the current knowledge on auditory systems of humans and insects and arachnids, with a focus on insect and arachnid's mechanosensitive hairs that react to sound.

2.2.1 Human Hearing System

Sound reaches our hearing system mainly into our inner ear and partially from the bones. The pressure pattern of compressions and rarefactions (related to atmospheric pressure) is called *acoustic pressure*. What we call *sound* is basically the way our brain interprets the

electrical signal produced by our ears in response to acoustic pressure [24]. The electrical signal produced by human hearing is composed of a series of pulses, of roughly the same height, that change in response to the pressure wave.

Sound can reach the inner ear in two ways, or, more commonly, a combination of the two, through our bones or by being collected and guided to the inner ear by the pinna [28]. No matter how the sound reaches the inner ear the sound is processed in the same way. An important function of the pinna is to make the change in impedance of the wave coming from the outside to the inner ear smoother, therefore reducing reflection [28]. When the acoustic wave reaches the end of the ear canal part of the wave will be reflected, while the remaining part makes the ear drum vibrate. The three bones in the middle ear (malleus, incus, and stapes) transmit and amplify the ear drum vibration to the oval window. The vibration of the oval window sets the cochlea's fluid in motion, which then sets the cochlea's membranes into a wavy motion [28]. These membranes control the bending of the hair cells inside the cochlea. They bend more when the fluid's flow is stronger. The bending of the hair cells acts as a valve, controlling the firing pulses of the nerves [28]. The more the oval window vibrates, the more the hair cells bend, and eventually, more pulses are sent to the brain. Figure 2.6 gives a graphical representation of the human ear.

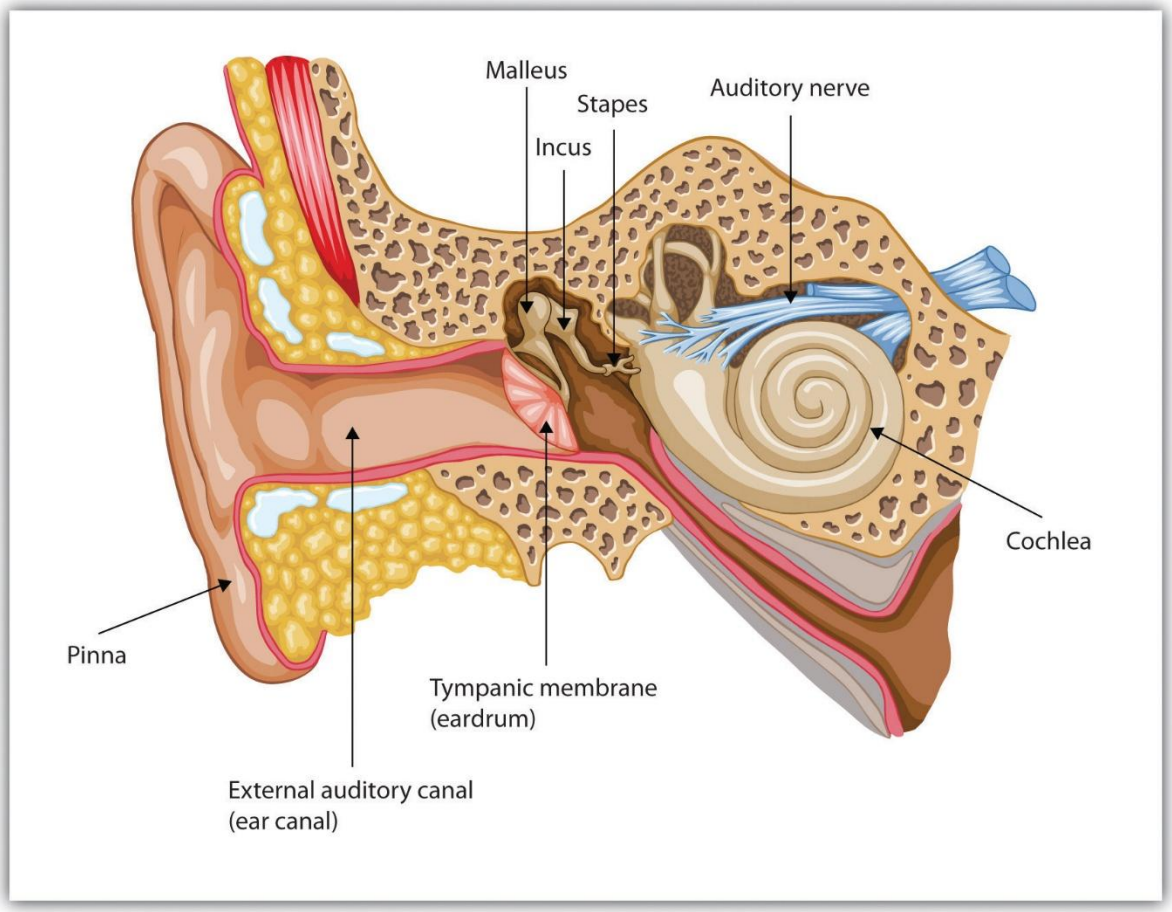

Figure 2.6: Schematic diagram of human ear. Image taken from [29].

2.2.2 Insect Hearing Systems

Insects are capable of hearing sound transmitted through different media, air, water, and even solids. The signals are used for locating predators or prey and for several social interactions. With insects being the most numerous and varied fauna in the world, it should not surprise to know that they also have the most morphologically diverse hearing organs. Hearing organs in insects can have different body location and structure. Nevertheless, they are united by the presence of chordotonal organs. These organs are used in insects to convert different mechanical stimuli, such as acoustic signals or motor movements, to nerve impulses; even though the way this happens is still not clearly understood [30]. Albeit the hearing organs of insects can take different shape and size, they can be classified into four main groups: trichoid sensilla, Johnston's organs, subgenual organs and tympanal organs (Figure 2.7).

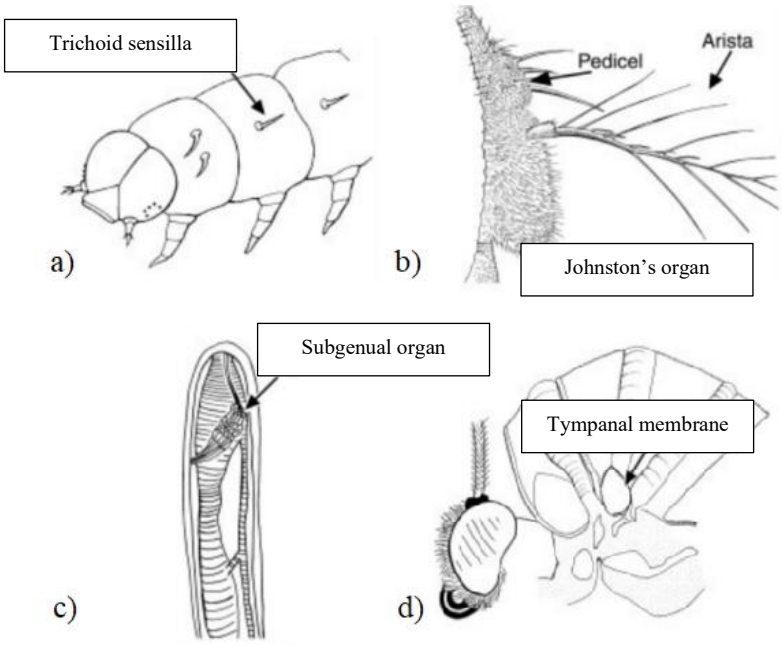

Figure 2.7: Graphic representation of the four main types of insect hearing organs. Trichoid sensilla (a). Johnston's organ, located in the pedicel, (b). Subgenual organ, SO, (c). And tympanal organ, for which the tympanal membrane, can be seen from the outside (d). Adapted from [30].

Trichoid Sensilla (TS), or Trichobothria, Figure 2.7a, is a projection of the cuticle, with a shape resembling a hair, connected at their base by one or more bipolar sensilla [30]. These sensilla are bound to a membrane in their socket and can vary in length depending on the insect (reaching up to 1.5 mm) [31]. Generically, these sensilla are sensitive to near-field air vibration. An example is the caterpillar of the *Barathra brassicae* moth (Figure 2.7a) which uses TS to detect the sound emitted by the wings of predators and respond with defensive reactions [32]. As this organ is the inspiration of this research, a more detailed description follows in chapter 2.3.

Johnston's Organ, Figure 2.7b, is an organ present in most insect species. In all the insects where this organ is present, the antennal flagella is fit loosely in a particular concavity, allowing it to vibrate. The organ is located at the base of the antenna, in the pedicel, and converts antennal vibrations into neural signals via a chordotonal organ [30]. It can have different functions and sizes depending on the insect. In the *Toxorhynchites brevipalpis* mosquito, the

Johnston's organ of the female is less sensitive than the male counterpart. Nevertheless, it can detect antennal deflections as little as ±0.0005° induced by air particle displacements of ±11nm, whence having a much higher sensitivity than any other sound detection organs in other insects [33].

Subgenual Organ (SO), Figure 2.7c, is a chordotonal organ present in the legs of most insects. It is used to detect vibrations through solids [30]. It can have several uses, for example, it is fundamental in lacewing communication [34] and it is used for oviposition by parasitic wasps [35]. Little is known about this organ and further research is required to understand better its structure.

Tympanal Organs, Figure 2.7d, are the most complex, but best studied and described insect hearing organs. They can detect sounds at a few kilometres of distance and can vary greatly across insects to accommodate different frequency detection [30]. They are generally made of three parts [30, 36]:

1. Tympanal Membrane (TM), the ear drum. It is easily visible from the outside and it is made of a thinned region of exoskeleton (Figure 2.7d shows the TM of the butterfly *Hamadryas Feronia*).
2. An internal tracheal sac, filled with air. It is directly connected to the internal face of the TM.
3. One or multiple chordotonal organs which are connected either directly or indirectly to the TM.

TM can occur in any parts of the body. For example, in the scarab beetle *Euethola humilis*, it is located on the neck. This allows the animal to have some degree of control over their auditory sensitivity. When the insect is moving the neck is stretched, exposing the TM, and can pick up ultrasound. Meanwhile, when the head is retracted ultrasound auditory responsiveness disappears, as the TM is covered [37]. Tympanal organs can have different purposes and have

adapted to hear specific frequencies for that. For example, the tympanal organ of the butterfly *Hamadryas Feronia* is used mainly in communication between conspecifics [38]; while the lesser waxmoth *Achroia grisella* has evolved to respond to mating communication and bat echolocation's signals, responding respectively by approaching or evading [39].

2.3 Hair Mechanoreceptors

Trichoid comes from Latin, and it is composed of the word *trich*, meaning "hair", and the suffix *-oid* (from *oides*) which means "resembling". **Sensilla** (plural of sensillum) stems from the Latin word *sensus*, meaning "sense", and they refer to simple sensory receptors. Therefore, we could loosely translate *trichoid sensilla* as "hair-like sensory receptor". In fact, often this is simply referred to as "hair receptor" or "hair mechanoreceptor". This term includes all hair shaped sensory systems that respond to a mechanical stimulus. TS can be classified in different types based on shape of the hair, overall structure, and sensing purpose. This chapter will describe the structure of hair mechanoreceptors, bristles and trichobothria, with a major focus on the latter. Other mechanoreceptors and TS like receptors will also be summarised.

2.3.1 Hair Mechanoreceptor Structure

The cellular organization of sensilla in insects is quite uniform despite their different purposes and sensing modalities. For hair mechanoreceptors we have two common parts; a cuticular component at the top, composed of the hair or club protruding outside and the dome developing around it, and a set of cells, with the sensory neuron cell at its centre, beneath it. By looking at the development of the simple bristle hair mechanoreceptors of flies one can better understand its structure. Interaction of specific genes "decide" which cells in the epidermis will have a "sensory" fate. The "chosen" cell becomes a bristle mother cell (*bmc*) and will undergo two divisions (Figure 2.8a). The first splitting produces the sensory neuron and thecogen mother cell (*smc*), lying lower, and the trichogen and tormogen mother cell (*tmc*),

lying higher. The second division sees the *tmc* splitting into the two cells tormogen (*to*) and trichogen (*tr*), while the *smc* splits into the sensory neuron cell (*sc*) and the thecogen (*th*) [40].

At this point the four cells are oriented parallel to the epithelial and are oriented side by side (Figure 2.8b). The *sc* slides downwards, partially leaving the epithelium (Figure 2.8c, left). The *th* at this stage lies above the neuron (*sc*), the latter will then pierce it, while *tr* grows around the thecogen, and in turn *to* grows around the trichogen, basically enveloping each other (Figure 2.8c, centre). At this point the tormogen is the one at the highest position, and remains the only cell bordered by the epithelium. During this process a glial cell, most likely of epidermal origin, appears at the base of the sensory cell, enveloping the axon and the basal part of the neuron (Figure 2.8c, centre, the glial cell is the only one non-coloured) [31, 40]. Glial cells comprehend a wide number of cells that provide support to the neurons and serve several functions, from helping the development of the neurons and their function to helping in the reaction of the nervous systems to trauma and disease [41]. At this point the cell grows (Figure 2.8c, right), the *tr* will form the hair shaft, while the *to* will form the hair socket and joint membrane basal to the hair. Moreover, the dendritic sprout of the *sc* remains inside the *th*, while the glial cell encloses the neuron's axon [40].

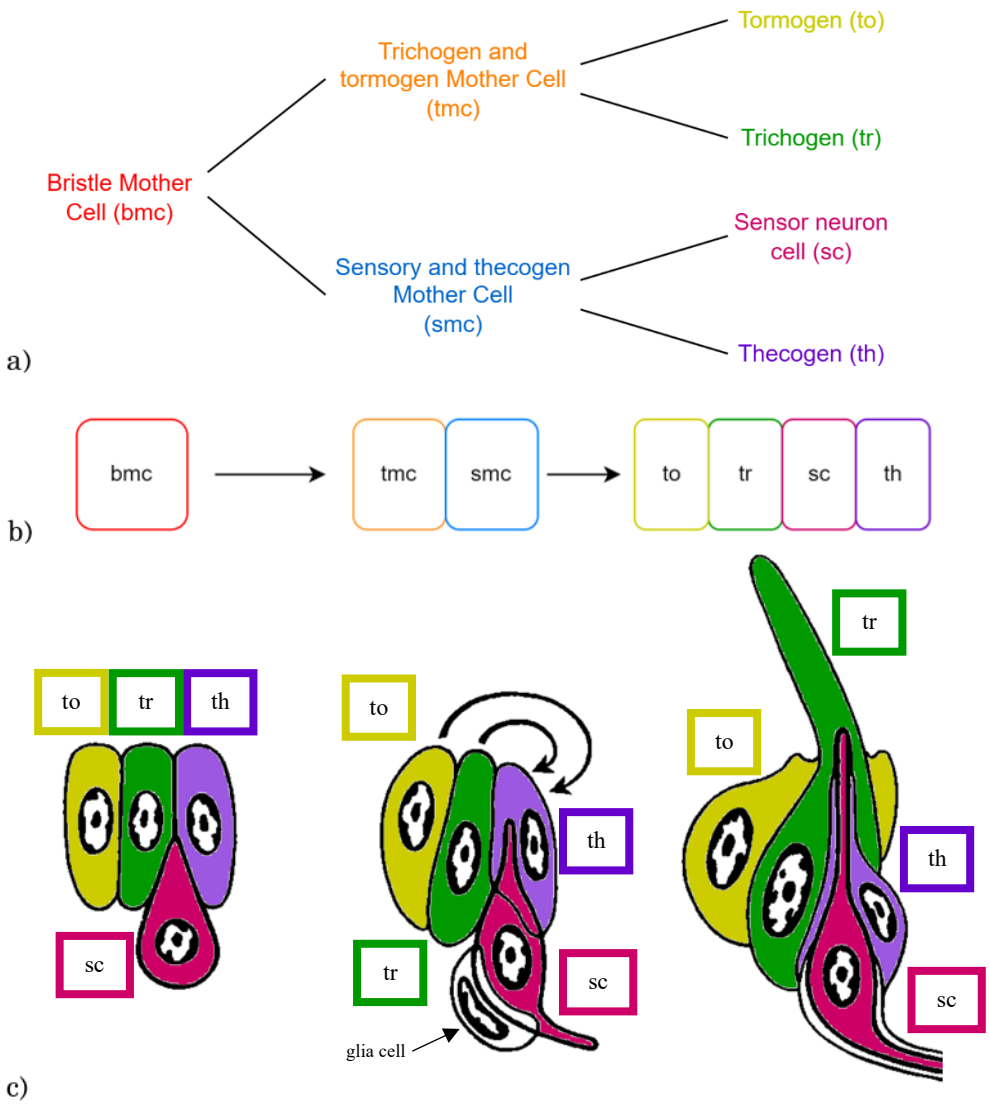

Figure 2.8: Development of mechanoreceptor. Cell division tree (a), cell division at the epithelium (b), graphical representation of the mechanoreceptor formation (c). The cells and names have been colour coded for easy recall. Image (c) adapted from [40].

The high-level operation of the hair mechanoreceptors is quite simple. When a mechanical stimulus moves the hair structure, the sensory cell is stimulated by being stretched or compressed, which in turn generates an electric signal. The sensilla can have different modifications to accommodate the reception of diverse mechanical stimuli. The hair can have a different shape (e.g., club, long and thin, circular, flattened, etc.), length (from a few micrometres up to a few millimetres and diameter (several micrometres). The cuticle can also have different shape and can support the hair in different ways depending on the application, for example, it can direct the hair towards only one axis, stopping the movement of the hair in

other directions. The receptor cell can also show directional sensitivity. Electrical activity is produced only in the intended direction of operation and deflection in the opposite might not produce a signal at all. Sensitivity of the receptors can be very high, even the smallest deflection below thermal noise can produce electrical spikes [31, 42]. Figure 2.9 shows an example of a cricket hair sensilla. The hair acts as a lever, a large deflection at the apical region of the hair translates into a small deflection at the basal region. The displacement angle, α, can be evaluated by considering the length of the hair.

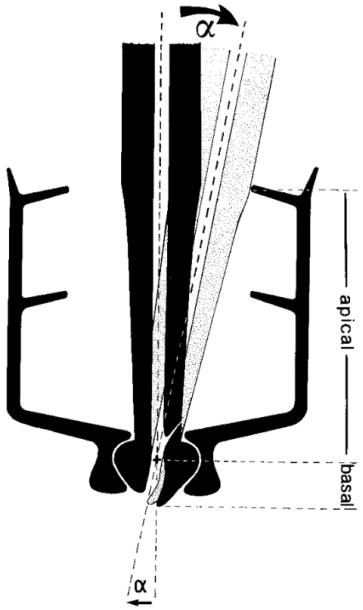

Figure 2.9: Schematic of cricket hair mechanoreceptor. Image taken from [31].

Hair mechanoreceptors are usually of two types:

- **Bristles** mainly respond to touch.
- **Trichobothria (or filiform sensilla)** mainly respond to air currents and sound.

2.3.2 Bristle Mechanoreceptors

Bristles (Figure 2.10) are one of the most common mechanoreceptors, they usually respond to direct touch. The hair shaft is bent to give the mechanoreceptor mono-directionality. Bending the hair downwards will move the hair base, and consequently the dendrite upwards, exciting the neuron. They can have several purposes, for example they are present in the neck of the

honeybee to monitor the position of head and thorax. Other insects may have them in other positions for other purposes. For example, in some flies they are present across the whole body to measure the position of the head, wings, etc [31].

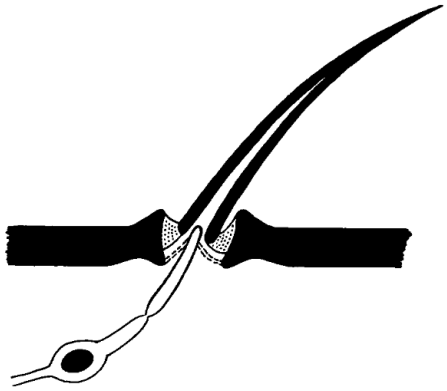

Figure 2.10: Schematic of a generic bristle hair mechanoreceptor. Image taken from [31].

2.3.3 Trichobothria

Trichobothria (plural of trichobothrium), is composed of *trich* (hair), and the Latin *bothrium*, meaning cup, referring to the cup-shaped cuticulum from which the hair protrudes outside (Figure 2.11). Although the name itself does not specify that these mechanoreceptors react to air flow and/or sound, the usage of this name often refers to this specific purpose. In the 70s German researchers referred to trichobothria with more purpose specific names, for example hörhaare (hair of hearing) or ferntastsinnesorgane (distance tactile sense organ) [43]. Nevertheless, none of these are still in use nowadays. Sometimes they are referred to as "filiform sensilla" or similar name to indicate the shape of the hair shaft. Filiform sensilla or trichoid sensilla are names typically used for insects, while trichobothria seems to be the preferred choice for arachnids.

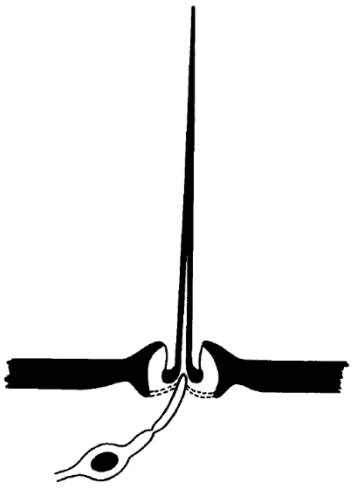

Figure 2.11: Schematic of a generic trichobothria. Image taken from [31].

The hair shaft here is mostly deflected by air currents, low-frequency sound, or medium vibration but can also be shaped to allow other purposes (e.g., gravity, vibration, tactile, etc.) [31, 32, 43-45]. The hair socket (or *bothrium*) is typically structured in a way that allows the hair to deflect only in one axis direction, but on some occasions, for example in spiders, they allow movement in multiple directions [31, 43-45]. The bothrium also serves the purpose of limiting the amplitude of motion, and therefore damage to the sensilla [45]. The hair in trichobothria can have different shapes. It can be rod-like, flattened, club-shaped, spoon-shaped, twisted, its surface can be flat or rough with ridges, and so on [31, 32, 43-45]. The hair is always hollow inside [45]. At the basal region, the hair can be hinged, most common in insects (Figure 2.12a), or suspended, most common in arachnids (Figure 2.12b). In the case of hinged structures, the restoring force of the hair is given by the hinged shape in the socket; while, in suspended structure it is given by radial fibrils [45]. Often, trichobothria are positioned across the body in arrays, of the same exact hair (to increase sensitivity, or provide directionality), like in the case of the *Barathra brassicae* [32], or of different sizes (to be sensitive to different frequencies) like in some scorpion species [44] or the cerci of crickets [31]. They can also have different placements on the body, and therefore serve diverse purposes [45].

a) 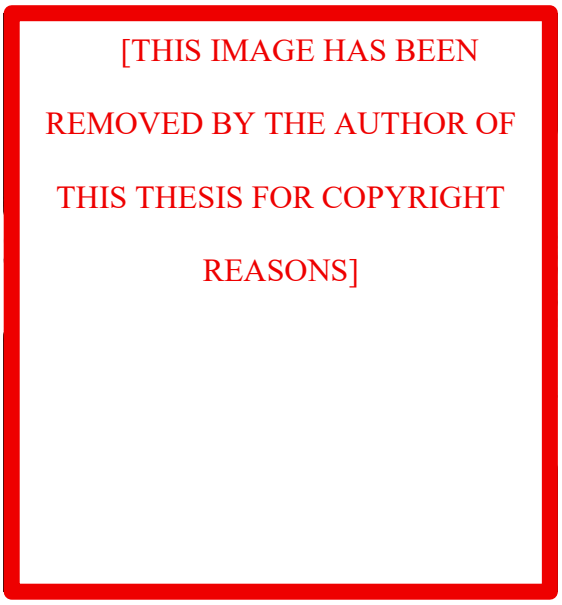

b) 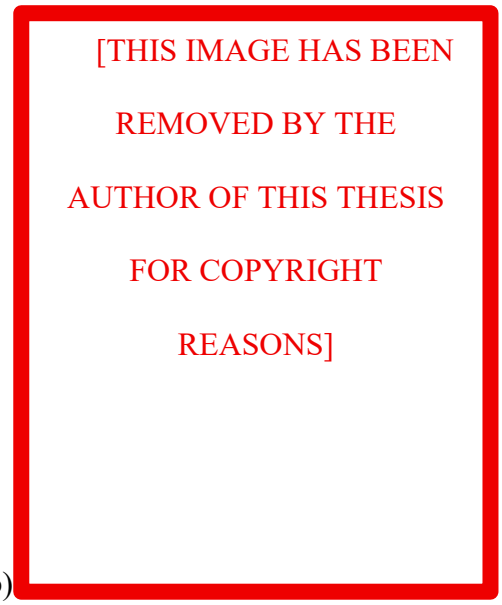

Figure 2.12: Reconstruction of (a) hinged trichobothria of an Acheta cricket and (b) suspended trichobothria of a Tegenaria spider. Images taken and modified respectively from [46] and [47].

The basal area of the hair is composed of an elastic tissue, while the hair itself is rigid. This gives a high difference in stiffness between the two regions that allows for the energy of the airflow to be deflected to the basal area instead of being lost by bending of the hair shaft. This ensures that the energy is efficiently transferred at the elastic tissue responsible for signal generation [48, 49]. The difference in aspect-ratio between the basal region and the protruding hair also ensures maximum efficiency, as the shorter is the basal area compared to the hair shaft the higher is the strain at the elastic tissue [48]. Zhang et. al, proved this phenomenon by simulating a simplified cantilever model and the stress experienced by the elastic component (Figure 2.13) [48].

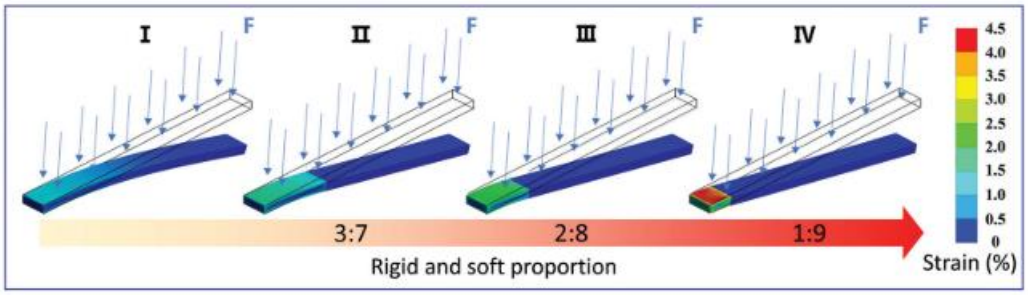

Figure 2.13: Stress analysis of a simplified trichobothria in cantilever shape, composed of different aspect-ratios between a soft and elastic material and a rigid one. From left to right the ratios soft to rigid are 1/0 (only soft), 3/7, 2/8 and 1/9. Image taken from [48].

Some researchers have reported a resonant frequency to sound in trichobothria, whilst others doubt this conclusion, saying the spectrum of frequencies to which the trichobothria reacted was very wide, with no clear resonances [32, 43, 45]. Another plausible conclusion would be that the animals can control the stiffness of the basal area, therefore allowing the trichobothria to discriminate different frequencies [43, 49]. This seems reasonable as developed numerical models of TS show that the resonant frequency depends mainly on torsional stiffness of the trichobothria, and size of the hair [50-53].

2.3.4 Other Insect Mechanoreceptors

Other insect mechanoreceptors exist. Mainly the campaniform sensilla and the scolopidial organ. **Campaniform Sensilla** (Figure 2.14) are characterized by the presence of a cupola instead of a hair shaft (from here it takes the name, *campana* means “bell” in Latin). The cupola is inserted in the shaft and produces a signal whenever it is deformed. For this reason, they are usually placed in parts of the body that may experience a deformation. Of utmost importance is their presence near wings, and often near the base of hairs. Research has also shown their operation as gyroscope oscillators [31].

Figure 2.14: Schematic of a generic campaniform sensillum. Image taken from [31].

The **scolopidial organ** (Figure 2.15) is a mechanoreceptor placed inside the insect's body. It is therefore important in the detection of mechanical stress within the body of the insect. It is for example involved in other insect hearing organs, such as the tympana of crickets or the mosquito's Johnston's organ [31].

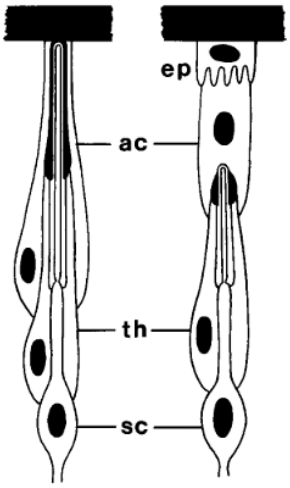

Figure 2.15: Schematic of a generic scolopidial organ with the separate parts that compose it. Epidermis (ep), attachment cell (ac), thecogen cell (th) and sensory cell (sc). Image taken from [31].

2.3.5 Similar Receptors

In insects, other receptors more or less similar to mechanoreceptors exist. It is argued for example that mechanoreceptors might be derived from **contact chemoreceptors** (**taste sensilla**), as the latter has mechanosensitive cells [31]. Another similar receptor is the **olfactory sensilla** [46], its resemblance can be seen in Figure 2.16. Hill et. al, even refer to the olfactory antenna of the *Culex quinquefasciatus* mosquito with the name "trichoid sensilla", since these

sensilla are hair-like [54]. The infrared receptor of the *Melanophila acuminata* beetle (Figure 2.17), is a thermoreceptor believed to be descendent from mechanoreceptors, as its essential principle of operation is a cuticle expansion given by a change in temperature that squeezes the dendritic tip, exciting the neuron [55].

Figure 2.16: Schematic of trichobothria (left) and olfactory sensillum (right). The sensory cell (sc) is enveloped by the thecogen (th), trichogen (tr), and tormogen cell (to). The axon is enveloped by the glia cell (gl), and the whole epithelium (ep) is underlain by the basal lamina (bl). The outer dendritic segment (od), which is enclosed by the dendrite sheath, runs through the outer receptorlymph cavity (orl). In mechanoreceptors, its tip, which contains the tubular body (tb), is supported by the socket septum (ss) and attached to the hair shaft, which is suspended in the joint membrane (jm). The figure shows the similarity between the two sensilla. Image taken from [46].

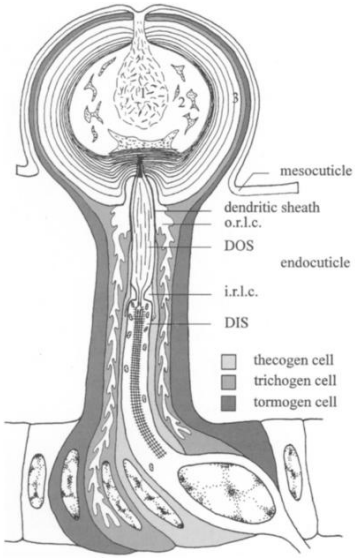

Figure 2.17: Schematic of the Melanophila acuminata beetle's infrared sensillum. Image taken from [55].

2.4 Sensing methodologies

Sensors convert a measurand (input) into an appropriate measurement value (output). In this thesis, sensors are referred to as devices that convert a mechanical quantity (e.g., force) into an electrical quantity (e.g., voltage). Actuators instead, are the opposite, converting electrical quantities into mechanical ones. Some devices can also do both and are employed in a different way based on the application, in that case they are usually referred to as transducer. Figure 2.18 shows a simple principle for sensors and actuators with a few examples.

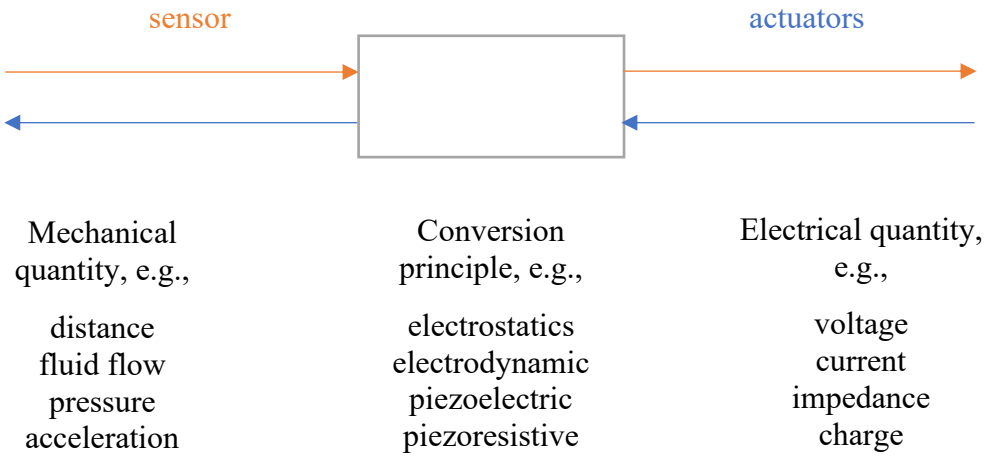

Figure 2.18: Conversion principle of sensors and actuators, and example of input and output quantities.

Before delving into the current sensor technologies that are inspired by insects and arachnids' hair mechanoreceptors, or more widely by hair, this subchapter aims at explaining the basics of the main sensing methodologies. This thesis will focus only on capacitive, piezoelectric and piezoresistive sensors for three reasons, they are the most widely used in the market, they are the ones used in other hair sensors and, lastly, they were the methods considered for the sensors developed in this work due to their simplicity of implementation to the sensory structures. A higher level of detail will be given on piezoresistive sensing as it is the one that worked best for this thesis, while the other section will explain the reason behind the exclusion of the other methods from this work. Some of the other common sensing mechanisms are electromagnetic, inductive and photoelectric, but given their complexity to implement them in the sensor structures proposed in this thesis they will not be described.

2.4.1 Capacitive sensors

The physics underlying capacitive sensors is electrostatics, i.e., the study of electric conductors, non-moving electric charges, dielectrics and DC potential sources. The most common, and simple, capacitive geometry is the one of two parallel plates (Figure 2.19), and it is the main one used in capacitive sensors. Capacitance between two parallel plates is calculated as in equation (2.3) [56].

$$C = \frac{\varepsilon_0 \varepsilon_r A}{d} \tag{2.3}$$

Where,

C capacitance, measured in farads

ε_0 dielectric constant of vacuum

ε_r relative dielectric constant of the material between the plates, 1 for vacuum

A area of the plate in square meters

d space between the two plates in meters

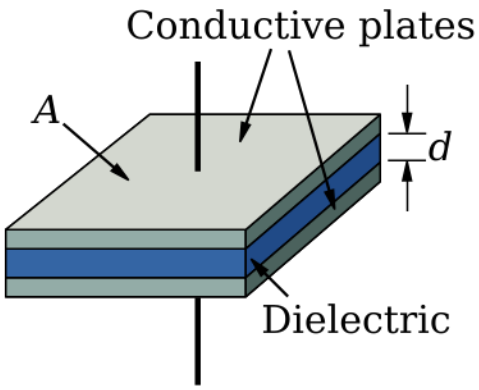

Figure 2.19: Schematic of parallel plate capacitor. Image taken from [57].

Equation (2.3) is at the base of the principle of capacitive sensors. Other geometries would have altered equations, but the principle of the sensor is the same in all cases, i.e., change one of the parameters in the equation to result in a change of capacitance that can be measured by appropriate circuitry [56, 58]. In most cases the dielectric stays constant, therefore the changes are made to either the distance of the plates, or their overlap. By changing the distance *d* of the plate (e.g., by pushing one plate down in a force sensor), the capacitance will change in a non-linear manner. Alternatively, one can measure the impedance as

$$Z = \frac{1}{2\pi f C} \tag{2.4}$$

In this case measuring the impedance of the capacitor for a change in distance, the change will be linear. Figure 2.20 shows a simplified diagram.

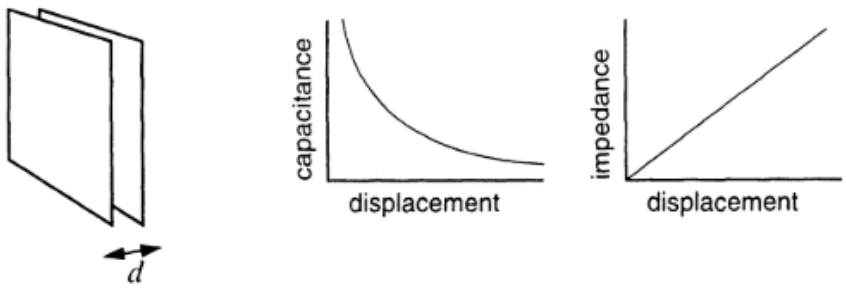

Figure 2.20: Capacitance sensor with plate distance variation. Image taken from [56].

In the case of same area plates, unwanted changes might occur if the plate is displaced in the two unwanted axes. To solve this issue the plates might be underlapped or overlapped and of different sizes (Figure 2.21). This can work because the average overlap of the two plates should not affect the signal, and the base capacitance will not vary in case of this unwanted translational motion.

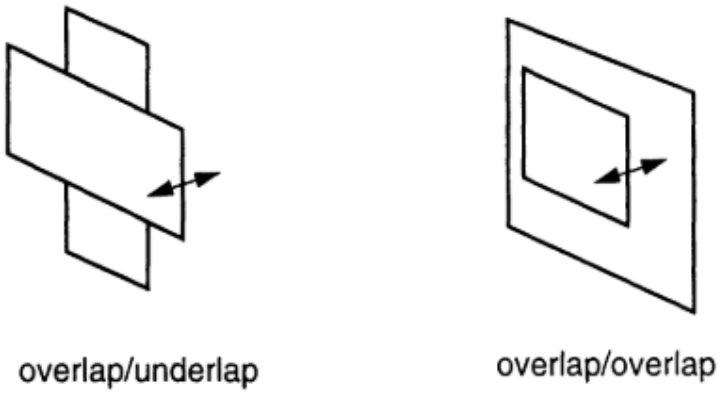

Figure 2.21: Examples of overlap/underlap configurations in capacitive sensors. Image taken from [56].

Another method of sensing is by varying the area of overlap A (Figure 2.22). This configuration can also be subject to unwanted motion of the plates distance and tilt, but these issues can be easily mitigated by appropriate design. Area displacement can occur linearly or by rotation.

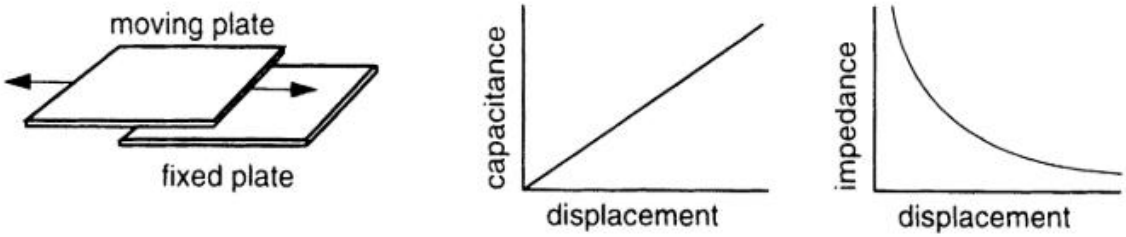

Figure 2.22: Capacitance sensor with area overlap variation. Image taken from [56].

In some sensors (especially in the chemical field), the change can also occur in the dielectric and therefore the change in capacitance is given by a change in the relative dielectric constant ε_r. Another method described in literature is the one of planar capacitive sensors [59], in which the two plates are placed side by side (Figure 2.23), nevertheless the capacitance in this case is usually much lower than conventional configurations and the variation is even smaller.

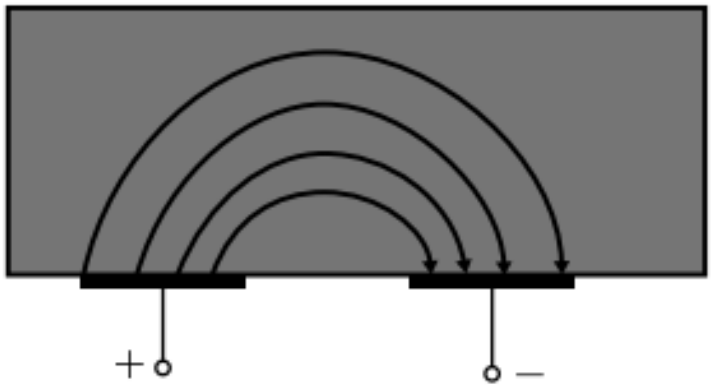

Figure 2.23: Planar capacitive sensor configuration. Image taken from [59].

Capacitive sensors have the advantage of introducing lower electrical noise to the measurement system compared to other techniques; meaning that the noise of this sensor is mainly given by the amplifier, and other sections of the circuit [60]. Other advantages are low temperature sensitivity, low 1/f noise and low power consumption [60, 61]. Nevertheless, the capacitance of sensors is usually very low, in the range of picofarads and below, and the measurement system can be affected by parasitic capacitances (often in the picofarads range), these are unavoidable and unwanted capacitances found between components of a circuit [56]. Capacitance changes are often below the picofarads range, this means that parasitic capacitances are usually higher than the changes in the sensor, which might affect the

measurements. They can be reduced by having the conditioning circuit closer to the sensor itself, but even this has limits as even amplifiers will have some parasitic capacitances [56]. Other disadvantages of capacitors are their relatively high voltage of operation and often the difficulty in manufacturing a high aspect ratio gap that is narrow enough to produce feasible measurements [56]. Often the fabrication of small enough gaps is also sensitive to defects, moisture and thin-film damping. Several readout and conditioning circuits for capacitive sensors exist in literature and they can change in resolution, power consumption, or can be application specific, they will not be described in this thesis as they were not used but the following references contain conventional readout method, latest progress in literature and comparative reviews [56, 58, 61-71].

Albeit more details are included for the exclusion of this method from the thesis in **4.2 Design ideas for artificial acoustic hair sensors and** results, together with performed experiments and simulations, the main reasons are:

- Difficulty for the inclusion of cables or connection between the plates and circuitry
- Difficulty in producing a narrow enough gap
- Low capacitance change, in the range of fF or aF (from simulation)
- Low reproducibility of a consistent gap size
- Defects given by evaporation to produce thin-film metal coatings
- The fact that capacitive sensing is active, i.e., it increases the power draw

2.4.2 Piezoelectric sensors

Piezoelectricity is a word that comes from ancient Greek. It combines *piezo*, meaning to squeeze or press, and *elektron*, meaning amber, an early source of static electricity. Therefore, it loosely means ‘electricity due to pressure’. In 1880, the Curie brothers discovered that certain materials, like quartz and topaz, generate electric charges when mechanical forces are applied.

They called this the *direct piezoelectric effect*. A year later, Lippmann theorised an *inverse piezoelectric effect* should exist too. The Curie brothers confirmed his theory. During the First Great War piezoelectricity was first used in sonars. Research into new materials and applications grew in the following decades. In the Second Great War, several research groups discovered synthetic materials that out-performed natural ones like quartz. Today, research focuses on new, lead-free materials, with comparable qualities to commercially used ones. There is also work on piezoelectric microelectromechanical systems (MEMS), piezoelectric polymers and 3D-printing of piezoelectric structures [72-74].

The physics behind piezoelectricity goes beyond the scope of this thesis, but if the reader is interested in them a good reference is [72]. The basic principle is that some materials exhibit mechanical-electrical interaction. When these materials deform, they show changes in electrical polarization. If electrodes are connected to the material, voltage changes can be measured. The inverse piezoelectric effect, instead, causes deformation of the material when voltage is applied to the electrodes. Depending on the direction of the mechanical force and resulting electric polarization, piezoelectricity is distinguished by different modes. In accordance with literature, the space direction for the following subchapter is denoted by [1, 2, 3] instead of [x, y, z] or [i, j, k, l, m, n], Figure 2.24 illustrates this notation with Cartesian coordinates. The basic equations used in literature for piezoelectricity is a reduced notation of the so-called *d*-form or strain-charge form that ignores thermal effects, shown in equations (2.5) and (2.6) [72]. Other forms exist in literature, the *e*-form (or stress-charge form), and the rare *g*-form and *h*-form. There are symmetries in piezoelectric materials that can simplify equations (2.5) and (2.6), but they are material specific and not reported here.

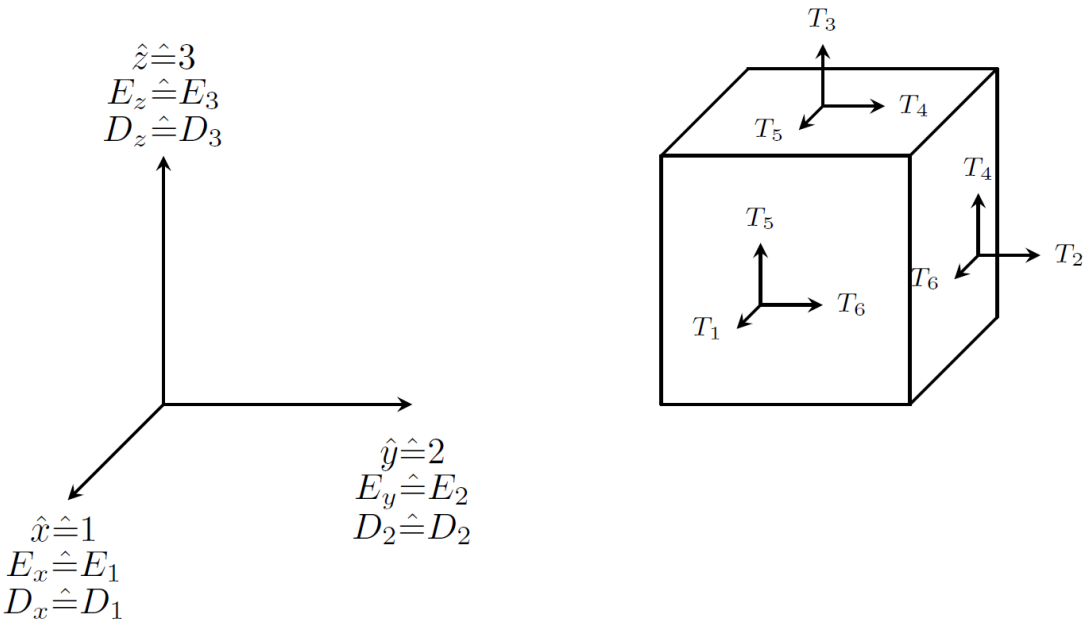

Figure 2.24: Common notation for reduced set of equations for piezoelectricity with respect to xyz Cartesian coordinates.

$$\begin{bmatrix} D_1 \\ D_2 \\ D_3 \end{bmatrix} = \begin{bmatrix} \varepsilon_{11}^T & \varepsilon_{12}^T & \varepsilon_{13}^T \\ \varepsilon_{21}^T & \varepsilon_{22}^T & \varepsilon_{23}^T \\ \varepsilon_{31}^T & \varepsilon_{32}^T & \varepsilon_{33}^T \end{bmatrix} \begin{bmatrix} E_1 \\ E_2 \\ E_3 \end{bmatrix} + \begin{bmatrix} d_{11} & d_{12} & d_{13} & d_{14} & d_{15} & d_{16} \\ d_{21} & d_{22} & d_{23} & d_{24} & d_{25} & d_{26} \\ d_{31} & d_{32} & d_{33} & d_{34} & d_{35} & d_{36} \end{bmatrix} \begin{bmatrix} T_1 \\ T_2 \\ T_3 \\ T_4 \\ T_5 \\ T_6 \end{bmatrix} \tag{2.5}$$

$$\begin{bmatrix} S_1 \\ S_2 \\ S_3 \\ S_4 \\ S_5 \\ S_6 \end{bmatrix} = \begin{bmatrix} d_{11} & d_{21} & d_{31} \\ d_{12} & d_{22} & d_{32} \\ d_{13} & d_{23} & d_{33} \\ d_{14} & d_{24} & d_{34} \\ d_{15} & d_{25} & d_{35} \\ d_{16} & d_{26} & d_{36} \end{bmatrix} \begin{bmatrix} E_1 \\ E_2 \\ E_3 \end{bmatrix} + \begin{bmatrix} s_{11}^E & s_{12}^E & s_{13}^E & s_{14}^E & s_{15}^E & s_{16}^E \\ s_{21}^E & s_{22}^E & s_{23}^E & s_{24}^E & s_{25}^E & s_{26}^E \\ s_{31}^E & s_{32}^E & s_{33}^E & s_{34}^E & s_{35}^E & s_{36}^E \\ s_{41}^E & s_{42}^E & s_{43}^E & s_{44}^E & s_{45}^E & s_{46}^E \\ s_{51}^E & s_{52}^E & s_{53}^E & s_{54}^E & s_{55}^E & s_{56}^E \\ s_{61}^E & s_{62}^E & s_{63}^E & s_{64}^E & s_{65}^E & s_{66}^E \end{bmatrix} \begin{bmatrix} T_1 \\ T_2 \\ T_3 \\ T_4 \\ T_5 \\ T_6 \end{bmatrix} \tag{2.6}$$

Where,

D_i electric flux density

ε_{ij}^T electric permittivities for constant mechanical stress

E_i electric field density

d_{mkl} piezoelectric strain constant

Sensing methodologies

T_p mechanical stress

S_p mechanical strain

s_{ijkl}^E elastic compliance constant for constant electric field density

According to the constitutive equations of piezoelectricity (2.5) and (2.6), there are 18 possibilities in total to couple the electrical and mechanical components of the material (d_{11}, …, d_{36}). Each possibility belongs to one of the four possible modes of piezoelectric coupling, longitudinal (L), transverse (T), longitudinal shear (S_L) and transverse shear (S_T). The mechanical stress in a specific mode causes a macroscopic change ΔP of the electric polarization in one direction [72]. Figure 2.25 illustrates the four modes in a cube. Table 2.2 summarizes the link between piezoelectric strain constants, mechanical stress and flux density with the four modes. Described in detail below.

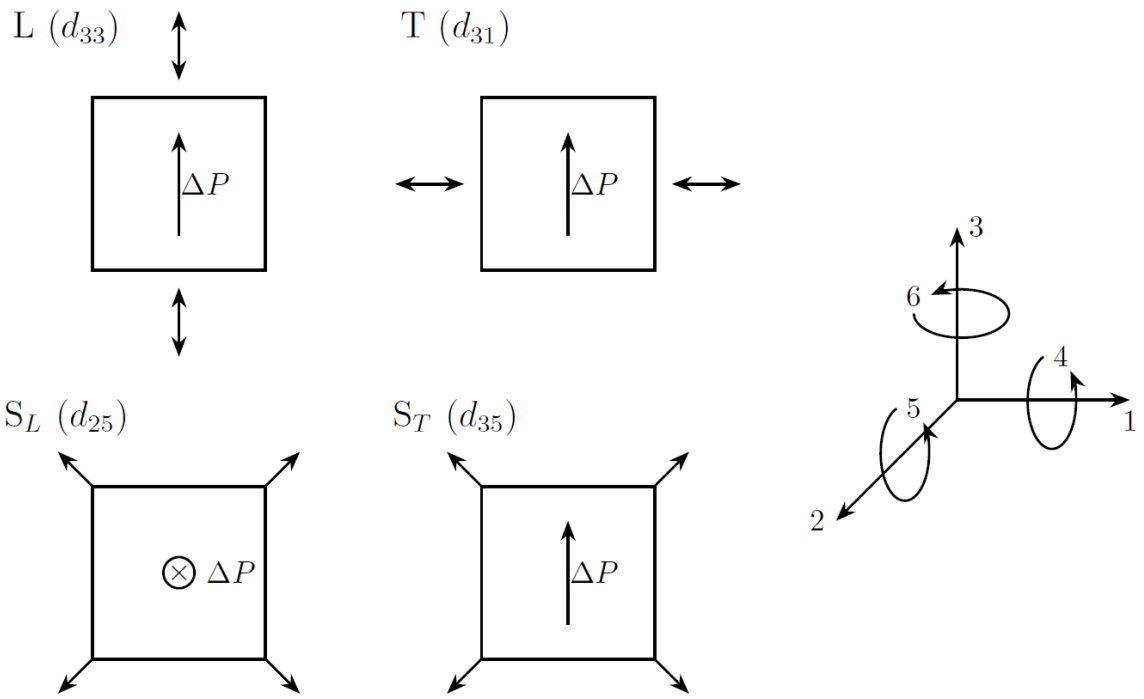

Figure 2.25: Examples of the four modes of piezoelectricity, longitudinal (L), transverse (T), longitudinal shear (S_L) and transverse shear (S_T) in a cube; producing a ΔP macroscopic electric polarization change.

Table 2.2: Piezoelectric strain constant d_{ip} assigned to the four piezoelectricity modes, longitudinal (L), transverse (T), longitudinal shear (S_L) and transverse shear (S_T). Image taken from [72].

	T_1	T_2	T_3	T_4	T_5	T_6
D_1	d_{11}	d_{12}	d_{13}	d_{14}	d_{15}	d_{16}
	L	T	T	S_L	S_T	S_T
D_2	d_{21}	d_{22}	d_{23}	d_{24}	d_{25}	d_{26}
	T	L	T	S_T	S_L	S_T
D_3	d_{31}	d_{32}	d_{33}	d_{34}	d_{35}	d_{36}
	T	T	L	S_T	S_T	S_L

- In the case of **longitudinal mode** (L) the stress produces a change of electric polarization in the same direction. This mode is characterized by the following piezoelectric strain constants d_{11}, d_{22} and d_{33}.
- In the case of **transverse mode** (L) the change of electric polarization is perpendicular to the applied mechanical load. This mode is characterized by the following piezoelectric strain constants d_{12}, d_{13}, d_{21}, d_{23}, d_{31} and d_{32}.
- For **longitudinal shear stress** (S_L) the polarization changes perpendicular to the plane in which the piezoelectric material is sheared. This mode is characterized by the following piezoelectric strain constants d_{14}, d_{25} and d_{36}.
- For **transverse shear stress** (S_T) the polarization changes in the plane in which the piezoelectric material is sheared. This mode is characterized by the following piezoelectric strain constants d_{15}, d_{16}, d_{24}, d_{26}, d_{34} and d_{35}.

Often, the electromechanical coupling factor k^2 is included to rate the efficiency of conversion from mechanical to electrical energy (and vice versa), it is calculated as per equation (2.7), with the indices pq referring to the direction of applied mechanical loads and electrical quantities, respectively [72]. Depending on the material the coupling factors differ

significantly. For example, certain materials, like cellular polymers provide large values for k_{33} but small k_{31} values. There is no piezoelectric material that is perfect to all applications, therefore one needs to find the correct material for the specific application based on the material parameters. Reference [72] gives a good comparison between the several materials, provides values for the most common ones and general advantages and disadvantages.

$$k_{pq}^2 = \frac{d_{pq}^2}{\varepsilon_{pq}^T s_{pq}^E} \tag{2.7}$$

The change of polarization state of piezoelectric materials under a mechanical load can be read out as a change in electric charge. And if it is connected to electrodes the electrical charge can be measured as a change in voltage. Circuits to interpret the output of a piezoelectric sensor are described in [72].

2.4.3 Piezoresistive sensors

Changes in conductivity for telegraph cables was an issue in the 19th century, this motivated observation of conductivity under strain. In 1856, William Thomson reported for the first time a change in resistance when iron and copper where elongated [75]. Motivated by this work, Tomlinson extended measurements of change in conductivity in other metals under mechanical load and electrical current [76, 77]. The following decades saw a general interest in research for this phenomenon, and in 1935, Cookson first used the term '*piezoresistivity'* to describe it, most likely coined after piezoelectricity [78]. In 1950, Bardeen and Shockley predicted large conductivity changes in semiconductors [79], and only four years later it was shown by Charles Smith in strained silicon and germanium [60]. Nowadays piezoresistive sensors represent a big portion of the MEMS sensors market [60].

Considering a rectangular cuboid (Figure 2.26), the electrical resistance (R) measured between its ends is calculated with equation (2.8). It depends on its length (l) and width (w) and height (h) of its cross-section, and the material's resistivity (ρ) [60]. Applying a mechanical load at one end of the cuboid while holding the other stationary will apply strain to the material. For an elastic change in length there will be a longitudinal strain, equation (2.9), which will also change the width of the material due to contraction, in proportion of its Poisson's ratio, υ, equation (2.10). Ultimately, the relative change in resistance can be written in terms of strain as equation (2.11), and the gauge factor (GF) is defined as in equation (2.12) [60]. Metals experience a small resistivity change with strain, while semiconductors are generally higher, with a high dependence on the dopant concentration and doping method involved [60].

$$R = \frac{\rho l}{wh} \tag{2.8}$$

$$\varepsilon_1 = \frac{\Delta l}{l} \tag{2.9}$$

$$\Delta w = -\upsilon \varepsilon_1 w \tag{2.10}$$

$$\frac{\Delta \mathrm{R}}{\mathrm{R}} = \frac{\Delta \rho}{\rho} + (1 + 2\upsilon)\varepsilon_1 \tag{2.11}$$

$$GF = \frac{\frac{\Delta R}{R}}{\varepsilon_1} \tag{2.12}$$

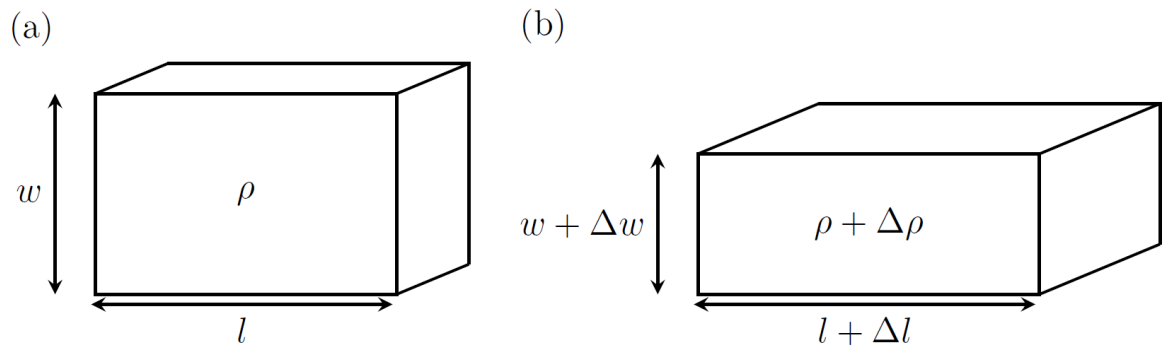

Figure 2.26: A rectangular cuboid and the parameters that allow the evaluation of its resistance, length, l, width, w and material's resistivity, ρ (a). When the rectangular cuboid is under mechanical stress all three values can potentially change, leading to a resistance change (b).

The electrical resistance (and its variance) of a piezoresistor can be monitored in a variety of techniques. The most common one is to force a known current through a resistor (R_{pr}) and measure its voltage drop. This is done with a method called *four-wire measurement* (Figure 2.27a), this is usually involved in multimeters and ohmmeters. The change in voltage is simply calculated using Ohm's law, equation (2.13). Unfortunately, in this method there is no way to compensate for temperature induced change in output, which is often larger than the one induced by a mechanical load. Another method that can be used to convert a resistance change in a voltage signal is to apply a voltage across a resistor and a piezoresistor and measure the output voltage across the latter, this is often called *voltage divider* (Figure 2.27b). Here there can be temperature compensation if the other resistor (R_{tc}) has the same temperature coefficient of the piezoresistor, but no mechanical loading applied, as they will both change at the same rate due to a change in temperature. Equation (2.14) shows how the voltage output can be calculated (and thence any resistance changes). A disadvantage of this measurement method is that the sensitivity of the piezoresistor drops by a factor of two or smaller [60]. Nevertheless, in the above stated methods there is a main issue, the voltage offset is usually much larger than the induced voltage changes induced by stress in the piezoresistor. This is a problem because

data acquisition circuits have a finite resolution, therefore these small resistance changes might be buried under the offset voltage.

$$V_{out} = IR_{pr} \tag{2.13}$$

$$V_{out} = V_{bridge}\frac{R_{pr}}{R_{pr} + R_{tc}} \tag{2.14}$$

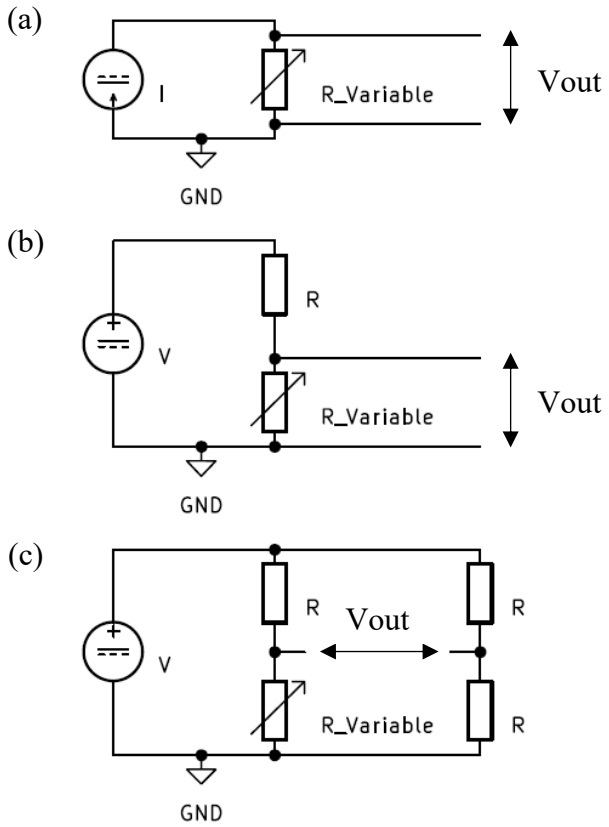

Figure 2.27: Most common ways to transduce a resistance change into a voltage, four-wire measurement (a), voltage divider (b) and Wheatstone bridge (c).

The most used circuit for resistance-induced voltage changes is called *Wheatstone bridge* (Figure 2.27c). First described in a tedious and confusing way by Christie in 1833 [80], it was described better and linked to Ohm's law by Wheatstone ten years later, highlighting its importance for the output null method [81]. Albeit Wheatstone quoted Christie in the English version, this does not appear in the German and French versions (the most common languages in the European scientific world in the 19th century), which is probably the reason why this

configuration is remembered by the latter's name [82]. The biggest advantage of this circuit is that it allows, if properly balanced, to cancel the voltage offset, i.e., the output will be zero if there is no strain on the piezoresistor. Compared to the 4-wire configuration, the sensitivity is reduced by a factor of four if we only use one mechanically loaded piezoresistor (this is also called *quarter-active configuration*). The sensitivity can be increased if the circuit is composed by two or four more piezoresistors (respectively *half-bridge* and *full-bridge* configurations) on the mechanically loaded element. These configurations are often used to add sensitivity to more directions (for example to measure transverse and shear stress). In the half-bridge configuration, we have the same temperature and stress sensitivity as in the voltage divider (with the added advantage of output nulling) [60]. Further signal conditioning circuitry is usually involved at the output to perform amplification, filtering, noise compensation, non-linearity correction and other operations to improve the signal further. References [60, 73] give a comprehensive description of the different methods.

2.5 Past hair-like bioinspired sensors

Since the 2000s there has been interest in the use of hair-like structures across nature as inspiration for the creation of sensors. Therefore, this subchapter serves as a summary of the research done on these sensors. The subchapter attempts to create a historical timeline of the progress made in this field for the different sensing methods. Different sensing methodologies have been used by different research teams, the main ones being capacitive, piezoresistive and piezoelectric. Some researchers have made used of the triboelectric phenomenon and in 2024 the first papers using optical methodologies have been reported. The production techniques involved in the production of the sensors are mainly the common Micro Electromechanical Systems (MEMS) ones, with only one sensor being produced via 3D printing in 2020. In 2018 Han et al. wrote a review about hair-inspired sensors from the 2010s and provide a comparison

between them [83]. In 2020, Rajasekaran et al. proposed the first 3D-printed hair-inspired sensor [20].

2.5.1 Piezoresistive hair-inspired sensors

In the year 2000, Ozaki et al., presented at the IEEE 13th Annual International Conference on Micro Electro Mechanical Systems pioneering research showing two designs of sensors modelled after the hairs of insects [1]. These are, to my knowledge, the first hair-inspired sensors. The first one is represented by an array of cantilevers with a strain gauge at the bottom, Figure 2.28a. This iteration can only detect the force component of air flow acting in the front or the back of the sensor, i.e. 1-DOF (Degree Of Freedom). The second one instead is cylindrical, and it can also measure the direction angle of the airflow (2-DOF), Figure 2.28b. These sensors are piezoresistive.

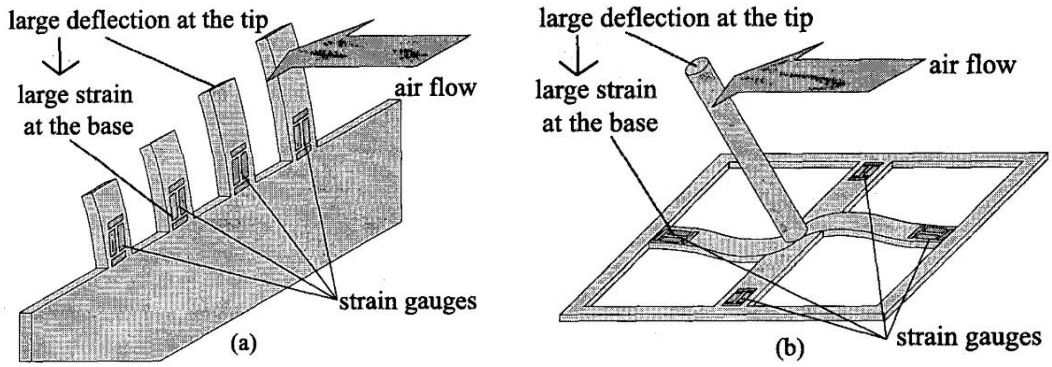

Figure 2.28: Schematic diagram of the hair-inspired sensors developed by Ozaki et al. [1]. 1-DOF sensor (a) and 2-DOF sensor (b).

The reported response of these first sensors was quite good, and it shows sensitivity between tens of cm/s to ~2 m/s [1]. The response of the 1-DOF sensors seemed to be more linear, with the 2-DOF showing a logarithmic trend (Figure 2.29).

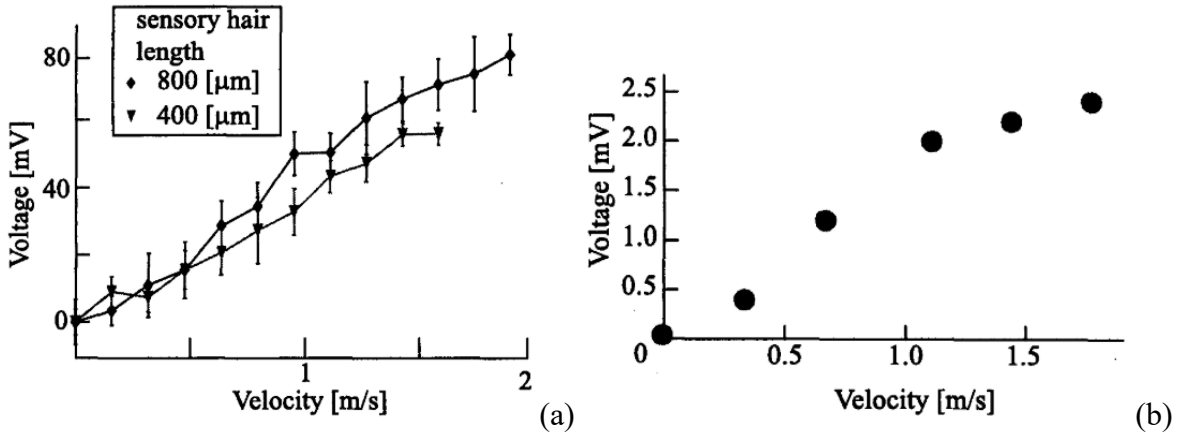

Figure 2.29: Relationship between the airflow and the electric signal output of the sensors produced by Ozaki et al. [1]. Response for different lengths of the 1-DOF sensor (a), and response of the 2-DOF sensor (b).

A dependency of the sensor's response to different hair sizes was recorded [1]. The 2-DOF sensor also shows a relationship between the direction angle and the output voltage, allowing to understand the direction of the airflow, Figure 2.30.

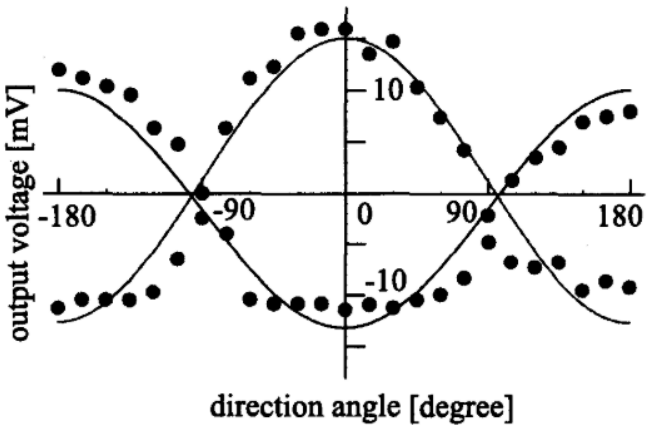

Figure 2.30: Relationship between the airflow angle and the output of the 2-DOF sensor produced by Ozaki et al. [1].

In 2015, Ko et al. proposed an acceleration hair-inspired sensor (Figure 2.31). These sensors have a resolution of 0.576 mV/g, a range of ±5 g and a noise equivalent input acceleration resolution of 86 mg [2].

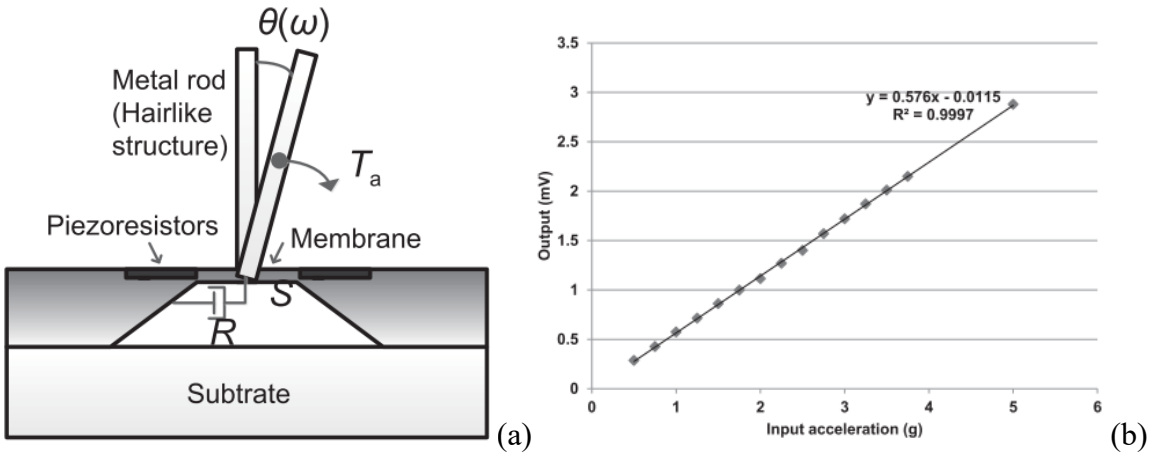

Figure 2.31: Diagram of acceleration hair-inspired sensor developed by Ko et al. [2] (a), and its recorded response (b).

Maschmann et al. proposed a piezoresistive carbon nanotube hair-inspired sensor (Figure 2.32) that has a measurements threshold of less than 1 m/s, a limit of 10 m/s and a resistance change between 1.3 % and 1.8 % per 1 m/s changes in air speed [3]. Slinker et al. later showed an alternative version of this sensor showing resistance changes between 1% and 5% per 1 m/s changes in air speed [4].

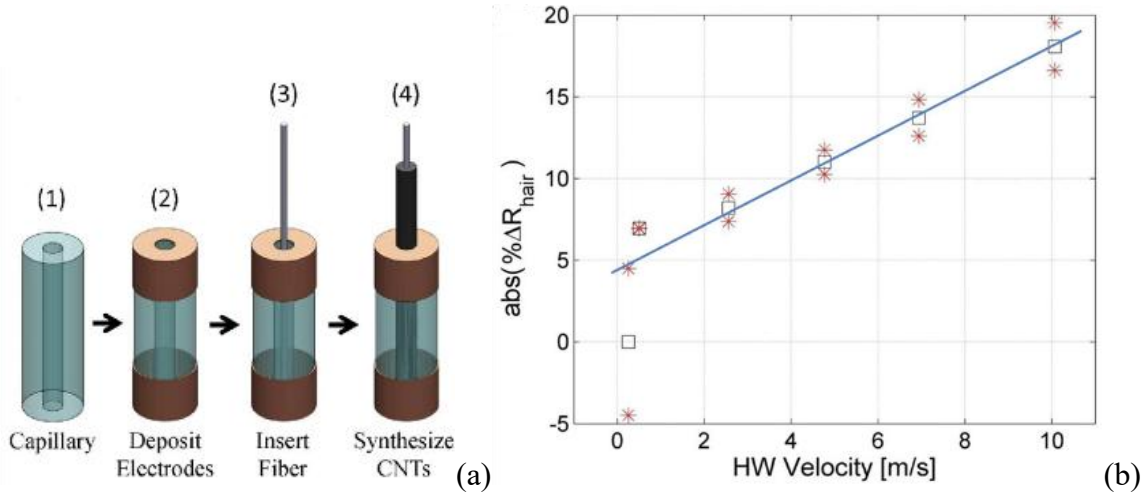

Figure 2.32: Carbon nanotube (CNT) based hair-inspired sensor developed by Maschmann et al. [3], production process (a) and results to an applied airflow (b). In the plot the squares are the time-averaged measurements taken by the sensors, and the red stars are the error bars that represent the ±2 standard deviation from 7 complete ramping cycles.

Shi et al. developed a force hair-inspired sensor that used liquid metal as the piezoresistive component [5]. The researchers applied normal and shear stress to the sensor showing a change of resistance in both cases and in two directions, Figure 2.33.

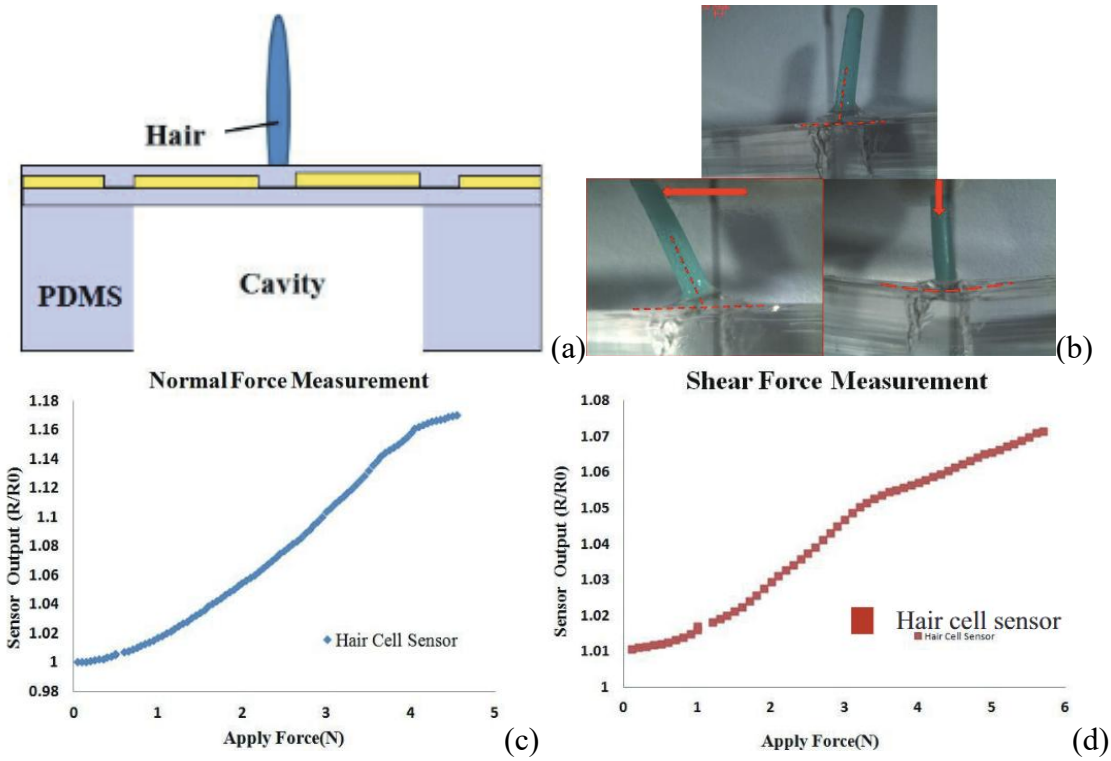

Figure 2.33 Diagram of force hair-inspired sensor developed by Shi et al. [5], the section in yellow is the liquid metal (a). Photos of the produced sensor deformed under normal or shear stress. Sensor's output due to normal force measurement (c) and due to shear force measurements (d).

Han et al. proposed a force hair-inspired sensor produced entirely with polymers (Figure 2.34), and showing great resistance changes in resistance for hundreds of micrometre displacements and able to take measurements in 3 axes, making it unidirectional [6].

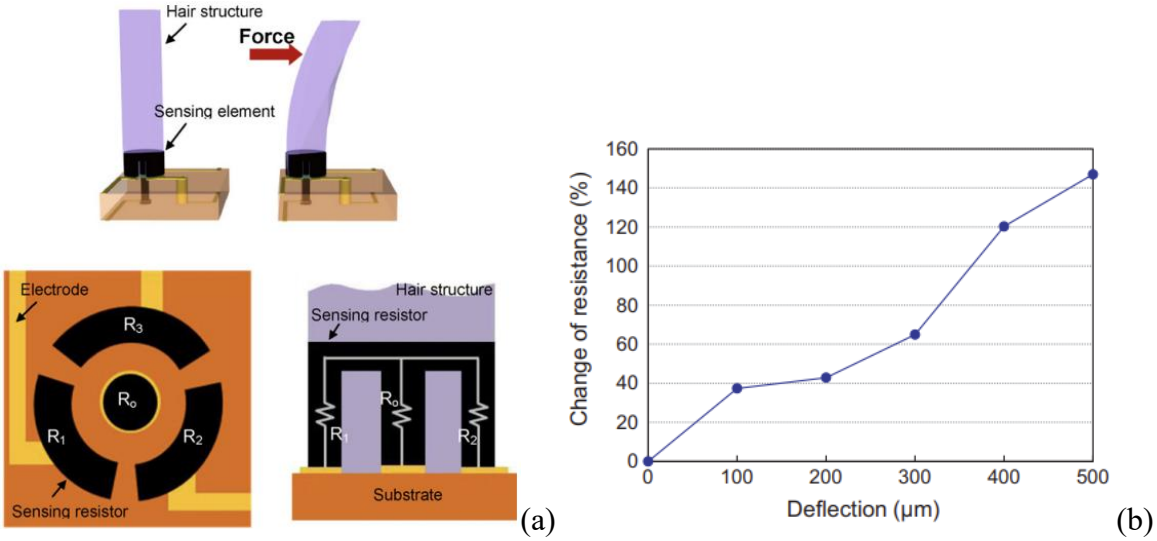

Figure 2.34: Diagram of the sensor proposed by Han et al. [6] with horizontal and vertical section view of the sensing element (a), and its response (b). In the sensing element, R_0 does not vary, and the changing/sensing resistances are only R_1, R_2 and R_3.

Qualtieri et al. proposed a piezoresistive sensor inspired by the lateral line of fishes [7]. It is a curved cantilever-like structure (Figure 2.35). This sensor shows a 1.38%/mbar change in resistance when a flow is applied in the direction opposite of the curvature, and 0.2%/mbar resistance variation for a flow applied in the direction of the sensor's curvature [7]. This research group later produced a parylene-coated version for underwater use [8], and it investigated its use in array for freestream flow measurements [9].

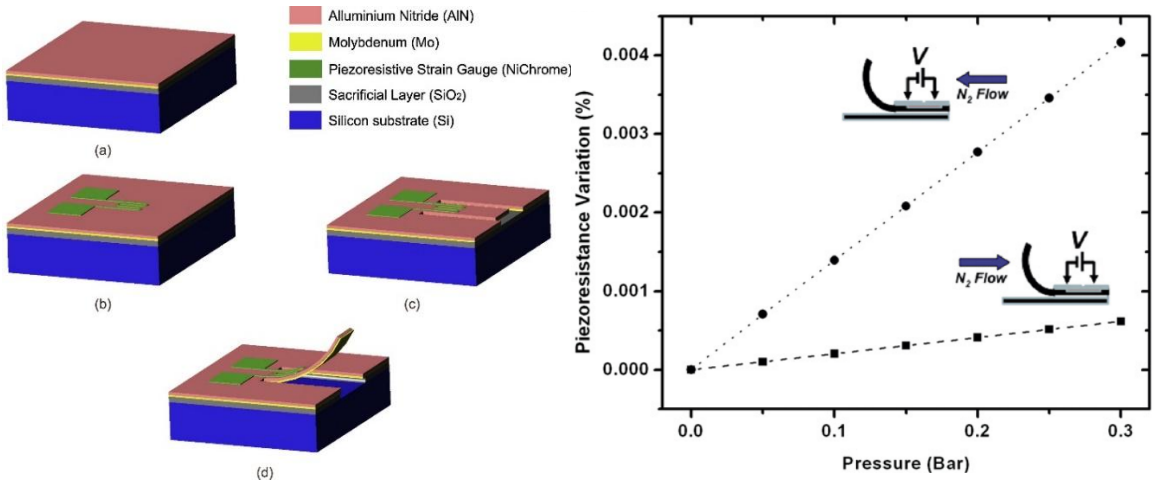

Figure 2.35: Production process of the sensor proposed by Qualtieri et al. inspired by lateral line of fishes, left, and its response to nitrogen flow, right [7].

Kottapalli et al. in their artificial hair sensor also replicated the cupula around the hair that is found in some fishes [10, 11]. Testing of their sensor showed that the inclusion of the cupula enhanced the response both in air and water, Figure 2.36. They recorded that cupula, compared to the naked hair sensor, improved the response from 22 mV/(m/s) to 77 mV/(m/s) and the resolution from 0.039 m/s to 0.018 m/s.

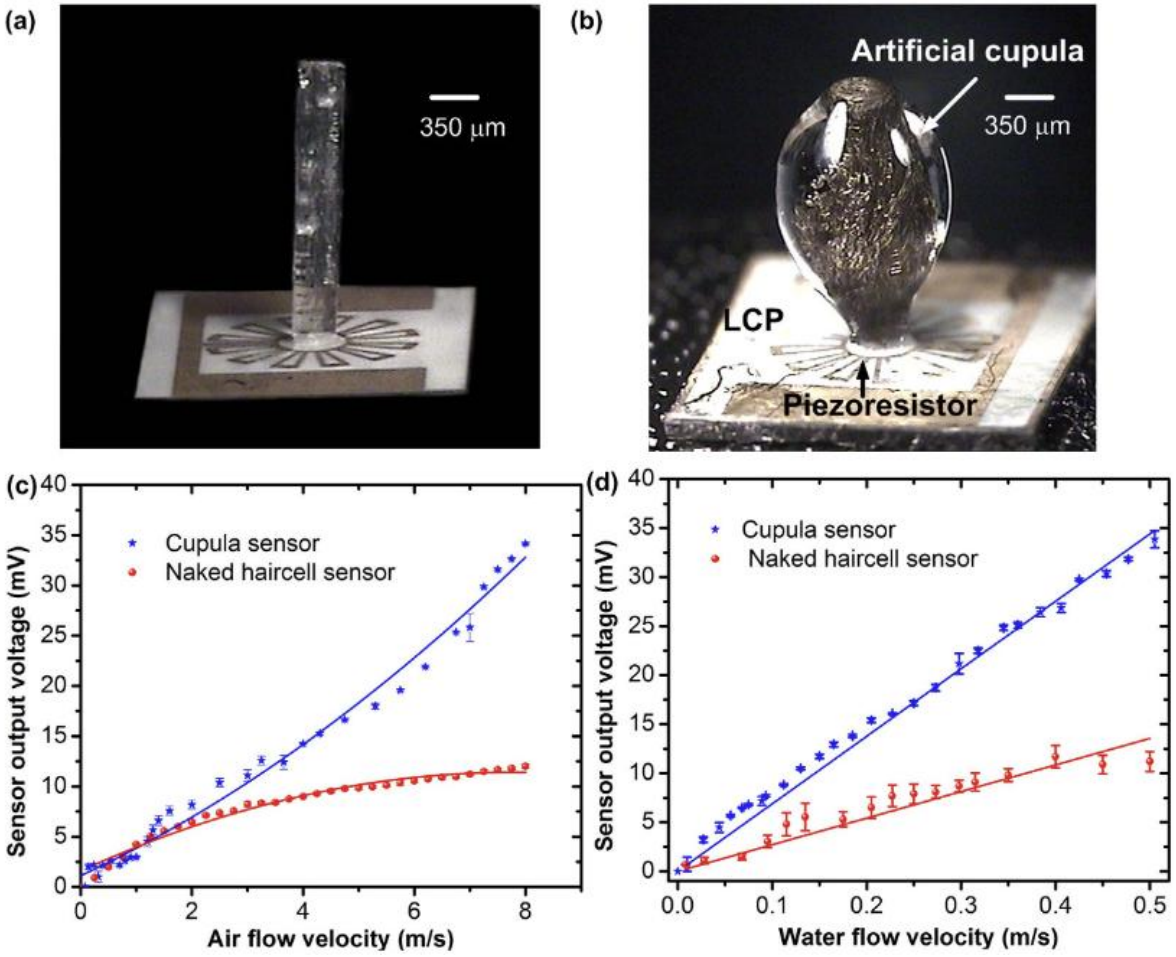

Figure 2.36: Flow sensing experiments of the sensor produced by Kottapalli et al. [11]. Naked hair cell sensor (a). Hydrogel-dressed sensor showing the hydrogel cupula (b). Experimental results of air flow sensing conducted in wind tunnel (c) and results of the water flow sensing experiments conducted in the water tunnel (d).

Shen et al. produced a flexible hair-inspired sensor similar to some of the sensors that were proposed in the last decade, but they made it in an array of four to allow for directional sensing, Figure 2.37a. Moreover, they included temperature compensation directly on the body of the sensor. The sensors showed a detection range of 0-40.5 m/s with a resolution of 4 mm/s [12]. The array showed potential for omni directional sensing, but it requires further improvements as it can be seen in Figure 2.37b.

(a)

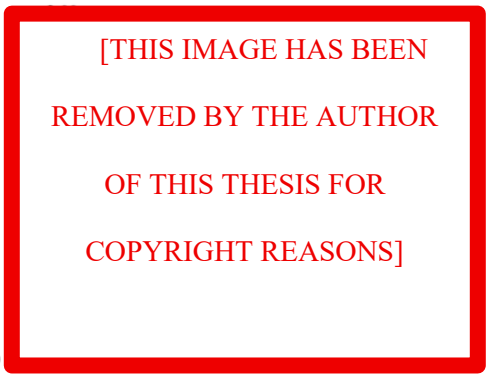

(b)

Figure 2.37: Diagram of the flexible hair-inspired sensor proposed by Shen et al. [12] (a), and its results for omnidirectional sensing (b).

Tran et al. instead of developing an ad-hoc hair-inspired sensor used four commercially available piezoresistive force sensors on a PCB and a 3D-printed artificial hair to transform airflow into pressure to the force sensors, Figure 2.38. The sensor shows an angular resolution of 2.25˚, a flow resolution of 4.93 mm/s and a sensitivity of 9.24 mV/(m/s) in single mode and 20.3 mV/(m/s) in differential mode [13]. Single mode refers to the response of a singular force sensor, while differential mode refers to the difference of the outputs of two opposite force sensors. Moreover, it is reported to have a range of 0-500 m/s. The biggest disadvantage of this sensor is undeniably its size. The hair is considerably bigger when compared to the previously presented alternatives, the artificial hair has a diameter of 3 mm and a length of 20.6 mm, this size does not even include the cupola (not shown in Figure 2.38) and the bottom section with the force sensors. Previously reported hair-inspired sensors are typically a few millimetres tall.

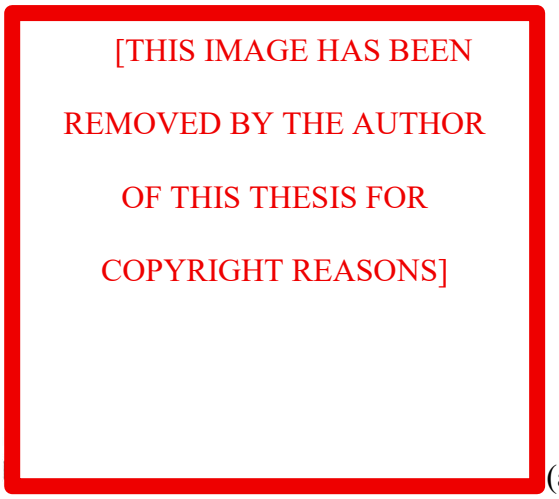

(a)

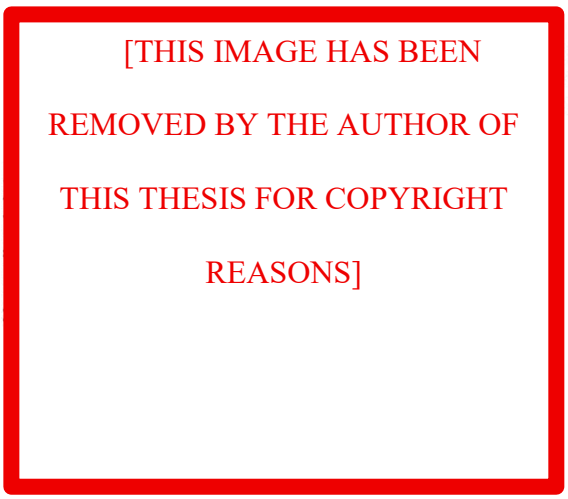

(b)

Figure 2.38: Diagram of the hair-inspired sensor presented by Tran et al. [13] (a), and normalized output due to airflow in different directions (b).

2.5.2 Capacitive hair-inspired sensors

In the 2000s two projects commissioned by the European Union have been of particular importance for hair-like inspired sensors. Apart from being one of the first projects creating hair-inspired sensors, their importance is given by the collaboration between entomologists and engineers. The sensors designed throughout these projects are capacitive. The first project is the Cricket Inspired Perception and Autonomous Decision Automata (CICADA) project, which ran from 2002 to 2005 and saw the collaboration of four universities [84]. The goal was to combine interdisciplinary knowledge in the creation of MEMS sensors inspired by the cerci (trichoid sensilla) of the crickets. The goal was also to develop an array of such sensors for airflow sensing. Such arrays were successfully produced (Figure 2.39) and showed directionality in 1-DOF and could perform a range of measurements between 0.1 m/s to 1 m/s [14]. The possibility to change the stiffness of the sensor (and therefore its sensitivity) via a different voltage bias was hypothesized. The artificial hairs were up to 1 mm tall. It was also suggested that such system could allow sensitivity to acoustic signals.

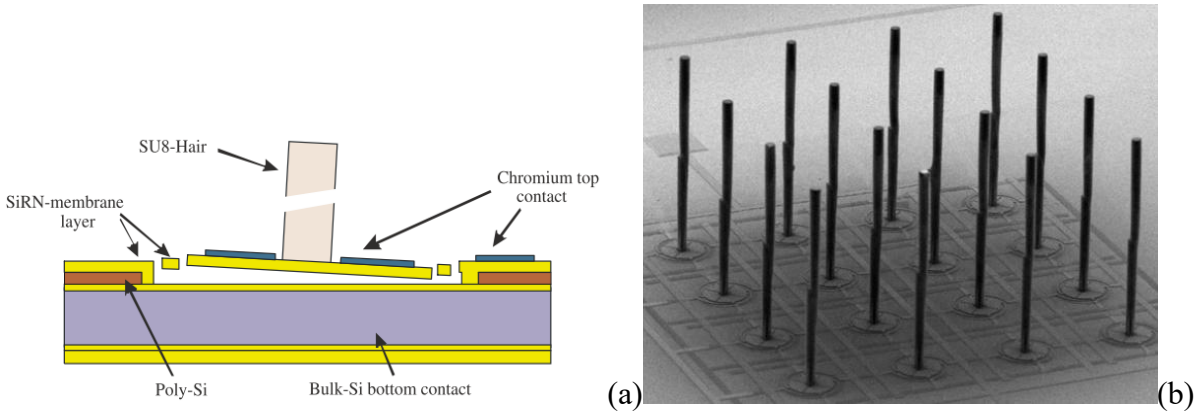

Figure 2.39: Hair sensors produced during the CICADA project [14, 84]. A diagram of the hair-inspired sensor (a), and a picture of the array of sensors, with the hair being ~1 mm tall (b).

From 2005 to 2010 seven universities collaborated on the Customized Intelligent Life-Inspired Arrays (CILIA) project, of which only two had worked also on CICADA project, The University of Reading and Universiteit Twente [85]. This project built upon the previous by investigating further the sensor's response, improving the sensor's geometry and presenting its application. The acoustic sensitivity of the sensor was proved by using a laser doppler vibrometer (LDV) and a speaker, showing the angular rotation of the plates at the sides of the hair, which served as the top capacitive plates, Figure 2.40 [15]. In the same paper Krijnen et al. modelled the transduction mechanism and predicted that with circular plates with radius of 100 microns (as in Figure 2.39) the sensitivity would be 9.0 pF/rad, while changing them to rectangular membranes 200 microns wide and 100 microns long the sensitivity would increase to 15.4 pF/rad [15].

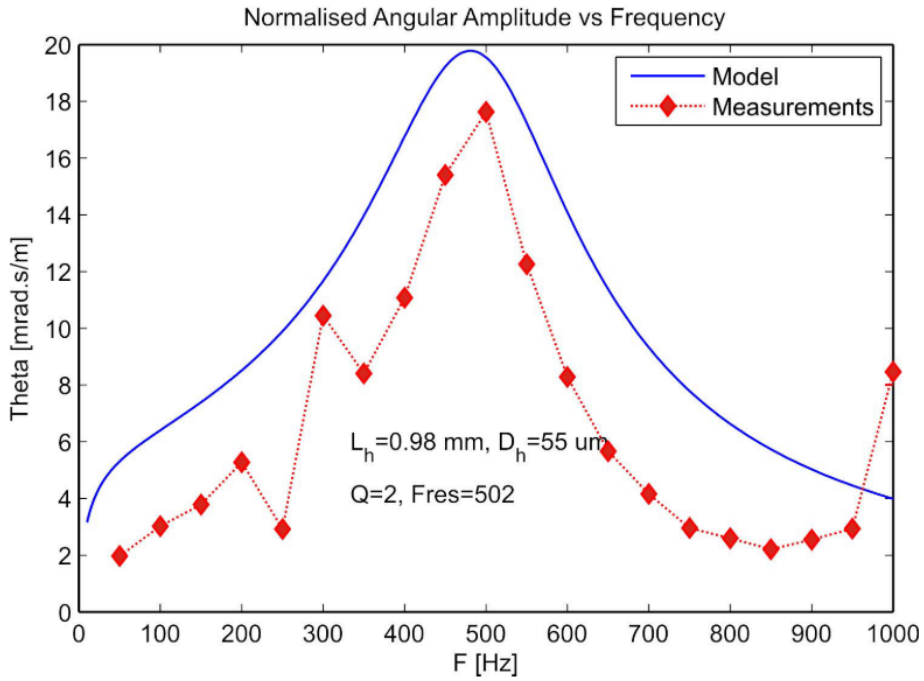

Figure 2.40: Angular rotation of the capacitive plates of the hair-inspired sensor in [15], normalized to 1 m/s flow-velocity amplitude obtained from measurements and as predicted by the model. L_h and D_h are the length and diameter, respectively, of the cylindrical hair.

The hair with squared capacitor plates was later produced (Figure 2.41) and its experimental electric response recorded for a flow frequency of 120 Hz due to different voltage bias (Figure 2.42). Wiegerink et al. proved that a different bias voltage changed the response of the sensor, changing the magnitude of displacement and the sensor's resonant frequency [16]. The sensor was further optimized by Izadi et al by reducing the curved capacitive plate [17]. Dagamseh et al. used these sensory arrays for flow pattern recognition [86], dipole source localization [87] and for high-resolution flow field visualization [88]. Izadi et al., inspired by the superficial neuromast found in fishes, altered the fabrication process of this hair-inspired sensor to insulate the electric part from liquid with the purpose of using these sensor arrays underwater [89]. It is important to note that these sensors were designed to work combined as arrays instead of alone since the capacitance of only one sensor, and its capacitance variance, was too little.

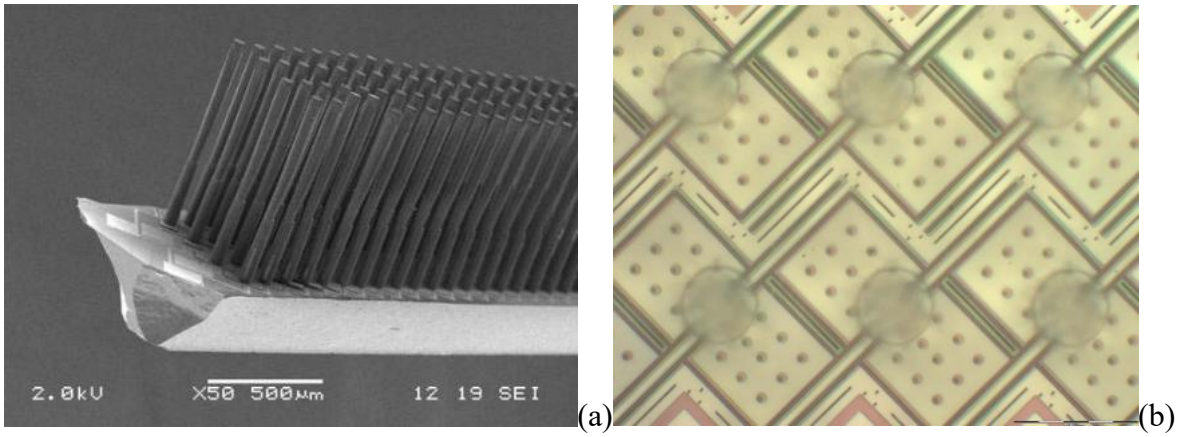

Figure 2.41: Photograph of the sensor array produced during the CILIA project with squared capacitive plates (a), top view of a section of the array (b) [16].

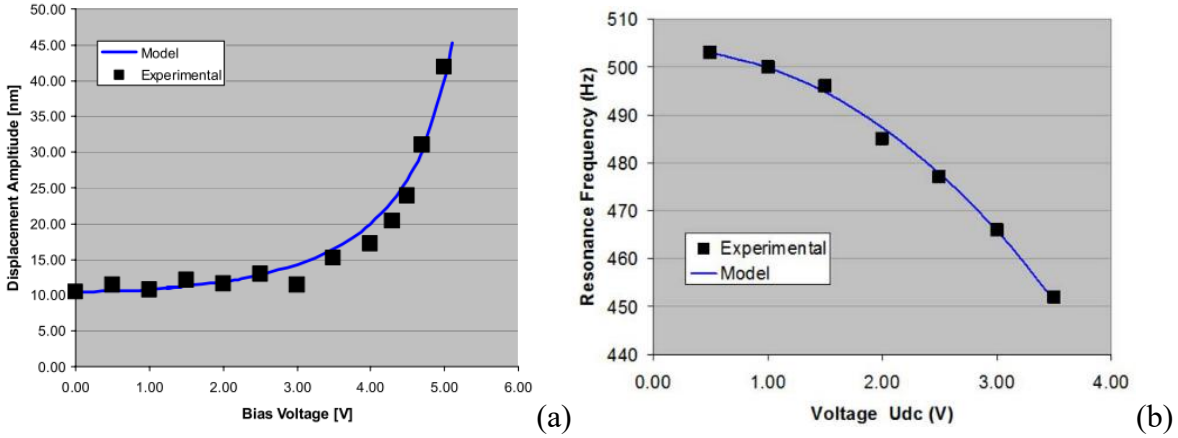

Figure 2.42: Displacement of the sensor produced in [16] due to a 120 Hz air flow for different bias voltages (a), and effect of different bias voltages to the resonant frequency.

In the 2010s some research groups kept working on these sensors and improving them even after the end of the CICADA and CILIA projects. Droogendijk et al. did plenty of research in the electrostatic change of stiffness of the spring of the sensor to tune its response [90-92]. Meanwhile, Dagamseh investigated the damping factor as the main source of thermo-mechanical noise in this sensor and the need to reduce it to increase the sensor's sensitivity [93]. Moreover, inspired by the club-shaped trichoid sensilla of crickets, Droogendijk et al. modified the hair at the top of this sensor to produce a hair-inspired accelerometer that shows low sensitivity to air flow, Figure 2.43 [94]. A similar structure has been used for a gyroscope mechanism as well [95, 96].

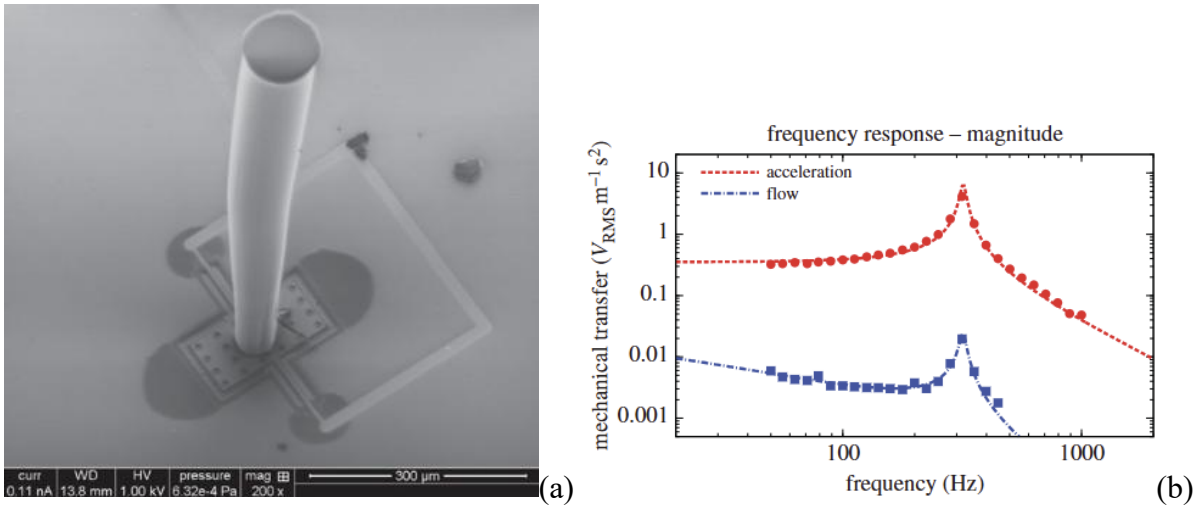

Figure 2.43: Image of the hair-inspired accelerometer developed by Droogendijk et al. [94] (a) and its response to acceleration and airflow (b).

While in Europe there was a lot of focus on capacitive hair-inspired sensors, in Asia and America, researchers seemed more focused on using strain gauges and piezoresistivity. Moreover, while in Europe, due to collaboration with entomologists, there seemed to be more focus on inspiration from insects, in Asia and America there seemed to be a growing interest in the lateral line of fishes for the hair-inspired sensors. At the University of Illinois, Zhifang et al. reported the fabrication of a hair-inspired sensor (Figure 2.45a) that reacts to a limited ranged of 0.2 to 1 m/s with a non-linear resistance change, Figure 2.45 [97]. Chen et al. presented the use of these hair-inspired sensors in arrays where each hair had a different orientation, Figure 2.45b [98]. They later presented a modified version of this sensor for underwater application with high sensing velocity and angular detection [99]. Yang et al. showed the use of these hair-inspired sensors in array for localizing and tracking hydrodynamic events and reported the ability to measure variations of water flow down to 0.1 m/s [100]. At the University of North China, a hair-inspired hydrophone (Figure 2.46) with a great directional pattern and a sensitivity of -197.7 dB (0 dB = 1V/mPa) was fabricated by Xue et al. [101].

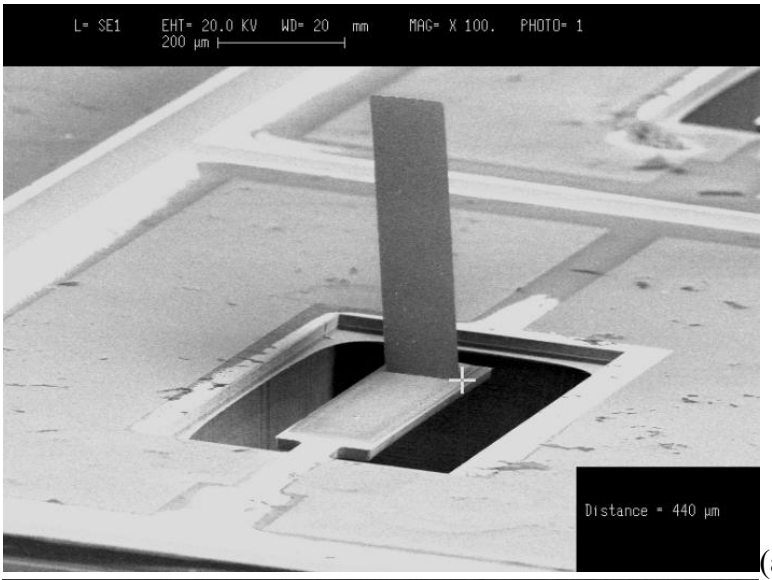

(a)

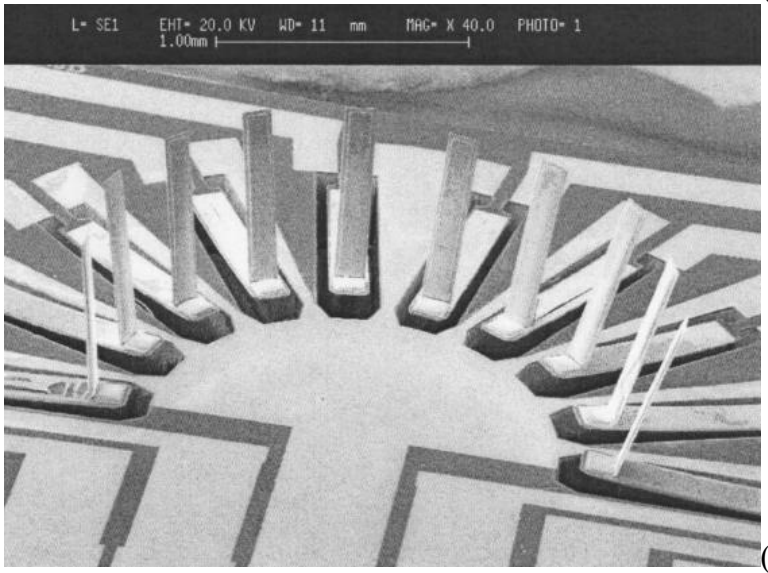

(b)

Figure 2.44: Sensor inspired by the lateral line of fishes produced by Zhifang et al. [97] (a), its implementation in array by Chen et al. [98] (b).

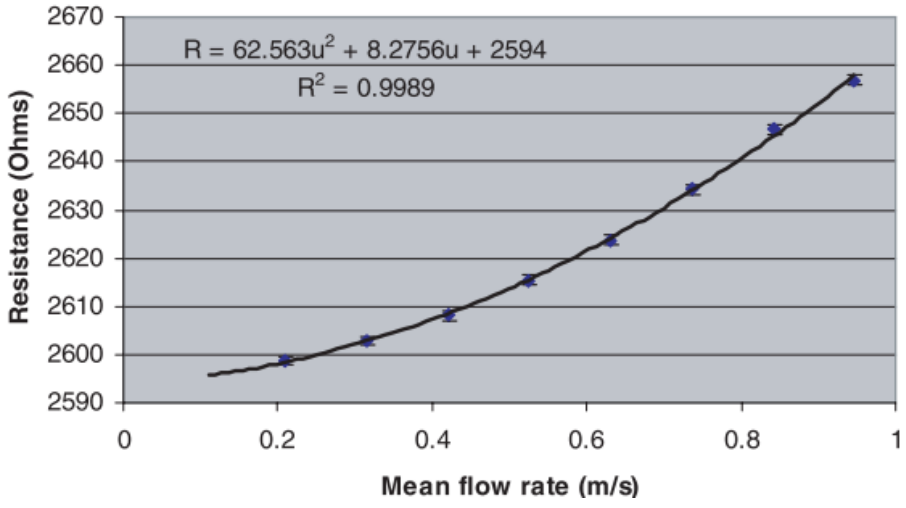

Figure 2.45: Electrical response of the sensor inspired by the lateral line of fishes produced by Zhifang et al. [97].

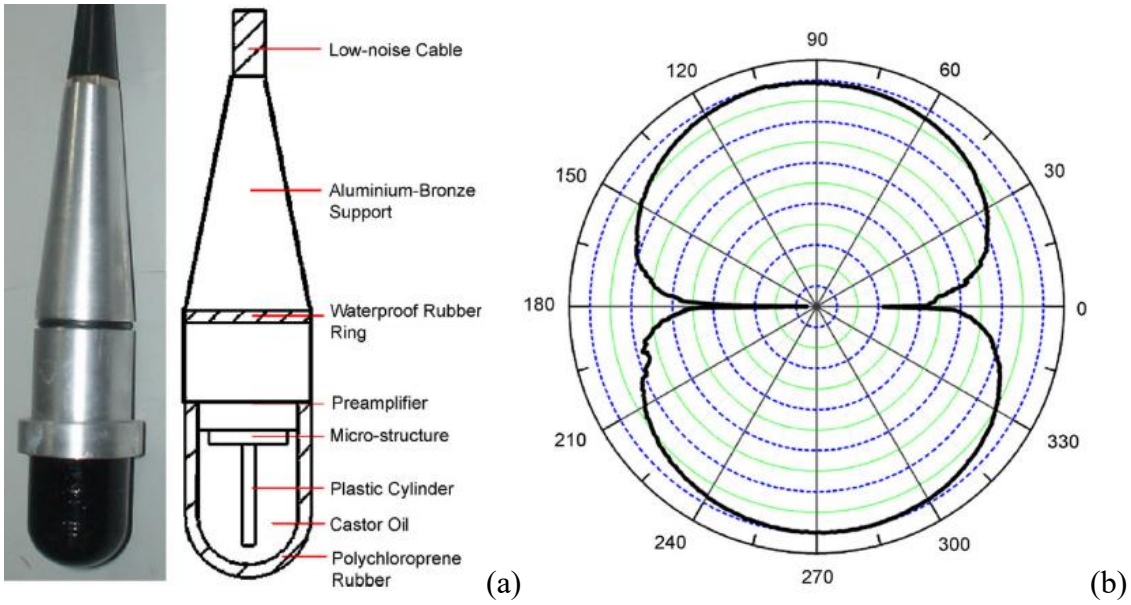

Figure 2.46: Hair-inspired hydrophone reported by Xue et al. [101]. Packaged hydrophone and diagram (a) and its directivity pattern (b).

2.5.3 Piezoelectric hair-inspired sensors

The 2010s saw a worldwide increasing interest in academia in hair-inspired sensors, taking inspiration from insects, arachnids and fishes. In this decade the geometries produced became more variegated and researchers began using also piezoelectric components for the sensing part. Abdulsadda et al. developed an array of piezoelectric hair-inspired sensors and used machine learning to predict the position of objects based on their signal response [102]. They placed this array on a prototype of body length 10 cm (Figure 2.47), and showed that the array and neural network were able to locate a source of movements between 1 and 2 body lengths away with a maximum localization error of 0.3 cm [102].

[THIS IMAGE HAS BEEN REMOVED BY THE AUTHOR OF THIS THESIS FOR COPYRIGHT REASONS]

Figure 2.47: Prototype of piezoelectric hair-inspired sensors array developed by Abdulsadda et al. [102].

Already in 2009 Bia et al. theorized the use of a half-coated piezoelectric fibre as a hair-inspired sensor to measure airflow [103]. But it is a few years later that they developed such sensor and tested it [104, 105]. Due to the use of different electrodes on the body of the hair-shaped sensor, a directional response is possible, Figure 2.48.

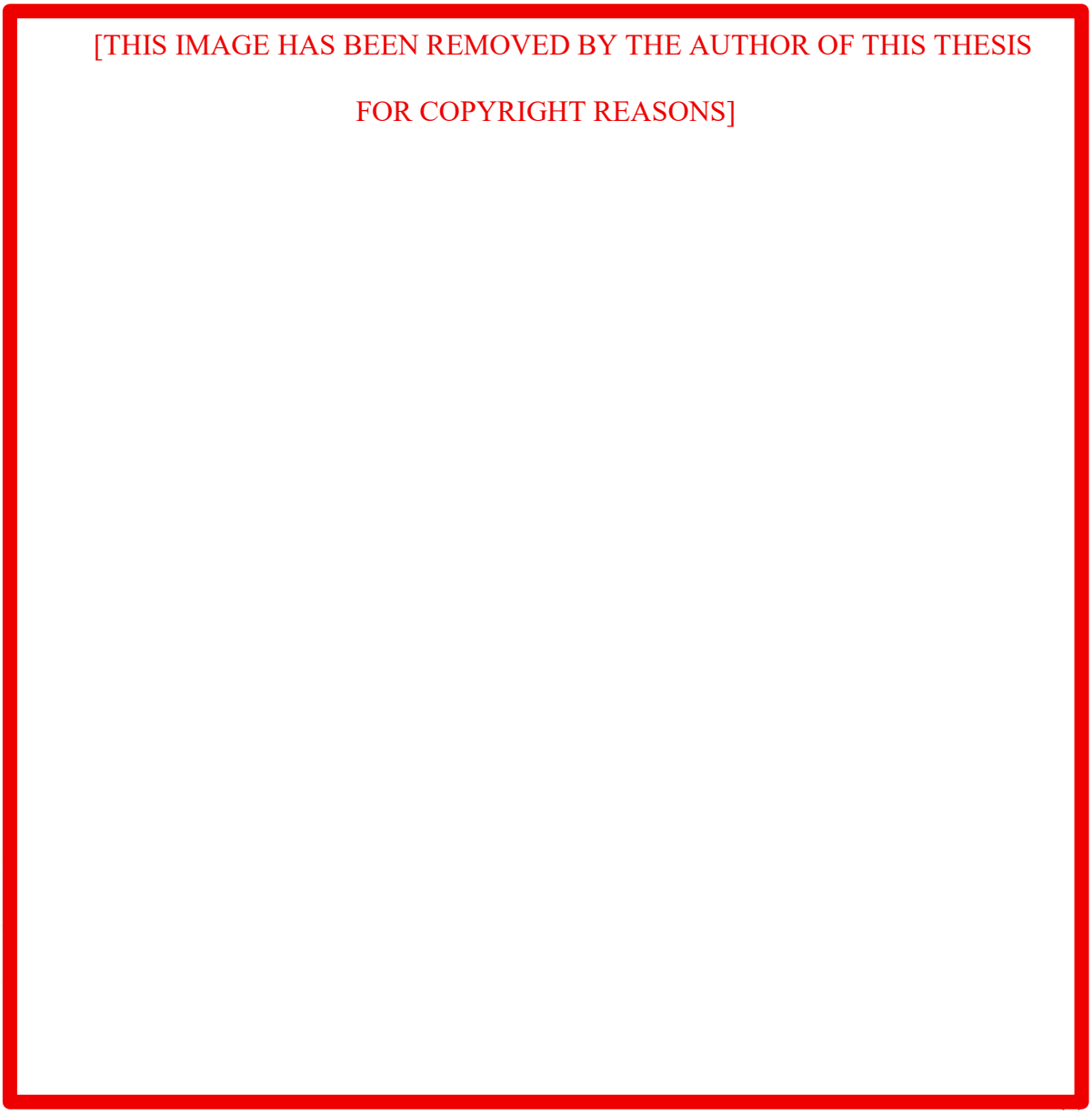

Figure 2.48: Schematic diagram of piezoelectric airflow hair-inspired sensor developed by Bian et al. (a) and top view showing the four surface electrodes (b) [105]. Output charge of the sensor at different angles (c), Q_a is the charge difference between electrodes 1 and 3, Q_b is the charge difference between electrode 2 and 4.

Asadnia et al. developed a piezoelectric hair-inspired sensor with a range of detection of flow velocities with amplitudes of 8 and 60 mm/s and a resolution of 3 mm/s, Figure 2.49

[106]. The sensor can work underwater, and it has been used in array for flow imaging applications [107].

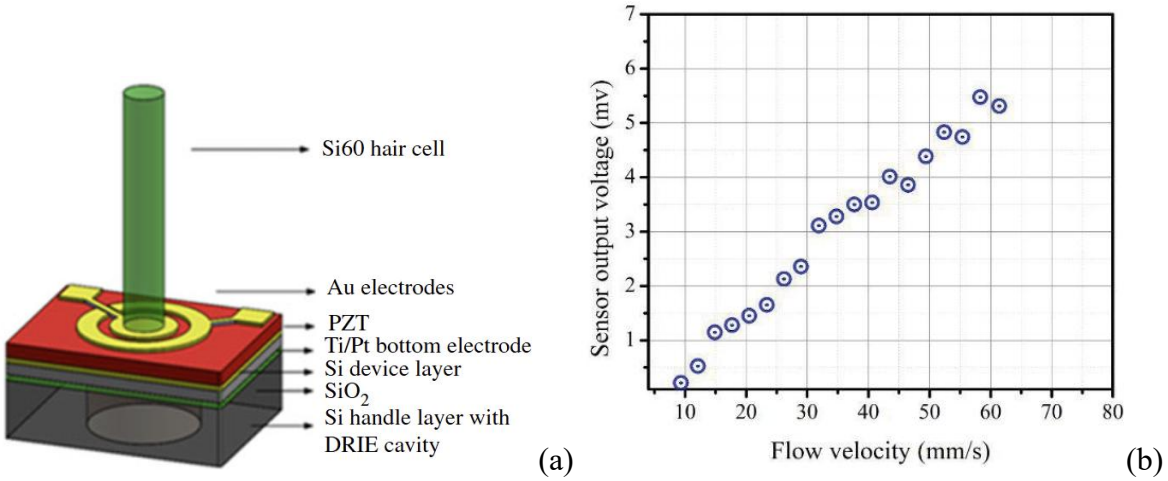

Figure 2.49: Schematic diagram of piezoelectric airflow hair-inspired sensor developed by Asadnia et al. [107] (a) and its electrical response due to underwater flow [106] (b).

Inspired by the canal lateral lines of cave fish *Sinocyclocheilus macrophthalmus*, Fu et al. developed an array of piezoelectric hair-inspired sensors and the fish's canal lateral line to measure underwater dynamic flows, Figure 2.50 [108]. The sensor array is reported to measure dipole sources vibrating at 100 Hz with 0.3 mm amplitude at a maximum detectable distance of 96 cm, and that the limit of detectable pressure from each singular sensor of 3.1 Pa [108].

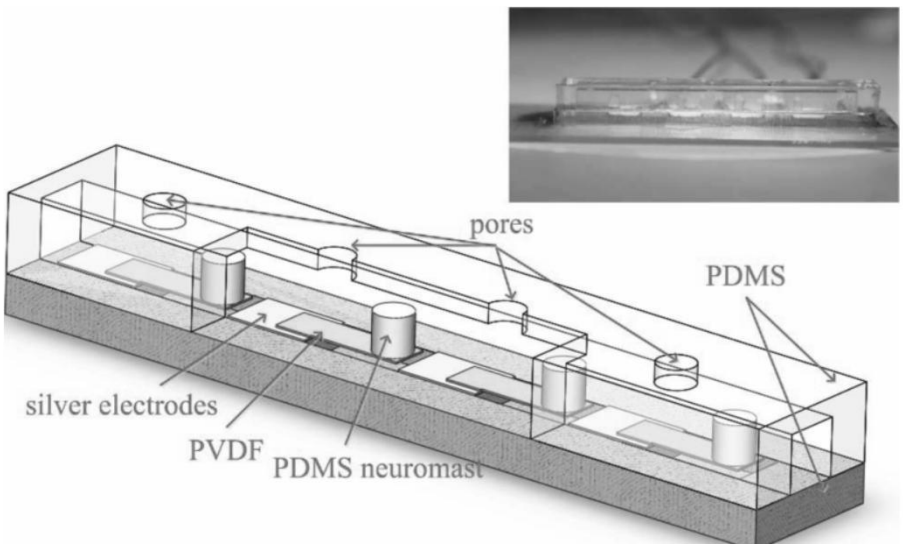

Figure 2.50: Diagram of piezoelectric dynamic flow hair-inspired sensor array developed by Fu et al. inspired by the canal lateral lines of cave fish Sinocyclocheilus macrophthalmus [108].

Jin et al. used a flexible array of piezoelectric acoustic particle velocity hair-inspired sensors for speaker recognition purposes, Figure 2.51. Speaker recognition is used to identify the speaker that is talking, as opposed to speech recognition where the system recognizes the speech only. The hair-inspired sensor array showed outstanding capabilities, with a speaker recognition rate of 95.3% and, when compared to commercially available microphones, an error rate reduction of 75% [109].

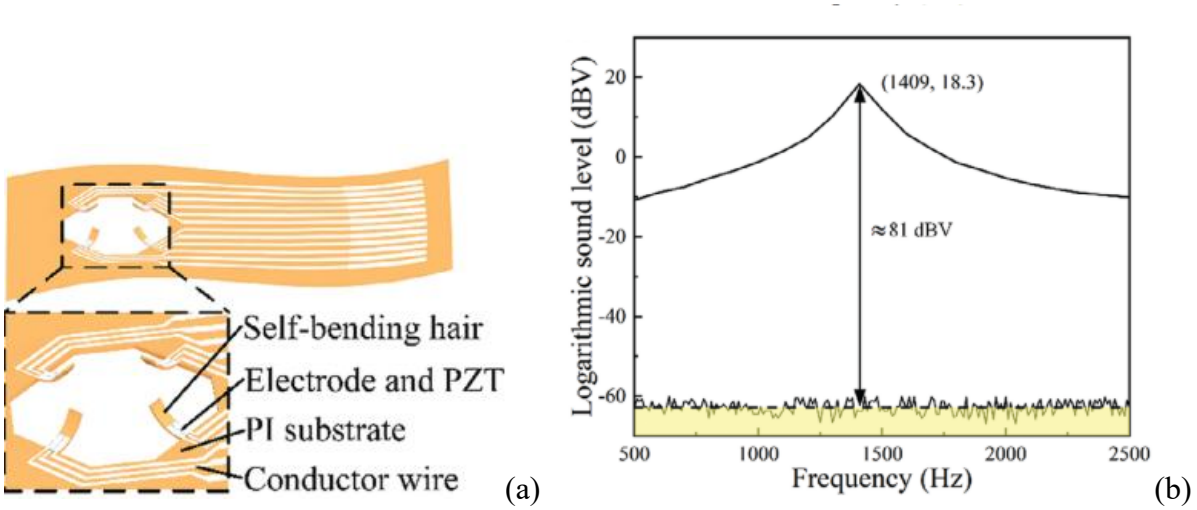

Figure 2.51: Diagram of the flexible array of piezoelectric acoustic particle velocity hair-inspired sensors developed by Jin et al. [109] (a), and its acoustic response (b).

Wang et al. made a theoretical study to optimize a piezoelectric hair-inspired sensor inspired by the curved trichobothria found in spiders. Their simulation found out that bent hairs, compared to their straight counterpart, are supposed to be up to 10 times more sensitive for acoustic detection in the 1-500 Hz frequency band, and 1.5 times more sensitive for tactile load detection [110]. Of course, follow-up studies to see if these simulations translate well in the real world need to be conducted.

2.5.4 Magnetic hair-inspired sensor

In 2014 Alfadhel et al. introduced a hair-inspired sensor based on a magnetic sensing mechanism [111]. The hair parts of the sensor are made of iron nanocomposite (Figure 2.52a), and they are implemented on a giant magnetoimpedance (GMI) thin film. When a fluid flow

moves the hair structures, they bend and cause a change in magnetic field in the GMI film, consequently changing its impedance. At a power consumption of 31.6 µW they managed to measure airflows up to 190 mm/s with a sensitivity of 24 mΩ/(mm/s) and a resolution of 0.56 mm/s, Figure 2.52b. Meanwhile in water it is possible to measure flows up to 7.8 mm/s with a sensitivity of 0.9 Ω/(mm/s) and a resolution of 15 µm/s, Figure 2.52c. When reducing the power consumption to 80 nW the sensor, for water flows, retained a 32 µm/s resolution [111].

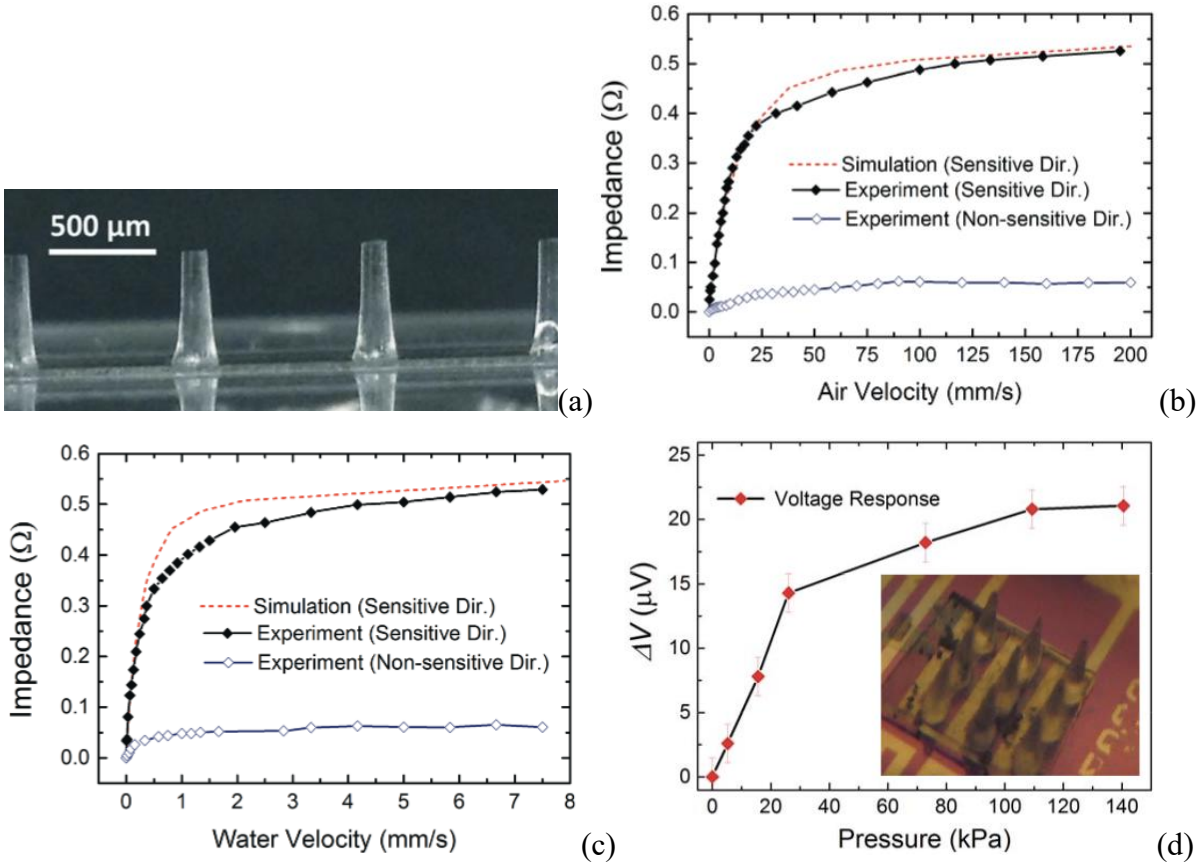

Figure 2.52: Photo of the micro-hair structures of the magnetic hair-inspired sensor produced by Alfadhel et al. [111] (a). Response of the sensor due to air flow (b), water flow (c) and applied pressure for force sensing in a Wheatstone bridge configuration [112] (d). The plot in (d) has an inlet showing a photo of the sensor during experimentation.

The same structure has been also applied for force sensing, showing, at a power consumption of 75 µW, a sensing range of 0-120 kPa and a resolution of 2.7 kPa [112]. Due to its sensitivity to different pressure, the use of this sensor as a tactile sensor has been suggested, and tested, as well [113, 114].

2.5.5 Optical hair-inspired sensors

In 2015 the first hair-inspired sensor that makes use of an optical read-out method was presented [18]. Herzog et al. used an LED to light a cylindrical artificial hair and a photodiode facing the tip of the hair. When a flow deflects the artificial hair a change in light intensity is detected by the photodiode. The researchers included two of these sensors in a canal-like structure inspired by the fishes' canal lateral lines, Figure 2.53. The sensors were able to detect flow rates of about 10 µl/min (corresponding to a flow velocity of 185 µm/s) and up to 1000 µl/min [18]. This sensor is supposed to be used within pipes using the sensor's openings as inlet and outlet.

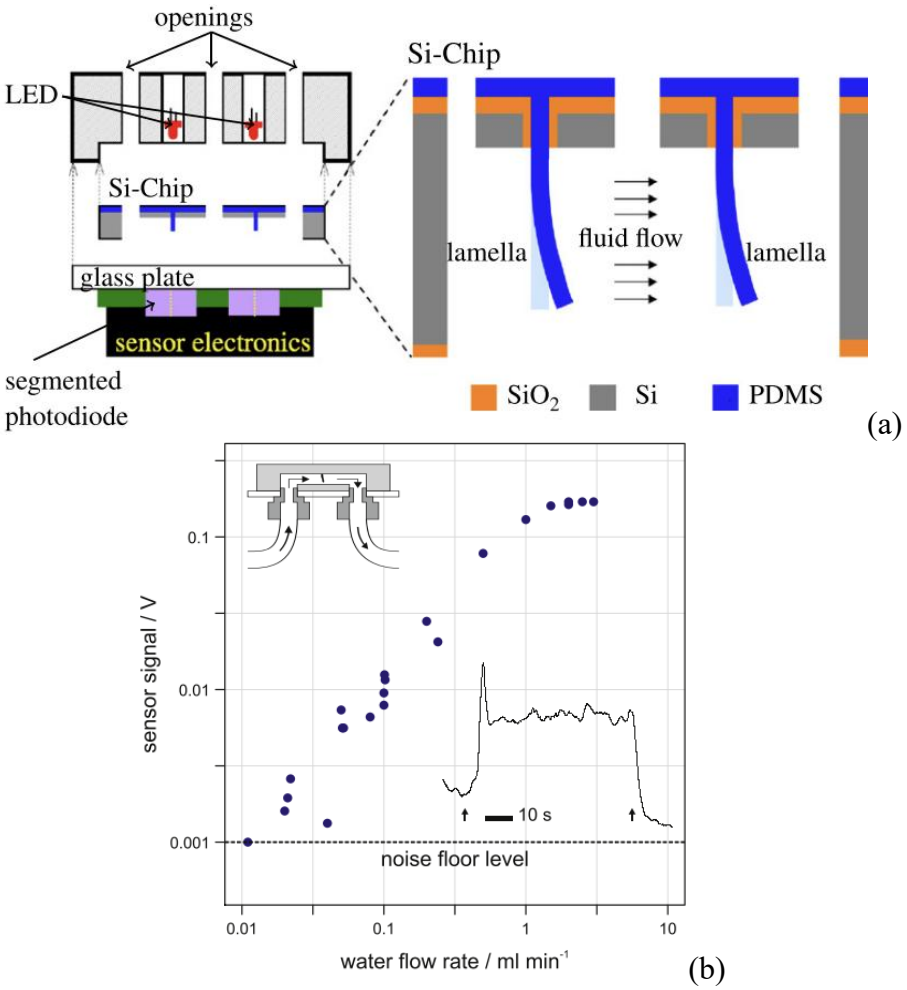

Figure 2.53: Diagram of optical flow-rate hair-inspired sensor produced by Herzog et al. [18] (a) and its electrical response (b). The plot of the response also shows on the upper-left corner a diagram of the experimental setup, and on the lower-right corner an inset showing the response in time to a 0.2 ml/min flow rate.

In 2024 Li et al. claim to have invented the first all-optical hair-inspired sensor [19]. And while the sensor engineered by Herzog et al. uses an optical read-out method [18], the integration of the optical method is not a part of the sensing body itself. Li et al. instead have integrated fibre tapers and a transparent microbubble in their sensor as the sensing component of the hair-inspired sensor, Figure 2.54. This section will not go into the fine details of how optical sensing works but will only summarize the findings of the paper, if the reader wants to know more details they are referred to read [19]. Instead of measuring an electric signal, the deflection of the hair produces shifts in the light's wavelength itself, showing good directionality, distinguishable signal patterns due to different stimuli (direct touch, breeze, pressure on the tip and water droplets) and good sensitivity [19]. The sensor has a directionality in the radial plane of 32.31 dB, maximum displacement sensitivity of 0.052 pm/µm and maximum force sensitivity of 3.994 pm/µm. Meanwhile, in the axial direction of the hair, the displacement sensitivity is 1.570 pm/µm and the force sensitivity is 0.986 pm/µm. The research team tried to apply different stimuli as well, such as breeze or water droplet, and managed to record different spectral profiles based on the frequency, direction and amplitude for the different profiles, this can allow for identification of the source of displacement on the hair-inspired sensor [19]. The research team also mounted the sensor on the cheeks of a cat-resembling robot and managed to see discernible shifts when the robot was standing up or down, but none while moving or staying stationary, Figure 2.55. This suggests the possibility to detect different stimuli, like airflow while the robot is moving. The fact that the sensing component is light based means that it does not suffer from common noises and interferences found in electrical-based sensors, and it allows for excellent temperature-displacement decoupling capability [19].

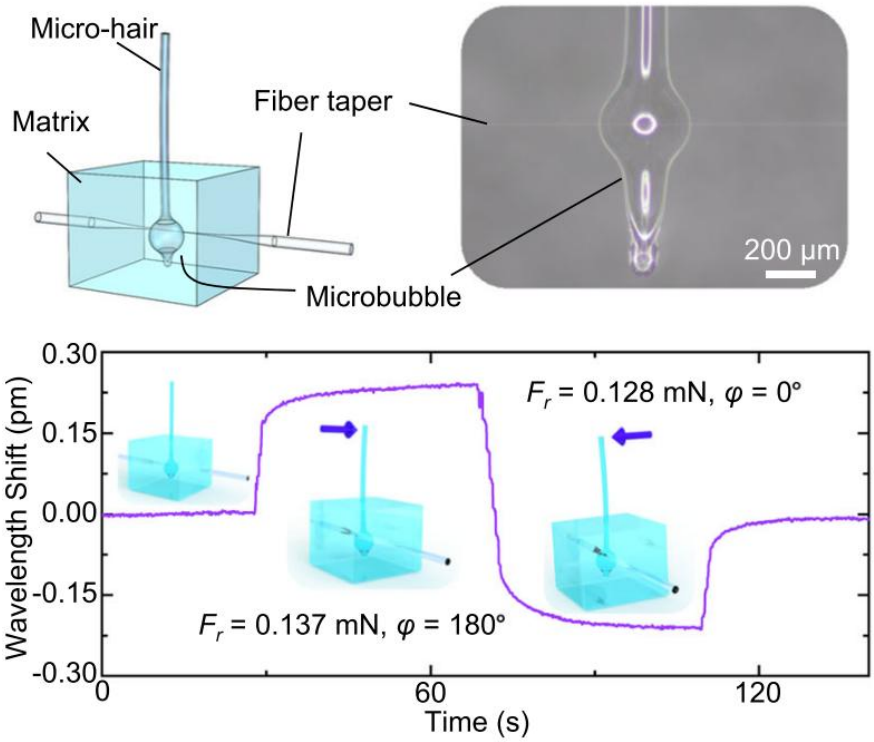

Figure 2.54: Diagram and top-view photo of the optical hair-inspired sensor developed by Li et al. [19] (top), and wavelength shift caused by a force applied to the artificial hair in different directions (bottom).

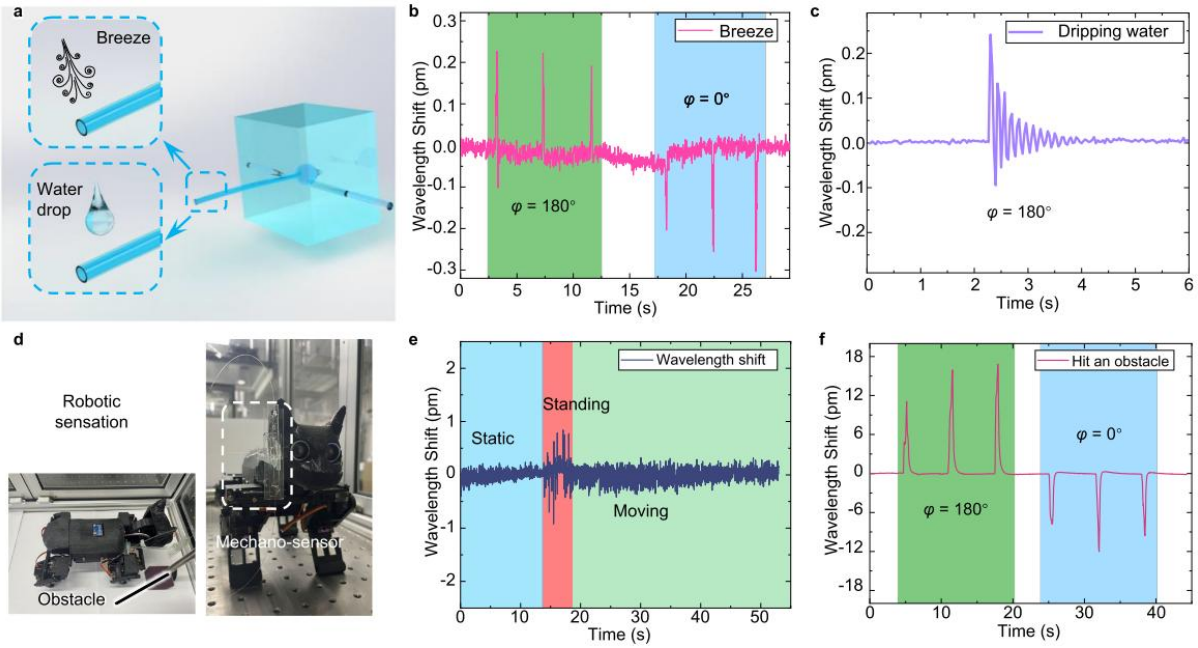

Figure 2.55: Schematic illustration of breeze blowing and water drop dripping on the optical hair-inspired sensor developed by Li et al. at different angles, φ [19] (a). Responses of the sensor to breezes (b) and as a water droplet is dripped on the artificial hair (c). Photograph of the cat-resembling robot equipped with the sensor (d). Responses of the sensor in stationary, standing, and moving states (e). Responses of the sensor when hitting an obstacle while advancing (φ= 180°) and retreating (φ=0°) (f).

Later that year, Zhang et al. proposed a hair-inspired sensory array that uses an optical mechanism to detect changes in air flow [115]. The mechanism is quite similar to the one developed in 2015 by Herzog et al. [18], but it differs from the fact that the light source is directed at the tips of the artificial hairs (instead of coming from the bottom) and a camera is used for detection at the bottom of the hair instead of photodiodes facing the tip, Figure 2.56. The array is also more numerous than the only two artificial pillars used by Herzog et al., and it also seems that it does not involve a casing with inlet and outlet, therefore allowing for flow to come from different directions. The authors identified a correlation between sensor output and flow velocity but a study to characterize the sensor's response is needed [115].

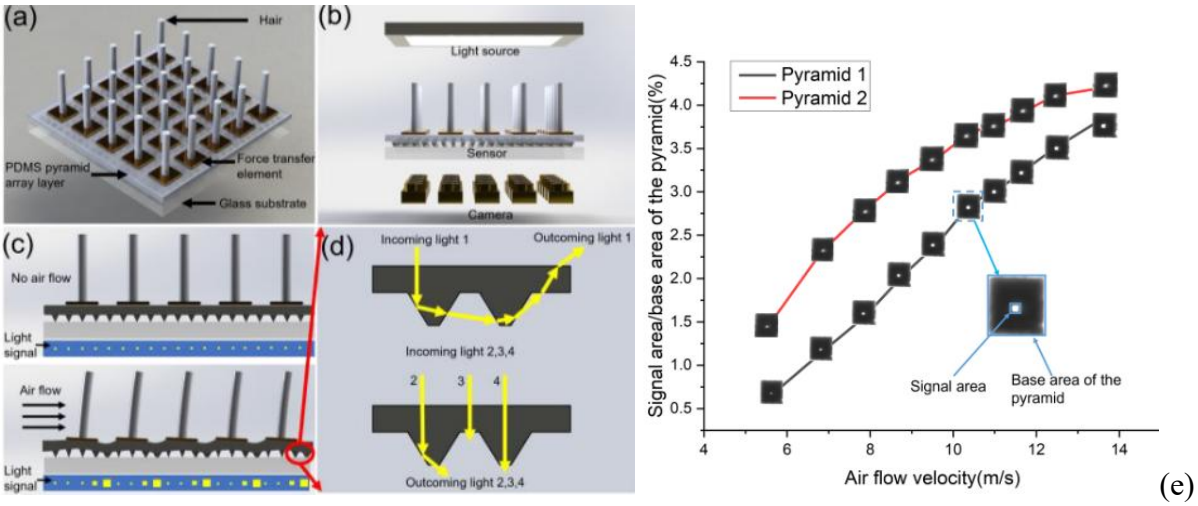

Figure 2.56: Schematic diagram of the sensor array developed by Zhang et al. and its sensing principle [115]. The sensor array structure (a) and the configuration of the light source and camera for capturing light signals (b). Sensing principle of the optical hair sensor array (c) and (d). Relationship between the ratio of the output light signal area to the base area of a pyramid and the air flow velocity (e).

2.5.6 Triboelectric sensor inspired by the human cochlea

Albeit the sensor developed by Kang et al. is not strictly hair inspired as the previously described ones, it is still inspired by the human cochlea and the cilia in it [116]. Moreover, the sensing component is a triboelectric array of hair-shaped components, Figure 2.57. Therefore, it was decided to include it in this review. This innovative sensor is self-powered; therefore, it surpasses the limitations of constant powering sensors. Moreover, by changing its structure it

allows to tune the acoustic frequency at which it reacts [116]. In this way, by creating arrays of differently tuned sensors it is possible to acquire a sound with already separated frequency bands without the need of further computation. The produced sensors have a sensitivity of 860 mV/Pa on their resonant frequency an improvement compared to non-biomimetic sensors with sensitivities of 28 mV/Pa [116]. The triboelectric output of the sensor is of 1.3 V. The frequency of the sensor is tuned by changing the radius of the diaphragm structure, smaller radius means higher frequency, and consequently, a bigger radius is tuned to a lower frequency (**Error! R eference source not found.**). Kang et al. proceeded to use these sensors with a machine learning algorithm to verify the sensor's reliability. The fabricated sensor demonstrates a high accuracy range from 91% to 99%, showing excellent capability in distinguishing different frequency elements [116].

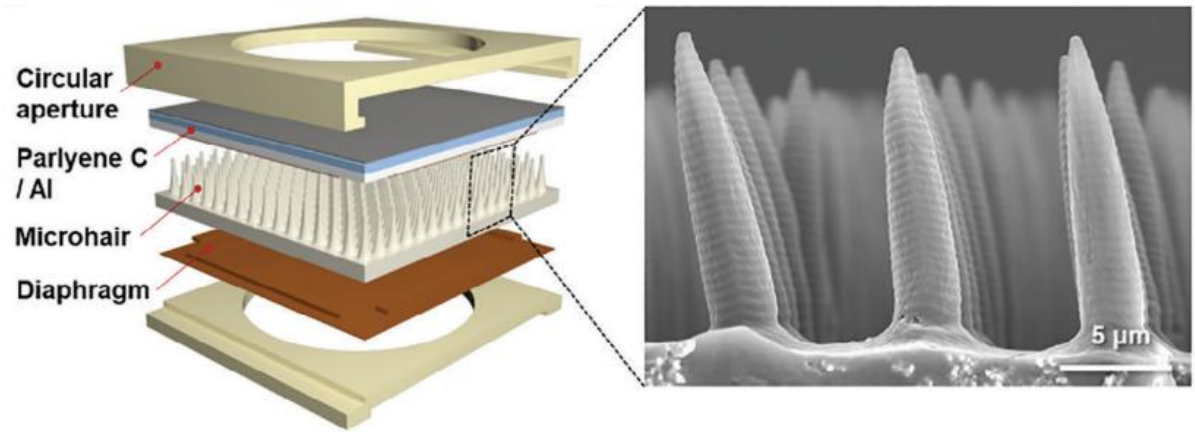

Figure 2.57: Diagram of the triboelectric cochlea-inspired sensor produced by Kang et al. [116].

2.5.7 3D-printed hair-inspired sensor

In 2012, 3D-printing began being investigated as an alternative manufacturing technique for sensors. In the following years research in this field gained momentum with hundreds of papers being published per year, with several 3D-printing techniques being used, different transduction mechanisms and different applications [21]. 8 years later, Rajasekaran et al. proposed the first 3D-printed hair-inspired sensor for air flow detection, Figure 2.58 [20].

Albeit this sensor is capacitive, it was decided to report it in a separate section given the fact that it is, to the best of the author knowledge, the only 3D-printed hair-inspired sensor created before the one presented in this thesis.

This sensor was printed using the two-photon polymerization technique, and the four capacitive plates were created using E-beam metal deposition, depositing 100 nm of silver. The bottom four capacitive plates are instead represented by PCB contacts to which the sensor is glued on top with silver paste. The sensor was found capable of measuring flows between 5 m/s and 10.2 m/s, while the actual sensitivity was not reported, plots of the response are shown in Figure 2.59 [20]. The sensors also show directionality in the measurements. Albeit, 3D-printing was not using an electroactive resin or material for the body of the sensor, and the printing and metal deposition techniques are on the more expensive and complex end, this pioneering paper showed the possibilities of 3D-printing as a technology for hair-inspired sensors.

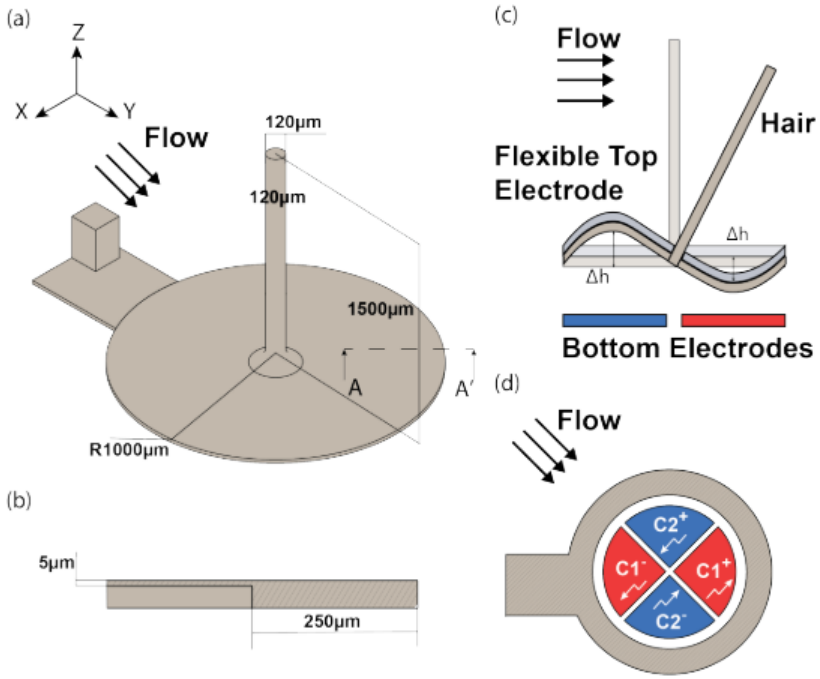

Figure 2.58: Design of the 3D printed artificial hair flow sensor developed by Rajasekaran et al. [20] (a). Zoomed in view of section A-A' (b). Schematic showing principle of operation under airflow and deflection of the bottom section (c) and capacitance change for each electrode under this deflection and airflow direction (d).

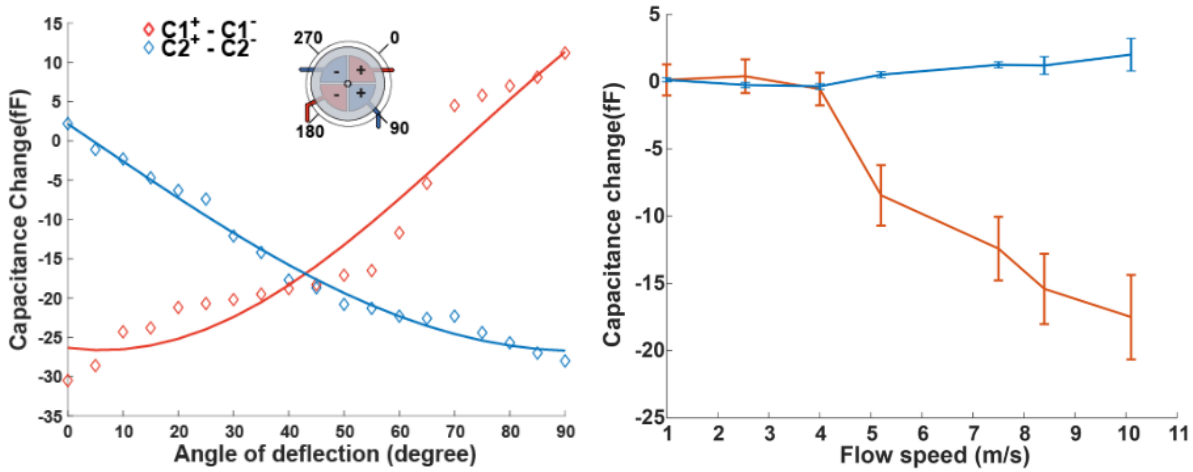

Figure 2.59: Electric response of the 3D-printed hair-inspired sensor produced by Rajasekaran et al. [20]. Differential capacitance changes due to different angles of deflection (left), and differential capacitance changes due to airflow applied on the 0˚ direction.

2.5.8 Importance of material selection for hair-inspired sensors

In 2020, Zhang et al. investigated the importance of having two materials with different elastic properties for the hair shaft and the sensing unit in hair-inspired sensors, and their aspect-ratio [48]. They did this producing a piezoresistive sensor, but since their focus on the two-material structure was fundamental to this thesis, it was decided to report it in a separate section.

The Zhang et al. study was inspired by the fact that in some insects and arachnids has been recorded a difference in Young's modulus between the softer basal area and the stiffer hair shaft. This allows for high mechanical efficiency as the hair shaft does not bend due to a force applying on it, instead the stress is deflected to the basal area, where the dendrite is, so the area responsible for transduction [48]. They also studied the importance of aspect ratio between stiff and soft area. They found out that a smaller soft area at the base allows to experience higher strain in the component responsible for transduction, therefore enhancing its sensitivity, Figure 2.60. The simulated sensor was then manufactured and tested by dripping water droplets at different distances. The results showed a clear resistive change based on the height at which the water droplets fell, Figure 2.61.

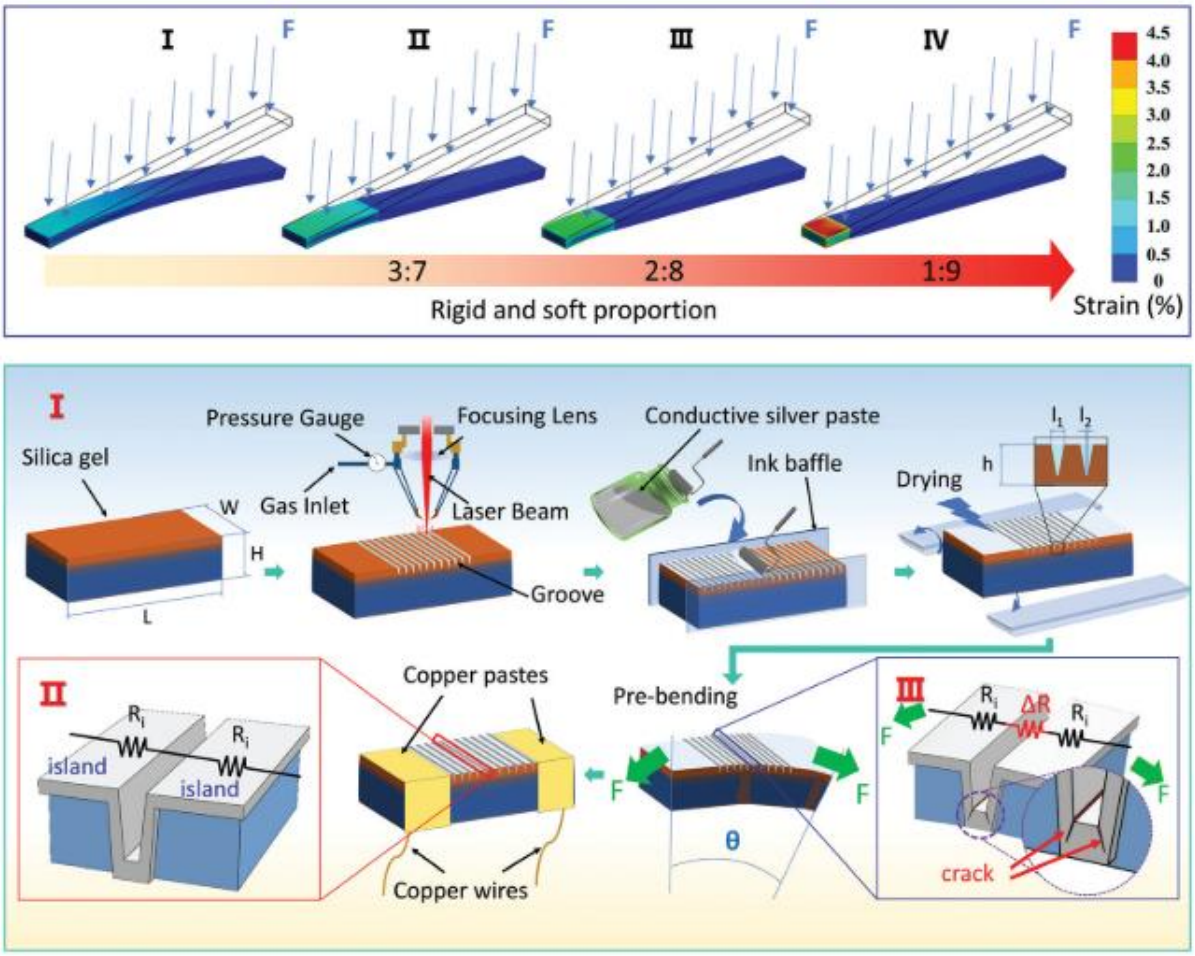

Figure 2.60: Stress analysis of the cantilever composed of two different shear modulus, G, materials under the same pressure: a flexible material (G = 1.5 MPa) and a rigid material (G = 30 GPa) conducted by Zhang et al. [48] (top). Manufacturing process of their hair-inspired sensor (bottom).

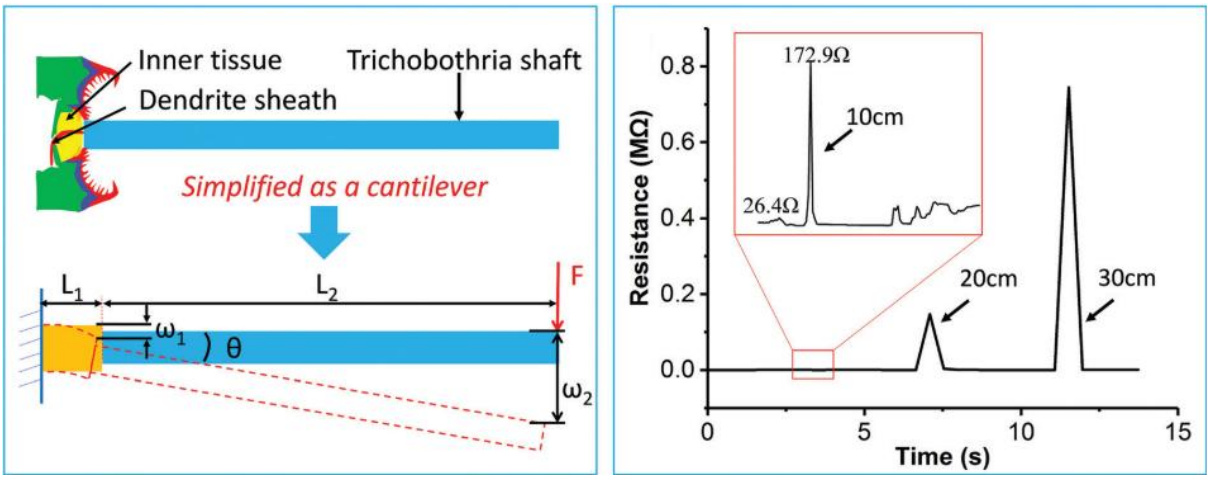

Figure 2.61: Schematic representation of the hair-inspired sensor created by Zhang et al. [48] (left), and its electrical response due to water droplets dropped from different heights (right).

3

Methodology

"It matters little how much equipment we use; it matters much that we be masters of all we do use."

Sam Abell

This chapter introduces the equipment and software used in all stages of the research. It gives insight on their principle of operation, but some more in-depth explanation for each component will be given on the subsequent chapters to expand on an application basis. The chapter is organized following an ordinate manufacturing process structure from its design to its final experimentation. Nevertheless, some of these processes often overlapped or repeated back and forth during the realization of the sensor. In some scenarios, some processes were also skipped as they were not ready to be used at that stage of research.

3.1 Sensor Design – Computer Aided Design

To develop the sensor structure, Computer Aided Design (CAD) was used. This was essential for the sensor construction (explained in 3.2), but it also allowed for quick design and visualization of the sensor. CAD refers to the use of computers to aid in the creation, modification, analysis and optimization of a design [117]. The selection of CAD software is diverse. It can include specialized versions for specific industries, or the presence or not of tools to analyse the physical properties of the design. Since only simple design capabilities were needed in this project *Shapr3D* software was selected for its ease of use, simplicity, and availability on different platforms.

3.2 Sensor Simulation – Finite Element Analysis

Historical records show that the concept of approximation of theory can be dated at least as early as the 3rd century BC, when Archimedes proposed the use of known easy to measure geometrical figures to represent and model more complex geometrical shapes. Examples are the use of a known length of straight lines to measure the perimeter of a circle, known area of triangles to measure the area of a circle and known volume of tetrahedral to measure the volume of a cylinder (Figure 3.1). In 1960, Clough further developed this method and coined the name Finite Element Method (FEM) [118]. From this point onwards research on FEM gained

momentum and in the late 60s NASA developed NASTRAN, the first general purpose Finite Element Analysis (FEA) package software [119]. Here FEA refers to the interpretation of the results provided by FEM. Many other companies developed other packages, and nowadays FEM and FEA represent the most used numerical tools to simulate complex real-world problems.

Figure 3.1: Concept of discretization with known geometries used by Archimedes, taken from [119].

FEM involves splitting the domain of an object into a set of finite subdomains, referred to as *elements* [119]. The set of elemental equations required to solve the global problem are systematically solved and combined into the global system of equations to obtain a final solution. The elements are connected to each other via points called *nodes*, each of them has a set of *degrees of freedom* (DOFs). DOFs can be different physical properties, such as displacement, current, etc. DOFs will rule the formulation of algebraic equations and the unknown variables for which the models need to be solved, while the nodes will represent the interactions between elements. The global DOFs represent the unknown variable of the problem and will change based on the specific application. The higher the number of elements the higher will be the computational power required, and subsequently the time required to solve the model. Nevertheless, the higher the number of elements in a model the closer will be the result to the real-life counterpart. For this reason, it is important to have a good balance

between the number of elements and the best yielded approximative result, to not result in "infinite" computation power/time.

Nowadays, FEA is used in a wide range of applications including stress analysis, heat conduction, electrostatics, fluid flow, and others. There are other computational methods, but they are outside the scope of this thesis, and hence they will not be introduced. The main reason why FEA was used for the work of this thesis is the wide variety of problems it can be applied to, no restriction on the element size, and that a combination of materials and structures can be used within a single model. Moreover, FEM is supported by a wide variety of commercial packages, while other methods are generally more niche. The chosen FEA commercial package for this project is COMSOL Multiphysics.

3.2.1 COMSOL Multiphysics

As mentioned earlier several commercial packages support FEA, some are specific to certain applications only, while others are vaster, and others provide only the tools necessary to set up FEM and would require the user to provide the fundamental physics equations that describe the model. COMSOL allows the user to easily build the models in CAD and modify them even within the simulation for parametric study, it already contains different packages specific for certain applications, and, compared to some competitors, allows easy integration of different physical phenomena in the same model/simulation. The latter was widely used within this project as it allowed easy simulation of mechanical structures under stress produced by acoustic waves or airflow. For the acoustic and airflow artificial hair sensor, the COMSOL simulation made use of Multiphysics modules (version 6.3). These modules make use of different physics modules, pair them, and make their computation more efficient (compared to just using multiple modules at one time). The most used one was the *Acoustic-Structure Boundary*, which coupled the *Solid Mechanics* module and the *Pressure Acoustics Frequency*

Domain one, basically helping in the computation of how acoustic waves interact mechanically with a surface. Another important module is the *Electromechanical Forces*, which, coupling the *Solid Mechanics* and the *Electrostatics* modules, helps with the computation of the electrostatics force in a body based on mechanical deformations or displacements. *Electric Currents* was another module involved in simulation of artificial hair sensors. Albeit no Multiphysics module could couple it with *Solid Mechanics*, they were tested together. Below is a description of how the simulation was set-up in COMSOL for the results of Chapters 4 and 5, meanwhile Chapter 6 provides further details on the COMSOL Simulation that was required for those experiments.

3.2.2 Geometry and Materials

In COMSOL the geometry of the hair was recreated from scratch rather than importing the STL file that was used for printing for the simple reason that having the geometry created through COMSOL allowed parametric studies (e.g., studies when you change a section of the geometry and compare how it affects the results). Apart from the geometry of the sensor, a box enclosing it was also created. This box is simply supposed to represent the air around the sensor. Different sizes of this "air box" were tested and they showed no differences in the acoustic results, but a bigger box resulted in longer computational time. Therefore, the box was made big enough to enclose fully the sensor, plus a ~10% more.

Then, the materials had to be assigned for different components. Whenever it was possible the materials from the COMSOL library were used, but often (as in the case of the 3D printed materials), a custom material had to be created. Based on the type of simulation different material properties were requested by the software. For example, for using the *Solid Mechanics* physics module the material density, the Young's modulus and the Poisson's ratio were required. When presenting the COMSOL results in the subchapters below, the values that were

used to obtain those results will be specified. For the air box described above and the metal layers the COMSOL's material library was used.

3.2.3 The Solid Mechanics physics module

The *Solid Mechanics* module is intended for performing general structural analysis of a body. It solves the equations of motions with a constitutive model for solid material. It computes the displacement, stress and strains of the body [120]. This module was applied to the whole geometry, except the airbox. The default settings of this module were left untouched. A *Fixed Constraint* was added to the face of the bottom of the sensor (to make the sensor immovable from that point). In some simulations *Prescribed Displacement* was used. This simply allowed a point, an edge, or a boundary of the body of the sensor (e.g., the tip of the artificial hair), to be selected, and force a displacement in the selected axis and for a selected distance. Figure 3.2 and Figure 3.3 show a selection example for a fixed constraint and a prescribed displacement, respectively.

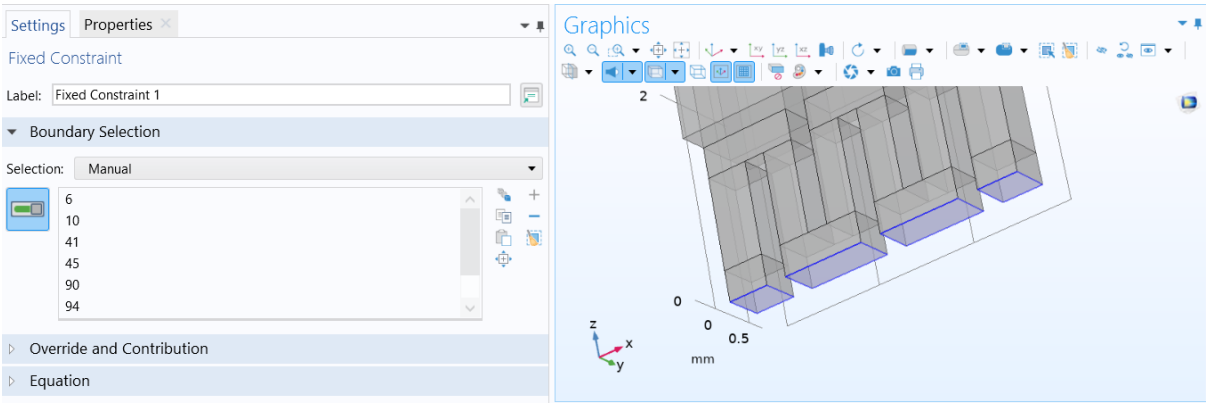

Figure 3.2: COMSOL fixed constraint selection example. In this case the bottom of the sensor has been selected as a fixed constraint (selection in blue). Here is where in the real world the base of the sensor would be, but by selecting the bottom as a fixed constraint we are fixing it as if the base was there, while reducing the computation by removing the base itself.

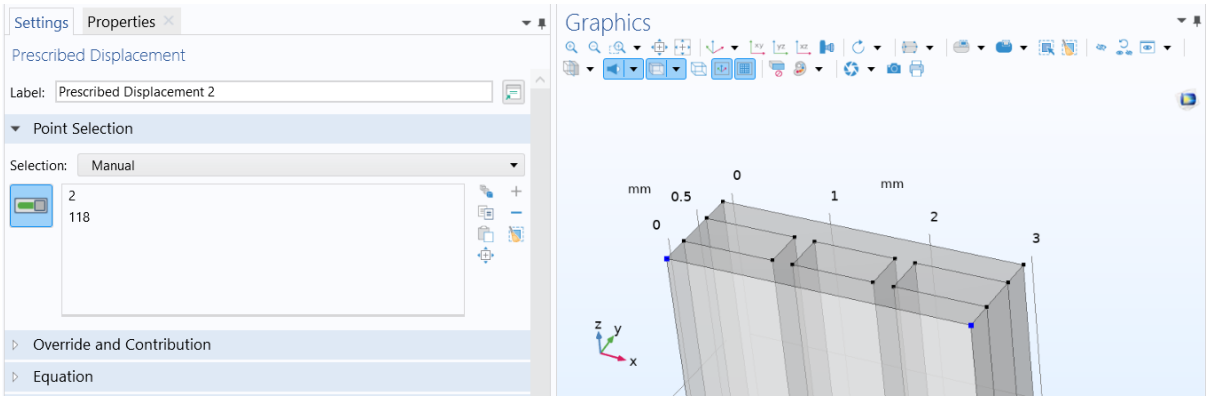

Figure 3.3: COMSOL prescribed displacement selection example. In this case two points at the tip of the hair of the sensor have been selected (selection in blue).

3.2.4 The Pressure Acoustics Frequency Domain physics module

The *Pressure Acoustics Frequency Domain* module computes the pressure variations for the propagation of acoustic waves in fluids at rest condition and is applied to the air box [121]. This module is designed to work in frequency domain studies and to simulate frequency-dependent sources, as opposed to the *Pressure Acoustics Time Explicit* module. In this project it was used to simulate the propagation of a wave produced by a speaker at singular frequencies. The main settings for this module are the *Plane Wave Variation*, applied to the boundary walls of the air box and the *Sound Hard Boundary (Wall)*, applied to the base of the sensor as that section should not move (this is similar to the fixed constraint of Figure 3.2).

3.2.5 The Electrostatics physics module

The *Electrostatics* module is used to compute the electric field, electric displacement field and potential distribution in dielectrics under conditions where the electric charge distribution is explicitly prescribed [122]. This physics interface solves Gauss' Law for the electric field. In the setting zero charge is set to the air surrounding the sensor (as this is the dielectric) and then the ground and terminals need to be set on the body sensor depending on the actual sensor geometry. The terminal was then set to *Voltage,* and the voltage level was specified in volts.

This type of study was used for simulations of capacitive type sensing. Figure 3.4 shows a selection example for the ground and terminal.

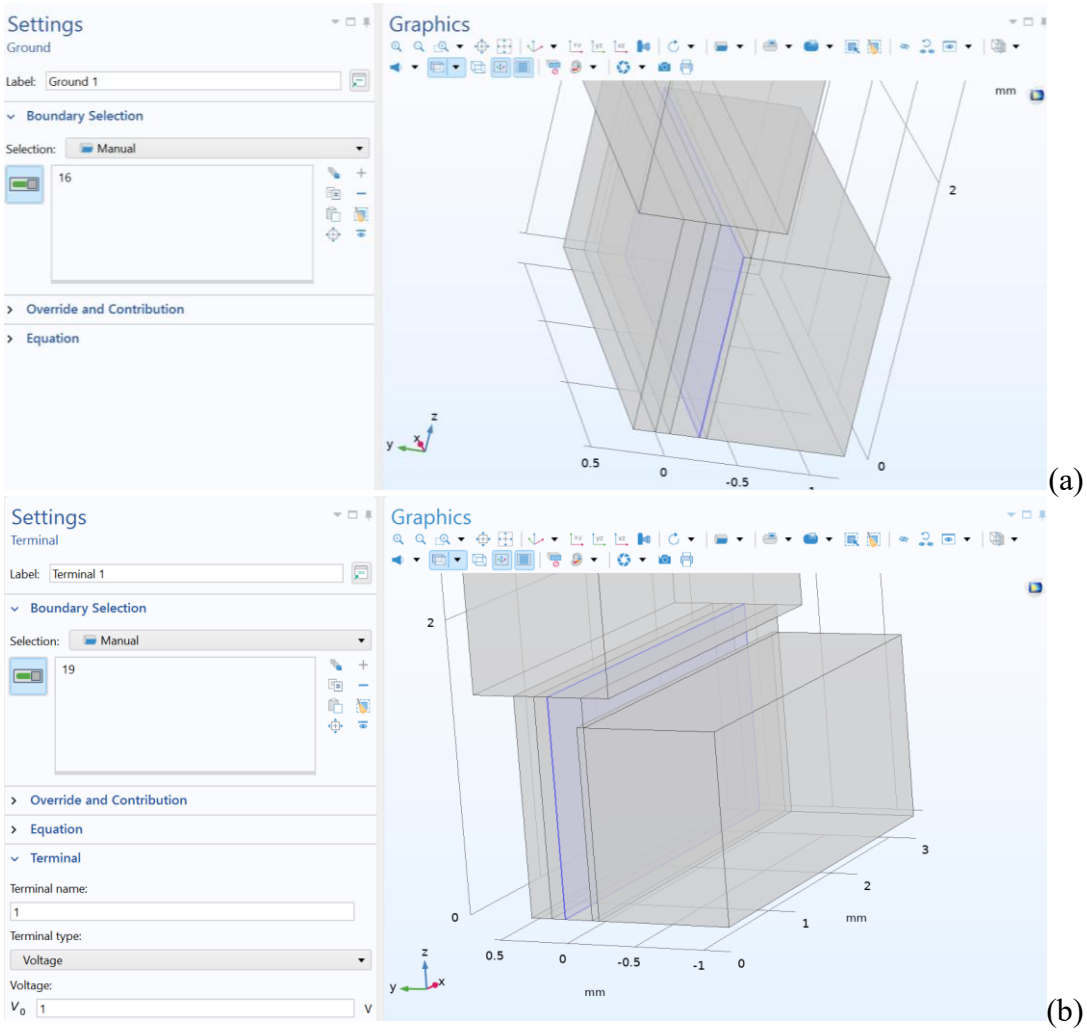

Figure 3.4: COMSOL electrostatics ground (a) and terminal (b) declaration (selection in blue). The terminal settings allow for the selection of the applied voltage.

3.2.6 The Electric Currents physics module

The *Electric Currents* module computes the electric field, current and potential distribution in conducting media in conditions where the inductive effects are negligible. This module solves current conservation equation based on Ohm's law [123]. Here, similarly to the *Electrostatics* module the ground and terminals need to be set on the body sensor based on the sensor's geometry. The terminal type was then set to *Current*, and the current level was

specified in amperes. This type of study was used for simulations of piezoresistive type sensing. Figure 3.5 shows a selection example for the ground and terminal.

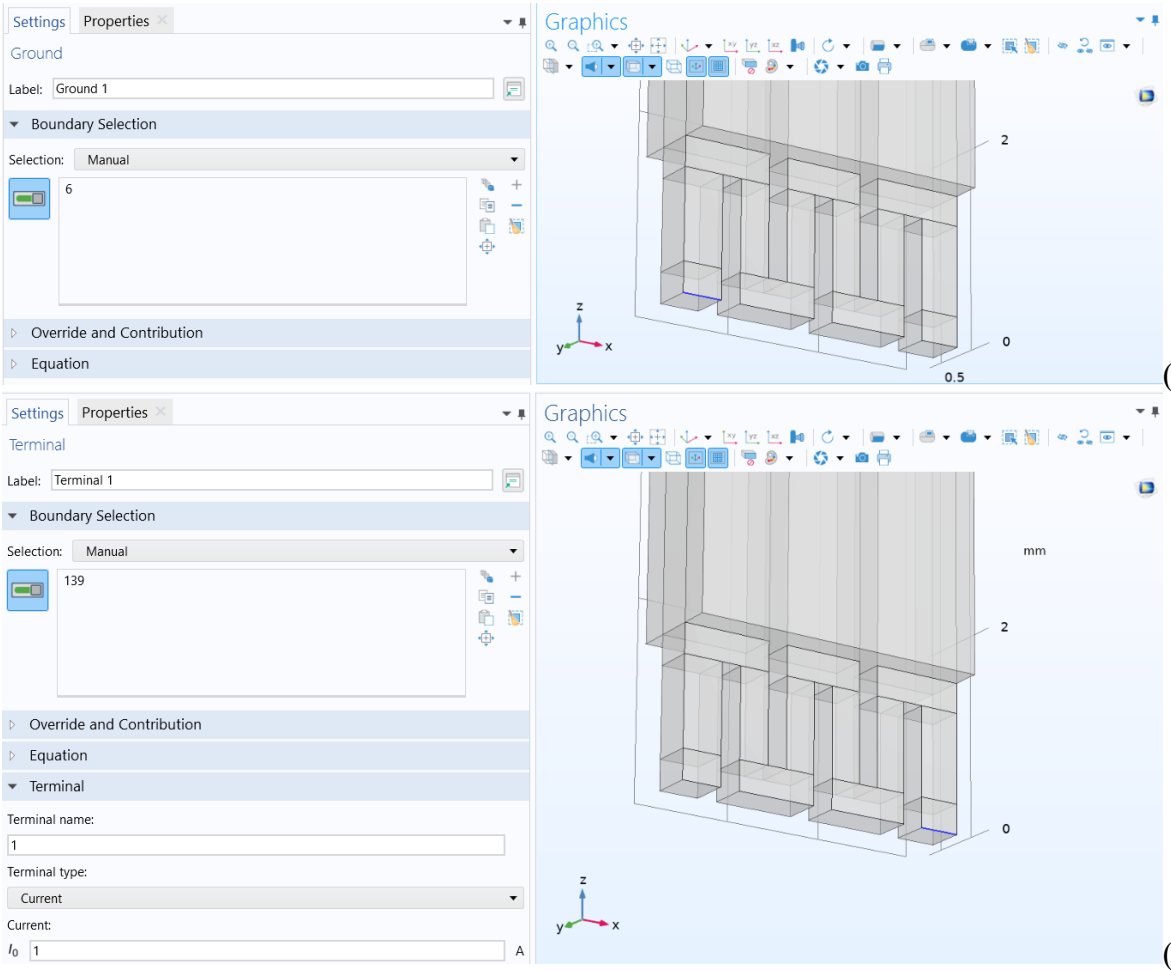

Figure 3.5: COMSOL electric currents ground (a) and terminal (b) declaration (selection in blue). The terminal settings allow for the selection of the applied current.

3.2.7 The Solid-Thin Structure Connection

The *Solid-Thin Structure Connection* is a COMSOL Multiphysics node that allows the connection of thin layers on the surface of a body and the body itself. The thin layer in this way is not created as a geometry, but its thickness is specified at the surface of a body in the *Shell* module. The connection node just ensures proper connection in the evaluation of a simulation between the thin layer and the main body [124]. The surfaces that are selected in *Shell* also need to have a material specified in the material selection and need to be appropriately selected in the physics modules (e.g., for terminal and ground in *Electrostatics*). In this project this was

used to simulate the thin metal layers deposited on the sensor's body. The use of this connection allows a bigger meshing size for the body and reduces the computation of nanometre and micrometre range layers. The selection of the surfaces for *Shell* resembles the ones in Figure 3.4.

3.2.8 The Study type

COMSOL allows different types of studies, for example, frequency-domain, time-dependent or simple stationary. In the case of studies coupling the pressure acoustics and the solid mechanics two type of studies were used one after the other. The *Eigenfrequency* study was used to understand the different frequency modes for the object. Then, the first frequency was used to perform a frequency-domain study with a frequency sweep around that frequency. This is done to save computation power and processing time. Eigenfrequency is quite precise and fast in getting the different eigen frequencies and different types of displacements given by these frequencies. The first frequency is usually the resonant frequency that allows the artificial hair sensor to move in a cantilever way. To join the eigenfrequency and frequency domain studies a script needed to be used in COMSOL and can be found in Appendix **A.1**. The alternative to this study would be to create a frequency sweep in the frequency domain over many frequencies. This, depending on the frequency range and frequency step of the sweep can take a long time, even hours or days. If we also add a parametric sweep to this (for example repeat the study for different artificial hair lengths), the computation time becomes vastly greater. Moreover, with large steps or small ranges of frequencies, one could reduce the computation time but at the cost of result precision. Knowing this, one can easily understand how efficient it is to use one first study to know the actual resonant frequency and follow this up by a frequency domain study with small step and range (e.g., 1 Hz step and a range ±20 Hz the resonant frequency) to better understand the sensor's mechanical behaviour around the frequency identified in the previous eigenfrequency study.

In theory, it would be possible to pair the study described above with the electric physics modules. However, this would increase the computation time greatly, and in case of errors it would be a huge loss of time. Moreover, the meshing required by these studies is finer (see below), and this alone, increases computation time. Therefore, the studies for the electric modules were conducted using the stationary study and coupled with the *Solid Mechanics* producing a prescribed displacement. In this way the prescribed displacement would create the desired deformation, and the electrostatics or electric current study will compute the value of interest for the simulation, like capacitance or resistance. Another reason for this approach is that, while the acoustic studies perform well in predicting the resonant frequency, as you will see in Chapter 4, it performs poorly in predicting the actual displacement. Therefore, the studies with a prescribed displacement from the input of the user allow greater flexibility. The user can for example first perform experiments in the real world and see how much change in a value a certain displacement induces, or they could test what is the minimum displacement required for the electrical change to be detected by a certain circuitry.

3.2.9 Meshing

An important component for the study is also the creation of the *Mesh* for a geometry. **Meshing** refers to how we split the domain of an object into a set of finite subdomains before performing a study. If the meshing is finer, the simulation will be more precise, but it will take longer to compute, and, on the contrary, if coarser, the simulation will take less time to compute and less hardware resources, but the results precision will be impacted negatively. Figure 3.6 shows a coarse and a fine mesh. Table 3.1 shows an example of how results and computation time are impacted in an eigenfrequency study of the structure in Figure 3.6. Unless otherwise specified the meshing in the studies was set to “Physics-controlled”, this means that each module would control and impact the meshing differently without the user’s input. For the acoustic type of simulation, the meshing detail did not need to be very small, on the other hand

the meshing details on the electric type of simulation greatly impacted the results, especially for the meshing size around the terminal and ground.

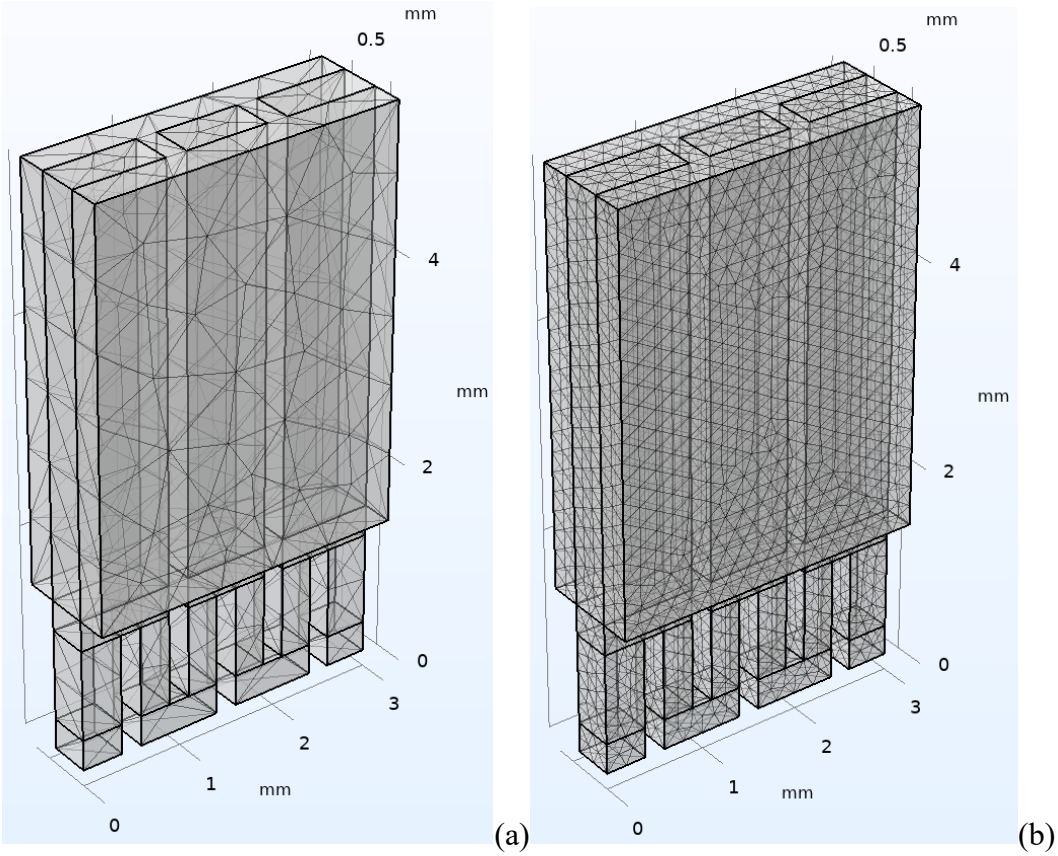

Figure 3.6: Coarse mesh (a) and extra fine mesh (b) in COMSOL.

Table 3.1: Comparison of meshing type (controlled by user) in eigenfrequencies study.

Type of mesh	*Computation time (seconds)*	*First eigenfrequency (Hz)*
Extremely coarse	5	115.40
Extra coarse	5	115.27
Coarser	6	112.55
Coarse	6	112.06
Normal	6	111.30
Fine	7	110.86
Finer	8	110.1
Extra fine	15	109.47
Extremely fine	628	109.19

3.2.10 Analytical model for cylindrical hair-like sensors

An alternative to FEA would be the use of analytical models. Analytical models are often less precise than FEA simulations but require substantially less time to compute. Moreover, analytical models can allow the use of optimization methods to optimize the design of the hair sensor [125, 126]. In 1978 Fletcher proposed a detailed mechanical model to account for the acoustic hair-like receptors in insects [51]. The model has been since reproposed and used by biologists and engineers, sometimes with simplification or added details [50, 52, 53]. In Appendix A.2 the mechanical model based on Humphrey et al. is presented [53]. This model was considered in the beginning of the project, but it was soon disregarded mainly because the project moved away from cylindrical hairs and began using solely squared hairs (as you will see described below). Another issue was the need to evaluate experimentally the torsional stiffness and damping ratio. Despite its early dismissal, the model is included in this thesis's appendix to provide a thorough and complete overview of the methodologies explored.

3.3 Sensor Construction – Additive Manufacturing

Additive Manufacturing (AM) (commonly referred to as "3D printing") is defined by International Organization for Standardization ISO/ASTM 52900:2021 as the "process of joining materials to make parts from 3D model data, usually layer upon layer, as opposed to subtractive manufacturing and formative manufacturing methodologies" [127]. The different AM technologies are described below, followed by a description of the processing process, from CAD design to finalized physical object.

While the process described above is common of different AM methods, the standard ISO/ASTM 52900:2021 defines seven different AM process categories, described below. Table 3.2 shows the main advantages and disadvantages of the different techniques.

- **Binder jetting (BJT)**, this technique creates two dimensional layers by depositing a liquid bonding agent on a powder form material [127, 128].
- **Directed energy deposition (DED)**, this method uses a focused thermal energy (often a laser beam) to melt a material as it is being deposited [127, 129]. This method can be used to create 3D objects from scratch as well as for repairing, joining, or coating purposes. Albeit ceramic, polymers and metal composites can be used with this technique, metal is the most common [129].
- **Material extrusion (MEX)**, it is a process in which a material is extruded through a nozzle or orifice [127]. Albeit the extrusion can happen in different modalities, the most common is by melting the material with heat before forcing it through a nozzle. It is one of the most common methods used in AM, as the printers can be quite inexpensive compared to other techniques [130].
- **Material jetting (MJT)**, this process is similar to 2D inkjet printers, droplets of the material are directly deposited in the building stage [127, 131]. Ultraviolet (UV) light is used to solidify the material, and, once the layer is solid, the building stage moves down, allowing the printer to produce the next layer [131].
- **Powder bed fusion (PBF)**, this technique makes use of a powder bed of material and a thermal energy source. The latter is used to selectively induce fusion of specific regions of the powder particles to create a layer of the model [127, 132]. The printer adds and smooths the powder for each layer.
- **Sheet Lamination (SHL)**, in this process sheets of the materials are shaped as desired, stacked and then bonded to form a part [127, 133]. This is one of the cheapest and easiest AM methods, nevertheless, industrial applications are still currently limited [133].

- **Vat photopolymerization (VPP)**, this method makes use of a reaction called photopolymerization. When visible or UV light hits liquid photopolymers, it induces their polymerization, solidifying them [134]. In this technique the photopolymer resin contained in a vat is selectively cured by using light to create each layer of the physical object [22, 127].

Table 3.2: Advantages and disadvantages of different AM techniques [23].

AM technique	*Advantages*	*Disadvantages*
Binder jetting	Suitable for metals, ceramic, sand and food. Lower material waste. High speed. Good reproducibility. High geometric freedom.	Low resolution. High cost of printer. Bulky machinery. Complex post-processing.
Directed energy deposition	Suitable for polymer, metals and ceramics. Highly controllable microstructural features. Can be used to repair or add features to objects.	Low resolution. Low speed. Low geometric freedom. Needs plenty post-processing. Very high cost. Bulky machinery.
Material extrusion	Large variety of materials. Low cost. Very mature.	Low resolution. Low speed. Needs manual change of nozzle for resolution change during print.

Material jetting	High speed. Low cost. Ease in producing multi material objects. Scalability.	Extremely complex process. Issues in the depositions of droplets. Nozzle clogs often. Limited choice of materials. Low accuracy.
Powder bed fusion	Suitable for metals, ceramic, sand and food. High geometric freedom.	Low accuracy. Low speed. High cost.
Sheet Lamination	High speed. Low cost. Wide choice of materials.	High material waste. Weak inter-layer bonding. Labor-intensive.
Vat photopolymerization	High printing speed. High resolution. Possibility to print layer-by-layer instead of point-by-point.	Limited choice of materials. High cost (low-cost printers are emerging).

Each of these processes are subdivided consequently in different techniques depending on the application process and curing principle. Nevertheless, since VPP is the technique used in this project only the discrimination of its different processes will be described here. VPP was chosen for its resolution/cost ratio, its printing speed and the possibility to print layer-by-layer instead of point-by-point with some of its techniques.

Stereolithography apparatus (SLA), this technique is often considered one of the first AM technologies. In this VPP, the tank is transparent, allowing the resin to be cured by a laser beam according to the layer information. After a layer is cured the building platform moves in the Z direction by a layer thickness height. The process is repeated until the full model is completed. The accuracy of the printed parts depends on the diameter of the laser beam, called spot size,

which usually provides the highest accuracy between VPP technologies. Since the laser can hit only one point in the tank at a time, this technology is often quite slow, with a print speed in the range of 10-20 mm/h [22]. Figure 3.7 shows a typical SLA printer and its components.

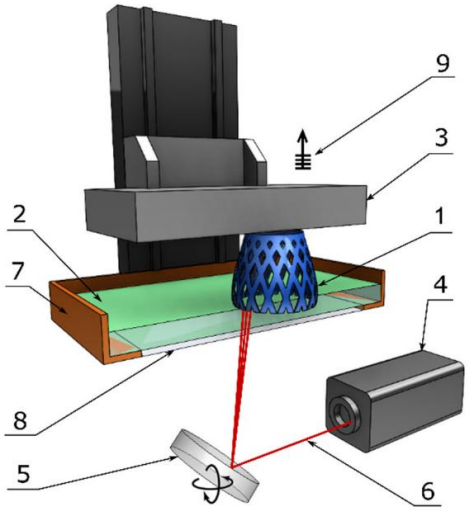

Figure 3.7: Diagram of a SLA machine, taken from [22]. 1 – 3D printed model, 2 – liquid photosensitive resin, 3 – building platform, 4 – UV laser source, 5 – XY scanning mirror, 6 – laser beam, 7 – resin tank, 8 – resin tank's transparent window, 9 – layer-by-layer elevation.

Digital Light Processing (DLP), this method is almost identical to SLA, the only difference rests in the curing method. While SLA has a mirror reflecting the laser source, DLP uses a digital light projector. For this reason, this technique is faster since the digital screen projects the UV light on the whole layer instead of the mirror moving the laser beam at different points. Nevertheless, the digital light project is composed of different pixels, therefore each layer will result pixelized and the whole model "brick-like". The resolution of the model depends on the size of the pixel of the projector. Figure 3.8 shows a typical DLP printer and its components.

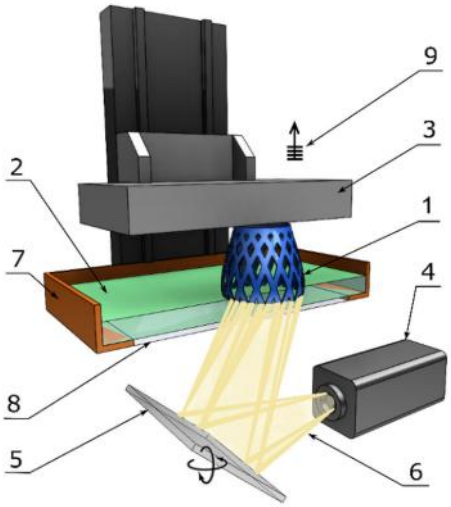

Figure 3.8: Diagram of a DLP machine, taken from [22]. 1 – 3D printed model, 2 – liquid photosensitive resin, 3 – building platform, 4 – light source, 5 – digital light projector, 6 – light beam, 7 – resin tank, 8 – resin tank's transparent window, 9 – layer-by-layer elevation.

Continuous Digital Light Processing (CDLP)/Continuous Liquid Interface Production (CLIP) is an improvement of the DLP technique. Instead of a normal glass window, the vat has an oxygen-permeable window. This window can form a dead zone that permits the resin to flow between the interface of the printed part and the window itself. This uncured resin flow greatly increases the resolution of the printed model, while also decreasing printing failure caused by peeling force. Additionally, CDLP/CLIP machines are designed to continuously move the build platform, this allows for printing at high speed (several hundred mm/h), while reducing the "brick-like" effect in the Z axis. For this reason, the models have isotropic mechanical properties. This means that CDLP/CLIP have a higher resolution than DLP in the Z-axis, while being the fastest VPP technology [22]. Nevertheless, its cost is greater than conventional DLP, for example the company Carbon (the only company with the patent for CDLP), sells the printers only on a subscription basis, and depending on the device the prices can range from $40,000 to $150,000 per year [135]. Figure 3.9 shows a typical CDLP/CLIP printer and its components.

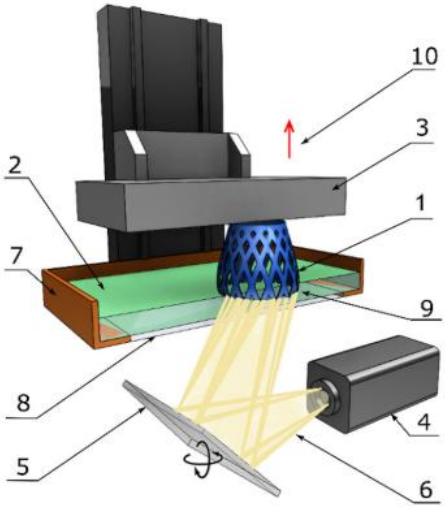

Figure 3.9: Diagram of a CDLP/CLIP machine, taken from [22]. 1 – 3D printed model, 2 – liquid photosensitive resin, 3 – building platform, 4 – light source, 5 – digital light projector, 6 – light beam, 7 – resin tank, 8 – resin tank's oxygen-permeable transparent window, 9 – continuous elevation.

In this project an Asiga MAX X27 DLP printer was used, which provides a 27 µm pixel resolution in the XY-axes and, depending on the chosen resin, a Z-axis resolution that goes from 10 µm to more common 50 µm or 100 µm [136].

3.3.1 Additive Manufacturing Preprocessing

Once the model is designed in the CAD software, it is exported in a STL format; the main format used to prepare data for 3D printing. STL is often wrongly referred to as an acronym for "standard triangulation language". Nevertheless, ISO/ASTM 52900:2021 specifies that this comes from its early development in CAD for the STereoLithography process and was then extended as the standard file format for all other 3D printing processes. STL basically converts the designed 3D structure into a network of triangles to communicate the model geometry to the machine responsible to build the physical part [127]. The size of the triangles rules the resolution. The smaller the triangles, the higher the resolution, and the more accurate the physical model will be manufactured compared to its digital counterpart.

The STL file is then imported in the AM software, which allows the user to place the model on the build platform (Figure 3.10). The models are then split by the printer's software into

different layers in the XY plane (parallel to the printer platform surface). The AM printer uses these layers to reproduce the 3D model into a physical object by printing them in the Z direction. The layers can be of different thicknesses, defined by the user, material limits, AM process type, and the printer specifications [22]. The software may also allow the user to specify different settings per different groups of layers. Figure 3.11 shows the interface to modify these parameters for different sections of the model, in this example, in column 1 (which includes 30 layers) the Exposure Time is 3 seconds, while in column 2 (which includes the next 6 layers) the Exposure Time is 2 seconds. Lastly, the software can also allow the user to see how the model is split into different layers. This can be used to double check that the layers are being printed correctly or as reference in case the user must stop the process at a certain layer.

Preprocessing is the name of the process that goes from the preparation of the model in CAD (design), its export in STL and preparation of layers, to the selection of AM printer settings. It basically covers all the tasks required prior to the AM process itself.

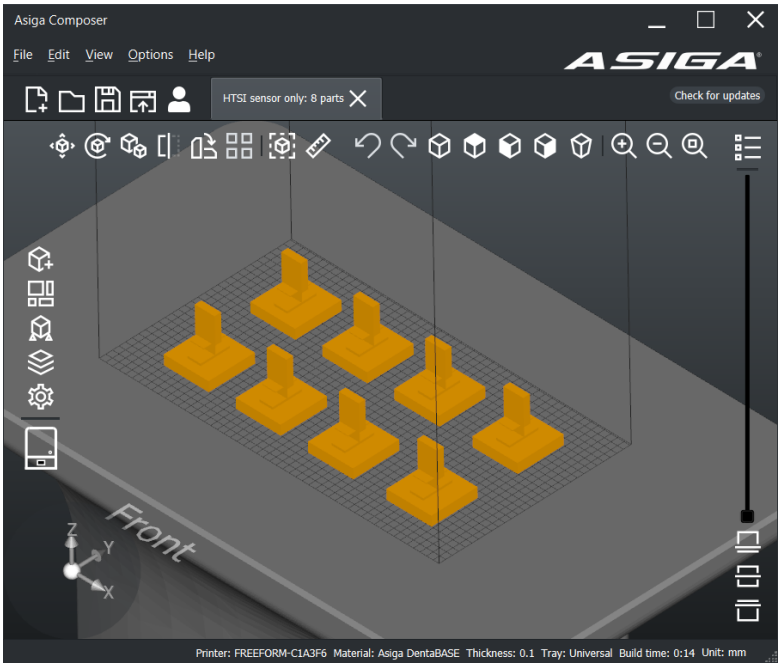

Figure 3.10: Asiga Composer screenshot (Asiga MAX X27's software) showing the placement of STL files on the build platform.

Figure 3.11: AM software screenshot of the setting that can be applied during the processing stage. The columns represent different groupings of layers, while the rows represent the different parameters that the user can modify.

3.3.2 Additive Manufacturing Processing

The AM **processing** phase is essentially as described above for the different technologies. Different printers and technologies might have different settings and offer diverse degrees of control on the process (e.g., curing time for each layer, speed of movement of the building platform between layers, etc.). Printers might offer some sensors to improve the manufacture of the object, or to control that the printing process is proceeding correctly and stop it if there are any issues. In DLP, the only thing that the user can do during this stage is pausing the build when reaching a certain layer (Figure 3.12). This allows the user, for example, to change the building tray with a different resin to create a model that is composed of different materials and show different properties. Between tray changes the excess of resin was cleaned from the build platform. After the printer has finished building the physical object the user can remove the object from the build platform essentially starting the postprocessing phase.

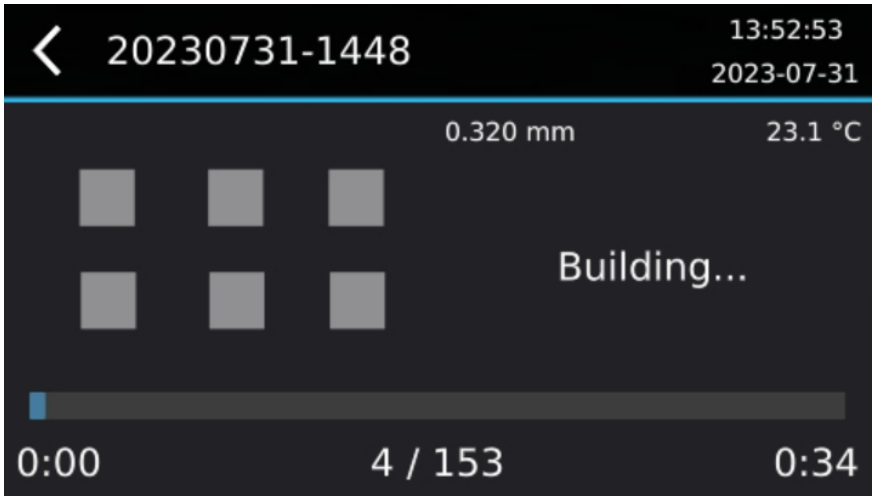

Figure 3.12: Front panel of Asiga MAX X27. By clicking on the upper-left arrow "<" the user can pause the process. Once the arrow has been clicked, the printer finishes to print the currently processed layer and stops before the next layer. The front panel also shows the layer being printed and its number in the bottom-centre, in the bottom-right it shows the time left to complete the print and, in the bottom-left, the time that has passed.

3.3.3 Additive Manufacturing Postprocessing

Postprocessing techniques can differ between AM technologies, and it refers to the whole process required to make the printed object usable for the designed application. When using photopolymerization, usually two practices take place in this phase. The first is to rinse the built model in a wash solution, the most used is isopropyl alcohol (IPA), to get rid of any resin residue [22]. Dedicated machines can be used, or one can manually create an IPA bath in which to submerge the printed model. Asiga, in their user manual, suggests the use of two baths, a "dirty bath", to be used first, to remove the majority excess resin, and a "clean bath" to remove the remaining resin [137]. The "clean bath" would see IPA changed often. The user can even simply submerge the object in the resin, or it can also move it inside the bath to make sure the residues are appropriately removed. Next, to make sure the model is fully cured, the sample can be exposed to sunlight or exposed artificially to UV light [22]. This can improve the strength of the material. Asiga's user guide suggests a postprocessing UV curing time between 5 and 30 minutes [137]. Other postprocessing processes may be used, like exposing the model to heat, gluing different printed parts and so on.

It is important to remember that temperature, duration of curing process, rinsing time and other postprocessing treatment variables play a fundamental role in determining the mechanical properties of the finished object. For example, it was noticed through experimentation that too long a bathing time in IPA made flexible structures brittle, but too short a bathing time did not properly clean the samples. Of course, these parameters depend on geometry and dimension of each sample and there is not a specific time that works in every scenario. Care should be taken during postprocessing to reach the best mechanical properties a model has to offer.

In this project the samples were firstly removed from the build platform using a metal tool (Figure 3.13) and placed on a tissue to absorb part of the resin residues. Then, using tweezers the sample was introduced in the first bath of IPA for a few seconds, the vat was shaken gently to try and remove more excess of resin (Figure 3.14). The samples were then transferred to the "clean bath" of IPA for a time between 1 and 5 minutes, before being placed on a clean tissue to dry for a few minutes. Lastly, the samples were UV cured for 5 minutes in an Asiga Flash (Figure 3.15). In other sections the use of an ultrasonic bath was paired with either IPA or soapy water (using commercial dishwasher soap). This allowed to reduce the time of immersion in IPA or avoid using IPA at all, as the ultrasonic bath improved the cleaning capabilities of both. The reason to use soapy water instead of IPA was because IPA changes the structural integrity and the mechanical properties of the printed part [138].

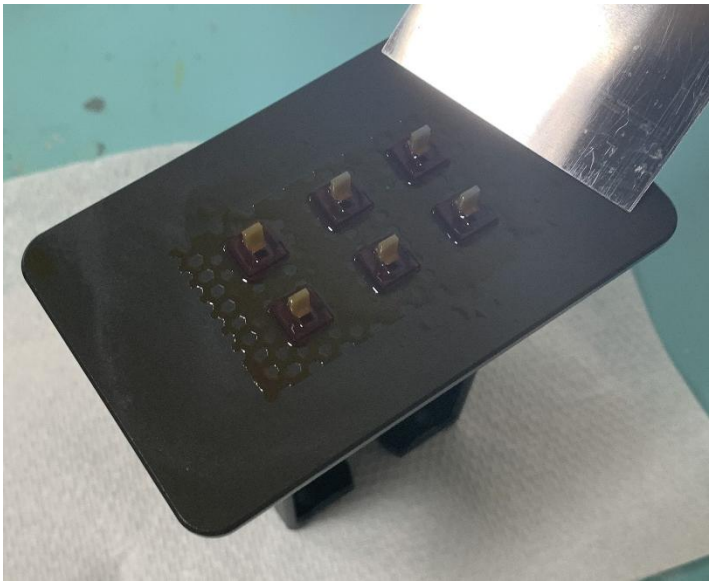

Figure 3.13: Build platform with printed objects, in the upper-right the metal scraper used to remove the models can be seen.

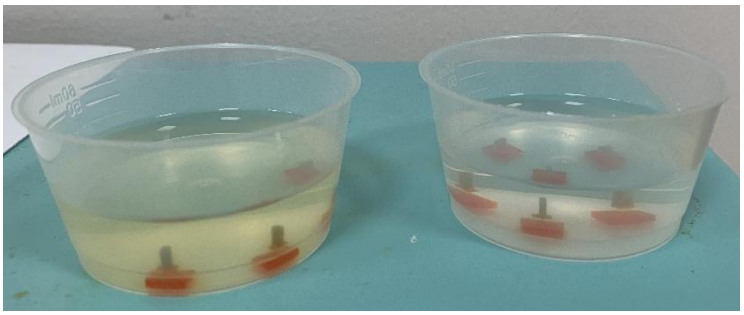

Figure 3.14: IPA baths with models inside. "Dirty bath" on the left and "clean bath" on the right.

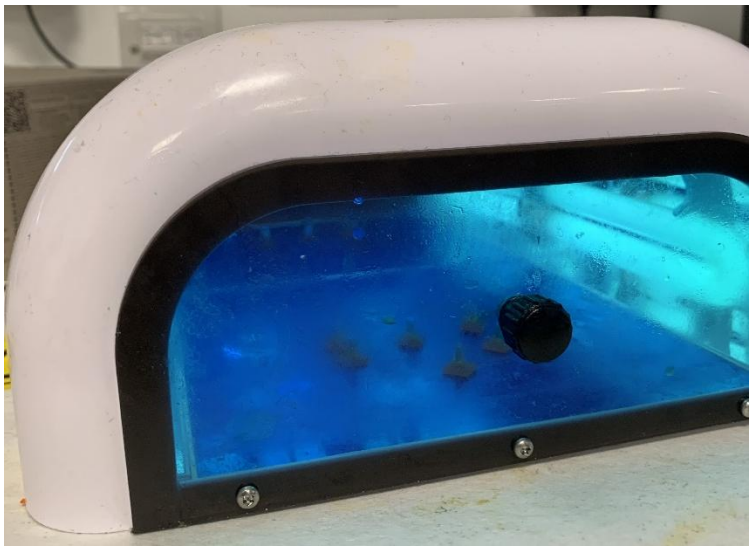

Figure 3.15: Asiga Flash being used for UV post-curing of 3D printed objects.

3.4 Sensor Electrical Integration – Metal Coating

The process of doing ulterior modification on a 3D printed structure technically still belongs to the “postprocessing” procedure. However, due to the complexity of the topic it was decided to treat this procedure in a separate subchapter. This subchapter will describe the different techniques that were used to coat the sensors with metal, their challenges, their limitations, and ultimately it provides a comparison between them. Different methods were used to produce the results in Chapter 3 and 4, for each result or section, the method involved for metal deposition is specified.

3.4.1 Evaporation

Evaporation is a type of physical vapor deposition (PVD), a thin film deposition technique. PVD includes a small cluster of atoms, or even individual atoms, which are not usually found in gas phase. These atoms are removed from a source (which can be solid or liquid), they transit in a vacuum chamber, and infringe on a solid surface, here the atoms stick and form a film [139]. It is important to note that due to this process, the properties of these thin films differ wholly from a thinner version of a bulk material [139].

In the case of evaporation, the process of detaching atoms from the source from the material happens thermally. A macroscopic region of metal is heated to the melting point and beyond [139]. With this technique the deposition occurs in line-of-sight with a distance in tens of cm between source and target, allowing a large area to be coated. In many sources the deposition happens at microns/minute at short distances, which scales as roughly the inverse of the distance squared, allowing hundreds of nm per minute for larger distances (thus, large areas) [139]. This method is commonly used to create the internal metallic coating of potato crisp bags for example.

Evaporation suffers from two major limitations. The first one is that the high temperature evaporated atoms arrive at a colder sample surface. For this reason, it is subject to several issues, such as wetting, nucleation, cluster formation, and agglomeration, which result in less-than-ideal properties [139]. The second one is the difficulty in forming alloy films as different materials have different temperature-vapor pressure relationships [139]. While the latter does not concern some applications (like this research), the former is a universal drawback. For these reasons, evaporation is rarely used in electronics.

In this project an Edwards E306 evaporator was used, together with aluminium foil. The aluminium foil was placed on a crucible where a large current is passed. The source is then heated until a flux of atoms is emitted (Figure 3.16). The evaporator took a long time to create a vacuum using liquid nitrogen (in some experiments it took up to 2 hours). The evaporation process would then last for a few seconds. No thickness monitor was available, and no post-measurement of thickness was conducted.

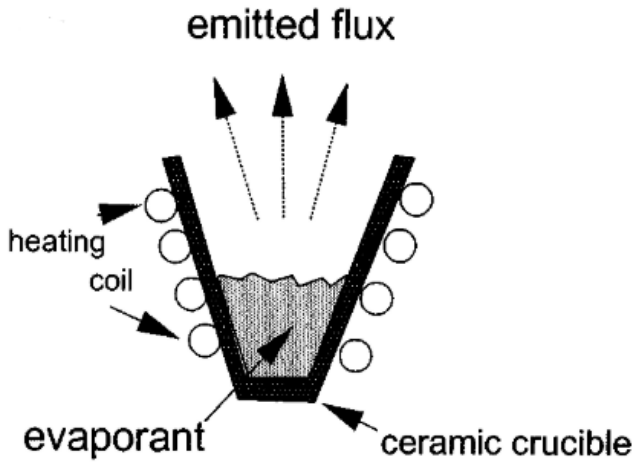

Figure 3.16: Schematic of a crucible source in an evaporator. Image taken from [139].

This process proved useful only if applied to the XY-axis of samples printed with DLP but not in the Z-direction. This is because at a micron scale it is possible to visualize clearly some sort of "step" between layers printed in the Z-axis, this means that the thin layer of metal was evaporated only between steps but not connected to each other. This was due to the line-of-

sight nature of this PVD technique. Meanwhile in the XY-axis albeit it is possible to visualize the separate pixels with a microscope, the surface is much smoother than in the Z-axis, this allows the thin-film to be deposited correctly. Moreover, the layer size in the Z-axis is often in tens or hundreds of microns, while the pixel size in DLP is often in tens of micrometre, therefore their "step" and spacing are greatly inferior, allowing metal atom clusters to touch each other and create a large layer. The presence of a step in the 3D printed material in the Z-axis is dependent on the printing settings as well as the resin, for the area of interest it was measured a ~20 microns step. Figure 3.17 shows a simplified schematic representation of the evaporated metal on a DLP printed sample. This and the long preparation time were the main reasons why this method was abandoned.

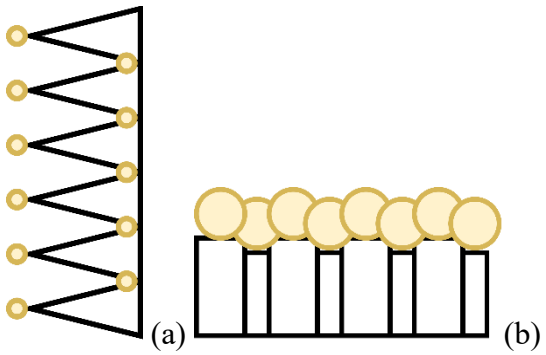

Figure 3.17: Schematic representation of metal evaporated particles (yellow) on a DLP printed model (white and black). Evaporation along the Z-axis (a). Evaporation along the XY-axis (b).

3.4.2 Sputter coating

Sputter coating, or sputter deposition, is another PVD technique, but the process differs intrinsically from evaporation in the way the atoms are detached from the source. Nevertheless, it is still important to remember, as stated earlier, that thin film deposited with PVD has different properties from a thin layer of a bulk material.

In this process the source used to create a thin film is called a target. A sputtering event begins when an energetic particle impacts the surface of the target. This energetic impact detaches kinetically part of the surface or near-surface atoms, which in turn move deeper within

the target and displace additional atoms [139]. During this kinetic collision process, atoms near the surface may be hit with enough energy to overcome the surface binding energy, and therefore be detached and emitted from the target [139]. These atoms, called sputtered atoms, are then deposited on another surface. The energy and angular distribution of sputtered atoms differ greatly from the evaporated ones. In sputtering the depositing atoms arrive with high kinetic energy and implant themselves on the surface of the specimen much more clearly than with the evaporator process.

Sputter deposition typically uses a plasma or ion beam as the energetic particle source hitting the target. A plasma is generated under vacuum by applying a voltage across an anode and a cathode, i.e., a diode. This is the basis for the majority of sputter PVD systems. In the past the majority of the systems used a simple dc or rf diode, nevertheless the majority nowadays use magnetrons as they are better performing and solve several flaws of previous systems [139]. A magnetic field is added near the cathode, this makes the electrons travel along the magnetic field lines and consequentially increase their path length. This results in higher plasma density [139]. A magnetron is a specific type of magnetic plasma enhancement where the Hall effect forms a closed loop. Different geometries exist to create this specific magnetic field, but the most common is a planar one (Figure 3.18), as the one used in this project's sputter coater, the Agar Automatic Sputter Coater AGB7341 [140]. The reason behind this closed loop field is to trap electrons and increase their path length near the cathode. This results in a higher probability of collision and scattering [139]. Magnetrons act as almost perfect diodes, and the current can be increased until the limits of the power supply or the target melts entirely [139]. Ion beam sputtering is another technique, but it will not be described here as it was not used and has a lower deposition rate (albeit it can also be used with non-metallic targets), it is described in detail in [139].

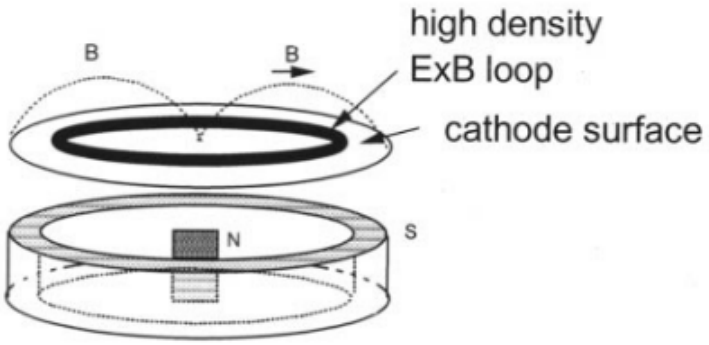

Figure 3.18: Schematic of a sputter coater's circular planar geometry. Image taken from [139].

The directionality of the coating in the sputter coater can, to a certain extent, be controlled by the pressure of the magnetron. Albeit it is always non directional, at lower pressures the deposition happens almost as line-of-sight, to a smaller degree than evaporation [139]. At higher pressures the sputtered atoms lose all their kinetic energy from the sputtering process and are considered thermalized with the background gas, creating an almost fog-like distribution [139]. This means that the pressure at which the magnetron operates will also vary the properties of the deposited film. In any case, the deposition of sputter atoms arrives in different directions, from normal incidence to grazing. This allows for an advantage/disadvantage. The advantage is what is called “step coverage” which is the ability (due to non-linear directions of coating) to create an almost uniform film over a step on the sample. This brings a clear advantage if we consider the issue described earlier with evaporation in the Z-axis side of the 3D printed samples (Figure 3.17a), as it allows a proper thin film to be deposited. The disadvantage is that you may coat a surface you are not interested in, or that is undesirable to coat. In the case of the manufactured sensors in this research, parts of the base (that was positioned perpendicular to the target) was coated as well. This was problematic as the sensing component was essentially short-circuited. The extra metal had to be scraped off afterwards with a scalpel. Masking is possible only to a limited degree (compared to evaporation). Nevertheless, design decisions can be taken to limit these problems

to some extent, and the advantage of "step coverage" was greater than the issues it could bring. There are ways to increase the directionality of sputter deposition, but they usually reduce the deposition of about 70% [139], they were therefore ignored. While both evaporation and sputter coating require the creation of vacuum to operate, in the author's experience the evaporator required between 1 and 3 hours to create vacuum conditions, while the evaporator required ~5 minutes. This made the latter quicker to operate.

3.4.3 Conductive paint

The use of conductive paints is quite common for several applications, and the research world shows the use of different conductive materials as the base of these paints, from graphite [141] and carbon [142] to metals like silver [143]. Some are even commercially available, easing their use. One of the most common is silver paint. It has also been used successfully to produce strain measurements [144]. In this thesis Agar AGG302 quick drying silver paint was used to produce strain measurements [145].

Application of the silver paint was done in two methods, brushing and spraying. Brushing is the easiest way to use conductive paints, but it presents some issues, such as non-uniform coating, and once dried it might be more susceptible to flaking and breakage, ultimately rendering the sensors coated with it useless. An alternative that produces a smoother layer of metal is spray painting. Agar in their datasheet suggest to use a paddle agitated pressure tank system, it suggests to keep the pressure to 2 to 2.5 bar, and using a nozzle between 1 and 1.5 mm [145]. They also suggest its dilution with a ratio 2:1 by weight product to dilutant [145]. The used dilutant was the one provided by Agar itself. It is important to consider that the properties of the paint are not the same as the bulk material contained in them.

Early experiments were conducted by using an airbrush kit produced by Gocheer. The provided pump system has a specified air pressure of 40 PSI (~2.7 bar, slightly above the one

suggested in the datasheet), while the nozzle sizes provided were below the suggested size, 0.2 mm, 0.3 mm and 0.5 mm, the former size was not used as it was deemed too small. After spraying the metal, as suggested in the datasheet, the samples were placed in an oven at 80 ˚C for 30 minutes. The results were promising with both 0.3 mm and 0.5 mm nozzles, and a variance in resistance was found when bending samples. Nevertheless, after repeated strain they would usually break the contact where the cables were attached. This section is also the one where at the bending of the sensor, most stress was applied. Moreover, it is impossible to control the thickness of the metal layer, and from some X-ray scans it was possible to see that some gaps did not contain any metal (Figure 3.19a), and that along the line of the coating the thickness changed from top to bottom, for example. In one of the experiments, it went from ~30 microns to ~60 microns (Figure 3.19b). These issues made reproducibility very hard. This might be mitigated by automating the process instead of doing it by hand, and with the airbrush always consistent on the same aperture. Further testing was conducted with a spray gun with a 1.4 mm nozzle, but the amount of silver paint coming out was too great and would make the sensors unusable as the paint deposited would be too much. The deposition of silver paint with an airbrush mostly occurs in line-of-sight, but some non-linear coating occurs as well across the edges.

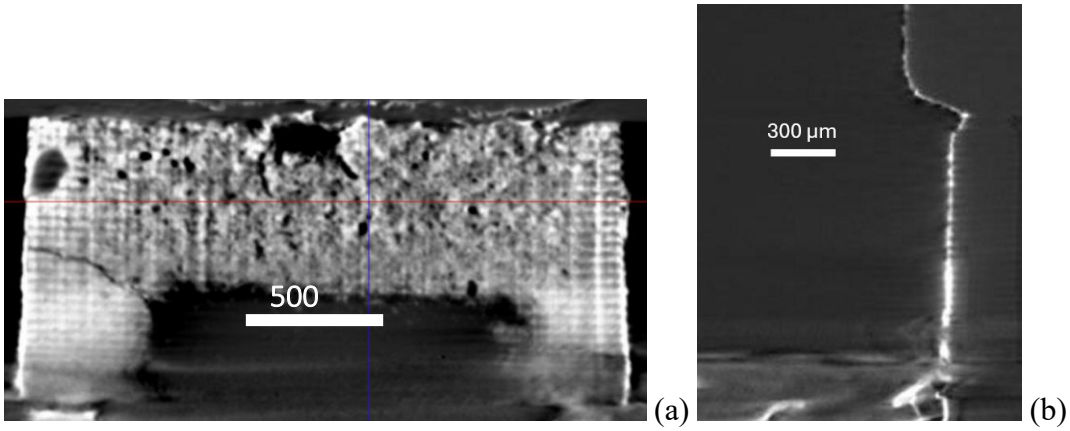

Figure 3.19: X-ray scan of a sensor coated with silver paint (shinier part) with an airbrush. Figure (a) shows the gaps where no metal was present, (b) shows a thickness variation along the coating.

While this practice is not as effective and controlled as other methods, it has some advantages, it is the cheapest way to add a metallic layer on a 3D printed part, it is the easiest to use, and potentially the least wasteful. It is also the quickest, as the preparation includes only mixing the silver paint with the solvent and connecting the whole spraying system. Most of the time is taken by cleaning the whole system with acetone after use. Silver paint was consistently used in the thesis research via brushing to help the fixture of cables to the sensor base and connect them to the sensing component, but its use for the main sensing part was deprecated. It is also very useful in early prototyping whenever a change in design occurs to understand the feasibility of a structure in sensing. The main issue remains the breakage after repeated bending and stress, and the unpredictability in thickness. An additional issue is that the silver paint needs to be mixed before each use (silver deposits at the bottom of the storage container), and this might vary the actual silver content of the paint at each use. Other paints might be affected less by these problems, but they were not tested nor considered since alternative techniques were used for electrical integration instead. The use of silver paint in this project is reserved only via brushing to the creation of electrical contacts for the sensor to connect to the circuit, or for increasing the conductivity of the sensor's terminals.

3.4.4 Spin coating

Spin coating is a widely used technique used to deposit thin layers of a material by using centrifugal forces. A usual process involved depositing a drop of fluid on a sample and then rotating the system at variable speeds. An Ossila spin coater was used which provides the possibility to select speeds between 120 RPM and 6000 RPM, with a speed stability lower than 2% [146]. The centrifugal force causes the fluid to spread on the surface (and off the edges) leaving only a thin film on the sample [147]. The film thickness depends on a wide variety of factors, from material dependent ones (like the viscosity, the dry rate, etc.), to the parameters chosen for the machine (like spin time, spin speed, etc.). However, as a rule of thumb, the

higher the speed and time of spinning, the thinner the coating. Film thicknesses can even be below 10 nm [147]. The major advantages of this technique are its repeatability, the ease of use, the low cost and the faster fabrication of thin film compared to other techniques [147]. There are four distinct stages to the spin coating process, Figure 3.20. In this project this technique was used with Agar's quick drying silver paint [145].

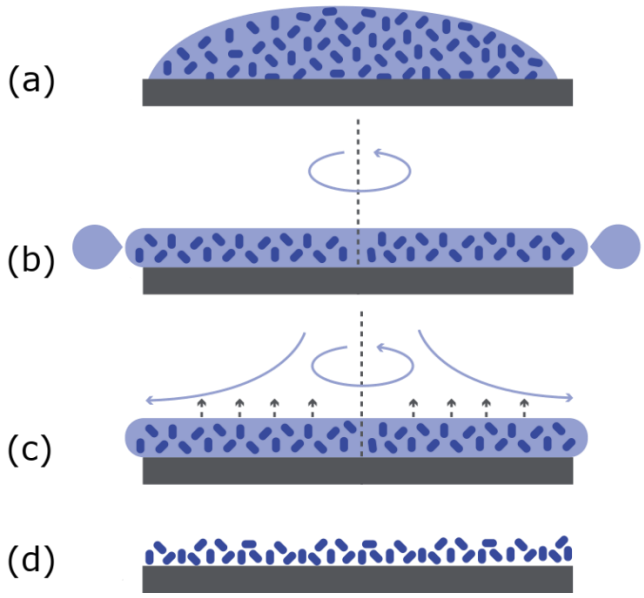

Figure 3.20: Different stages of spin coating. Image taken from [148]. Image remains the copyright of Ossila. Taken with permission from www.ossila.com.

The first step is the dispensing of the fluid or resin on the sample (Figure 3.20a). There are two types of dispensing methods. Static dispense is the deposit of a drop of fluid near the centre of the sample, before beginning the spinning process [147]. While, dynamic dispense is the process of applying the fluid on the sample while the latter is already turning [147]. The second method can result in less waste since you can deposit less material [147], but it can be harder to use in some scenarios, like samples being too small. The second step is the acceleration stage (Figure 3.20b). Here, the majority of the fluid on the sample is ejected at the edges as the system spins up [147]. After this, the system spins at a constant rate, this is the third stage (Figure 3.20c). At this point, the fluid gets thinner in a uniform way generally, but depending on the spinning parameters and material, there might be a thicker coating thickness around the rim of

the sample [147]. After these stages the viscosity of the fluid has a minor effect on the coating thickness and we enter the fourth stage, ruled by the evaporation of the solvent in the fluid (Figure 3.20d) [147]. This can start during the final rotation stage or when the rotation has stopped. After this, ulterior processes may take place to condition the coated layer further.

Plenty of mathematical models of this process exist, some easier and less precise, some more complex and more precise. The easier ones might only consider the spinning parameters (time and speed) or limited information on the fluid (viscosity, initial thickness, etc.), while the more complex it gets, the more parameters of the fluid need to be known (evaporation rate, solvent content, etc.). Moreover, some models mention Newtonian-fluid assumptions, while other are non-Newtonian. Tyona provides a comprehensive review of the different mathematical models [147], as none of them were used in this project for the reasons presented below, none will be reported here. It is also worthwhile to mention that many times people using this technique have tended to use empirical models that combine existing mathematical models with experimental data [148]. This allows the use of simpler models with less known data, but higher precision provided by precise measurements and the high reproducibility of this technique.

As stated above, in this project spin coating was used with the same silver paint that was brushed or sprayed. While other fluids can be created, the use of an already made one made sense to investigate the technique. This showed the limitations of this method, mainly that it works effortlessly only in flat geometries or wide geometries. It is harder to make it work for smaller areas, especially if they have a more complex geometry around them. This results in uncoated sections, layers that are too thick, or the fluid getting in parts where it shouldn’t. Moreover, masking is much harder with this technique at the small scale of this project. Therefore, after a few tests, this technique was abandoned. Some common defects are described by Tyona, such as comets, striations, chick marks, etc. [147].

3.4.5 Comparison of metal coating techniques

Table 3.3 attempts to summarize and compare the metal coating techniques described above. While it is not a comprehensive comparison, the main points of interest are described and may help in decision making. The comparison is made with a qualitative approach, more details for each coating technique are provided in their own section above.

Table 3.3: Comparison of the different metal coating techniques

	PVD (Evaporation)	*PVD (Sputter coating)*	*Conductive paint (brushing)*	*Conductive paint (spraying)*	*Spin coating*
Cost	High	High	Low	Low	Medium
Time required	High	Medium	Low	Medium	Low
Difficulty	High	Medium	Low	Low	Low
Material selection	Wide	Limited	Limited	Limited	Limited
Masking possibility	Yes	Yes, with limitations	Yes	Yes, with limitations	Difficult
Direction of coating	Line-of-sight	Limited line-of-sight, almost gas like	Direction of brush	Limited line-of-sight	Direction of fluid drop
Measurable thickness at application	With additional equipment	With additional equipment	Not possible	Difficult to estimate	Possible to estimate
Thickness range	Few nm to hundreds of nm	Few nm to hundreds of nm	Hundreds of microns	Tens of microns	Few nm to few microns
Quality of layer	Medium	High	Low	Medium	High

3.5 Sensor Structure Verification – micro-CT scan

Computerized tomography (CT) is a practice that takes different X-ray images at different angles of the same sample and, with the aid of computers and specific algorithms to reconstruct the scans, to create a 3D x-ray reconstruction of the specimen. The advent of better computers, combined with specific algorithms of reconstruction, allowed the introduction of this technology in the 1980s [149]. The use of this technology for sub-millimetre measurements is referred to as microscopic CT, or micro-CT. The technology is in practice the same, but it uses smaller arrays, and magnification means to capture generally smaller parts of a specimen. For example, the micro-CT scanner used in this research, the Bruker Skyscan 1172, can allow image reconstruction detecting sizes as small as 2 microns. To detect things at such small scales usually the volume of the reconstructed area is reduced. There have been numerous improvements in x-ray source and detector technology, algorithms and analysis software [149], but this subchapter is aimed at describing only the hardware and software that was used in this thesis work and the considerations that were taken to scan and analyse the manufactured sensors. The goal in using micro-CT scans was to verify that the structure of the sensors was 3D printed correctly, or with little error compared to the CAD design.

3.5.1 Scan acquisition and reconstruction

Figure 3.21 shows a simplified schematic of an X-ray tube. As previously stated, the X-ray images are taken at different angles of the same sample. These shadow images are taken over 180 or 360 degrees at a previously chosen fixed angle step. In most of the scenarios throughout this work the angle step was set at 3 degrees, as this provided a good ratio between quality of results and required capture time. The shadow images are collected by the photodetector and saved as TIFF files. The result of the acquisition is, then, a series of standard 2D X-ray captures of the sample. By rotating the object, we get a series of overlapping lines of X-ray absorption.

An array of superimposed lines is used to create a reconstructed slice in the plane normal to the z-axis for each row of pixels captured by the photodetector, ultimately generating a 3D array of voxels with a relative absorption line for each. In the reconstruction software the 3D array is reconstructed as an 8-bit grayscale image by selecting the maximum and minimum values of absorption. The minimum value is selected to obtain a resolution of the object without losing any information, while the maximum value is selected in a way that provides a clear contrast between different materials. Each of the reconstructed 8-bit images contains a slice of the volumetric reconstruction. Once they are put together, they can provide a 3D representation of the object of interest. Moreover, the software also allows the measurement of sizes of the specimens. This was the most common use of micro-CT scan in this work. In this way it was possible to see if some areas were over cured and much greater than the actual size of the design. This drove some changes in the DLP printing process.

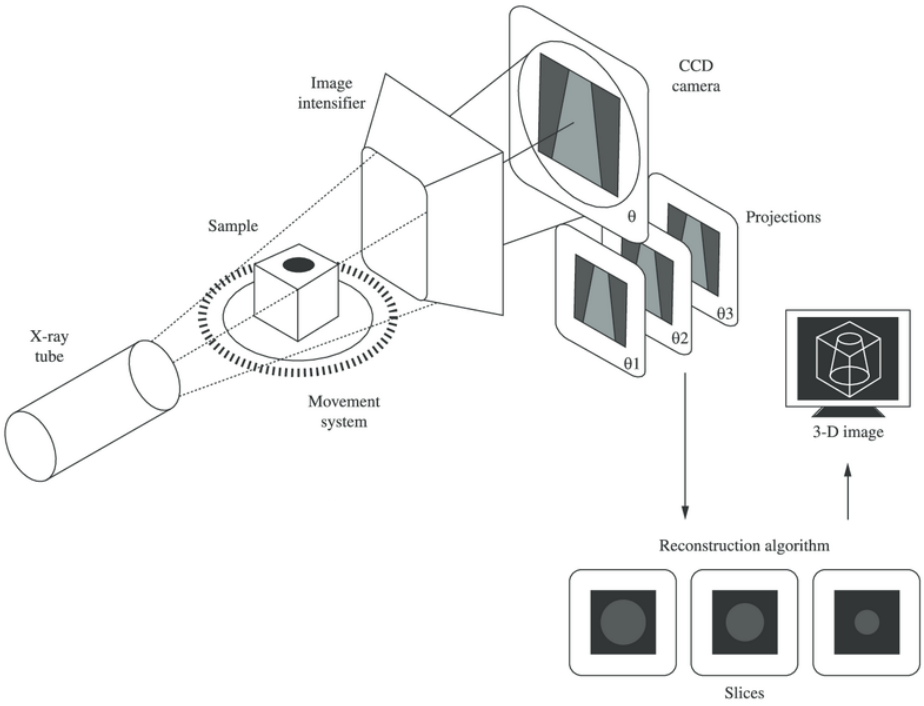

Figure 3.21: Schematic diagram of CT-scan acquisition process. Image modified from [150].

3.5.2 Challenges

The absorption coefficient of X-rays is linearly proportional to the material's density [151]. In some scenarios, like in biology [149], a relatively uniform attenuation coefficient and density of material could prove problematic in differentiating the different areas. In the case of multi-material 3D printing this issue might or might not occur depending on the used materials. For the materials used in this research a clear difference can often be seen, albeit in some cases it is hard to see overlaps at the junction where a different material has been used. On the other hand, when the metal layers are introduced on the sensor, sometimes, even for sub-micron layers finding the correct parameters to visualize the areas of interests can be challenging due to the huge difference in absorption. The inclusion of metal also presents another obstacle, the non-ability to measure the sub-micron thickness of interest when using thin-layer deposition. Moreover, the metal layers include a major issue, metal artifacts.

Metal artifacts are dark or bright streaks produced by beam hardening, photon starvation, edge gradient effect, scatter or a combination of these [152]. The amount and gravity of metal artifacts depends on the actual material, its size and shape, as well as the orientation in respect to the X-ray source (in the case of CT scans, which scan plane) [152]. This is usually a major issue in the medical field where metallic prothesis affect the accuracy of organ contouring [152]. In literature many papers have been published with metal artifact reduction algorithms, many are summarised in [152]. Nevertheless, in the case of my sensors usually the metal artifacts are reduced due to their thin size. Moreover, unlike in the medical field the size of the sensor and visualized parts is mostly known. Therefore, none of these algorithms were implemented and the bright and dark streaks were simply ignored during analysis. Still, it is important to know and recognize such artifacts, so no useful data is lost in the analysis process. The majority of metal artifacts in the sensor were produced when scans with silver paint and

cables were conducted. Figure 3.22, Figure 3.23 and Figure 3.24 show examples of metal artifacts in this research.

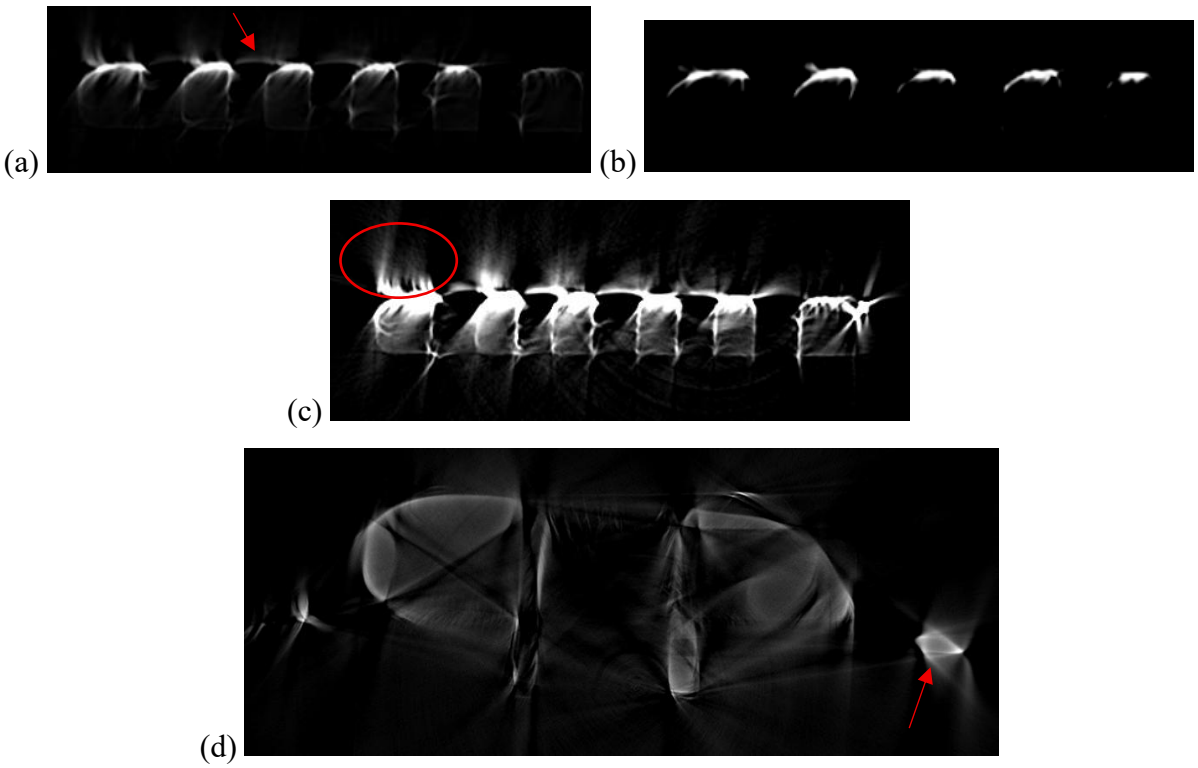

Figure 3.22: Examples of metal artifacts from the top view on a spring coated with sprayed metal paint. The red arrows and circle highlight examples of metal artifacts. Scan using the full contrast range (a), reducing the range from the light side (b) and reducing the contrast from the dark side (c). View at the base region where the tracks and cables usually are (d).

Figure 3.22, Figure 3.23 and Figure 3.24 show clearly that the direction of the scan affects the artifacts as well as the contrast. The top view is the most affected by artifacts, the bright strikes show near the metallic region in a clear manner even without further modifications on the contrast post-reconstruction (Figure 3.22a). Limiting the grayscale range (basically changing the contrast) from the bright side reduces the artifacts (Figure 3.22b), but also affects the visualization of scan, the metal seems thicker, and the plastic of the sensor disappears. On the other hand, by limiting the grayscale range from the darker side the artifacts worsen but the visualization of the plastic part of the sensor improves (Figure 3.22c). Lastly, the regions where more metal is present (at the base, where the tracks for silver paint and cables reside) the dark and bright streaks impact greatly the visualization of the specimen (Figure 3.22d). The front

view seems to be the least affected by the metal artifacts (Figure 3.23). The side view (Figure 3.24) shows more artifacts than the front view but less than the top view. For side and front view, leaving the contrast untouched makes the visualization of the plastic parts challenging (Figure 3.23a, Figure 3.24a). Meanwhile, as specified above, the plastic part becomes more visible when reducing the contrast from the dark side, at the cost of introducing more metal artifacts (Figure 3.23b, Figure 3.24b). In most scenarios, based on what the reason is for the CT scan being conducted, a balance between quality and artifacts must be reached.

(a)  (b) 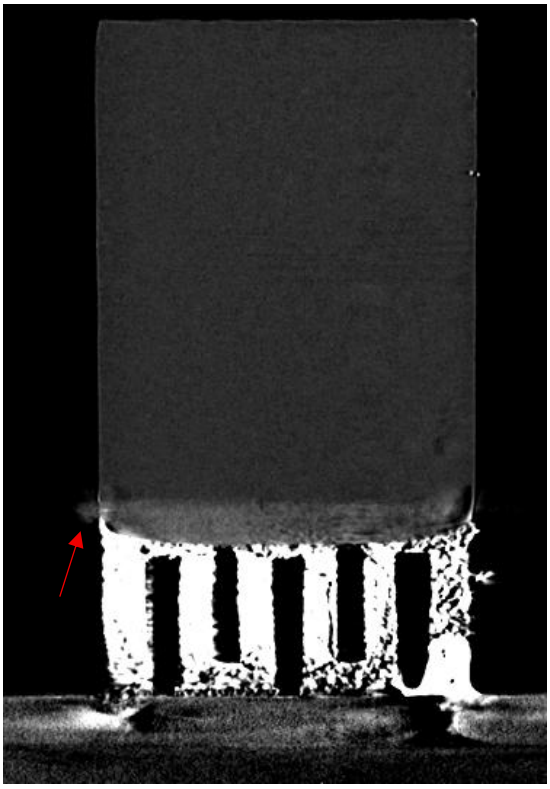

Figure 3.23: Examples of metal artifacts from the front view of the sensor. Scan using the full contrast range (a) and reducing the contrast from the dark side (b). The red arrow highlights an example of metal artifacts.

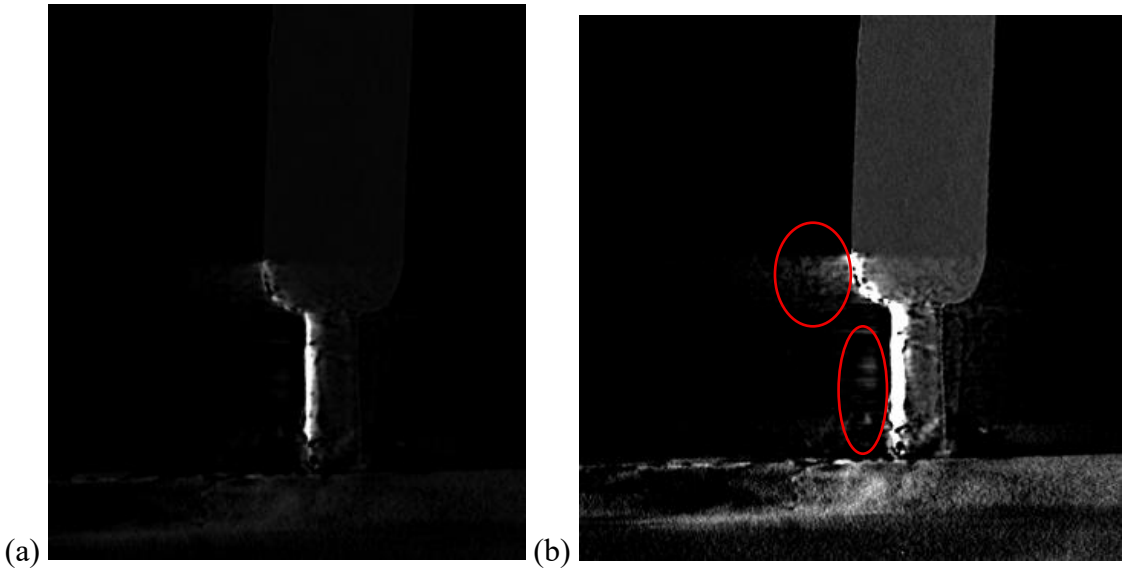

Figure 3.24: Examples of metal artifacts from the side view of the sensor. Scan using the full contrast range (a) and reducing the contrast from the dark side (b). The red circles highlight examples of metal artifacts.

3.6 Sensor Mechanical Experimentation – Experimental Modal Analysis

Experimental Modal Analysis (EMA) is technique developed to measure the vibration of the structure in terms of its temporal and spatial elements, so-called 'modal' properties [153]. EMA basically consists of applying an excitation force to a structure and measuring its response at different points. This analysis was important for the constructed sensors in order to know their mechanical responses. The vibration of the sensor body at different points was given thanks to the Scanning Laser Doppler Vibrometry (SLDV), described below.

3.6.1 Laser Doppler Vibrometry

The first use of a laser for fluid velocity measurements using doppler frequency shifts was recorded in 1964 [154]; just a few years after the appearance of the first laser. This can be considered the first use of Laser Doppler Vibrometry (LDV). Albeit in paragraph 2.1.5 the Doppler effect was described for sound waves; light waves are also affected by this phenomenon. Which is the basis for the principle of operation of the Laser Doppler Vibrometer

(also abbreviated LDV). Doppler frequency shifts of light pointed to a surface are directly proportional to the surface velocity of the moving object [155]. This is very convenient as knowing the frequency of the light pointed to the surface, we can measure the back-scattered light and its frequency shift caused by the moving surface. This enables the means of non-contact measurements of vibration velocity.

The simpler LDV allows direct measurement and record of the vibration of an object wherever the laser is pointing at [156]. The structure is comprised of a laser source, an interferometer, and a photodetector (see Figure 3.25). The laser source is traditionally a Helium-Neon (HeNe) laser [154-157], but in the last few years infrared (IR) solid state lasers have begun to appear in commercial LDVs [156]. Nowadays they are both commonly used, and each has its own advantages and disadvantages, depending on the application [156]. The interferometer combines the reference laser beam and the captured one using an acousto-optic modulator (Bragg cell). The working principle is simple, the measurement laser hits the test sample, keeping a reference beam within the LDV. Then, the sample's reflected light is capture by the photodetector, where it is re-combined with the reference signal [156]. The reflected light is Doppler shifted by a frequency, f_D, directly proportional to the sample's instantaneous velocity, v, according to equation (3.1) [156]. With n the refraction index of the medium where the sample is placed, and λ the laser's wavelength.

$$f_D = \frac{2\,n\,v}{\lambda} \tag{3.1}$$

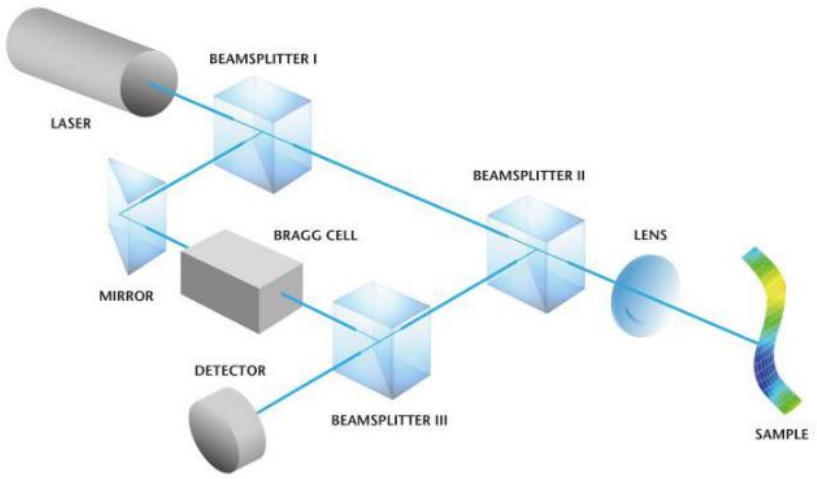

Figure 3.25: Laser Doppler Vibrometer optical layout. Image taken from [156].

The signal acquired with the detector is then demodulated using the ArcTan(I/Q) method, which makes it possible to easily evaluate both velocity and acceleration of the sample [156]. SLDV refers to a LDV that automatically scans multiple points. These vibrometers are equipped with a camera that allows visualization of small structures, and, with the aid of their software, assignment of multiple points to include in an overall acquisition [157]. This allows visualization of the movement of the structure across the assigned point. The total acquisition time, *t*, can be evaluated using equation (3.2) [156].

$$t = T\, n_P\, n_{ave}\, OL + t_{add} \tag{3.2}$$

Where,

T time required for one time measurement

n_P number of scan point

n_{ave} number of averages

OL overlap factor in percentage

t_{add} additional time factors (scanner movements, software processing time, etc.)

T is inversely proportional to the required frequency resolution, Δf. Moreover, additional time factors are often neglected as their figure is small [156].

$$T = \frac{1}{\Delta f} \tag{3.3}$$

The LDV used for this research is a Polytec MSA-100-3D. It is a 3D vibrometer, which is made of 3 single point interferometers pointing at the same point but from different angles (see Figure 3.26), which allows the calculation of vibrations in the three axis' [156]. In the case of this system, the first channel records movements in the Z-axis (the same direction of the laser source), and it can be used alone as a 1D vibrometer.

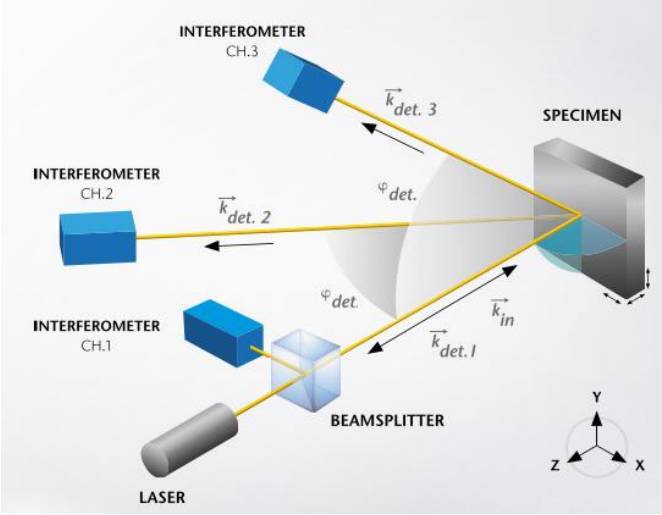

Figure 3.26: 3D Laser Doppler Vibrometer optical layout. Image taken from [158].

Although the vibrometer provides plenty of advantages for testing vibration, like being a non-contact method and being able to measure in the picometer domain, there are also disadvantages linked to it. The main disadvantages linked to this project are the following:

- As for MEMS, the samples tested are of small scale. This means that even low power lasers can be responsible for damage to these micro-scale objects, or even only modify the behaviour of the sample [155, 157]. This is due to the large temperature rise that the laser can induce on such small scales. The laser power output of the

MSA-100-3D is indicated as <5 mW in the system's datasheet [159]. To mitigate any issues given by this problem the laser intensity was controlled to not be too strong, and it was kept on for the shortest amount of time possible.

- The LDV measures along its line-of-sight, this means that if there is a misalignment between the sample and the laser source uncertainty of the velocity measurement can arise [157]. To mitigate this issue extra effort was placed in aligning the sensor. Moreover, the LDV software uses auto-compensation algorithms as well to reduce any misalignment errors.
- Optical scattering from specular surfaces may cause issues in the taken measurements [155, 157]. Reflective tapes could be used to mitigate this issue, but they could add mass and impair the measurement of these sensors further instead of resolving optical scattering. Therefore, no mitigation was applied in this thesis as the surfaces were not particularly specular.

3.7 Air flow measurements

This section explains instrumentation used for flow measurements. The first part includes an understanding of how the way the air flow moves around the sensor was measured. It is then followed by instrumentation used for air flow reference measurements.

3.7.1 Air flow around the sensor – Particle Image Velocimetry

Looking in a pond, one could observe debris move at the disturbance of the fluid of the pond. What one would be observing in reality is the velocity and direction of movement of the flow, with the debris is used to calculate said flow. One could argue that this is the most rudimentary form of "particle velocimetry". Nevertheless, what we define as Particle Image Velocimetry (PIV) nowadays is the "accurate, quantitative measurements of fluid velocity

vectors at a very large number of points simultaneously" [160]. A simplified PIV system is shown in Figure 3.27.

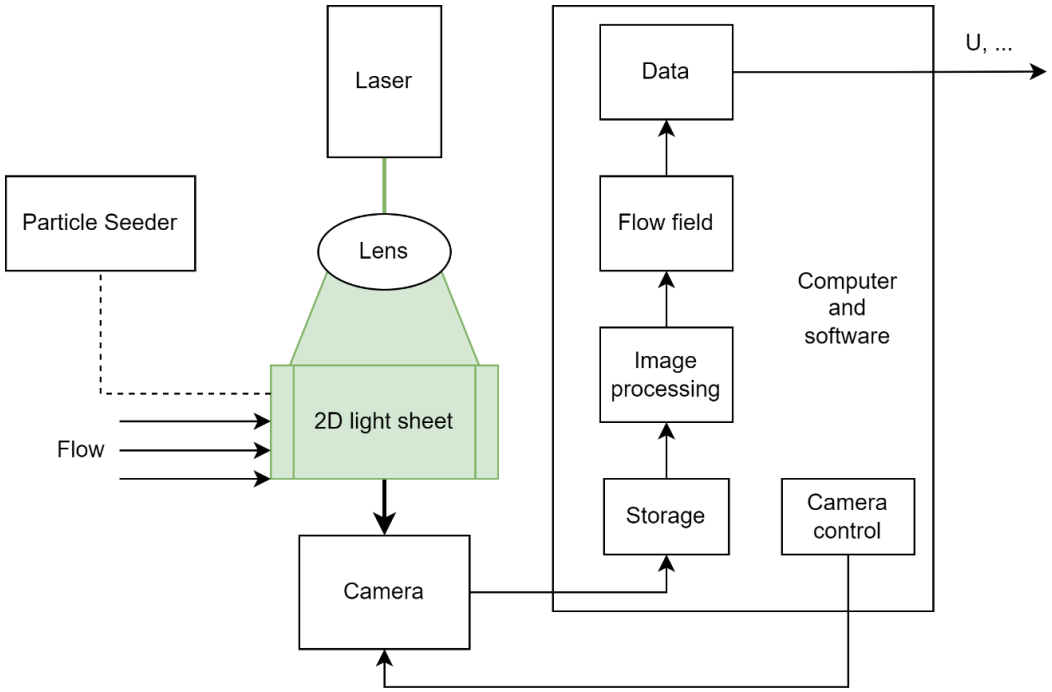

Figure 3.27: Block diagram of a simplified Particle Image Velocimetry system.

The principle of operation is quite simple, the particle seeder inputs in an enclosed space (like a vat) some particles to be used for the visualization of the flow (like the example above with the debris in a pond). The particles must be light enough to effortlessly move in the medium without much resistance for accurate representation. A method of illumination (i.e., laser) is used to light an area of interest for measurements, creating a "light sheet". This light sheet will light up the particles inside the vat and any structure of interest for camera acquisition. The means of creating the flow we want to measure can variate depending on the experiments (e.g., a speaker might play a constant frequency to see the effect on moving the air). A high-speed camera needs to be used to properly acquire many images with a short period of time in between them. The computer and software correlate the different images to evaluate how fast and in which direction the particles are moving, and hence direction and speed of the flow in the area captured by the camera. This last section was usually the

problematic part in the early development of PIV as it was stated above, but nowadays it is simplified thanks to the advancement in computer hardware.

In this thesis a custom-made PIV system was used at the Université de Tours in Tours, France. The laser is a generic MGL-F-532-2000-5 with PSU-H-LED. A Scheppach AIR CASE 2L air compressor connected to the seeding device aerosol generator LaVision VZ-20 10 bar is the particle seeder. The high-speed camera is a Phantom Miro 310 which has the capability to capture 3200 frames per second (fps) at maximum resolution (1280x800 pixels), higher fps are possible for lower resolution [161]. Phantom software PCC is used for recording, while ImageJ software is used to split the video file into an image sequence. DaVis 10 is the PIV software used to analyse the recorded images.

3.7.2 Air flow reference – Hot-wire anemometry

The first recorded anemometer in history is found in the 15th century, based on a swinging plate placed perpendicular to the direction of the wind, measurements of wind gusts were based on the angular displacement of the plate [162]. Similar instruments were developed later including springs, these pressure plates anemometers were widely used in the 20th century, but they've since been replaced by new instrumentation. Many instruments used to measure the velocity of the air flow are usually large in size, like rotating anemometers, sonic anemometers, pressure anemometers, PIV, and doppler lidars and radars. A particular small instrument falls in the category of cooling-rate-based anemometers, commonly called hot-wires. Hot-wire anemometry was already in use in the 20th century [163]. Their measurement principle is based on the cooling effect that air flow has on a heated wire, they can provide very precise measurements and are cable of good sensitivity at low air speeds [162, 163]. Due to the small size, and low cost, a hotwire anemometer was selected as the instrumentation to use as reference in the development of the air flow sensors of this text, the Sauermann Si-VH3 [164,

165]. Their disadvantage is their fragility that does not allow them to be used for strong winds and long periods of time making impossible their use outdoor [162]. However, the hot-wire is mainly used inside the lab, therefore in a controlled environment with not too strong wind. Another disadvantage of hot-wire anemometers is the frequent calibration needed due to their high sensitivity to temperature changes [162]. Even this should not impact this project due to the controlled temperature in the lab, and to the fact that the Sauermann Si-VH3 also measures the temperature, allowing for compensation [164, 165]. The Si-VH3 has a measuring range of 0-30 m/s and a resolution of 0.01 m/s for measurements in the 0-5 m/s range, and a lower resolution of 0.1 m/s for higher velocities [165].

4

Towards Additive Manufactured Bioinspired Artificial Hair Acoustic Sensors for Frequency Discrimination Purposes

"The profound study of nature is the most fertile source of mathematical discovery."

Joseph Fourier

This chapter will explore the work carried out in the PhD to explore the creation of 3D-printed insect bioinspired artificial hair sensors for audio acquisition purposes. The chapter begins with specifics about the COMSOL simulation model setup and its analytical alternative used at the beginning of the project, the experimental set-up, and, lastly, the different designs and their relative results. The chapter will conclude with prospects and possible future work to be conducted that builds from the knowledge acquired during this research. Part of this research was presented at IEEE Sensors 2023 [166].

The Fourier transform allows us to "deconstruct" a sound and inform us of its frequency content information. Without this, modern tools like speech recognition would not be possible, as it is from the frequency content of a sound that we can know what word has been spoken. Recalling section **2.2.1 Human Hearing System**, the way we hear is essentially done in the opposite way. The cochlea generates different neural spikes for different frequencies, these neural spikes are then combined into what we understand as the full words and sounds. The frequency discrimination of a sound in biological systems is done therefore at acquisition, mechanically, rather than post-acquisition, electrically. Given a parallel processing system, this clearly has advantages in terms of time and efficiency.

The literature review identified the insect's mechanoreceptors that were capable of sensing low frequency sound (**2.2.2 Insect Hearing Systems** and **2.3 Hair Mechanoreceptors**). This inspired the creation of bioinspired hair-like sensors that, based on structural differences (e.g., hair length), could react to different narrow frequency bands. The inspiration from insects was mainly taken as a starting point because they can react to low-frequency airborne sound, while our own hearing system is more complex. But the end goal (beyond this PhD), would be the creation of a sensor that acquires acoustic signals similarly to our ears. And ultimately, have a system that "hears" like us. Thus, the end goal is to use the study of nature as a fertile source of engineering discovery and inspiration, to surpass the need of Fourier's brilliant mathematical

discovery for acoustic purposes. Essentially creating a more efficient acquisition system that can help a wide variety of applications, e.g., speech recognition.

4.1 Experimental set-up for acoustic hair sensors

The sensor was placed under a Polytec MSA-100 3D-Laser Doppler Vibrometer (described in **3.6.1 Laser Doppler Vibrometry**). A loudspeaker was then placed in front of the artificially printed hairs. In some of the early tests smaller speakers were used, and they were held with a stand clamp on the same table where the LDV sits. But most tests were done by using a Visaton WS17E speaker held by a flexible articulating arm placed in a platform separated by the one where the LDV is situated. For many of the tests the speaker would produce a period chirp for a different range of frequencies (typically from 0 Hz to 2 kHz). Nevertheless, occasionally, after the periodic chirp was used to identify the resonant frequency of the artificial hair, the speaker was also used to reproduce a tone at the resonant frequency only. The tones were generated using the internal LDV's function generator at 10 V and then amplified by a Onkyo A-9010 amplifier. A reference signal of the speaker Visaton WS17E was taken using a Brüel & Kjær WH-3219 microphone, positioned 13 cm from the speaker (Figure 4.1). A figure of one of the early experiments is shown in Figure 4.2. In every experiment the speaker was elevated high enough for the hair sensor to be positioned in line with the centre of the speaker. The speaker was positioned parallel to the widest face of the hair-inspired sensor.

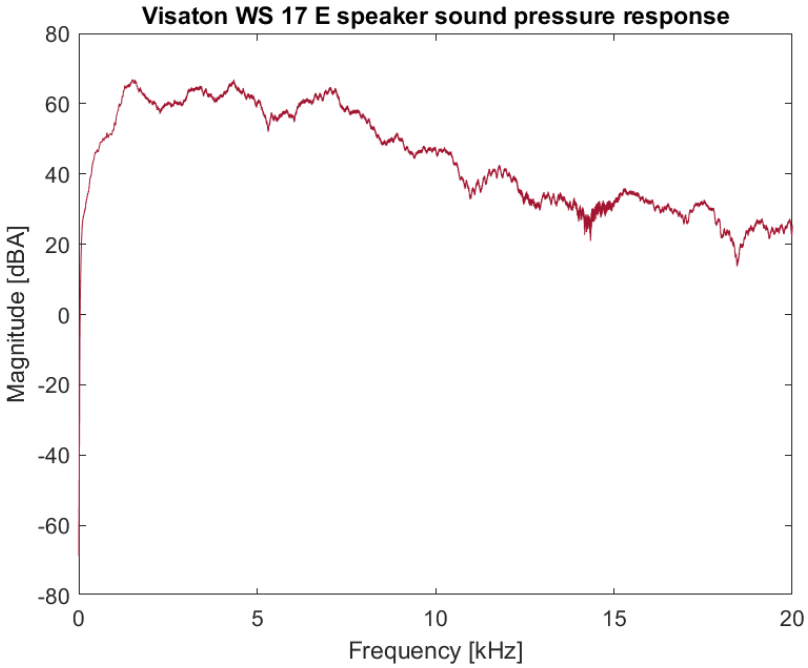

Figure 4.1: Visaton WS17E sound pressure response of a periodic chirp (0-20kHz) used to test the sensors acquired by a Brüel & Kjær WH-3219 microphone.

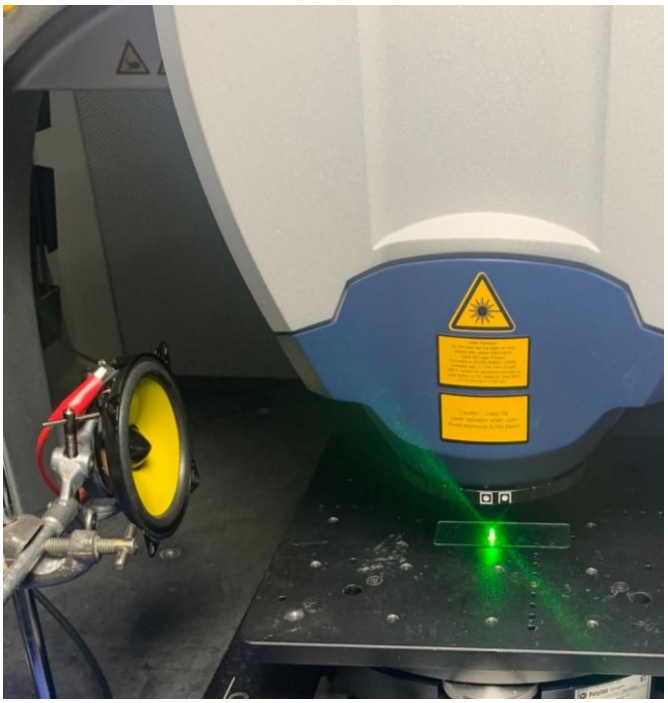

Figure 4.2: Simple set-up of experiments conducted with an LDV and a load speaker of the artificial hair sensor for acoustic purposes.

The LDV acquisition was done in FFT mode with an averaging complex value of 5, 1600 FFT lines and a rectangular window. The multipoint scans were done using a point density of ~0.48 points/mm in both X and Y axes. This would allow us to see the way the interested area

was moving (e.g., the tip of the artificial hair). And to ensure at which frequency the hair was moving like a cantilever.

4.2 Design ideas for artificial acoustic hair sensors and results

This subchapter will provide the several design ideas that were investigated throughout the work, followed by their results.

4.2.1 Cylindrical cantilever

The first design is most likely the simplest. It consists of a simple cylindrical hair that is expected to move as a cantilever for its resonant frequency regardless the stimulus. The hair is printed on a rectangular block to clamp it in one end (Figure 4.3). As this design was the easiest it was used at the same time as practice for learning 3D printing. Different cylinders were printed on the same block to test them at the same time. Two tests were conducted:

- Four hairs on the same block, with the same diameter (0.21 mm) but four different lengths: 3.35 mm, 1.5 mm, 1 mm and 0.75 mm (Figure 4.3a).
- Five hairs on the same block with the same length (3.35 mm) but five different diameters: 0.24 mm, 0.30 mm, 0.36 mm, 0.45 mm and 0.51 mm (Figure 4.3b).

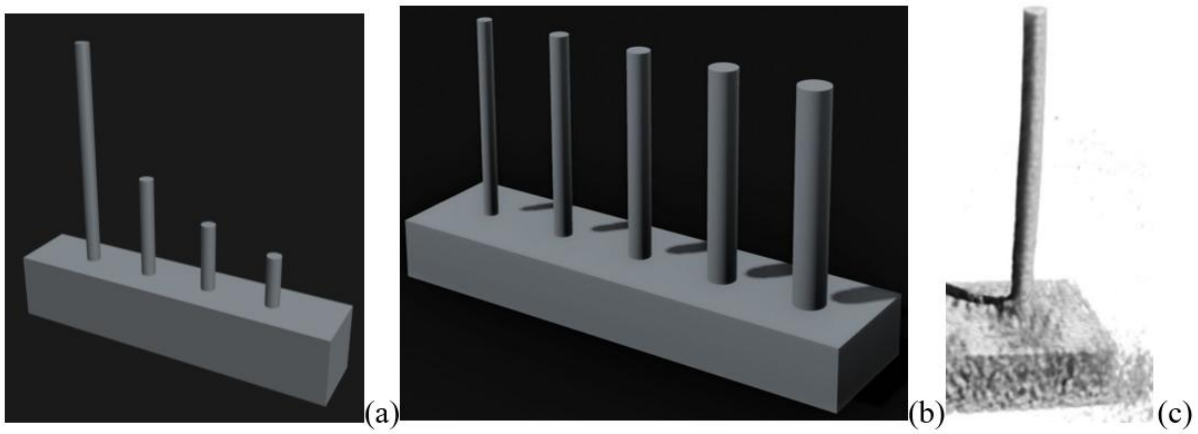

Figure 4.3: Model of cylindrical cantilever artificial hairs. Model for the test conducted for different hair lengths (a), different hair diameters (b) and a CT scan of one of the printed artificial hairs.

The issue with these artificial hairs was that the mechanical displacement was close to the noise floor when measured with an LDV, often difficult to discern, and it was difficult to see if it was cantilever like or not. Moreover, including something for electrical generation on the hair body would've been challenging given the small size. Lastly, the fact that this method relies on the bending of the hair makes the system highly inefficient as discussed by Zhang et al. [48].

4.2.2 Artificial hair inspired by the Hinged Trichoid Sensilla (HTS)

This artificial hair was inspired by the hinged trichoid sensilla (HTS) structure, Figure 2.12a, common in the caterpillars of *Barathra brassicae* [32]. The idea was to have some protrusions at the base of the artificial hair (similar to the ones of the caterpillar) that would serve as capacitive plates once coated with metal. Moreover, at the bottom of these plates the sensor structure had a different material, serving as a spring, with a lower Young's modulus to try and emulate the bi-material structure found in many insects and arachnids. What is found in some trichobothria is that the hair shaft is very stiff, to avoid bending, while the basal area is very soft, and it includes the dendrite. When some stimulus acts upon the hair shaft the energy is therefore not wasted in bending the hair, but instead, it is deflected to the basal area, responsible for the signal generation. Zhang et al. proved this mechanism in simulation showing that the stress is much higher on the soft area when a cantilever is made of two materials rather than one [48], Figure 2.60. This sensor was tested with cylindrical hairs and with squared looking ones that were inspired by the flat trichobothria of the adult *Buthus occitanus* scorpion.

4.2.2.1 Mechanical response

The design of this HTS inspired artificial hair sensor is shown in Figure 4.4. The first experiments for this design were made using only one material to 3D print the overall structure. Nevertheless, an acoustic response could not be clearly observed similarly as the cylindrical

hair discussed earlier. Therefore, the sensor was then manufactured using two materials. The hair structure was printed using Formlabs's Grey Resin (V4) and the rest of the structure is 3D-printed using a poly(ethylene glycol) diacrylate (PEGDA) based resin. PEGDA was mixed with the photoinitiator phenylbis (2,4,6-trimethylbenzoyl) phosphine oxide (Irgacure 819, 1% of PEGDA weight) and the photoblocker orange dye Sudan I (S1, 0.2% of PEGDA weight) [166]. PEGDA, Irgacure 819 and S1 were purchased from SigmaAldrich, used as delivered. The solution was sonicated in an ultrasonic bath (Clifton SW3H) for 30 minutes prior to use, for proper mix of the components. Once the sensors were 3D-printed, they were cleaned in isopropanol for 1 minute to remove resin residues. Before conducting the experiments, the sensors were initially left to rest for at least 2 days, in later experiments the sensor was instead UV post-cured for 5 minutes in an Asiga Flash [166]. The sensor structures are named after their dimensions in millimetres; Height, H, Width (for squared hair), W, Depth/Thickness (for squared hair) or Diameter (for cylindrical hair), D, and Spring Height, B. The sensors were printed with the default settings of the "Asiga Dentabase" material, the only change was made for the PEGDA-based resin section by increasing the exposure time to 10 seconds.

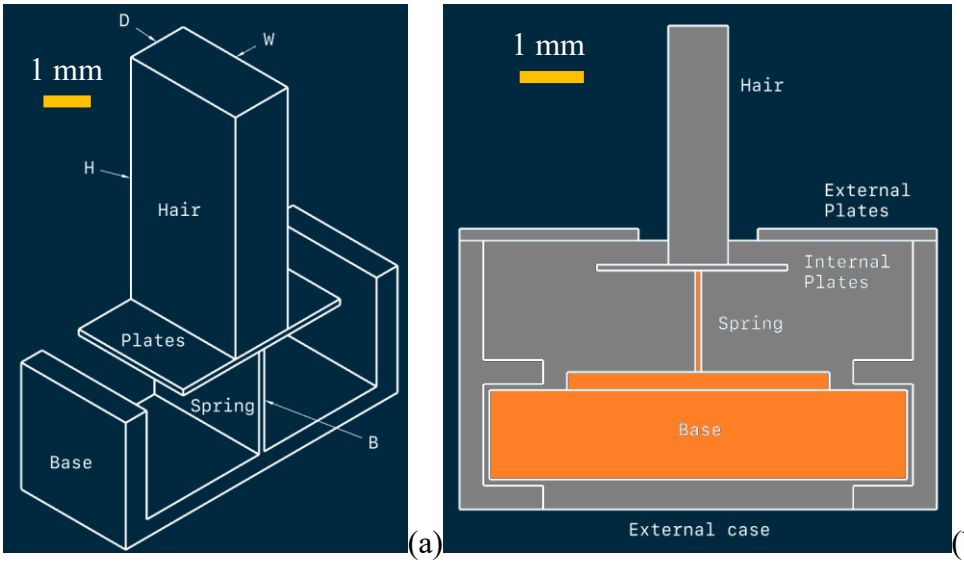

Figure 4.4: (a) Basic structure of the hair sensor used for mechanical testing. The diagram also includes the different design variables, hair height (H), hair thickness/diameter (D), hair width (W) and spring height (B). (b) Proposed final version of the hair in 2D, to allow for mechanical displacement to electric signal conversion. The external case with plates is

printed separately and slid in around the sensor structure. Internal and external plates are supposed to get coated with metal. Image first presented in [166].

The following results represent the displacement obtained through the LDV by testing of the sensor's mechanical response to a periodic chirp from 50 Hz to 2 kHz reproduced by a Visaton WS17E speaker at 13 cm of distance [166]. The face of the speaker was centred and parallel to the face of the hair-like structures in the direction of the expected cantilever-like movement with the sound pressure shown in Figure 4.1. Three different experiments were made on the mechanical structure and for this, three different structures were produced inspired by different shapes found in nature. The first experiment, **Shape Comparison**, was made to understand the response of the sensor to different hair shapes (Figure 4.5). On the same base four different sensors were 3D-printed, one cylindrical, H4D1, and three squared, H4W1D1, H4W2D1 and H4W3D1. A base height B1.7 was used for all hairs. The cylindrical hair and its nearest squared version (W1D1) have a similar response, albeit they have slightly different resonant frequencies (360 Hz and 330 Hz, respectively). For the squared hairs the wider the hair the lower the resonant frequency and the higher the displacement. For smaller hairs, the displacement of the resonant frequency is equal to other structural noise; this might compromise the conversion of the mechanical displacement into an electrical signal.

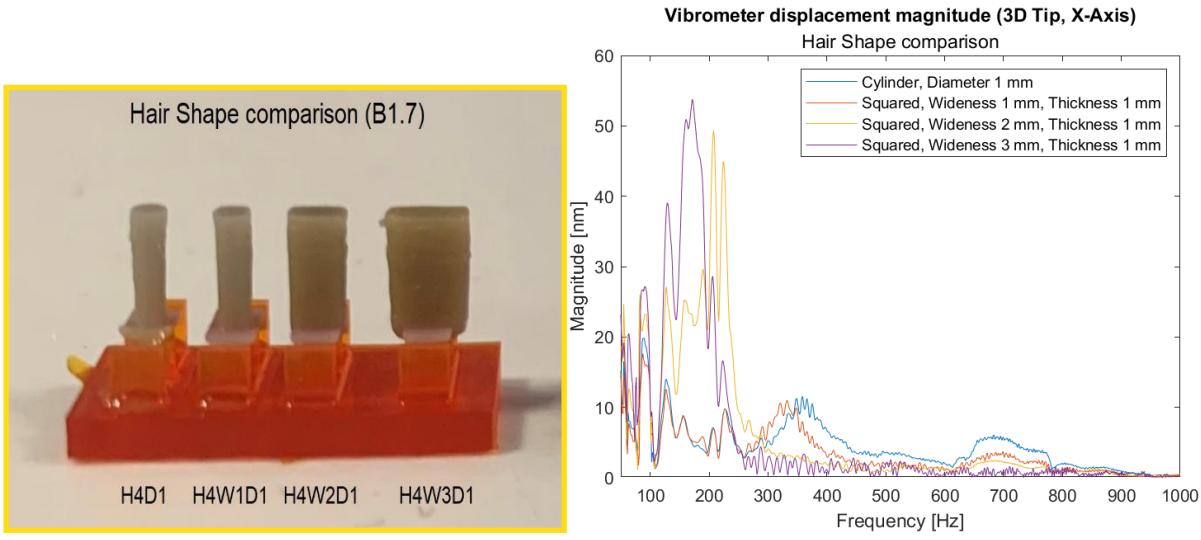

Figure 4.5: Photo of hair shape comparison structure (left). Displacement magnitude collected by the 3D LDV at the tip of the hair (right). Only X-axis displacement shown

(parallel to the speaker). Results for same spring height (1.7 mm) and different hair shapes. Plot first presented in [166].

The second experiment, Spring/Base Height Comparison, was conducted to determine the effect of different spring heights on the sensor's response [166]. The same hair (H4W3D1) was 3D-printed on bases with five different heights, B1.7, B1.5, B1.3, B1.0 and B0.5. The results (Figure 4.6) indicate that for a lower spring height there is a lower displacement at the tip and a higher resonant frequency. Moreover, for higher springs, the band of frequencies at which the hair produces cantilever-like movements is narrower. The cantilever-like movement of the B0.5 sensor is the region comprehended from 580 Hz to 1250 Hz, while for the B1.7 sensor it was recorded from 150 Hz to 200 Hz.

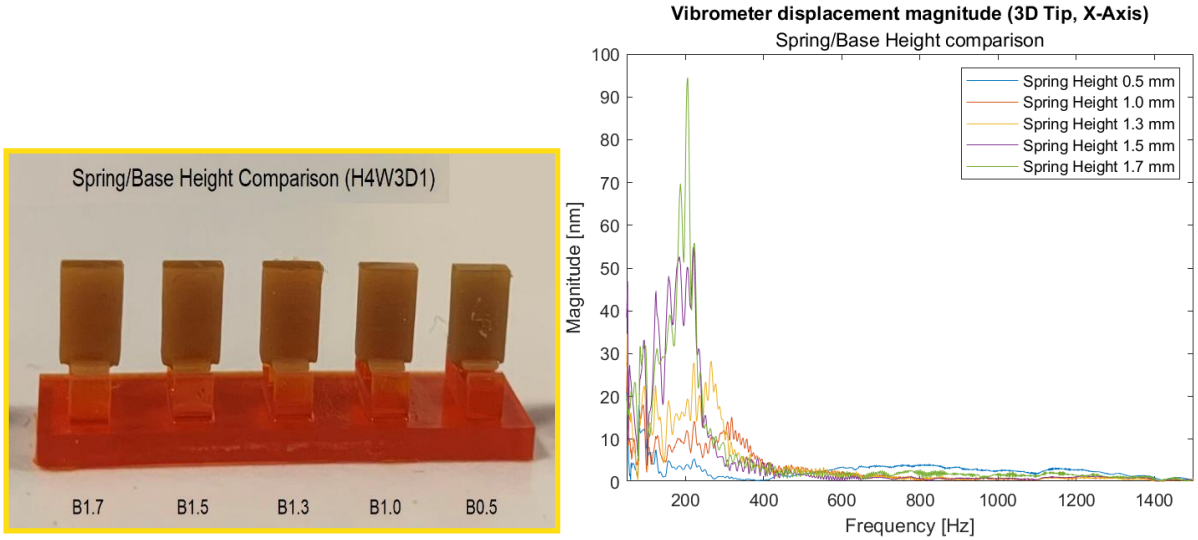

Figure 4.6: Photo of spring/base height comparison structure (left). Displacement magnitude collected by the 3D LDV at the tip of the hair (right). Only X-axis displacement shown (parallel to the speaker). Results for same hair structure (Height 4 mm, Width 3 mm, Thickness 1 mm) and different spring/base heights. Plot first presented in [166].

The third experiment, Hair Size Comparison, investigated the sensor's response when changing sensor height and depth/thickness, while having the same width and spring height (W3B1.7) [166]. Six different sensors were tested, a combination of three different heights H5, H4 and H3, and two different thicknesses D1 and D0.5. The results (Figure 4.7) showed that the higher the hair the higher the displacement and the lower the resonant frequency. An interesting observation is the fact that by halving the thickness of the hair, the frequency

response resembled the one of the next 1 mm shorter hair with 1 mm thickness, but with higher displacement (see H5D0.5 compared to H4D1 and H4D0.5 compared to H3D1).

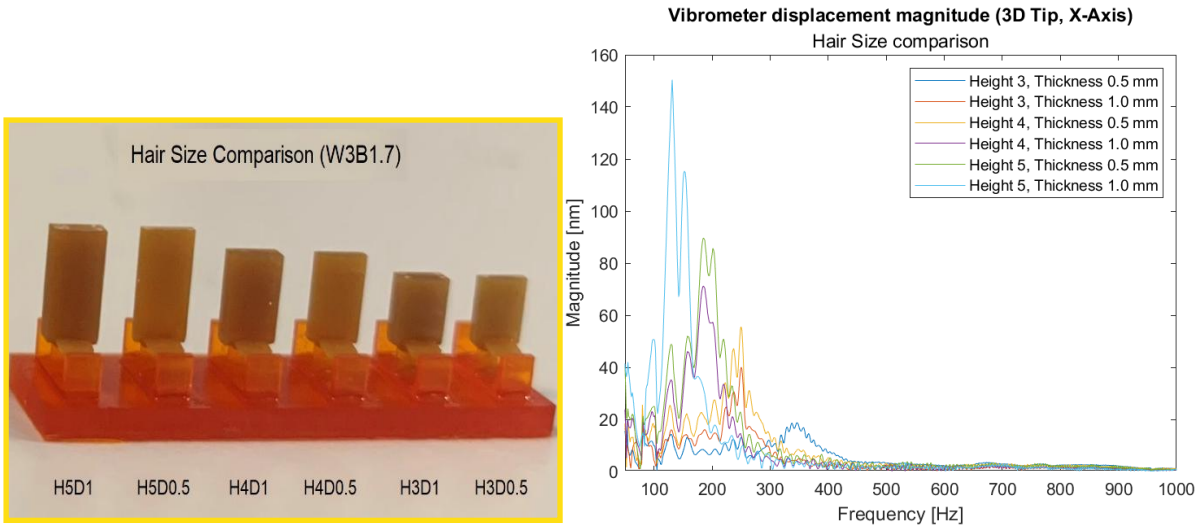

Figure 4.7: Photo of hair size comparison structure (left). Displacement magnitude collected by the 3D LDV at the tip of the hair (right). Only X-axis displacement shown (parallel to the speaker). Results for same hair width (3 mm) and spring height (1.7 mm) and different hair height and thickness. Plot first presented in [166].

Since the ***H4W3D1B1.7*** sensor structure was common for all three experiments, in Figure 4.8 their response from the previous experiments was placed in one plot to investigate the reproducibility of the sensor. The resonant frequency and displacement are comparable, but with some differences, with a resonant frequency standard deviation of 17.06 and a displacement standard deviation of 20.54. These discrepancies may depend on some or a combination of the following factors.

- **Time of experiment after printing**, the polymerization reaction continues after printing, changing its material properties [167]. For this reason, samples printed after the IEEE Sensors 2023 conference paper began using UV post-curing.
- **Cross-contamination** between the two different materials when changing the trays while printing, this can be improved by cleaning the tray and support between tray changes.

- **Time of immersion in isopropanol**, in our past experiments it was ascertained that longer immersion times made the sensor brittle. And in literature it is known that the cleaning method can alter the mechanical properties [138], therefore if the cleaning is not perfectly consistent the mechanical properties might be altered. Timing consistency between each print is fundamental to decrease inconsistency.
- **Misalignment of the tray**, when changing tray in our early work it was noticed that, in some instances, the plate and the hair were not properly aligned to the spring as per design [166]. More attention from the operator when inserting the resin trays can reduce this issue.
- **Slight variation in light intensity in DLP** might occur while printing, this can slightly affect the sample's properties, and it is outside user control [166].
- **Dimensional variations** might occur during the printing process, these might be mitigated by a better selection of the print parameters [166].

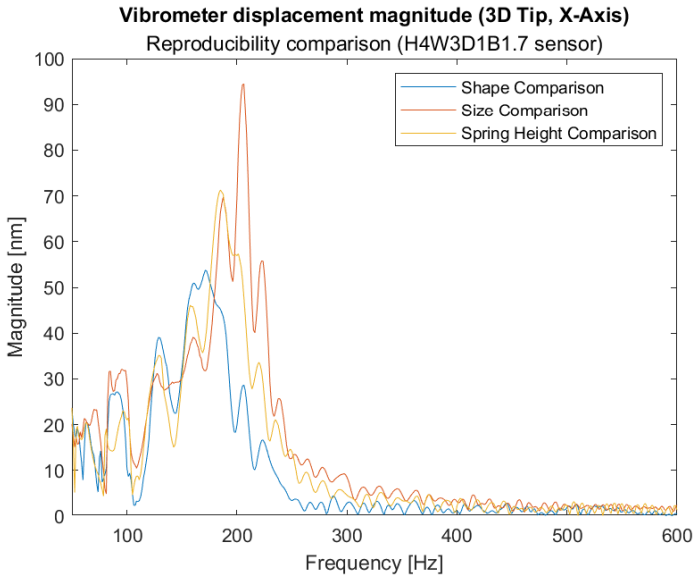

Figure 4.8: Displacement magnitude collected by the 3D LDV at the tip of the hair (X-axis) for the H4W3D1B1.7 (Height 4 mm, Width 3 mm, Thickness 1 mm, Spring Height 1.7 mm) sensor from the comparison experiments. First presented in [166].

After these results were presented an x-ray micro-CT scan of the sensors was taken and in all cases the sensor presented drastic overprints in the structure size, with thicknesses of spring

and plate being 3 times larger than the designed ones. Efforts were made to improve the quality of the 3D-printed samples by changing several parameters: the exposure times, Z-compensation, border exposures and wait times after separation and approach. Figure 4.9 shows one of the hair sensors presented in [166], and the improved result accomplished with better 3D-printing settings. Throughout the printing experiments it was also found that the plates could not be thinner than 0.3mm or they would lose structural integrity, either falling, curling up or curving down.

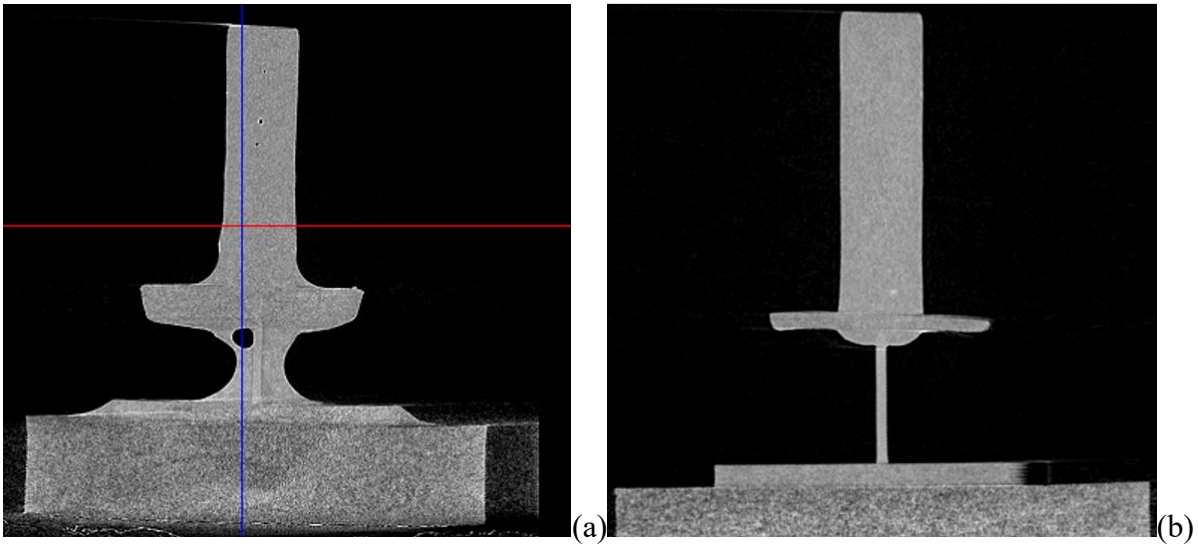

Figure 4.9: (a) One of the badly printed sensors presented in [166] and (b) improved version with different printing settings.

The new printed version still had the "Asiga Dentabase" settings as default, but a few changes presented in Table 4.1 were made. During these experiments it was also noticed that it was possible to reduce the exposure time for the spring up to 2 seconds. The result of a reduced exposure time was a reduced stiffness of the system, up to the point where the hair could move due to acceleration (sensor moved left and right), due to gravity (when the sensor was rotated) or airflow (when blowing air on it). Nevertheless, with a reduced exposure time, the sensors became also more brittle, and they would get damaged quickly.

Table 4.1: 3D-print settings used for the improved hair sensors printed in Figure 4.9b. The different columns for each part represent different printing settings for different print ranges of the part being printed.

Part	*Base*		*Spring*	*Plates*		*Hair*		
Print range from-to (mm)	0-0.1	0.1-1.9	1.9-3.6	3.6-3.75	3.75-3.8	3.8-3.9	3.9-4.1	4.1-7.9
Layer thickness (mm)	0.05	0.05	0.05	0.05	0.05	0.1	0.05	0.05
Exposure Time (s)	5	2	10	2	2	2.5	1	2
Z-compensation (mm)	0	0	0	0.15	0.15	0.15	0.15	0.15
Border Exposure	100	100	100	100	120	120	100	100
Border width (mm)	0	0	0	0	0.1	0.1	0	0
Two-step exposure border width (mm)	0	0	0	0	0.1	0.1	0	0
Wait time after separation (s)	0	0	0	0	10	10	10	5
Wait time after approach (s)	0	0	0	10	10	10	10	5

The experiments presented above were repeated with the improved sensor prints, like Figure 4.9b, using the settings from Table 4.1. For these printed sensors a better printing procedure was used to reduce misalignment when changing materials, cleaning the building tray amongst changes to reduce material cross-contamination and the use of UV post-curing, and more controlled time immersion in isopropyl alcohol. The results are presented in Figure 4.10. These results show that the same conclusions from the older hair sensor structures are valid (Figure 4.5, Figure 4.6, and Figure 4.7), but with different displacement magnitude and resonant

frequencies due to a slightly different structure. Meanwhile, Figure 4.10d shows closer resonant frequencies for this hair compared to older tests (Figure 4.8), showing that the procedure improvements improved the reproducibility of the sensor. The standard deviation of the frequency reduced from 17.06 to 8.85, and a displacement standard deviation reduction from 20.54 to 6.67 was obtained as well. Nevertheless, there is still a discrepancy in the response of the sensors indicating that there is still room for improvement.

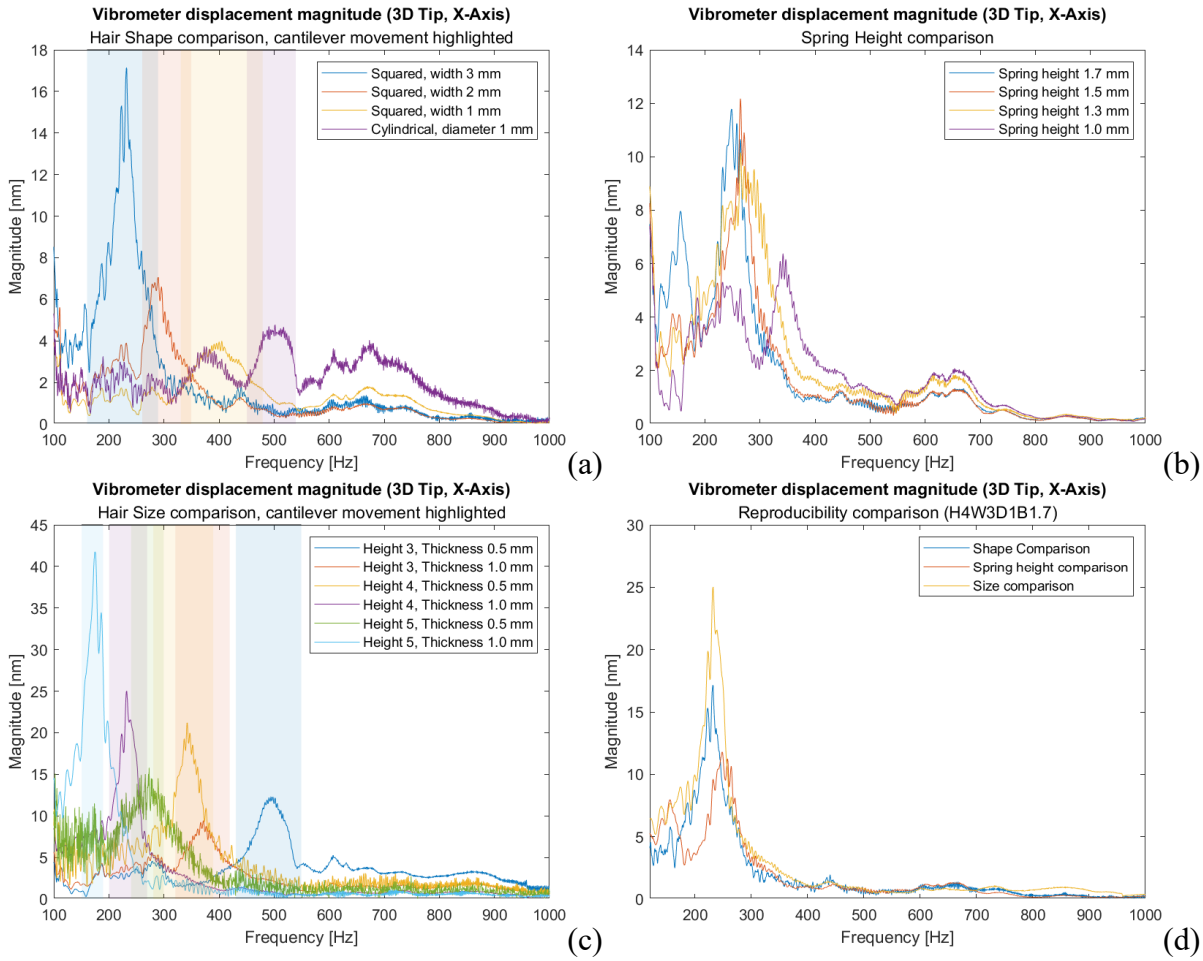

Figure 4.10: Displacement magnitude collected by the 3D LDV at the tip of the hair (X-axis) for (a) different hair shapes, spring heights (b) and sizes (c), using Table 4.1 print settings for the sensor structures. (d) Reproducibility comparison of the H4W3D1B1.7 hair sensor structure for three experiments.

COMSOL simulation for this sensor was conducted as described in Chapter 3.2 and their response was compared to the results acquired in Figure 4.10. For the grey material the Young's modulus was set to 2.8 GPa, as indicated in the datasheet [168]. The Young's modulus of the

PEGDA-based resin was set to 1.7 GPa. This was done by trying to get the H4W3D1B1.7 sensor response (from the Shape Comparison experiment) in COMSOL as close as possible to its LDV response in the shape comparison experiment. The Poisson's ratio and material density for both materials was set to 0.33 and 1158 kg/m^3, respectively. A parametric study was conducted to simulate all the other sizes and shapes.

Figure 4.11 shows the absolute peak frequency error of the COMSOL results for each hair sensor during geometric parametric sweeps that resembled the experiment comparisons of Figure 4.10. The results show a good agreement in peak frequency with the LDV results, with an average error of 5.1 %, a maximum error of 14.2% and a minimum error of 0.3%.

Figure 4.12 instead shows the displacement error when comparing COMSOL to the LDV response. In this case the error is much larger, with an average of -70.6%, a maximum error of 40% and a minimum -95.6%. Nevertheless, the displacement also depends on the power of the speaker at that frequency (Figure 4.1 shows the experimental pressure levels), thence, while in this case the results do not agree it could simply be due to a discrepancy in sound power levels.

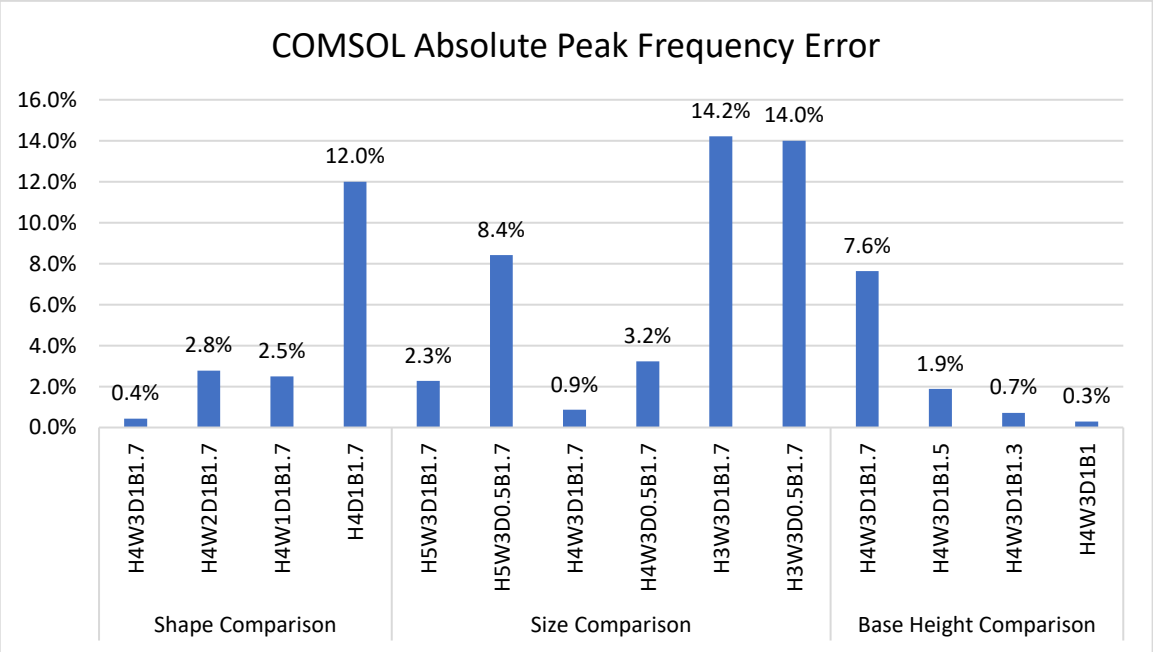

Figure 4.11: COMSOL absolute peak frequency error compared to LDV results.

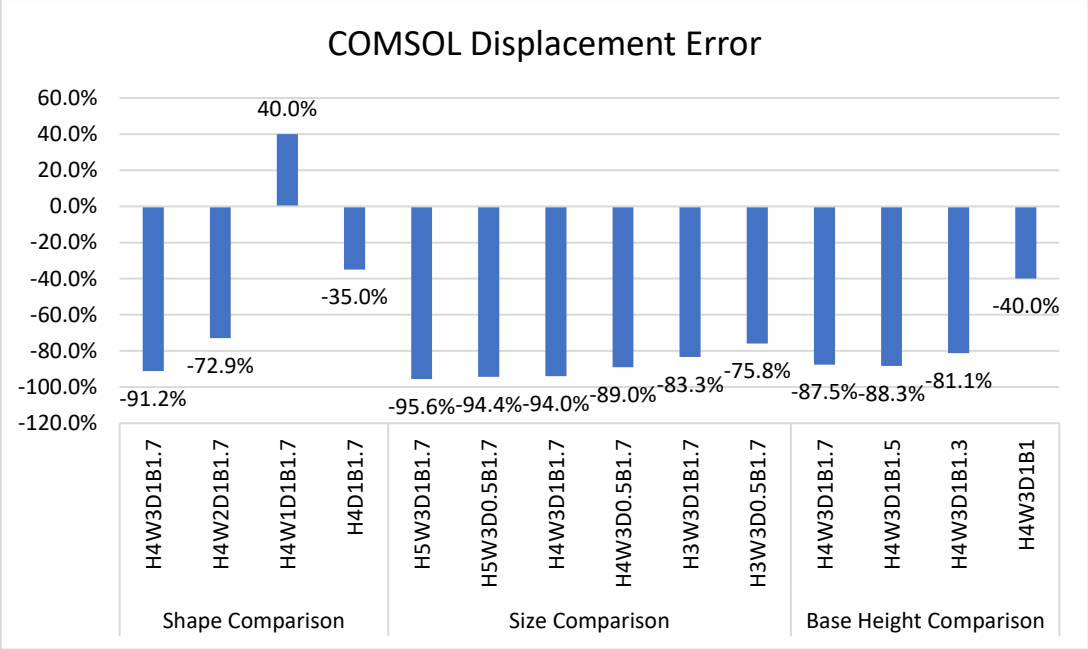

Figure 4.12: COMSOL displacement error compared to LDV results.

4.2.2.2 Electrical results (capacitive plates)

The plates of the hair sensor and some external plate beams were coated with Agar's quick drying silver paint to add conductivity (Figure 4.13). Thin cables were glued to the sensor to connect it to a Tektronix DPO2014 oscilloscope. It was unclear if any data acquired was from the actual sensor's response or interference from the speaker itself. Moreover, the process to paint the sensors and glue the cables broke multiple sensors, and in many cases the cable would just detach. Additionally, having a cable on the sensor structure itself could have impaired or modified its response by modifying the structure stiffness and/or damping. It was therefore decided to modify the design by removing the plates, as discussed in the section below.

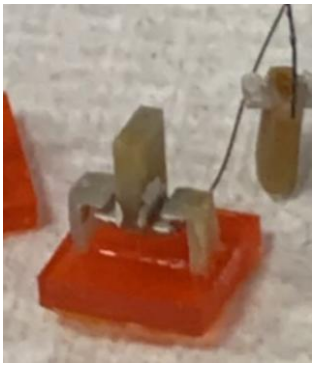

Figure 4.13: Picture of a sensor painted with silver paint.

4.2.2.3 Electrical stimulation (capacitive spring)

As mentioned in the earlier section it was decided to modify the design to render it simpler and to avoid placing the cables attached to the sensor structure directly. The new design removed the plates entirely and added a track on the base designed to hold the cable (Figure 4.14). An external block that was designed to represent the other side of the capacitive plate was designed as well.

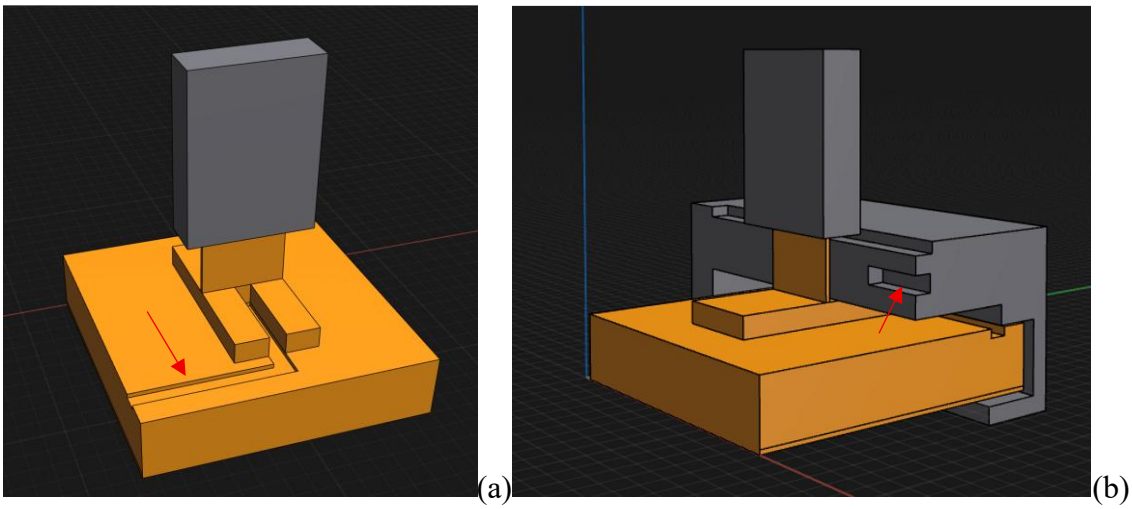

(a) (b)

Figure 4.14: HTS inspired sensor design without plates and with a cable track on the base (a). Design of the HTS inspired sensor' block that would serve as the other side of the capacitive plate (b). Red arrows indicate the tracks used to add the cables.

COMSOL simulation of the acoustic response of this hair inspired sensor was conducted and showed that there was a slight discrepancy in response in removing the plates from the sensor structure, a 30 Hz increase in resonant frequency. Deeming this reasonable, the next step was to print the sensor structure and the external block and use CT-scans to understand how small the gap between these two capacitive plates could be made. A gap of ~200 µm was possible, but the actual gap often showed ± 30 µm variances (Figure 4.15). The block and the sensor's spring were coated with aluminium using an Edwards E306 evaporator for 5 seconds, only one sensor was coated to investigate if this method could yield a usable sensor. Using a precise capacitive meter a 0.39 pF capacitance was identified, and some variances were

detected in tens of femtofarad, but it was not consistent, and these variances could have been attributed to stray capacitance, not to the sensor itself.

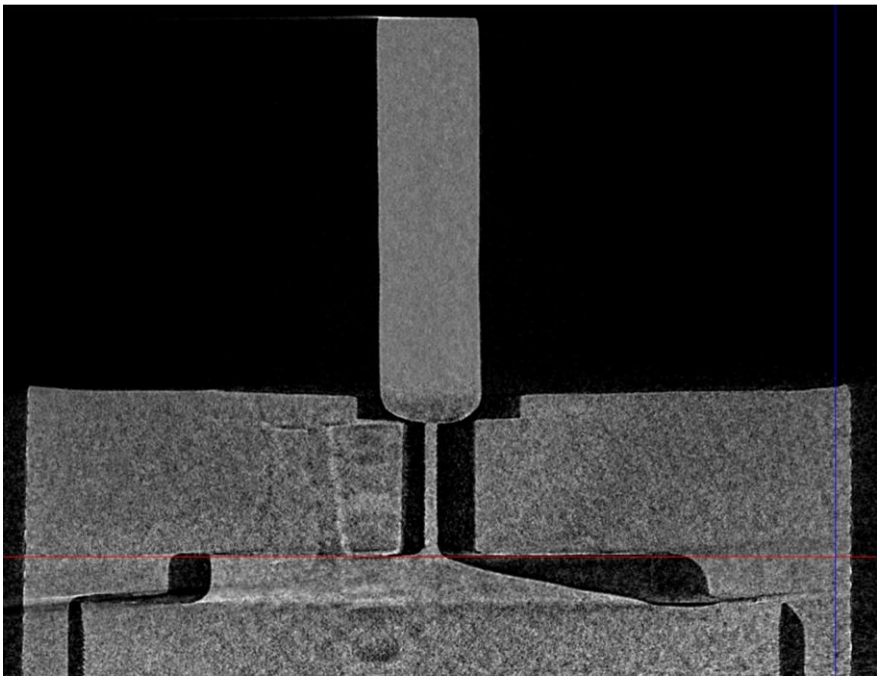

Figure 4.15: CT-scan of HTS inspired sensor with external block and sensor's spring as capacitive plates.

To investigate the sensor's possible response further it was decided to use COMSOL simulations with the electrostatics module and applying 1 V to the terminal. It was found that the sensor's base capacitance was ~181.69 fF and that for a displacement of 50 µm (as found with an LDV), the change in capacitance was of ~0.41 aF, around a -0.00023% change. Increasing the voltage to the terminals would in theory increase the change of capacitance, as well as reducing the gap. Nevertheless, due to difficulties in manufacture to reduce the gap, and to the fact that higher voltages could make the sensor deteriorate, it was decided to move to a new design idea.

4.2.3 Artificial hair inspired by the Suspended Trichoid Sensilla (STS)

Upon the failure of the capacitive HTS inspired sensor, described in section **4.2.2.3 Electrical stimulation (capacitive spring)**, new designs were investigated. Many arachnids have trichoid sensilla that differ in structure from the HTS. Instead of having the hair shaft

hinged structurally to the cuticle, the hair shaft is suspended by joint membranes, Figure 2.12b [45]. A bioinspired structure was designed and manufactured including two beams to represent the joint membranes and a hair shaft on top (Figure 4.16). The idea was to print the top and bottom separately and coat the interior face with metal to make them conductive (creating therefore one capacitor for each beam). The hair was printed with Formlabs General Purpose Resin, and with the PEGDA-based resin specified in section 4.2.2.1. Nevertheless, LDV tests showed that the acoustic response was poor to begin with – the cantilever-like movement was discerned only at noise level, with magnitudes below the ones showed earlier. This did not allow to collect a proper frequency response of the sensor. Alternative materials and design needed therefore to be investigated.

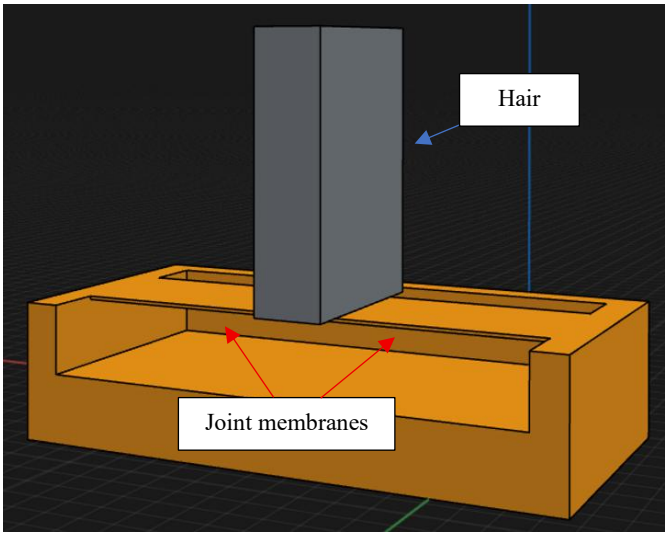

Figure 4.16: Initial design inspired by the suspended trichoid sensilla of arachnids.

A material that was considered is Formlabs Elastic 50A resin (V1). Its Young's modulus is below 10 MPa [169]. And it would therefore in theory be an appropriate alternative. In the attempt to design an omnidirectional sensor, instead of having two beams protruding at the bottom of the hair it was decided to have an overall flat surface printed with Formlabs Elastic 50A, and a cylindrical hair on top printed with Formlabs general purpose resin. The idea was to coat the bottom with metal. This surface would then be glued on top of a base that has 4 divided sections (after they are metal coated), Figure 4.17. This would create 4 capacitors with

a common ground, being able to sense 4 different directions. While this first version could have had issues like crosstalk or coupling of some or all the capacitances due to the common terminal, the idea behind this first test was just to prove that the concept was possible. A second iteration would have masked the part with the hair while being coated, creating 4 separate capacitors, each with their own pair of plates.

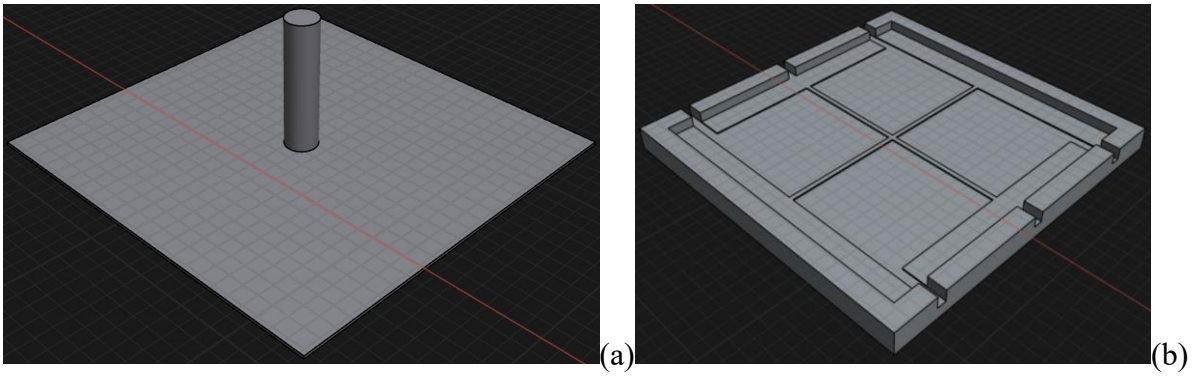

Figure 4.17: Omnidirectional sensor design inspired the suspended trichoid sensilla of arachnids. The top section (a) and bottom section (b) are designed to be glued together after being coated.

The two sections were coated with aluminium using an Edwards E306 evaporator for 5 seconds (Figure 4.18a). To unify the two sections together it was decided to use the general-purpose resin with a thin brush and UV post-cure it to harden it. In one of the capacitors a 0.207 nF capacitance was recorded (Figure 4.18b). The sensor could show visible capacitance variation when the hair shaft was moved by hand, but unfortunately, no acoustic response was recorded. Moreover, after a few days, the top plate bulged, showing that the structural integrity of the sensor could not be ensured (Figure 4.19). Additionally, the cables were too flimsy and often broke. This design was therefore halted at this point.

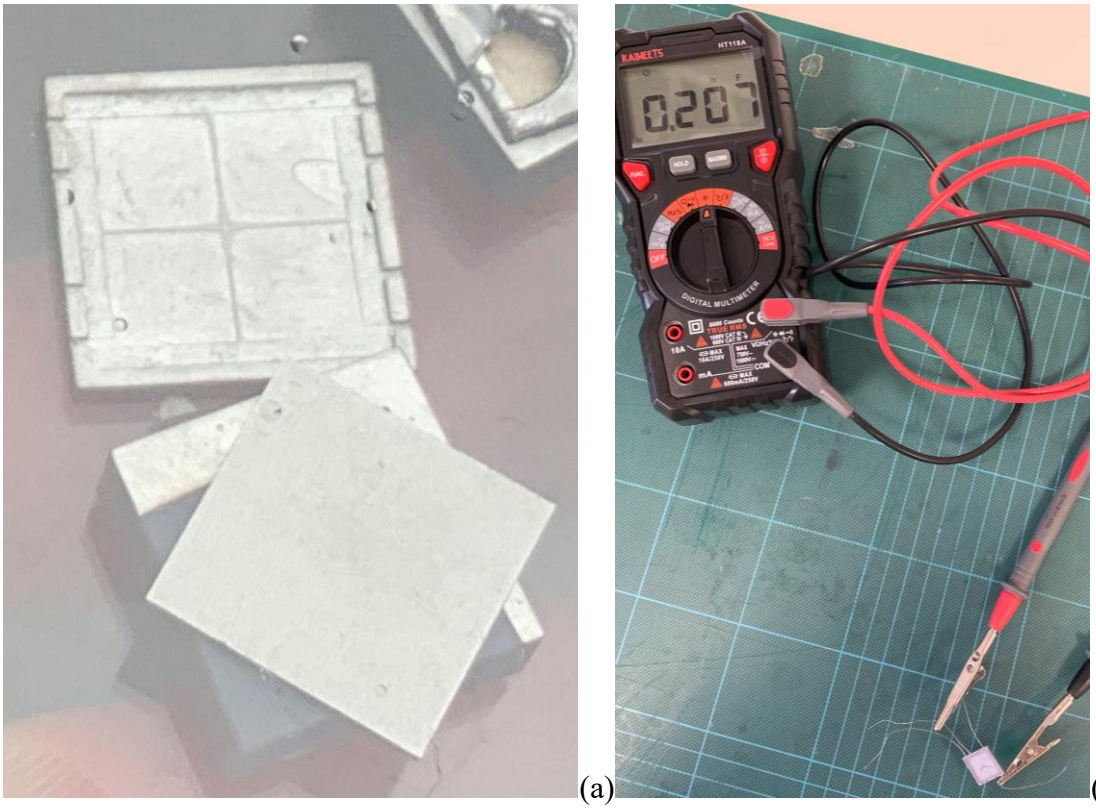

(a) (b)

Figure 4.18: Coated omnidirectional sensor inspired by the suspended trichoid sensilla of arachnids. The two sections right after coating (a), the part with the hair is upside down and supported by another printed block. Capacitance measurement once the two sections were joined (b).

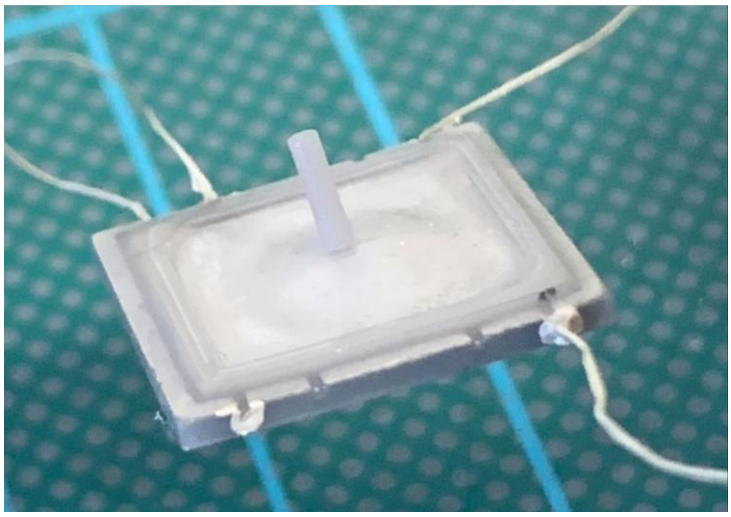

Figure 4.19: Sensor inspired by the suspended trichoid sensilla of arachnids after being metal coated and glued showing a bulged defect.

4.3 Conclusion and Future Work

The aim of this work was to develop a bio-inspired hair-like acoustic sensor fabricated via AM that can react to different frequency bands. This objective was achieved on the mechanical

side, albeit with room for improvement. Fabrication of the sensor using two different materials to mimic insect hair-like structures was successful and provided a satisfactory mechanical response (i.e., cantilever-like movements in different frequency bands). Meanwhile, appropriate structural changes provide designs with different frequency responses. Improvements in manufacturing have been stated, but they have room for improvement. 3D printing would allow the easy integration during manufacture of multiple sensory structures on the same base. Nevertheless, in this research unfortunately the mechanical displacement has not been converted in an electric signal. Therefore, the first goal for further work is of course converting the mechanical displacement in an electric signal. Several designs have been attempted, but more materials and sensing methods can surely be used.

4.3.1 Material and fabrication improvements

Some of the possible material and fabrication improvements for improving the functionality of the sensor are listed below.

- **Hydrogels**: Research in conductive and piezoelectric 3D-printable hydrogels is gaining momentum [170, 171]. These are materials that are much softer and could therefore allow for proper conversion. Of course, they need to be tested with a hair shaft on top, and their use strongly depends on whether the two materials are compatible. This method would also remove the need to include metal after, and it would render the whole structure 3D-printable instead of needing other processes after. Hydrogels need to be submerged in a liquid most of the time, therefore proper design choices need to be made, whether the hair is exposed on air or whether its response needs to be studied in fluid. The latter would also need to consider a method to transduce the waves from air into the fluid.
- **Laser Induced Graphene**: In the world of flexible and printable electronics, a technique that is often used is laser induced graphene [172]. The premise behind this is that certain

carbon-rich materials can have a portion of their surface turned into graphene by using a high-power laser. Graphene shows piezoresistivity, therefore this method is used for bendable electronics. It might be worth investigating the 3D-printing of such materials, or in alternative materials that can be sprayed on the surface of interest and then turned into graphene.

- **Conductive UV-curable resin**: In the 3D-printing research area graphene and carbon nanotubes are often included in UV-curable resins allowing conductivity and in certain cases piezoresistivity [173-175]. These could be other venues that could be investigated. Albeit it is important to note that often handling these resins constitutes a hazard for the operator, therefore this introduces more health and safety concerns.
- **Other material deposition methods**: Other material deposition techniques can be investigated, for example e-beam, which has been used in the past to create 3D-printed sensors [20, 176].

Another important consideration to be made is that to **sense higher frequencies** than the detected ones (>500 Hz), the sensor needs to be either stiffer or smaller, or both. And, as observed, sensitivity to a higher frequency often comes with lower displacement. This is most likely due to having air as the fluid in which the hair sensor is immersed. Having the sensor immersed in another fluid (e.g., water) can improve the response, especially at higher frequencies and would allow for miniaturization. Consideration for higher sensitivities therefore need to be made for allowing the sensor being immersed in fluid. Either by coating them with an isolating material, or by having complex design that isolate the electronics from the fluid.

4.3.2 Computational considerations

Once the sensor has been made to work fully, and for a wide range of frequencies, the logical next work that is needed is investigating their use in **arrays**. This includes the **computation** of these sensors for audio acquisition and algorithms that make full use of their capabilities. It will also be important to investigate their application (e.g., speech recognition) and compare it to current state-of-the-art applications. Parallel computing will of course be needed to make full use of these sensory arrays; one option could be the use of Field Programmable Gate Array (FPGA). In theory, these algorithms could already be studied a priori by using multiple parallel narrow frequency passband filters at the output of a standard microphone to simulate the presence of multiple narrow frequency band sensors.

Neural computing or spike computing is another field that has gained plenty of interest in the engineering world especially for sensory systems [177]. Currently there are no pure acoustic sensors that produce spikes at the output and to have acoustic neuromorphic sensing, event coding is needed instead [178, 179]. Having these arrays of sensors work would open the door to possibilities of developing a fully neural microphone, or in general a **neural acoustic sensor**, inspired by the way we hear and our cochlea's cilia. In a recent podcast, Dr Lenk specified that a draft paper is being prepared for a version of the cochlea-inspired sensor presented in [180] that is capable of directly generating spike signals [181].

4.3.3 Analytical model improvements

Adapting the **analytical model** for different geometries, like the proposed squared one, would allow for faster simulation pre-prototyping. And in general, it would ease the design of these sensors. Additionally, this would open the doors to optimization models that aim at optimizing designs for increasing the displacement of the hair shaft at the desired resonant frequency and thence improving its response.

5

Additive Manufacturing of an Airflow Hair Sensor Bioinspired by the adult *Buthus occitanus* Scorpion's flat Trichobothria

"The purpose – where I start – is the idea of use. It is not recycling, it's reuse"

Issey Miyake

The reuse of the acoustic sensor design (chapter **4**) for sensing other physical domain has always been one of the purposes of this project. A true bioinspiration from how nature adapted through evolution a similar mechanoreceptor for sensing different things (as already outlined in **2.3.4 Other Insect Mechanoreceptors** and **2.3.5 Similar Receptors**). During the experiments of the acoustic hair sensor, it was noticed that if the spring's elastic modulus was low enough, the sensor could also move due to wind, acceleration or gravity. It was therefore decided to investigate the sensor's structure response due to an airflow. After repeated failures in converting the mechanical displacement of the acoustic hair sensor in an electric signal it seemed clear that the issue was always one: the low displacement magnitude. Nevertheless, with the airflow sensor the displacement could be seen with naked eye and did not need the use of LDV to be detected. Amongst the possible applications of the proposed sensor are biomedical respirators, assistance for autonomous vehicles, wind measurements for meteorology or wind turbines, and wide-area flow cameras.

This chapter investigates the design modifications made to the acoustic hair sensor that allowed it to have airflow velocity sensitivity. The chapter will firstly introduce the first observed mechanical responses, the piezoelectric COMSOL investigation and lastly, the sensor's response and its characterization. Part of this research was first presented at IEEE FLEPS 2025 [182], and, later expanded in IEEE Sensors Journal [183].

5.1 Design and manufacture

The design of this sensor is an adaptation of the acoustic sensor inspired by the hinged trichoid sensilla, described in detail in **4.2.2 Artificial hair inspired by the Hinged Trichoid Sensilla (HTS)**. In summary, the idea is to use a squared hair shaft bioinspired by the flat Trichobothria of the adult *Buthus occitanus* scorpion instead of a cylindrical one. The hair shaft sits on top of a supporting beam, called "spring". Moreover, the hair and spring have two

different elastic moduli. The hair shaft is harder to avoid being bent and deflects all the energy to the spring at the bottom. Moreover, the spring is sputter coated with a platinum layer to add piezoresistive capabilities and convert the hair shaft displacement in an electric signal. For the sputter coater used in this project only a limited number of metals were available to be used, gold and platinum. For which the latter has the best gauge factor reported in literature [184]. In all the scenarios, the sensors were printed upright vertically to avoid using support beams, which could damage the sensor upon removal. Moreover, printing the sensor in this direction is the only way to print with multi-material, since the slices of the sensor model are made vertically, and the change of material can therefore happen only along this axis.

5.1.1 First airflow sensor iteration

The hair was fully 3D-printed with a ASIGA MAX X27 DLP 3D printer. In the first iteration the hair structure was printed using Formlabs's grey General Purpose Resin (V4) and the rest of the structure using Formlabs's Elastic 50A resin (V1). The acoustic hair sensor used a custom-made PEGDA-based resin, but Formlabs's elastomer proved to perform better under frequent and continuous stress, therefore being more durable and less brittle. Especially for large displacements. Once the sensors were manufactured, they were cleaned in isopropyl alcohol for 3 minutes in a Clifton SW3H ultrasonic bath to remove resin residues. The sensors were then UV post-cured for 2 minutes. In the first iterations two hair sensors samples were printed, their design and a CT-scan are presented in Figure 5.1. The first with a spring 1 mm tall and 400 µm thick (sample 1), and the second with a spring 1.5 mm tall and 300 µm thick (sample 2). In both samples the hair is 4x3x1 mm and the spring is 0.2 mm wide. The printing settings used in the Asiga for the layers of elastic 50A resin were the default ones of the Formlabs elastic FLELCL01 taken from Asiga's material open library [185]. For the remaining structure (using the grey resin), the specified settings were modified to print the hair accurately due to the resin being different, while the others remained as default:

- Light intensity: 19 mW/cm2
- Exposure time: 2 seconds for the first 2 layers, then increase to 3 seconds
- Z-compensation: 0.2 mm
- Wait time after approach and separation: 5 seconds

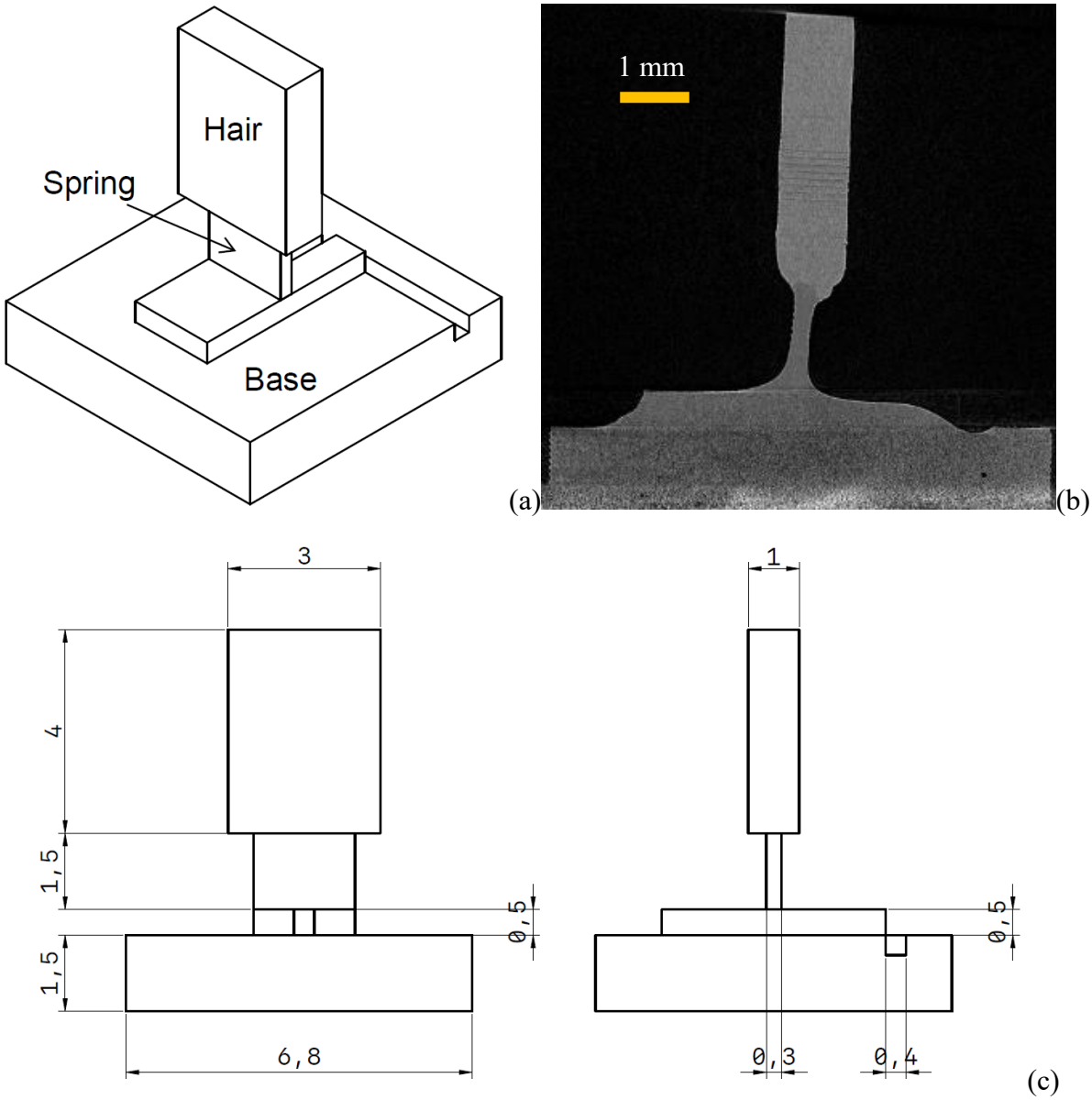

Figure 5.1: Basic diagram of the hair-like sensor (a). CT scan of a 3D printed sensor structure (sample 2) (b). Diagram of the sensor with dimensional annotations in mm (c).

This sensor was used for the first mechanical investigations as a proof of concept. However, once it was attempted to coat it with metal, masking it to provide a pattern for piezoelectricity purposes was challenging. Therefore, it was decided to print the spring directly in a pattern.

5.1.2 Patterned spring designs

Due to difficulties in masking the spring for the creation of a conductive layer, it was decided to print the spring itself in a pattern. The first pattern that was attempted was a “gate” pattern. This is simply two thin vertical beams and one horizontal beam on top. While this was easily printable, to make full use of the piezoresistive properties it was decided instead to introduce a serpentine design, common of strain gauges. This is given by the fact that the change in resistance across multiple thin vertical beams increases with the number of beams, as the overall experienced strain will be higher. It was also decided to stop using evaporation and begin using sputter coating to introduce metal on the spring. Evaporation took a long time and the experience in the lab was with the use of aluminium only, on the other hand sputter coating is faster and allowed to test both gold and platinum layers, known for having better piezoresistive properties than aluminium. For a full description and comparison of the considered metal deposition systems, refer to **3.4 Sensor Electrical Integration – Metal Coating**. Figure 5.2 shows a simple diagram of this sensor, and a CT scan of a printed and coated sensor. The spring is 0.4 mm thick, and its height is 1.5 mm. The serpentine design is made of four vertical beams, the two at the edges are 0.4 mm wide, while the inner beams 0.3 mm. The spacing between beams is 0.2 mm and they are connected by horizontal beams with a height of 0.3 mm. Other serpentine configurations with more and thinner beams were tested but were harder to print and had a high printing failure. Often only 1/6 sensors would print in one batch. In this first iteration, the base has a carved space that works as tracks to add wires to the sensors. The tracks have a hole with a 0.7 mm diameter, enough to have a standard breadboard-sized cable run through. Agar Quick Silver Paint (AGG302) was used to fill the

track while a cable was inserted in the hole. This ensured proper connection between the cable and the metal coated spring. Super glue was applied at the top of the track to ensure the strain of bending cables wouldn't break the connection. A strong advantage of this design is that, compared to a whole spring, this design had decreased stiffness. This advantage was particularly prominent after metal coating when usually the stiffness of the system would increase. With the old design with a whole spring, after metal coating the sensor would turn too stiff to sense airflow.

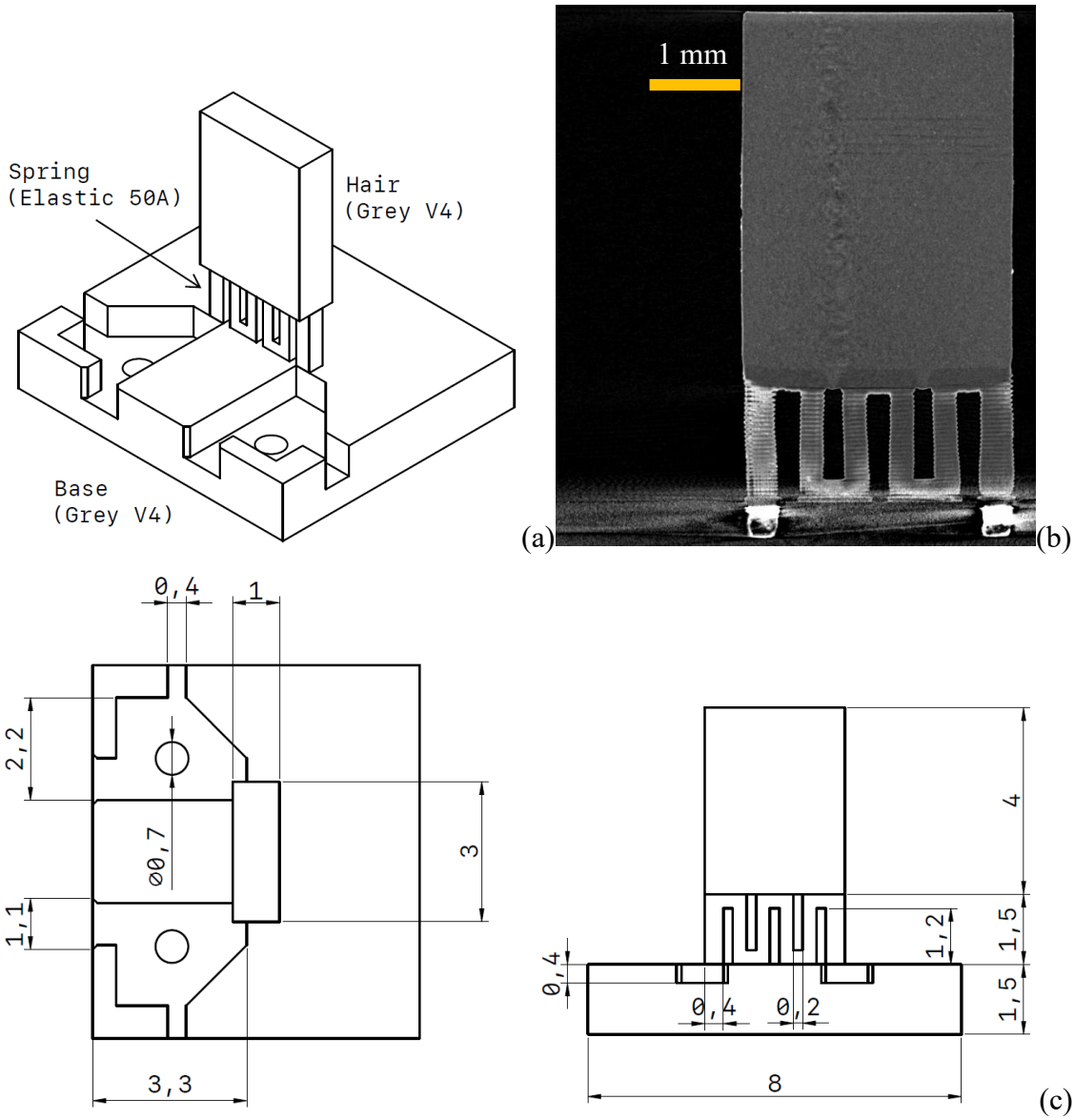

Figure 5.2: Basic diagram of the hair-like sensor with serpentine spring (a), it shows the name of the different parts, and the resin used for them. Coated sensor's CT scan (b). Image first presented in [182]. Diagram of the sensor with dimensional annotations in mm (c).

While some first iterations of this structure used Elastic 50A (V1), later prints used the newer Formlabs Elastic 50A (V2). For the spring section the same print settings were being used. The new resin showed a better success rate in printing and from CT scans the quality of the spring seemed smoother. In the CT scan of Figure 5.2, it is easy to see the different layers as produced by the 3D printing process. When using the new resin, it was not as noticeable. Moreover, to aid the sputter coating process the design of later sensors was modified with a reduction of the base area and having a sort of ramp in the front to allow a more direct exposure to the coating, Figure 5.3a. Moreover, some tests were performed with the hair shaft having the same thickness as the spring, and different thicknesses have been produced. Figure 5.3b shows printed hair sensors with different thicknesses between 400 μm and 900 μm. A mark on the base was done during printing for easy identification of the sensor's model. For example, the sensor in Figure 5.3a has a "4" on the base to indicate that it is a sensor with a thickness of 400 μm for hair and spring.

The default print settings were based on the "Formlabs Flexible Resin" file downloaded from the Asiga Material Library [185]. Nevertheless, some parameters were modified to allow for the correct print of the base and hair shaft and for the swap of material between sections, as specified in Table 5.1.

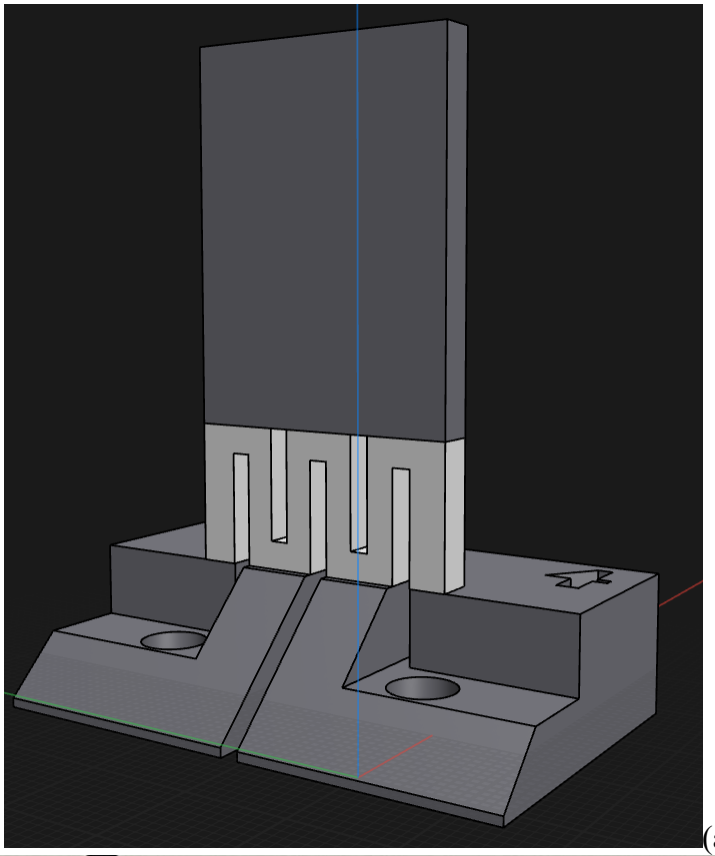

(a)

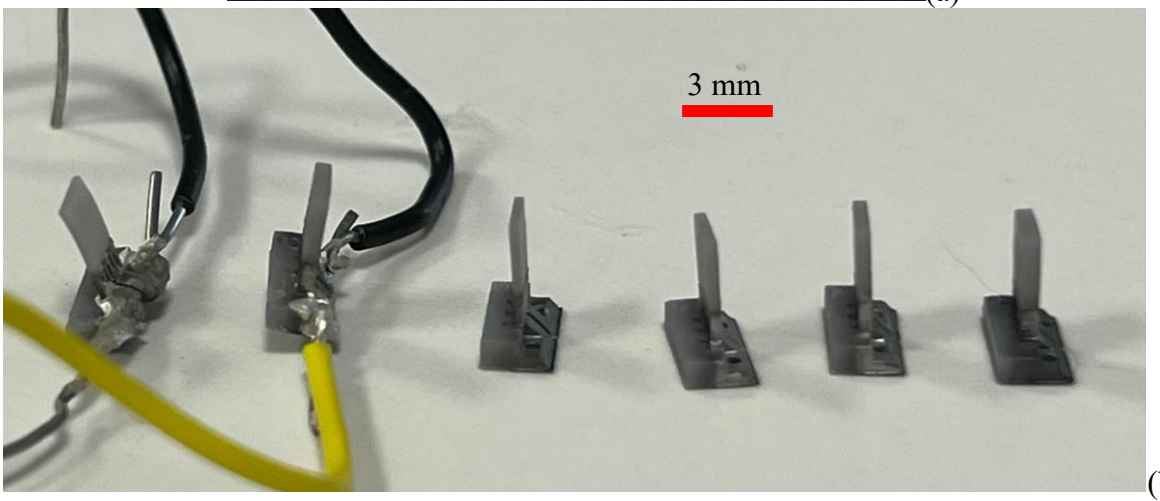

(b)

Figure 5.3: (a) Modified version of the sensor with serpentine spring and reduced base with a ramp to allow a more direct exposure to the sputter coated metal. (b) Printed sensors with different thicknesses, from left to right the thicknesses of the hair shafts and springs are: 400 µm, 800 µm, 500 µm, 600 µm, 700 µm and 900 µm.

Table 5.1: 3D-print settings used for the sensors using Formlabs Elastic 50A (V2). Table first presented in [183]. The different columns for each part represent different printing settings for different print ranges of the part being printed.

Part	*Base*		*Spring*		*Hair*	
Print range from-to (mm)	0-0.1	0.1-1.5	1.5-1.55	1.55-3	3-3.3	3.3-3.7

Layer thickness (mm)	0.05	0.1	0.05	0.05	0.05	0.1
Light intensity (mW/cm^2)	20	20	39.94	39.94	20	20
Exposure Time (s)	5	3	1.4	0.543	2	3
Z-compensation (mm)	0	0	0	0	0	0
XY-compensation (mm)	0	0	0	0	0	0
Approach pressure limit (g/cm^2)	100	100	45	45	45	45
Viscosity range (mm)	1	1	2	2	1	1
Wait time after separation (s)	5	0	5	5	2	2

5.1.3 Cableless design

The previous iterations of the sensor had the cables for creating electrical connections attached to the body of the sensor, this new design instead has a flattened-out base that is coated with platinum together with the spring and creates connection contacts, Figure 5.4. It was printed with a hole through it in case adding a cable onto the structure was needed. This section is then painted with Agar's quick drying silver paint to increase the conductivity of these connection contacts. This reduces the overall base resistance of the sensor, improving its response (since the resistance change will be higher and easier to detect once the sensor is bent). In the previous design (Figure 5.2 and Figure 5.3) the cables were a weak point, often breaking the sensor's body or the electrical connection. The new sensor design's connection pads allow the sensor to be glued with a conductive epoxy to a PCB connection track, but in the experiments described here the sensor was pressed with screws and bolts and two plates against a block holding cables (Figure 5.5). The cable block uses Agar's quick drying silver paint for the electrical connection between the cables in the holes and the protrusion coming up. Both plates and cable block were 3D-printed using the same setting in Table 5.1 for the base.

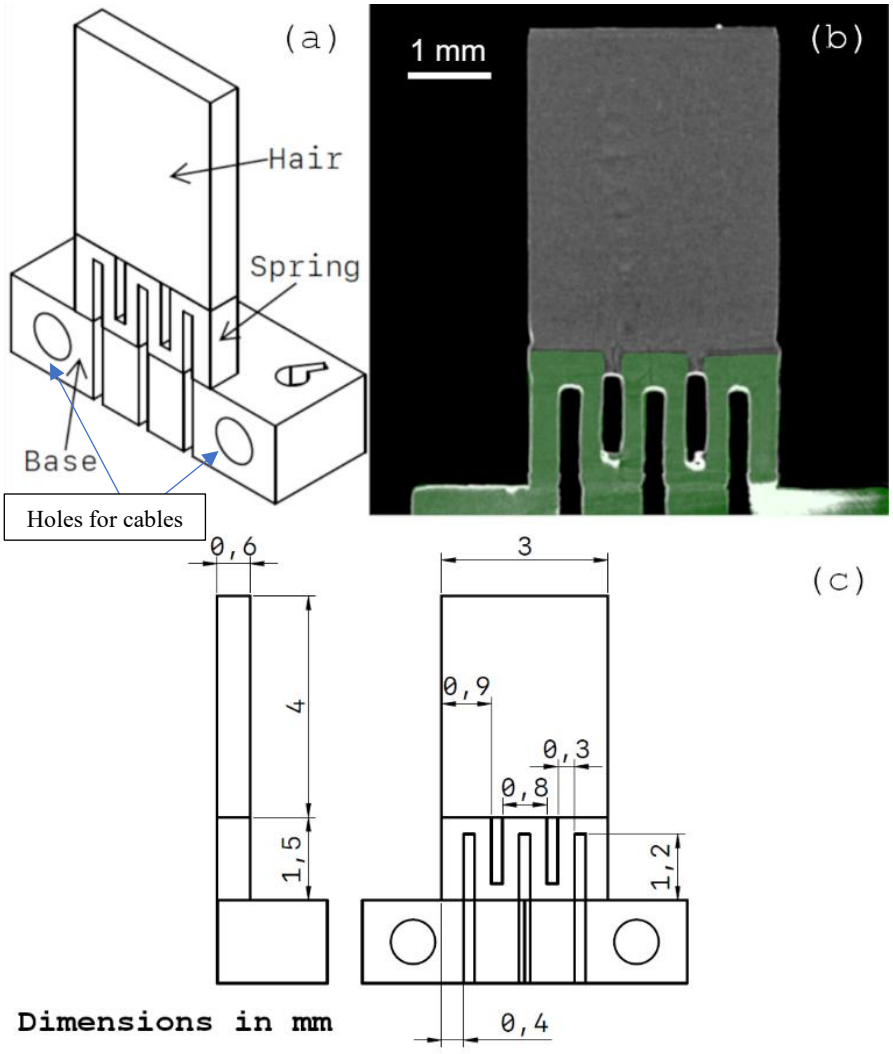

Figure 5.4: Artificial Hair Sensor diagram of the design with flattened base, with names of its different parts (a). Coated sensor's CT scan (b). The area coated with platinum is highlighted in green. Example of sensor diagram with dimensional annotations in mm (c). Image first presented in [183].

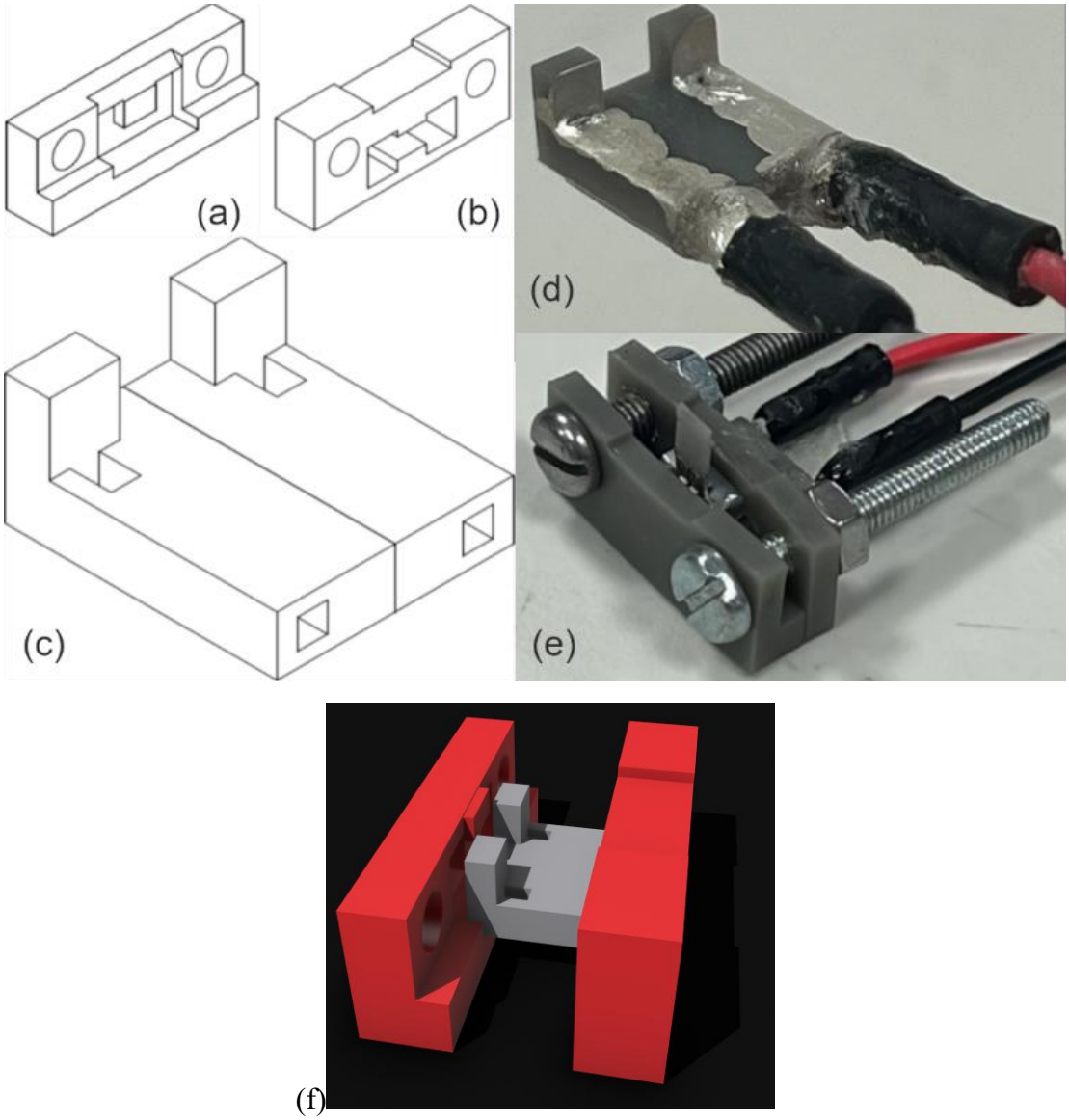

Figure 5.5: Cable holder and plates to hold the sensor still and add cables for electrical connections. Diagrams of the screw plates, (a) front, (b) back, (c) diagram of the cable holder, (d), printed cable holder with cable connections and (e) plates, screws, sensor and cable holder joint together. Additional perspective showing the screwing plates, in red, fitting the cable holder, in grey (f). Images (a)-(e) first presented in [183].

5.2 Mechanical investigation

The very first mechanical investigations were simply conducted by blowing to the sensor right after printing and cleaning it and noticing its displacement, their purpose was a simple pass-fail verification. The displacement of the sensor due to a person blowing was recorded using a Canon EOS550D digital single-lens reflex (DSLR) camera with a Canon zoom lens EF-S 18-55mm. The sensors were placed in front of a ruler to estimate the hair's displacement

while blowing on it from 5 cm and 30 cm of distance at about the same strength. While not tested with an appropriate scientific method (since human blowing cannot be replicated accurately), these photos helped in understanding that the material selection for this sensor could produce large hair tip displacements. The measured tip displacements were then used in the COMSOL simulation below. Figure 5.6 shows the sensor at rest, when blowing from 5 cm and when blowing from 30 cm. It could be noticed that when blowing from 5 cm, a ~3 mm displacement was observed (Figure 5.6b), while when blowing from 30 cm a displacement of ~1 mm could be observed (Figure 5.6c). Sample 1 showed a displacement between 0.5 mm and 1 mm when blowing between 10 cm and 5 cm of distance. Albeit this is not a proper measurement set-up to quantize the airflow experienced by the sensor it was used to understand the possible capabilities of this structure. Follow-up experiments were made directly after the sensor was coated collecting the sensor's output and presented below in the electrical results section.

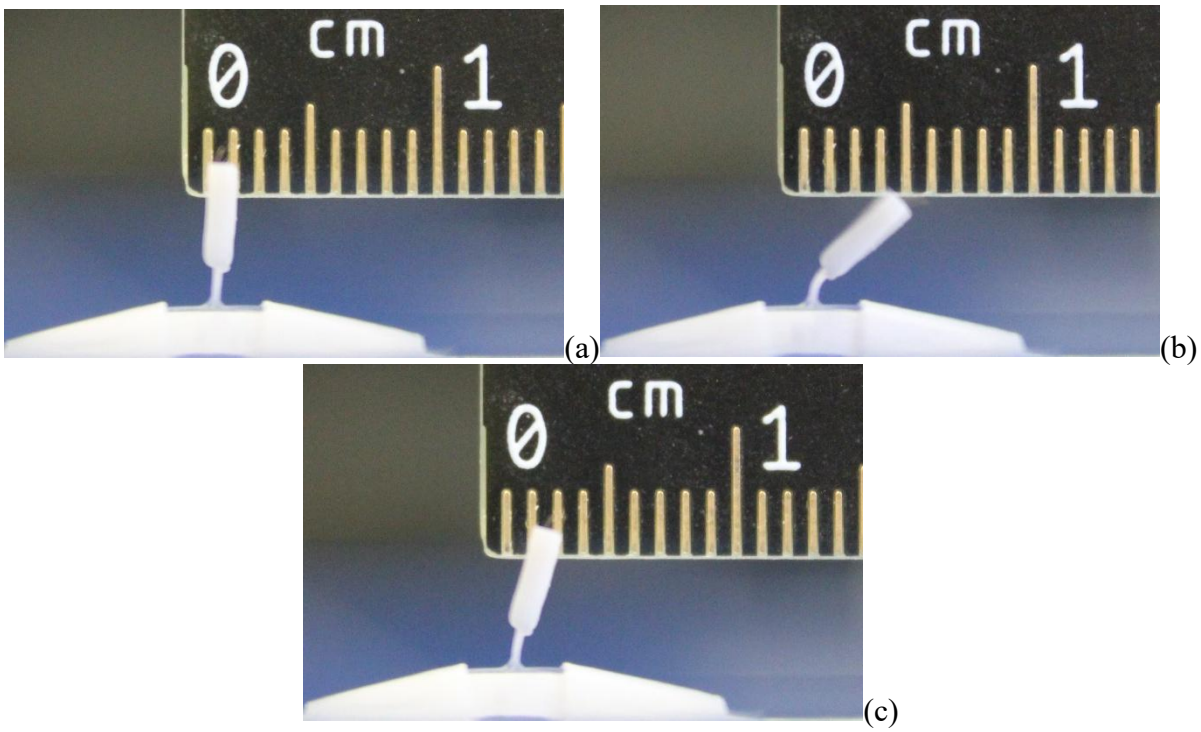

Figure 5.6: Pictures taken of an airflow hair sensor with Canon EOS550D, (a) at rest, (b) while blowing 5 cm away from the hair, (c) while blowing 30 cm away from the hair.

5.3 Piezoelectric COMSOL simulation

The sensor was built in COMSOL Multiphysics. These simulations were performed when the spring was considered whole and the "gate" pattern was thought to be placed on the spring during evaporation via masking rather than printing the whole spring in that shape. Any discrepancies to the designs shown above are attributed to this. On top of the spring a 0.11 µm aluminium sheet with a "gate" pattern was created (Figure 5.7). This represents a sheet of coated aluminium on the sensor's spring with thickness similar to that found in literature [175]. The gap between the two beams of this "gate" is 0.5 mm in height and 1.5 mm in width. This aluminium sheet represents the piezoresistive transduction in response to the hair displacement induced by the airflow. COMSOL uses a Solid Mechanics module to simulate a bending of the spring caused by a prescribed displacement on the tip of the hair (applied on top edge of the hair). To simulate the piezoresistive effect an Electric Current module was applied to only one side of the aluminium layer, with the terminal being the left end of the "gate" with 1 A applied and the ground to the right end of the "gate". The two physics modules were coupled using the Multiphysics Electromechanical Forces module.

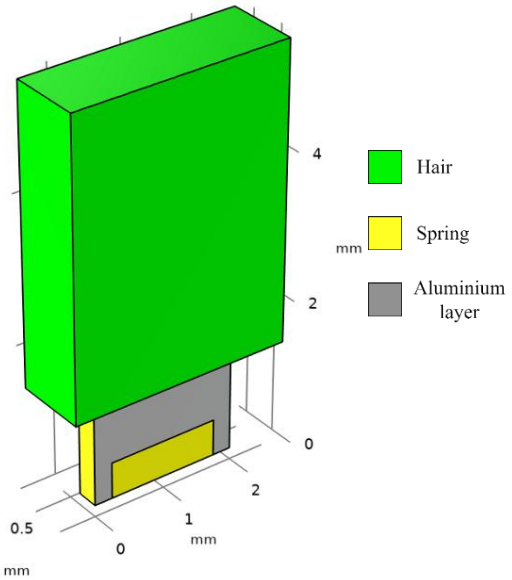

Figure 5.7: Sensor structure in COMSOL with aluminium layer on spring. Hair in green, spring in yellow, aluminium sheet in grey, bottom base omitted.

The simulation applied a prescribed displacement between 0.01 mm and 3 mm. The value of resistance when the sensor is at rest was evaluated by using only the electric current module without solid mechanics. The Young's Modulus of the grey resin was set to 2.8 GPa as per datasheet [168], while the elastic resin to 2.05 MPa as measured in [186]. The Poisson's ratio and material density for both materials was set to 0.33 and 1158 kg/m^3, respectively. The resistance values evaluated using a stationary study are reported in Table 5.2, and shown in Figure 5.8. The resistance change trend is logarithmic and in theory should be easily detectable with conventional circuitry.

Table 5.2: Resistance value and resistance change from rest position (ΔR) of the aluminium layer on the spring of the hair for different hair tip displacements in COMSOL.

Hair Displacement (mm)	0 (at rest)	0.01	0.05	0.1	0.5	1	2	3
Resistance (Ω)	1.7430	1.7436	1.7458	1.7486	1.7637	1.7746	1.7896	1.8005
ΔR (mΩ)	-	0.60	2.80	5.60	20.70	31.60	46.60	57.50

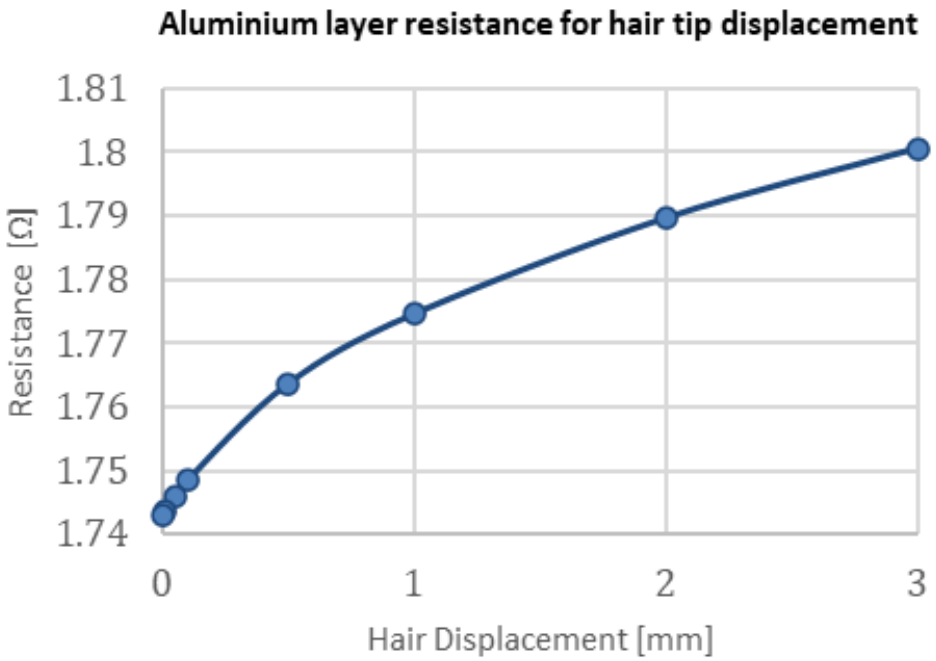

Figure 5.8: Resistance of the aluminium layer on the spring of the hair sensor for different hair tip displacements in COMSOL.

These experiments were repeated with the different spring patterns, and with gold and platinum layers instead of aluminium once the switch from evaporator to sputter coating occurred. Nevertheless, the properties of evaporated or sputter coated layers of a material differ from the bulk material itself. This means that it is challenging to simulate thin layers of metal in COMSOL as these properties' changes are not known. Therefore, while these simulations are surely informative and have helped in assessing if piezoresistive was a viable option; they could not be compared to real-world results and have been abandoned.

5.4 Electric results

5.4.1 Airbrush experiments

For the first electrical experiments an airbrush as the airflow source was used. The tested hair is the one represented in Figure 5.2. An Agar sputter coater (AGB7341) with thickness monitor was used to coat the spring of the sensor with platinum. The sputter coater was used for 120 seconds at 40 mA, for a measured thickness of 107.5 nm. The resistance of the sensor was measured with a standard multi-meter at 27.93 Ω. The sensor was tested in a voltage divider configuration with a 90.4 Ω resistor (Figure 5.9). The reason for using a slightly higher resistor in these preliminary tests is to ensure some sort of protection for the sensor from excessive power. A voltage source of 10 V was applied across the voltage divider. A Tektronix DPO2014 oscilloscope was used in AC-coupling mode to measure changes in resistance from an applied airflow. AC-coupling was used to be able to see small voltage changes in the oscilloscope. The VU low-pass filter of the oscilloscope was applied to the signal at 60 Hz. In all the experiments a velocity microphone (Knowles NR-3158) was placed beside the hair sensor as reference to understand if what was shown on the oscilloscope was an actual response of the sensor or noise. The screen of the oscilloscope was photographed, straightened with ScanDoc (Figure 5.10a), the plot points were exported with automeris.io (Figure 5.10b).

The airflow was applied using a Goocher airbrush with 0.3 mm nozzle and its 40-psi compressor. The outlet was set at the smallest radius. No paint was inserted in the airbrush as it was used only to create a concentrated airflow. The outlet of the airbrush was aligned with the hair of the sensor at different distances. A Sauermann Si-VH3 hot-wire anemometer was used to measure the equivalent airflow velocity produced by the airbrush at different distances. Figure 5.11 shows the experimental setup.

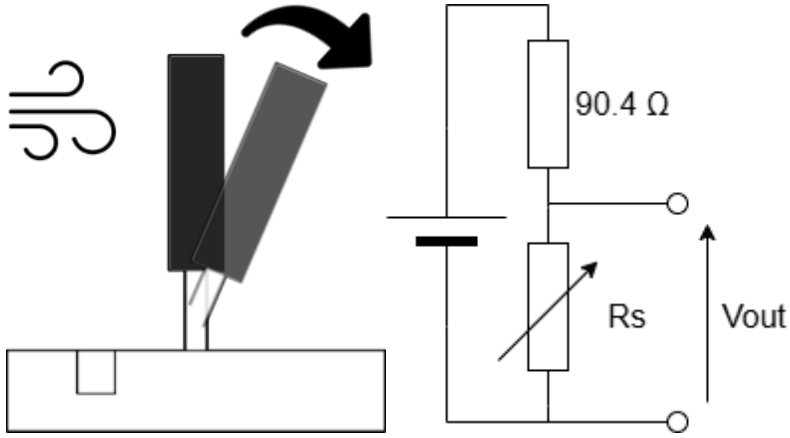

Figure 5.9: Functional diagram of the sensor's operation (left) and circuit of experimental setting (right). The air flow causes the sensor's structure to bend. The spring of the sensor, coated with platinum changes resistance Rs, which, in a voltage divider circuit changes the output voltage Vout. Image first presented in [182].

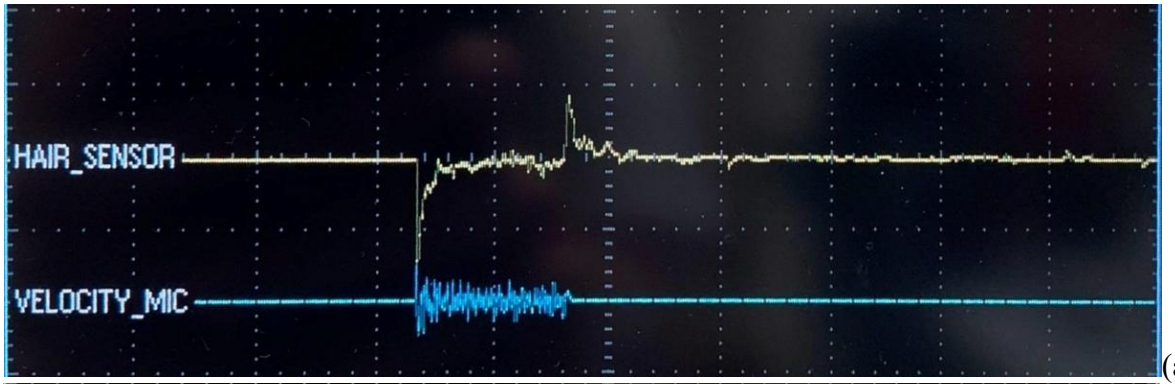

(a)

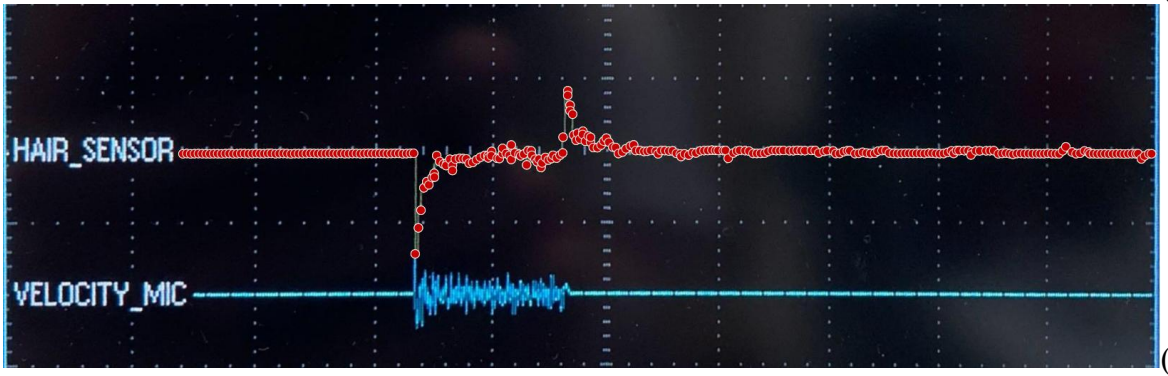

(b)

Figure 5.10: Picture of the oscilloscope straightened with ScanDoc of the data taken when the airbrush was at 3 cm distance (a) and its extracted points in automeris.io (b). The oscilloscope's X and Y axes were set to 1 s/div and 10 mV/div respectively. Image first presented in [182].

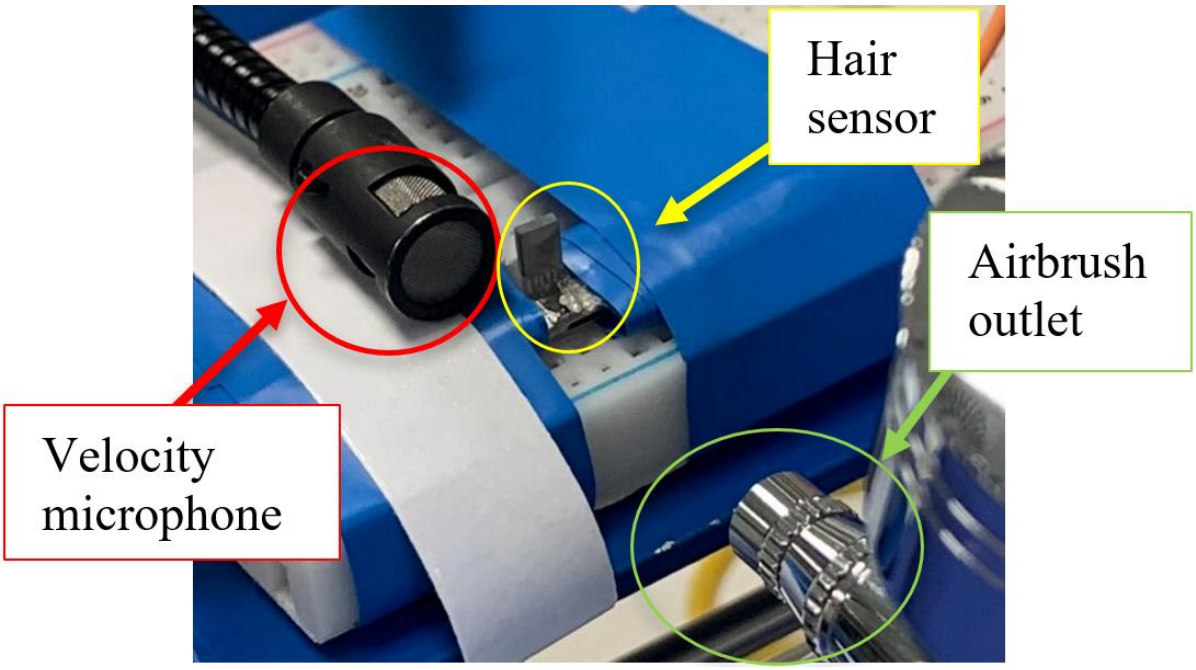

Figure 5.11: Experimental setup with airbrush at 3 cm distance. Image first presented in [182].

The mean output airflow velocity over 30 seconds of the airbrush at different distances measured by the hotwire anemometer are shown in Figure 5.12. It is important to note that the higher the distance the higher the standard deviation of the measured data points, i.e., slight decrease in accuracy. The standard deviation

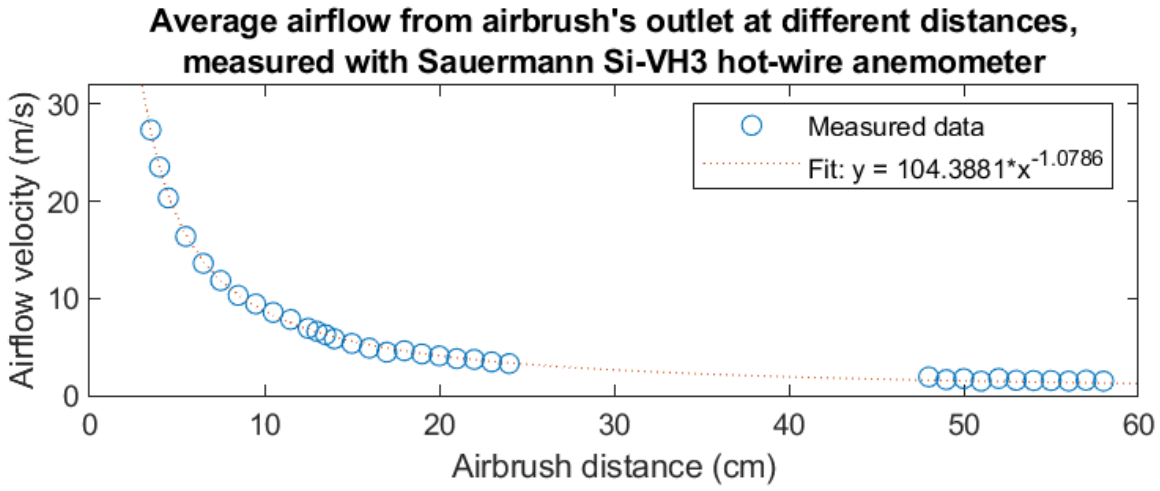

(a)

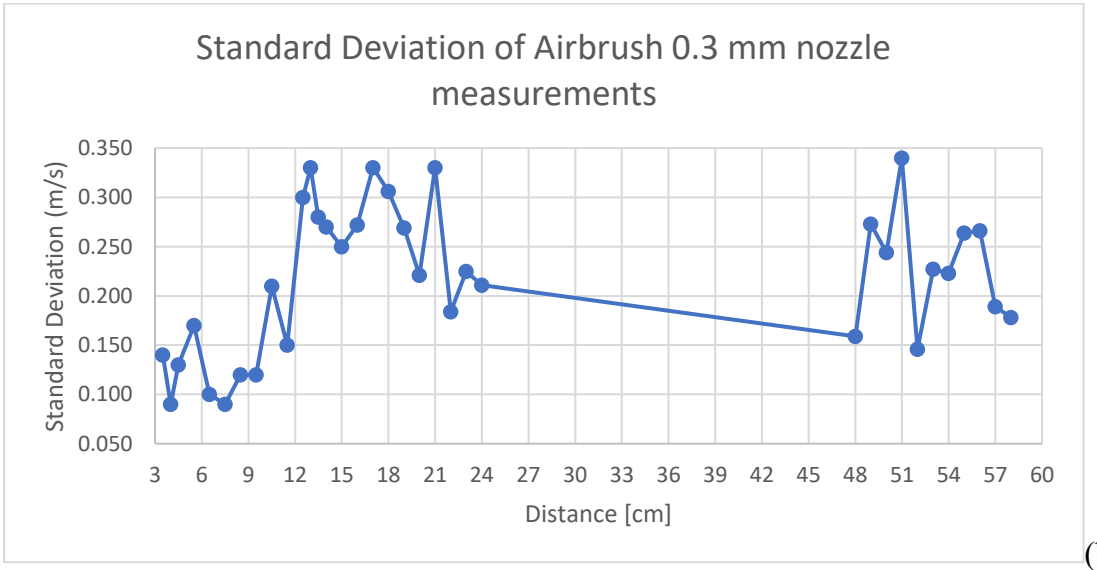

(b)

Figure 5.12: Average airflow velocity output of airbrush at different distances from the hot-wire anemometer (a). Standard deviation in the airbrush measurements (b). Image (a) first presented in [182].

The preliminary results shown in Figure 5.10 and Figure 5.13 show a clear dependency between the airflow strength and the voltage output of the sensor (therefore with its change in resistance). When the airbrush is turned on (to the right of the purple line) there is a sudden negative peak, indicating a drop in voltage across the sensor, and, consequently in its resistance. Meanwhile, when the airbrush was turned off one can notice a positive peak, signalling an increase in voltage across the sensor, and thus, in resistance. The transients shown in Figure 5.13 cannot be translated to the exact resistance change, but they are still representative of the way the sensor works. Plotting the peaks of positive voltage when the airflow has stopped, i.e.,

when the sensor is returning to its initial position (Figure 5.14), shows a trend between the peaks and airbrush distance comparable to the anemometer's measurements (Figure 5.12). Moreover, Figure 5.14 suggests a linear relationship between the sensor's response and the airflow velocity.

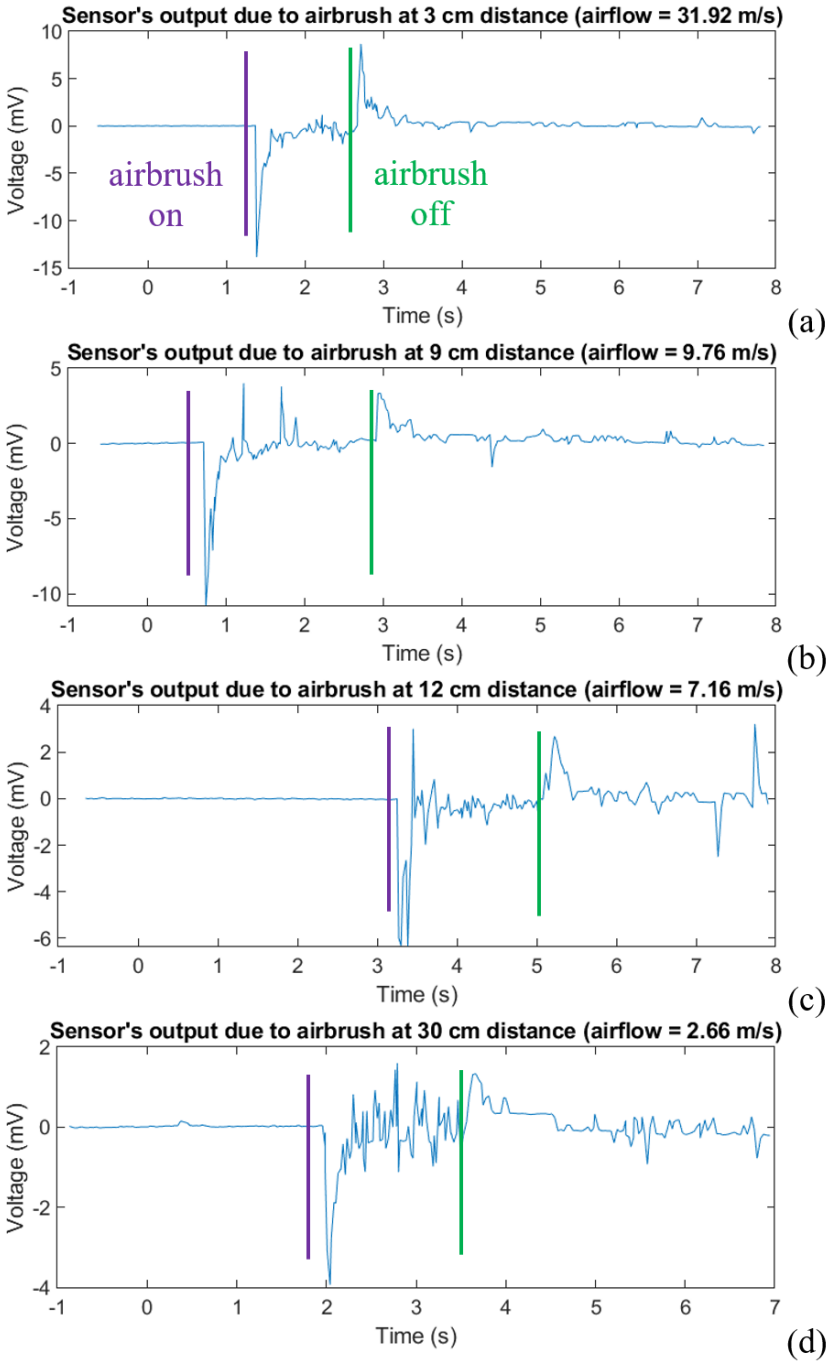

Figure 5.13: Voltage output measured across the sensor in voltage divider configuration in AC-coupling for airbrush distance of 3 cm (a), 9 cm (b), 12 cm (c) and 30 cm (d). To the right of the purple line the airbrush was turned on, while to the right of the green line it was turned off. Image first presented in [182]. Negative time points are an artefact of automeris.io.

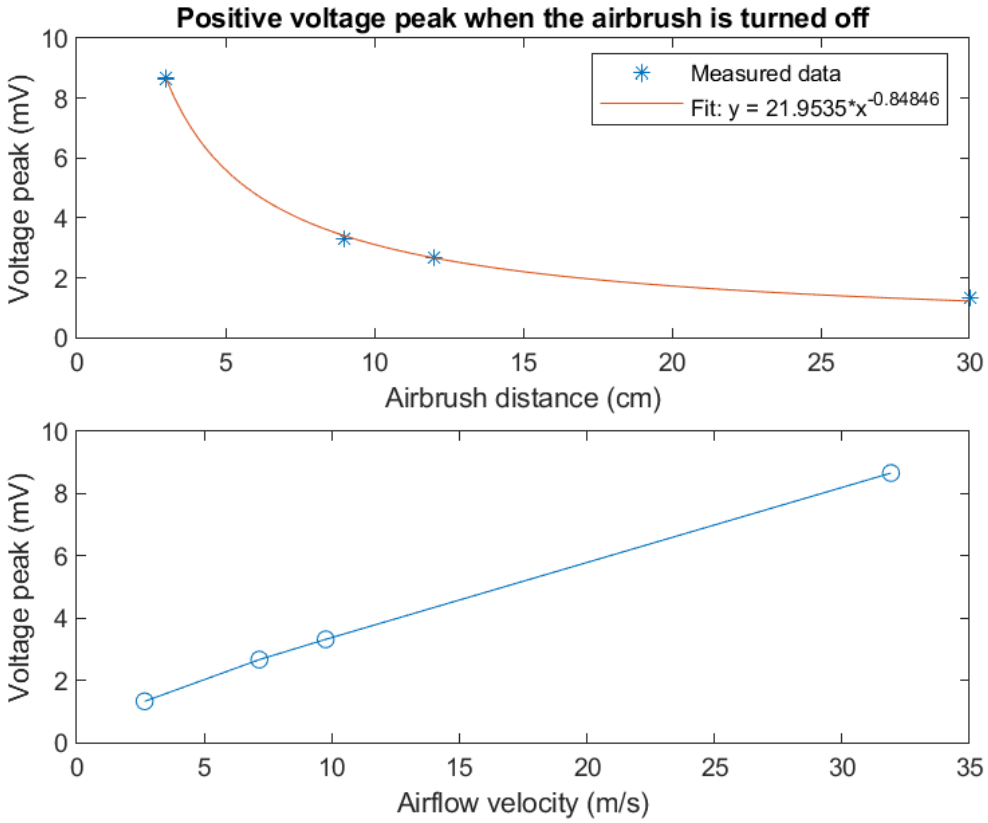

Figure 5.14: Positive voltage peak of the sensor's output when the airbrush is turned off (i.e., sensor returning to initial position). Plot versus the airbrush distance (top), and versus the airflow velocity (bottom). Image first presented in [182].

The presented results show a promising response of the sensor to different levels of airflow velocity. But they do not allow deep understanding of the response of the sensor in terms of resistance change of the coating of platinum on the 3D-printed spring. Therefore, a follow-up test was conducted with a different circuit using a Wheatstone bridge (Figure 2.27c). No amplification was used but only filtering from the oscilloscope, and the measurements were taken with an oscilloscope in DC-coupling. The results were collected with a laptop connected to the oscilloscope and the software TekScope Utility, removing the need to salvage the data from a picture as described above. This test used a hair sensor that had both spring and hair with a 400 µm thickness (Figure 5.3b), it was sputter coated with platinum for a thickness of 112 nm (as measured by the sputter coater's thickness monitor). The experiments with an airbrush were conducted and showed in Figure 5.15. These results suggest an upper limit between 23.40 m/s and 18.40 m/s and a lower limit between 7.16 m/s and 6.56 m/s.

Another hair sensor was tested with a hair and spring thickness of 800 µm. Albeit no output could be seen in the range of 13 cm to 3 cm, a signal was recorded at 3 mm distance (Figure 5.16). Using the anemometer's fit curve in Figure 5.12, this would translate to ~382.90 m/s. This velocity might be wrong as it was not recorded with a proper reference, but it does show the potential of 3D printing of arrays of this sensor, with slight differences for different ranges/sensitivities. Nevertheless, changing the distance of the airflow source can increase the noise on the airflow. And when pressing to the airbrush the outlet is often prone to movement, which introduced noise and inaccuracies. This warranted the use of a different airflow source.

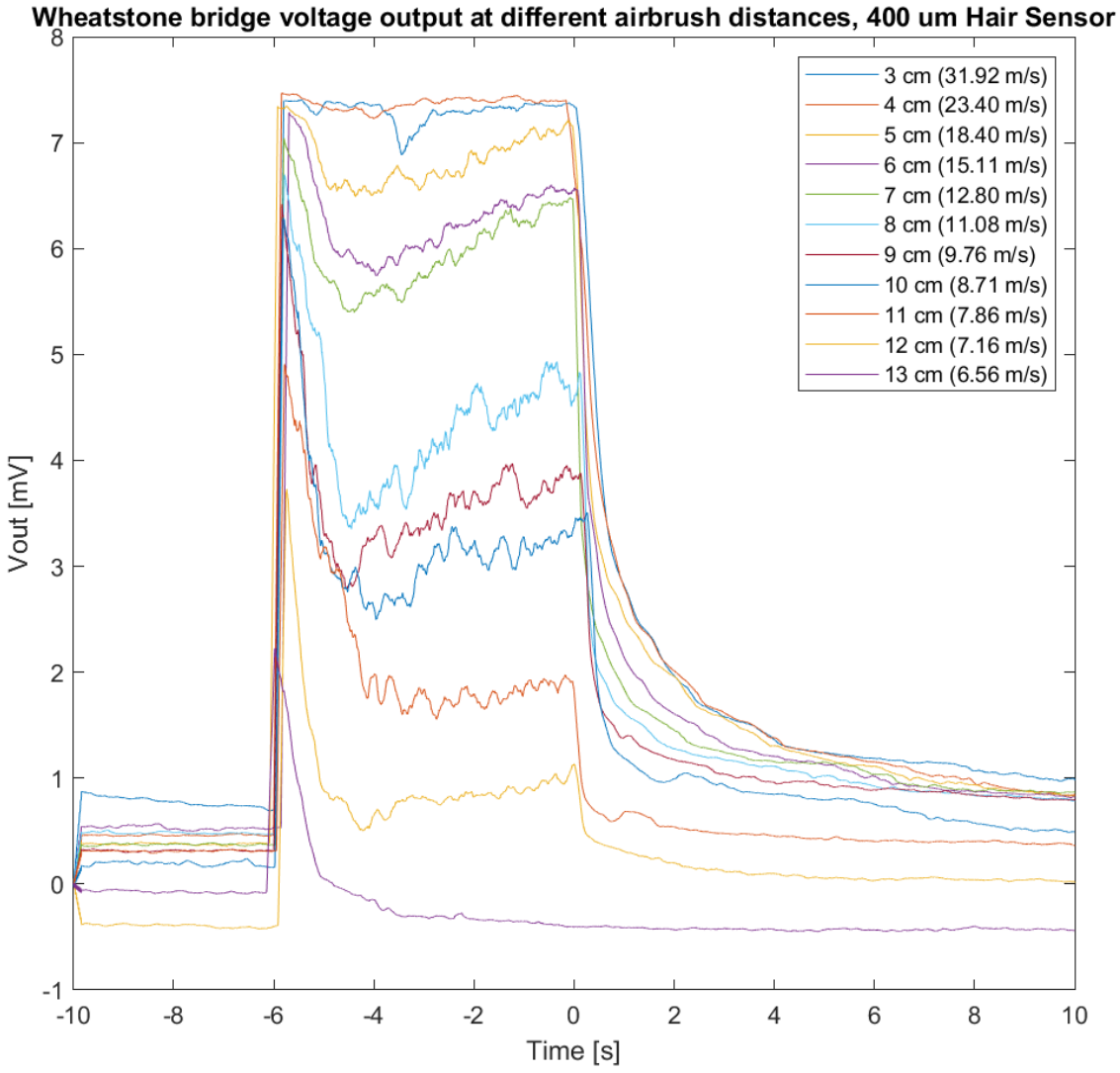

Figure 5.15: Voltage output measured at the output of a Wheatstone bridge using the 400µm hair sensor. Measurement taken with oscilloscope in DC-coupling for several airbrush distances. Negative time axis values are an artefact of the oscilloscope.

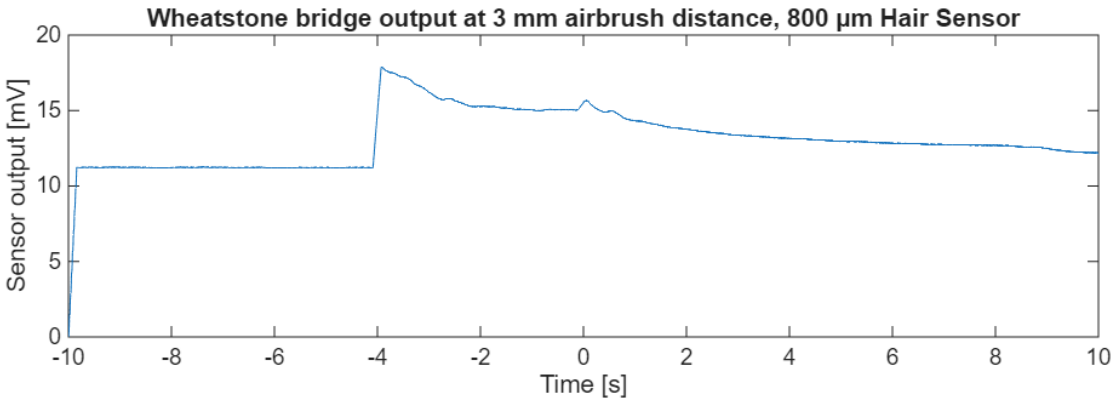

Figure 5.16: Voltage output measured at the output of a Wheatstone bridge using the 800µm hair sensor. Measurement taken with oscilloscope in DC-coupling for an airbrush at 3 mm distance.

5.4.2 Air compressor experiments

The next logical step from an airbrush is the use of an air compressor. It was attempted to use it without moving it back and forth like the airbrush and using variable pressures at the output but to no avail. Therefore, it was decided to use it similarly as with the airbrush, moving it at different distances. As the on and off was not on the outlet, this allowed at least to remove the uncertainty of pressing the nozzle and displacing it every time. The airflow output at different distances from the outlet of the Einhell Power X-Change PRESSITO air compressor was measured using a hot-wire anemometer similarly to the airbrush, Figure 5.17.

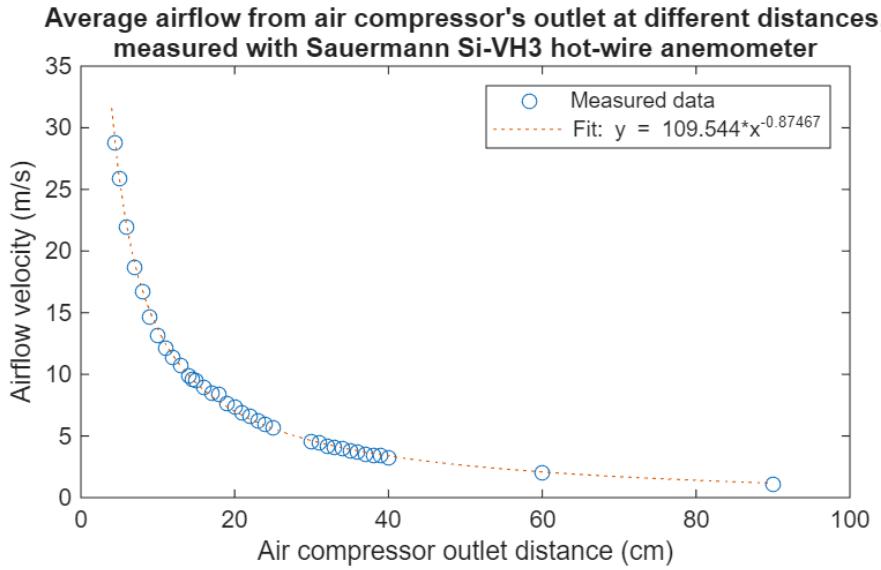

Figure 5.17: Average airflow velocity output of the air compressor's outlet at different distances from the hot-wire anemometer.

The same 400 μm thick sensor tested in Figure 5.15 sensor was tested using the oscilloscope and Wheatstone bridge as in the last few experiments conducted with the airbrush. To smooth the sensor's raw signal a 4th-order Butterworth 10 Hz low-pass filter was applied to the sensor's response, and it is plotted in Figure 5.19. The response seems to have a reduced overshoot and lower increasing trends while the air compressor was on. Nevertheless, it is hard to discriminate each curve when put together, this would make characterization much harder to understand what each voltage level means in terms of airflow velocity. It was decided to improve the response using an instrumentation amplifier (INA) at the output of the Wheatstone bridge, Figure 5.18. The improvement in sensitivity given by the Whetstone bridge has been described in section 2.4.3, and the instrumentation amplifier is used to amplify the resistance changes and make them more discernible. Texas Instruments INA126 was decided as the amplifier as it allows to either just use the internal gain of 5 or, by just applying one resistor between pin 1 and 8, increase the gain up to 10000 [187]. The results collected with the amplifier using the internal gain of 5 is shown in Figure 5.20. The response seems noisier, and while on the lower end it seems easier to discriminate the curves for different levels, at higher levels it is still hard. At this point it was decided to use a higher gain, but before it could be applied, in an attempt to reconnect the sensor to the circuit, the base of the sensor snapped and broke the sensor entirely. This is what drove the creation of the cableless design described in section 5.1.3.

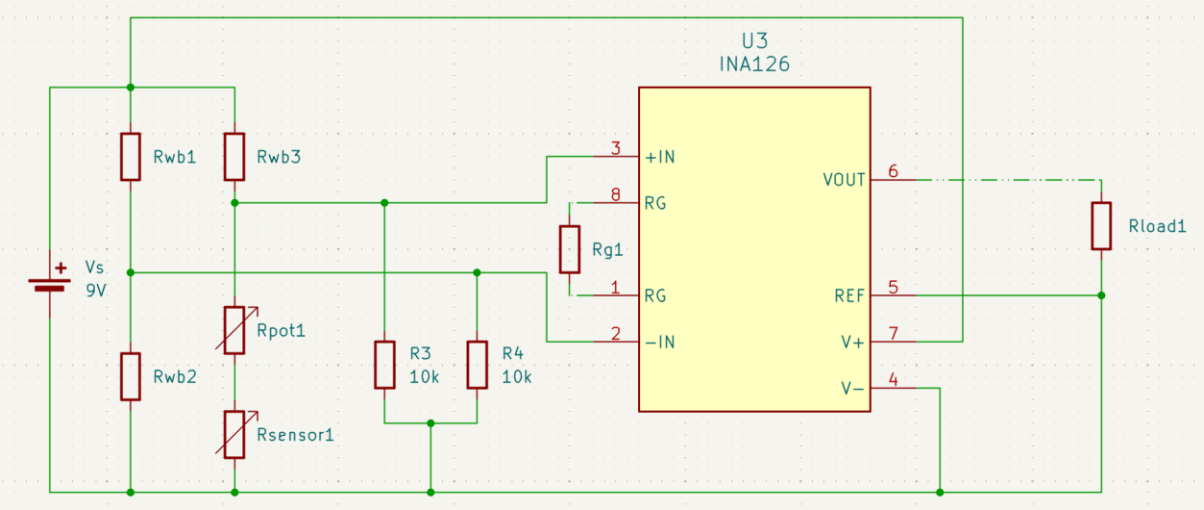

Figure 5.18: Circuit diagram used to test the artificial hair sensor (Rsensor1). Rload1 represents the oscilloscope used to record the output data. Vs is a bench-top variable voltage source.

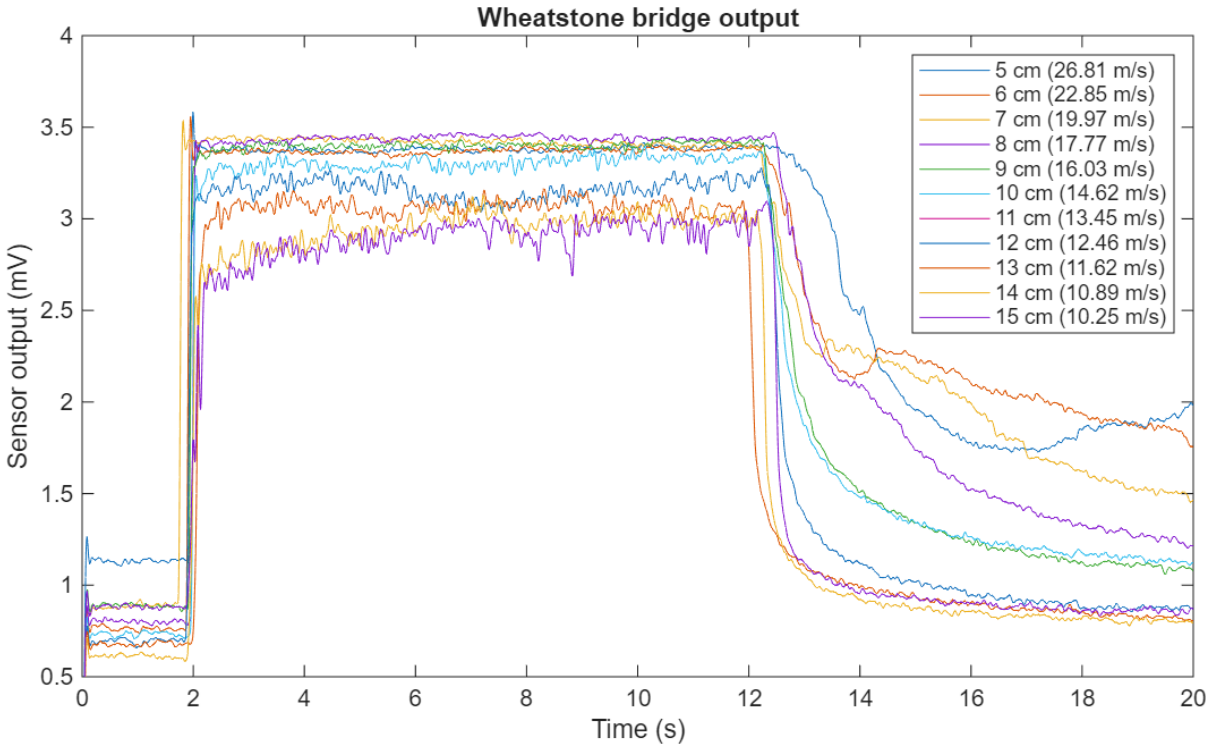

Figure 5.19: Response of 400 µm thick sensor using an air compressor at different distances. Output collected at the Wheatstone bridge output. The legend contains the distance of the air compressor's outlet and the equivalent airflow velocity calculated using the fit curve of Figure 5.17.

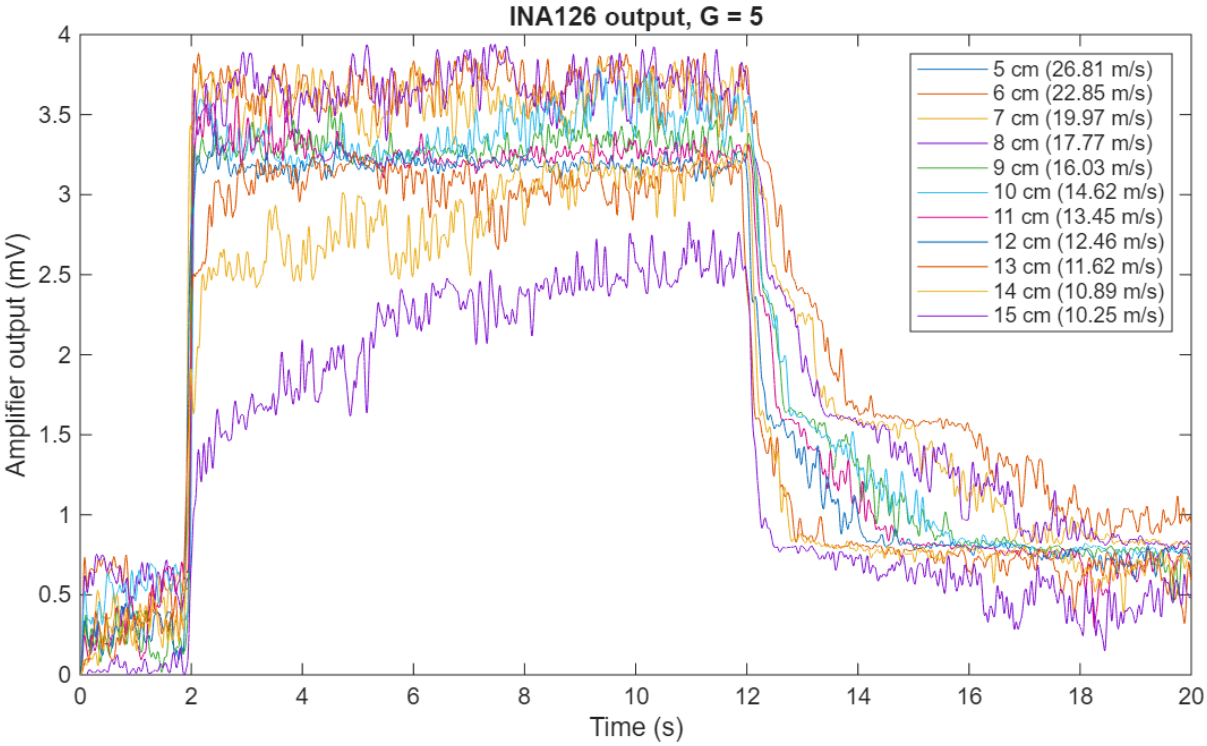

Figure 5.20: Response of 400 µm thick sensor using an air compressor at different distances. Output collected at the INA126 instrumentation amplifier output. The legend contains the distance of the air compressor's outlet and the equivalent airflow velocity calculated using the fit curve of Figure 5.17.

Once the cableless design was developed there was the issue of having a batch of sensors already coated but not readily available to being used with the cable holder (Figure 5.5). To not waste them it was decided to cut the front of the base of the sensors (Figure 5.3) using a small sharpening tool (MaAnt D1), to render them similar to the design of Figure 5.4. After carefully cutting the front section of the base, Agar's silver paint was used to make the sides conductive and render these sensors usable with the cable holder. Before attempting to test new sensors with the new design there was an attempt at increasing the gain of the INA126, but it seemed like no matter what resistance was placed between pin 1 and 8, the output of the amplifier became erratic. It seemed like the absence of a virtual ground for the amplifier was the reason for the bad response with gain resistors. This pushed to develop an overall better conditioning circuit (Figure 5.21). This circuit separated the voltage sources for the Wheatstone bridge and the amplifier to reduce any crosstalk noise and avoid saturations when the amplifier

gain was increased above 5. Moreover, the common-mode and differentiation filters helped removing electromagnetic interferences and other high-frequency noise sources.

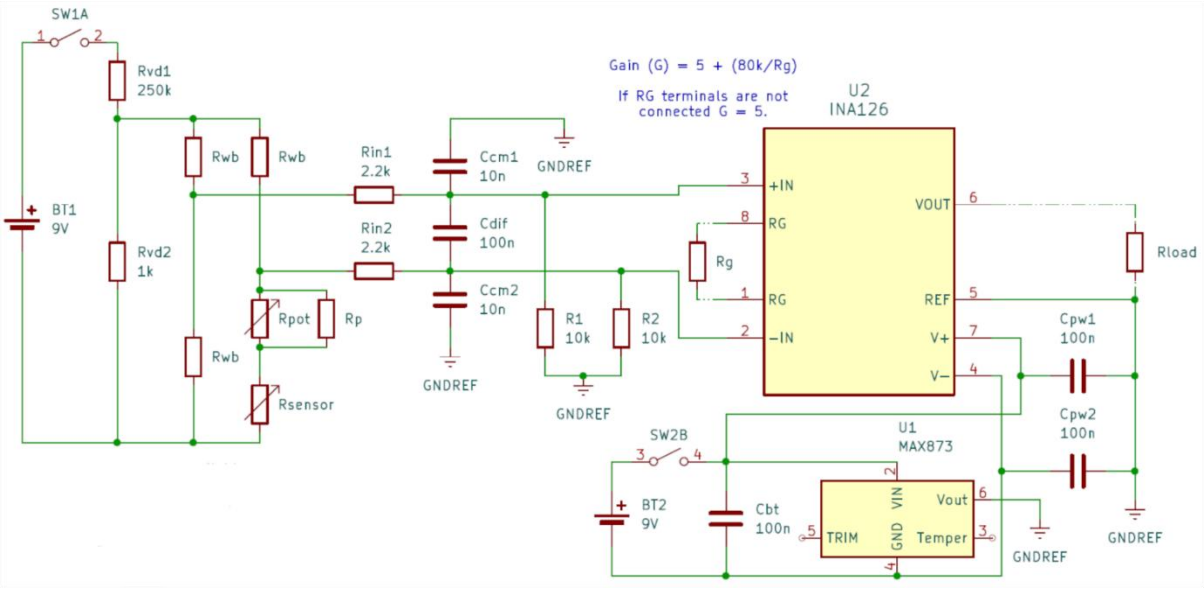

Figure 5.21: Circuit diagram used to test the artificial hair sensor (Rsensor). Rload represents the oscilloscope used to record the output data. Image first presented in [183].

At the output of the first battery, a voltage divider is used to reduce the voltage from 9 V to 36 mV. This was done because higher voltages increased the resistance of the sensor beyond the measurable range. The bridge's resistors, R_{wb}, were selected to be as close as possible to the base resistance of the sensor, R_{sensor}. To increase the sensor's resistance up to a similar value to the bridge's ones, a potentiometer, R_{pot}, with a parallel resistance, R_p was applied. The parallel resistance is placed to limit the range of the potentiometer. The output of the bridge is connected through a differential and common-mode filter to an instrumentation amplifier INA126. The common-mode and differential and filter's cut-off frequencies, f_{cm} and f_{dif}, are given by

$$f_{cm} = \frac{1}{2\pi R_{in1} C_{cm1}} \tag{5.1}$$

$$f_{dif} = \frac{1}{2\pi (2R_{in1}) \left(C_{dif} + \frac{1}{2} C_{cm1} \right)} \tag{5.2}$$

The input resistors and common-mode capacitors must be equal, $R_{in1} = R_{in2}$ and $C_{cm1} = C_{cm2}$. Moreover, the differential capacitor is sized at least ten times the common-mode capacitor, $C_{dif} \geq 10C_{cm1}$. In this case the differential and common mode filter have a cut-off frequency of 344.49 Hz and 7.23 kHz, respectively. The gain, *G*, of the INA126 is calculated as specified in its datasheet [187] by

$$G = 5 + \frac{80000}{R_G} \tag{5.3}$$

The gain resistor (R_g) used for the INA126 was 150 Ω, resulting in a gain of ~538. A MAX873 was used to create a virtual ground reference. The change in resistance of the sensor can then be detected as a change in volts at the output of the INA126. A Tektronix DPO2014 oscilloscope was used to collect the voltage output of the circuit. The oscilloscope was then connected to a laptop to collect the signal using the TekScope Utility software. The room's electromagnetic interference was filtered with the oscilloscope's low-pass filter using a 60 Hz cut-off frequency. The oscilloscope was set at 4s/div for the x-axis and the y-axis was varied between 1 V/div and 200 mV/div to get optimal measurements. The results of the sensor with spring and hair 600 μm thick and a platinum layer of 112 nm are shown in Figure 5.22 and Figure 5.23. Compared to the 400 μm sensor (Figure 5.20) most of the sensor's responses are more easily distinguished from one another. Most likely this is given by the much higher gain. Still, it is hard to discriminate a proper output for each airflow. This is likely given as well by the presence of inaccuracies in moving the compressor's outlet.

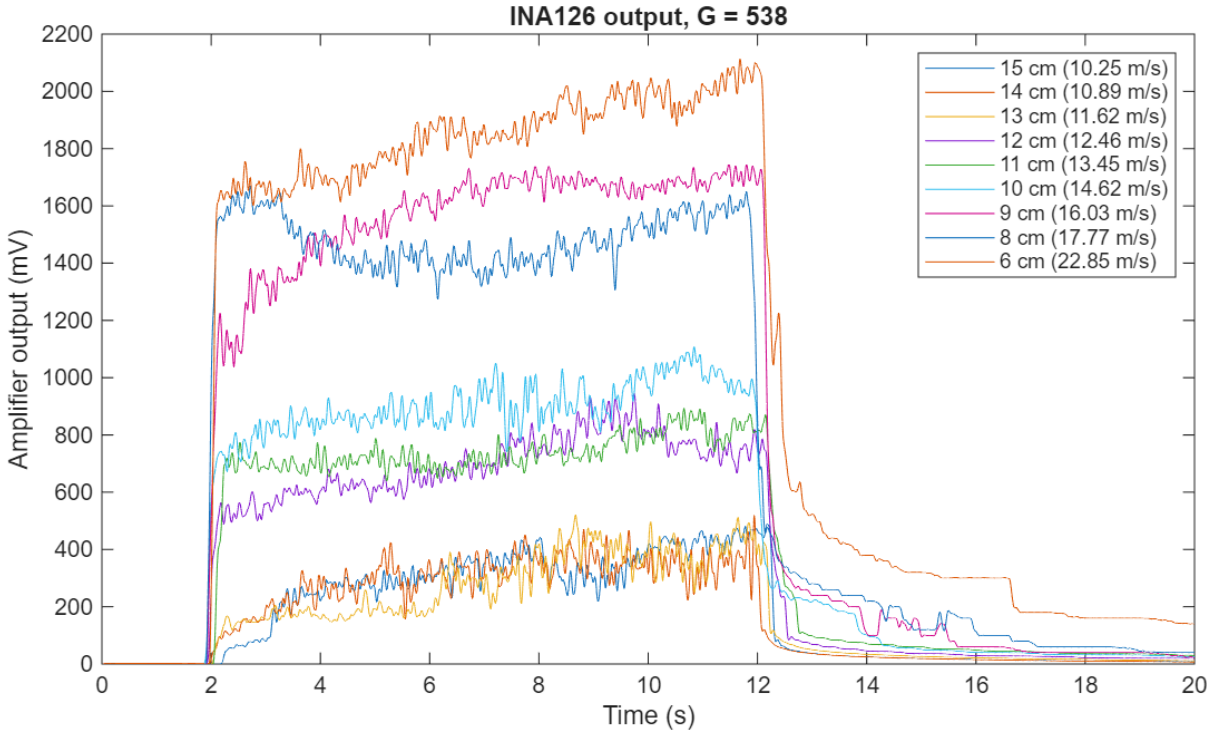

Figure 5.22: Response of 600 µm thick sensor using an air compressor at distances between 15 cm and 6 cm. Output collected at the INA126 instrumentation amplifier output. The legend contains the distance of the air compressor's outlet and the equivalent airflow velocity calculated using the fit curve of Figure 5.17.

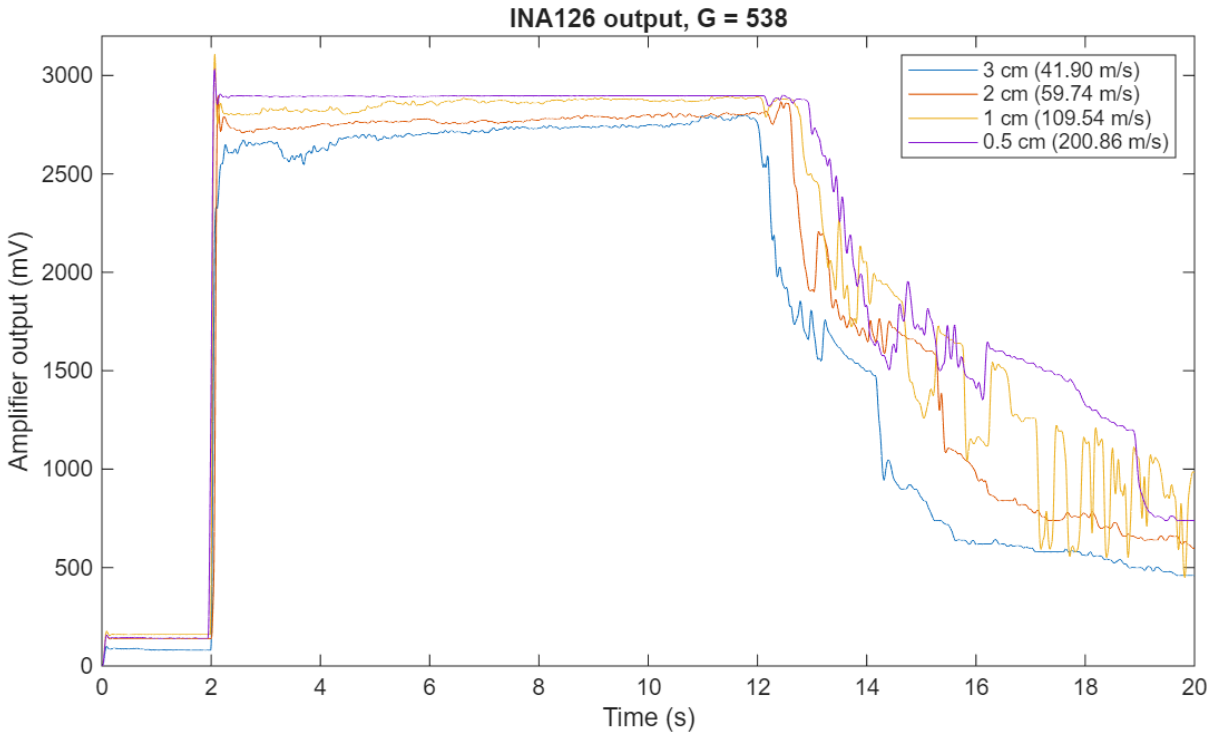

Figure 5.23: Response of 600 µm thick sensor using an air compressor at distances between 3 cm and 0.5 cm. Output collected at the INA126 instrumentation amplifier output. The legend contains the distance of the air compressor's outlet and the equivalent airflow velocity calculated using the fit curve of Figure 5.17.

Figure 5.23, arrives at measuring an estimate of 200 m/s when the compressor's outlet is at 0.5 cm distance from the sensor. At this distance the sensor would reach the back plate of the cable holder and basically saturate mechanically. If we take the lower range suggested by Figure 5.22, ~11 m/s, and this upper range value, ~200 m/s, it seems clear that the sensor is in theory capable of sensing a wide range of airflow velocities. Albeit this upper range value could be too high since there was no appropriate reference, and it was estimated by the anemometer's fit curve; it is still indicative of the wide range the sensor could be capable of sensing.

5.4.3 Wind tunnel experiments

To improve the airflow conditions when testing the sensors it was decided to use a wind tunnel instead of having the outlet of an airflow source move. An Armfield C2 subsonic wind tunnel was used to test the sensor under different speed conditions. The wind tunnel's motor can be set between 15 RPM and 1650 RPM. At 1650 RPM the motor takes 8 seconds to reach maximum speed, and it takes another 8 seconds to return to rest. A Sauermann Si-VH3 hot-wire anemometer was used to measure the air flow velocity. To hold the sensor a plate similar to Figure 5.5b was printed with a cylinder at the bottom that could fit a 4 mm metallic rod. A tool holder arm was used to hold the metallic rod with the sensor and the anemometer inside the wind tunnel. The sensor and the hotwire anemometer were positioned at the same height, with the sensor offset by 1 cm behind and 1 cm laterally from the anemometer (Figure 5.24). This is to ensure maximum reliability from the hotwire anemometer as a reference, but, at the same time, to not cover or disturb the airflow measured by the sensor. All the experiments were conducted in a temperature-controlled room, and the Sauermann Si-VH3 hot-wire anemometer was used to measure the temperature as well. The temperature during the experiments at all speeds remained controlled at around 22.8 ˚C. The first sensor to be tested in the wind tunnel was an artificial hair sensor (AHS), with spring and hair 600 μm thick and a platinum layer of

155.9 nm. The gain resistance for the circuit in Figure 5.21 was changed to 15 Ω, to increase the gain to ~5338.

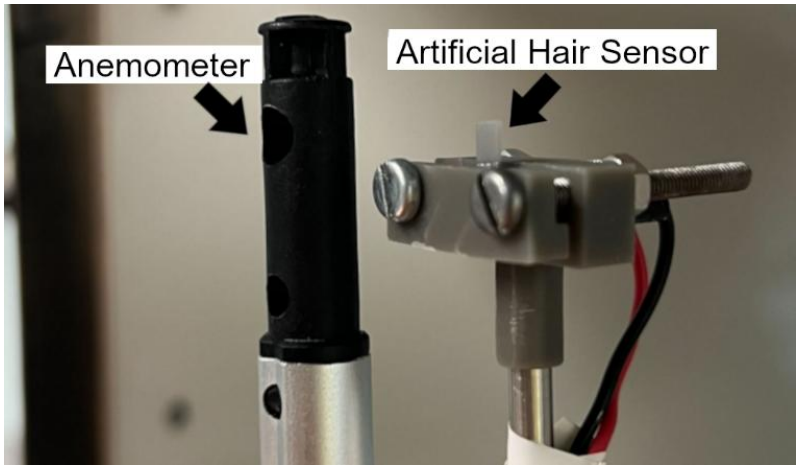

Figure 5.24: Picture of anemometer and hair sensor in the wind tunnel. Image first presented in [183].

5.4.3.1 Characterization of the sensor's response

Measurements were taken in steps of 100 RPM, starting from 1600 RPM downwards. Considering this, the wind tunnel allows for a range of measurements between >1 m/s and 22.3 m/s. Figure 5.25 shows an example comparison of the anemometer airflow signal and the AHS signal at 1600 RPM. Since the anemometer outputs results at 1 sample per second, in order to properly compare it to the AHS one, Figure 5.25 shows both its raw output, at 31250 samples per second (SPS), and its output averaged every one second. To smooth the sensor's raw signal a 4th-order Butterworth 10 Hz low-pass filter was applied to the sensor's response.

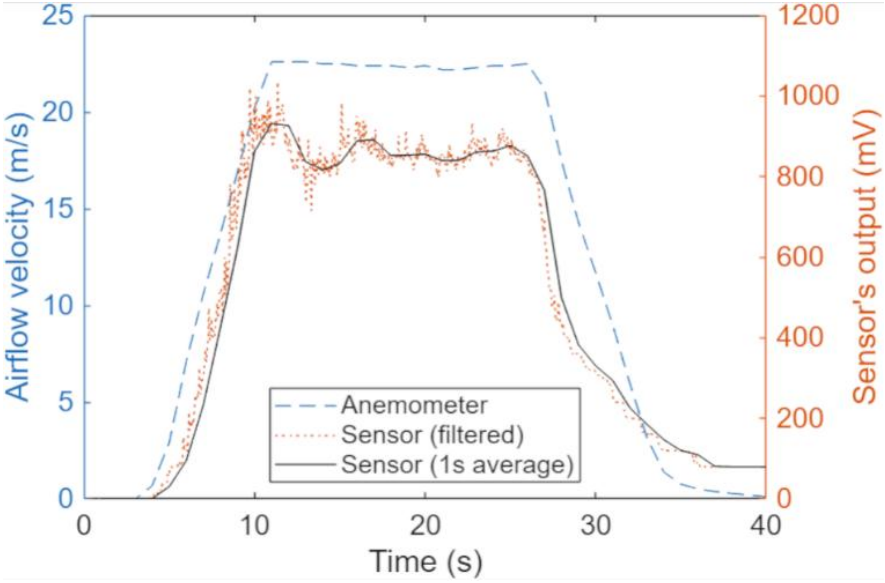

Figure 5.25: Response comparison between the anemometer and the 3D-printed AHS with the wind tunnel's motor speed set at 1600 RPM. Image first presented in [183].

The anemometer's readings were averaged (for the ~15 seconds the wind tunnel was on) to establish a reference value of airflow velocity per wind tunnel's motor speed. Similarly, the sensor's readings were first smoothed with a 10 Hz low-pass filter and then averaged to characterize the voltage level for each reference airflow velocity. Figure 5.26 shows the characterization of the sensor. Figure 5.27 shows the 1 second averaged response of the sensor for all the wind tunnel's testing conditions.

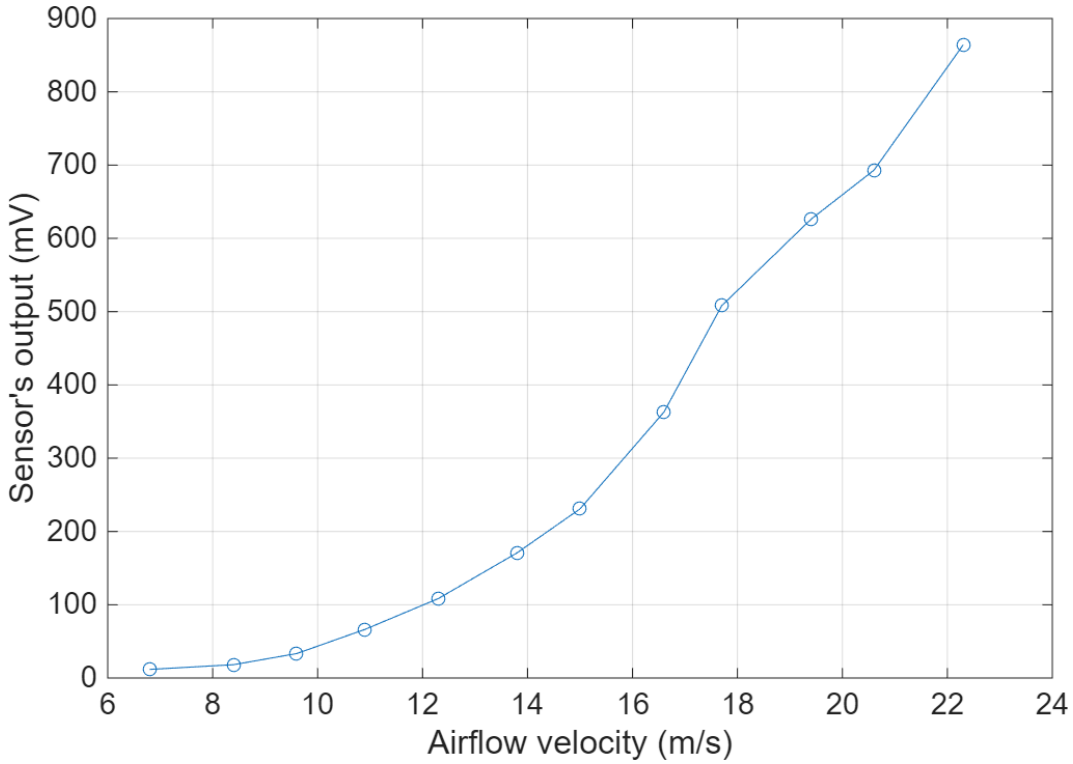

Figure 5.26: 3D-printed AHS characterization.

The sensor shows a non-linear response, which was expected since the sensory part is essentially a strain gauge, which are known for their non-linearity. The smallest airflow velocity that the sensor was able to sense was at 6.8 m/s (motor speed at 500 RPM). The sensor was able to measure up to the upper limit of the wind tunnel (22.3 m/s), but at that velocity the sensor was still not saturated to its maximum level. It was noticed in past experiments that the upper limit of these AHS was when bent up to the point that the hair shaft would touch the back screw plate (Figure 5.5b). Further testing will be required with stronger airflow velocity to understand the real upper limit the sensor is able to sense. The sensor's natural frequency has been studied using a Thor Labs TA0505D024W piezoelectric to make the sensor vibrate and a Polytec MSA-100 3D Laser Doppler Vibrometer to investigate its displacement. The piezoelectric was firstly used to produce a 0-50 kHz frequency sweep at 10 V and then repeated at with sweeps at 0-5 kHz. The natural frequency of the AHS is found at 550 Hz, which is above airflow velocity variations. Therefore, the natural frequency of the sensor does not impact its dynamic response.

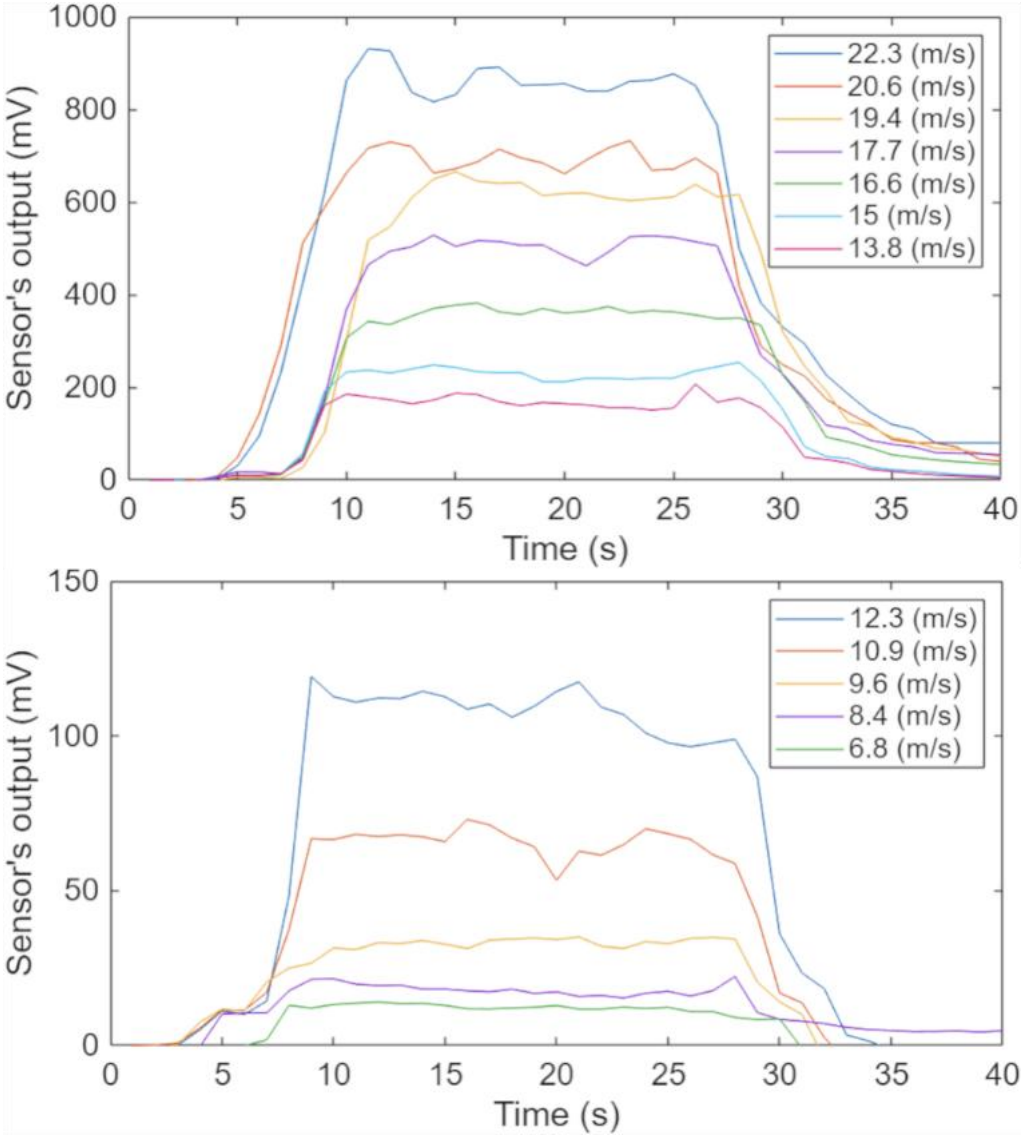

Figure 5.27: Sensor's response averaged for 1 second for all the different wind tunnel's testing conditions. Image first presented in [183].

5.4.3.2 Error Analysis of the sensor's response

To fully understand the sensor response an error analysis was conducted for its response. This section makes use of the previously conducted characterization and compares it to the filtered response, and for different averaging windows. Table 5.3 shows the average maximum, average minimum and absolute average amongst all airflow velocity for raw filtered signal, and for averaging windows that would be equivalent to measurements every 10 ms, 100 ms, 500 ms and 1 s.

Table 5.3: Artificial Hair Sensor error analysis for diverse averaging conditions. Table first presented in [183].

Averaging window size (samples)	Averaging window time equivalent	Average minimum error	Average maximum error	Absolute average error
Not averaged	32.5 µs	-40.54 %	21.59 %	0.75 %
313	~10 ms	-39. 14 %	21.48 %	0.75 %
3125	100 ms	-25.83 %	16.62 %	0.62 %
15625	500 ms	-14.56 %	11.03 %	0.49 %
31250	1 s	-13. 89 %	9.00 %	0.67 %

It is clear that the average minimum error decreases the most with averaging. This high likely due to the fact that in the measurement for motor's speed 800 RPM (10.9 m/s), there were four glitches produced by the oscilloscope. The applied filter helped in reducing the amplitude of these glitches but not eliminate them entirely. It was decided to not correct these glitches in post-processing since they could repeat with every signal acquisition method and proper mitigation should be part of the signal acquisition process. Moreover, for measurements at low airflow velocities the metallic rod supporting the sensor was subjected to high vibrations, and only big window sizes could properly smooth this error out. It is highly likely that the error in all cases would be smaller if the experimental conditions were improved. Another important consideration is that as the airflow velocity was reducing, the resolution of the analog to digital converter (ADC) of the oscilloscope was increasing. Of course, this would also contribute to having a higher error for lower speeds. Averaging the output of the sensor can help in increasing its precision, but at the cost of the time response. Hence, accurate analysis per specific application needs to be conducted on what is the best averaging to use. An interesting observation that can be made from Table 5.3 is that averaging every 500 ms yields, on average, more accurate results than averaging every 1 s, which indicates the noise is non-linear in nature.

5.4.3.3 Sensor's directionality

The sensor was tested with a precision rotary stage at different angles. The tests were made between 0˚ (AHS facing the airflow source) and 90˚ (AHS perpendicular to the airflow source) in steps of 10˚. The testing was conducted at 11.25 m/s for 10 seconds and averaged for the plot in Figure 5.28. The data was normalized for the measurements taken at 0˚, meaning that a value of 1 represents the full speed measurement and 0 means the sensor is at rest. The sensor shows sensitivity in one direction, with an approximative figure 8 response, which is expected for this type of sensors. This suggests that using more than one sensor, facing different directions can be used to extract airflow directionality information. Further work needs to be conducted in this regard.

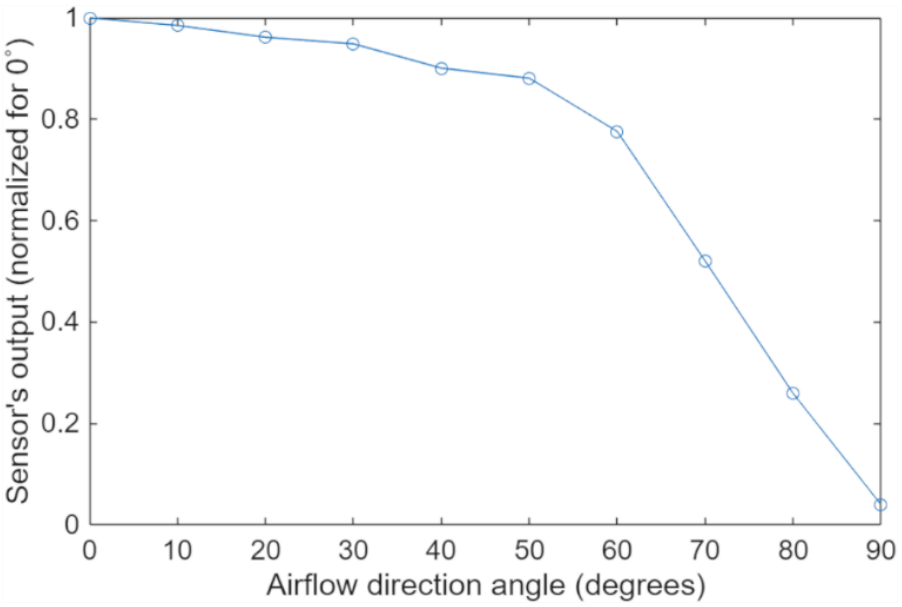

Figure 5.28: Directional response of AHS at 11.25 m/s. Measurements taken between the sensor facing the airflow source direction (0˚) and the sensor perpendicular to the airflow source (90˚). Values normalized for the response at 0˚. Image first presented in [183].

5.5 Conclusions and Future Work

A 3D-printed airflow artificial hair sensor inspired by the flat trichobothria of the adult *Buthus occitanus* scorpion has been successfully manufactured using DLP. It offers a wide range of measurements, the use of wind tunnel and a 600 µm thick hair sensor suggests a lower

limit of 6.8 m/s, and an upper limit >22.3 m/s. The upper limit needs to be further studied to fully understand the sensor's capabilities. The sensor has been characterized, and it was shown that the absolute average error remains <1% for different averaging window sizes. Other, less precise and reliable, experimental setup suggests upper limits of even 200 m/s for this sensor structure, and maybe higher for thicker sensors. Possibly, thinner sensors can sense weaker winds.

5.5.1 Further study for the sensor's response

Even though a sensor that works was produced more studies need to be conducted on this structure.

- It is possible to differentiate measurements with 1 m/s difference, but further studies are required to understand its **sensitivity** and the smallest measurable change in airflow. This is particularly important due to the non-linear response of the sensor.
- As already mentioned, studies need to be conducted to understand the real **upper range** of this sensor, i.e., what is the strongest wind it can measure. Since they were limited by the used wind tunnel, and the other experimental set-ups were not as reliable.
- Improvements in the **signal conditioning** are required. The Wheatstone bridge used in this project is unbalanced and does not reject temperature errors. The sensitivity and accuracy will also depend on averaging window size, ADC and acquisition circuit, more study needs to be done in this regard.
- **Directionality** should be investigated further. Section 5.4.3.3 shows that the sensor has directionality in at least one direction. Albeit this was a response from 0˚ to 90˚, we can expect an equal response going to -90˚. In past experiments using the air compressor, it was noticed that a response occurred in the opposite direction when the Wheatstone bridge was not properly balanced. In that case the voltage was reducing instead of increasing. Further

investigations therefore need to be conducted on the directional response when the flow is hitting the hair from the back (the face opposite to the platinum coating). To do this the conditioning circuit needs to be modified to allow for a negative voltage source. This will allow the response to go down when the AHS is hit with an airflow from the back.

- **Mechanical testing** needs to be performed to better understand the sensor response from e mechanical point of view.
- **Perform a reproducibility study** to fully understand if there is variability in the response of the sensors that have the same geometric structure and printing process. This will allow to have a statistical understanding of the sensor's response.

5.5.2 Material and fabrication improvements

The total **print time**, including the time for changing materials, is 40 minutes when an operator changes the tray. The Asiga Composer software estimates that the **material cost** to print 44 sensors is between $0.18 and $0.36. Reducing the size of the base would allow for lower cost per sensor and more sensors to be printed at one time, but they would be harder to handle. Still, more research needs to be done in this direction, including an improved cost analysis, and the creation of an automated system that can reduce the print time.

The use of DLP allows 3D-print smaller and thinner sensors, or bigger and thicker sensors. All these variables will affect the sensitivity and acquisition range of the singular sensor. Understanding the impact of these **geometrical variations** is of course another interesting avenue for further work. Increasing or decreasing the thickness of the sensor changes its stiffness, therefore in theory it is possible to create an array of sensors with wide sensitivities and range. Another possibility is to use two sensors at 90 degrees from each other to provide directionality of measurement. Investigating the different array configurations, and their signal handling, is of great importance for this project.

Coating the sensor's spring with platinum greatly affected the response of the sensor. To have a lower base resistance the platinum layer had to be thicker, and a thicker layer meant increased stiffness of the sensor. It is worth **investigating alternative transduction** solutions, similarly to what already mentioned for the acoustic sensor in section **4.3**. Possible alternatives include piezoelectric 3D-printable hydrogels [170, 171], laser induced graphene [172], and UV-curable conductive resins [173-175]. Moreover, in the last year platinum prices have increased greatly, thus, different solutions could reduce the cost of manufacture of each sensor as well. Lastly, the properties of a sputter coated layer of a certain material differ from the bulk material ones, making finite element analysis or any computational simulation challenging.

5.5.3 Applications

This sensor can prove useful for several **applications**, from biomedical respirators to autonomous robotics, and from simple single point airflow measurements to wide area flow cameras. Each application needs to study the use of this sensor appropriately. Additionally, coating this sensor with protective materials could allow it to also work **underwater** or in other fluids, therefore, with further study, the sensor's application possibilities can be increased further.

6

Investigation of airflow behaviour around hair-like sensors (Université de Tours Exchange)

"Great discoveries and improvements invariably involve the cooperation of many minds."

Alexander Graham Bell

As it has been said multiple times in this work, DLP-based 3D printing offers the compelling possibility of fabricating sensor arrays within one structure, highlighting its potential for integrated design applications. This has been one of the goals of this project and is one of the most important directions for future work. One issue in integrating arrays would be the correct placement and distancing of the sensors within the same structure. In order to understand better the sensor's boundaries for array applications it is important to learn the airflow behaviour around the hair shaft. This allows us to gain an understanding about the boundary layer of the sensor and consequently give us more information about the minimum distancing required in an array. This part of the research project has taken place at the Université de Tours in Tours, France in collaboration with two entomologists, Jerome Casas and Thomas Steinmann. The research was allowed by the particle image velocimetry set-up at the Université de Tours (described in **3.7.1 Air flow around the sensor – Particle Image Velocimetry**). The focus of the research was to use the PIV system to assess how COMSOL simulations need to be reliably setup for airflow testing and boundary layer considerations. Therefore, comparing simulation to experiments to account for unmodeled mechanisms that might show in the real-world.

This chapter will discuss the research conducted in Tours, present the results collected there, describe the COMSOL simulation set-up and, lastly, discuss possible future work. The research was conducted shortly-after the acoustic sensor was confirmed to mechanically discriminate different acoustic frequencies (**4.2.2.1 Mechanical response**). Alas, it was not possible to repeat this research at a later stage for the airflow sensors (Chapter 4) once they were developed. Nevertheless, future directions about repeating these experiments for the airflow sensors will be discussed. The research discussed in this chapter has never been published in any conference or journal paper.

6.1 COMSOL Airflow Simulation

The COMSOL Airflow simulation made use of the *Laminar Flow* module. Earlier simulation coupled it with the *Solid Mechanics* one, but it did not make a difference in results for the purpose of this project, and instead only increased the computational power required. Therefore, to reduce the simulation time, only the aforementioned flow module was used. The *Laminar Flow* module computes the velocity and pressure fields for a single-phase fluid in the laminar flow regime; in this case it was used to simulate the flow of air. This module solves the Navier-Stokes equations for conservation of momentum and the continuity equation for the conservation of mass [188]. Figure 6.1 shows the way the model is set up. The sensor is inside a "box" of air, all the faces of the box have been selected as an inlet, with the velocity field $0.05 \sin(t2\pi f_{flow})$ in the X-axis, where t is the time step, and f_{flow} is the frequency of the applied flow; similar to the frequency applied to the speakers in the PIV set up (described below). The surfaces of the sensors were selected as part of the Wall, as well as the bottom face of the air "box". The upper left point of the air "box" was selected a Pressure Point Constraint to act as reference pressure point.

Simulations were run in the time domain, from point zero to $1000/f_{flow}$ with a step of $10/f_{flow}$. The velocity line results compared and discussed later in this chapter were exported at a set plane around the hair. The horizontal plane was relative to the z-coordinate, or the height of the artificial hair (Figure 6.2a). Meanwhile the vertical plane went through the y-coordinate, or the width of the artificial hair (Figure 6.2b).

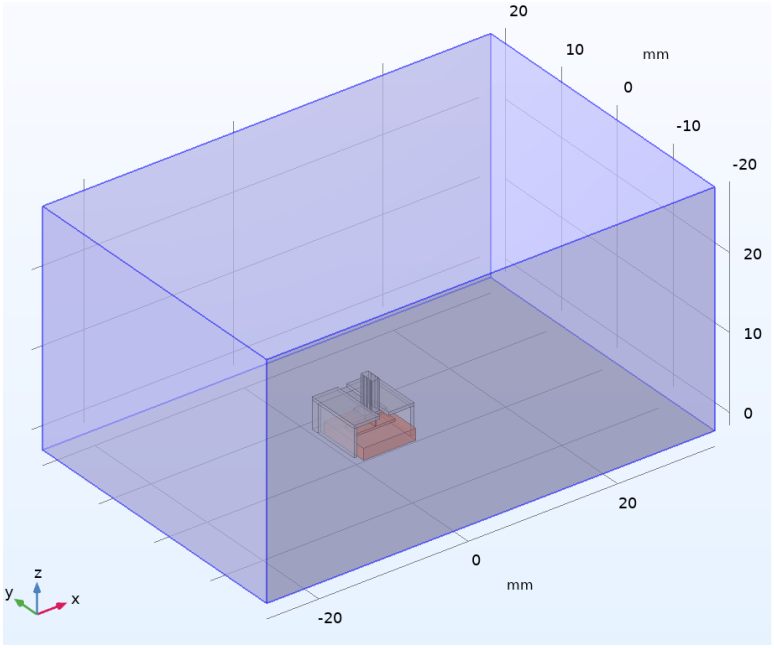

Figure 6.1: COMSOL set-up for laminar flow simulations.

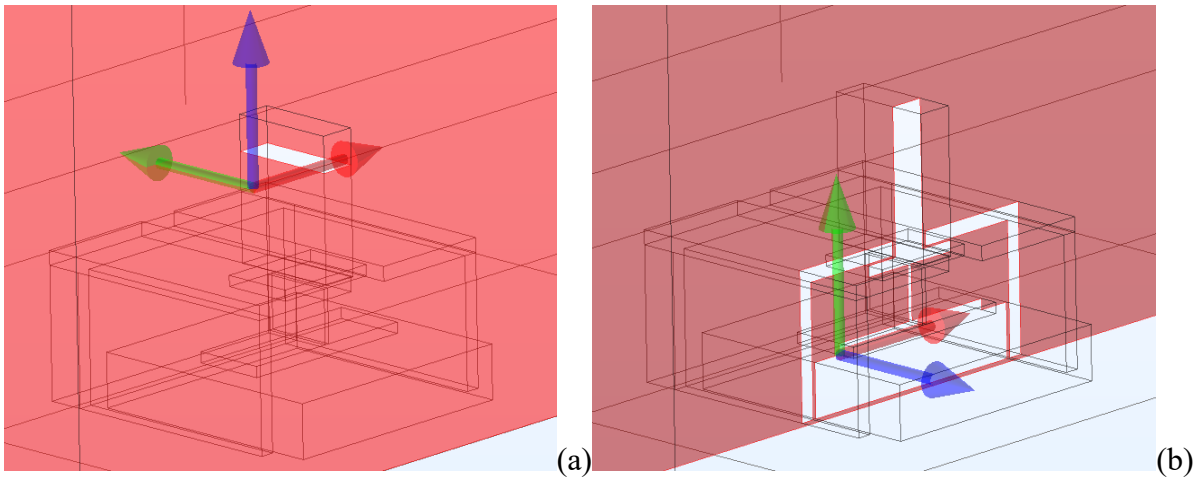

Figure 6.2: Visual representation of horizontal (a) and vertical (b) planes used to export airflow velocity data from COMSOL.

6.2 Particle Image Velocimetry Experimental Setup

Given the limitations of the camera used in the PIV system in terms of resolution per capture speed, it was decided to mainly test the sensor labelled as "H4W3D1B1.5", the sensor design and geometry is presented in **4.2.2 Artificial hair inspired by the Hinged Trichoid Sensilla (HTS)**. This is an acoustic sensor with a squared hair shaft that is tall 4 mm, wide 3 mm and thick 1 mm. The spring at the bottom is 1.5 mm tall. The reason for choosing this sensor amongst the others is that it has a low enough resonant frequency (260 Hz) to be tested at its

resonant frequency, and at lower and higher frequencies. Nevertheless, given that the resolution of the PIV does not allow us to visualize the hair shaft movement at the resonant frequency, it was decided to test a sensor with a cylindrical hair shaft as well. The cylindrical hair is 4 mm tall and has a diameter of 1 mm. The spring is 1.5 mm tall. The resonant frequency of the cylindrical hair is around 500 Hz (above the systems limitations). The experimental set-up includes the following, and its schematic is shown in Figure 3.27.

- A pair of Kinyo DO29 speakers
- Rigol DG811 signal generator
- Sphynx E-SAT1 amplifier
- PIV system
    - High-speed camera Phantom Miro 310 [161] with Phantom software PCC for recording. The lens used was a 50mm macro lens(AF micro Nikkor; Nikon, Tokyo, Japan) with the focus set at 0.23 m which gave us a field of view of 17 by 15 mm at a resolution of 800 x 600 pixels.
    - Laser Keri Photonics MGL-F-532-2000-5 with PSU-H-LED power supply [189].
    - Scheppach AIR CASE 2L air compressor connected to the seeding device aerosol generator LaVision VZ-20 10 bar.
    - ImageJ software to convert camera's outputs in image sequences.
    - DaVis 10 as the PIV software for analysing the results.

The first experiments were conducted with only one speaker, but due to the poor results, under Dr. Steinmann’s suggestions, two speakers were used. The speakers were placed at the left and right of the sensor, and they were placed equidistant to each other. The speakers are connected out of phase. The signal is generated at the chosen frequencies from the Rigol signal generate at 5 V peak-to-peak and then amplified by the Sphynx amplifier (knob set at the 4th "click" that can be felt while turning the knob from zero). The sample is in a chamber that is

filled with gas using the air compressor. In this way the PIV can light with the laser the gas particles and capture them with the fast camera to visualize the flow of air. The squared sensor was tested at 100 Hz, 200 Hz, 264 Hz and 300 Hz, and the camera sampling time was set at 20 times the signal's frequency, well above the minimum Nyquist's frequency requirement. The cylindrical hair was not tested at 264 Hz. For the 300 Hz signal the peak-to-peak voltage from the signal generator was increased to 9 V as with lower voltages the air particle displacement was hardly visible. Due to the hair shaft's light grey colour, it was hard to visualize appropriately the hair with the PIV, therefore the hair and plates were painted in black. Experiments were conducted in two ways, with the sensor upright and the hair shaft facing the camera and with the hair tip facing the camera, Figure 6.3.

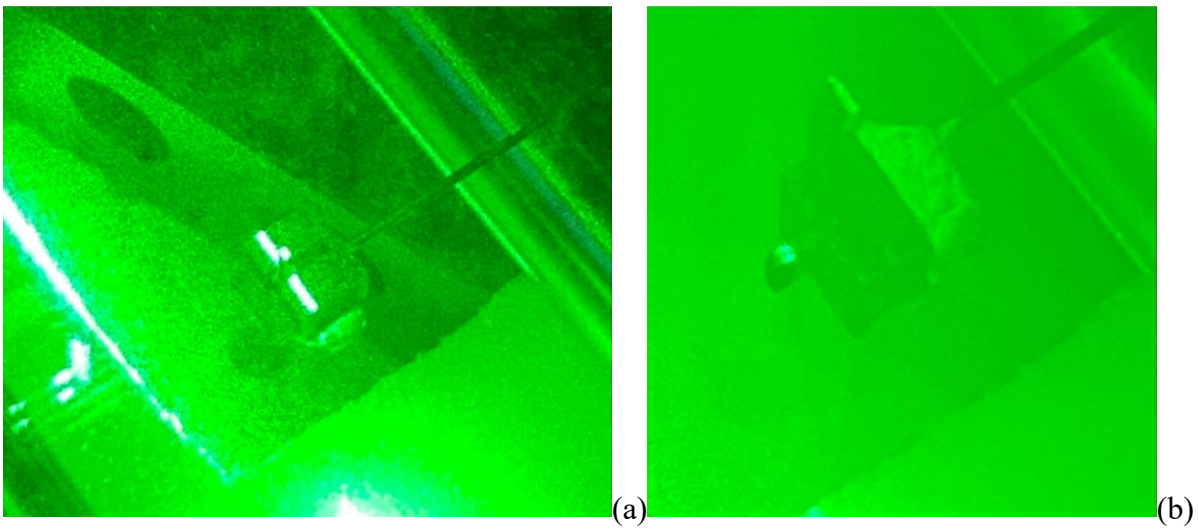

Figure 6.3: Photos of the sensor in the PIV experimental setup, being lightened by the laser sheet. Sensor upright with the hair shaft in the direction of the camera (a), and sensor at an angle to have the hair tip face the camera (b).

The video files are recorded in .tiff for around 1000 photos and then saved with the same extension as single images. This allows for import (once a correct time between pictures is set) in the PIV software. A rescaling is also done by taking as reference the thickness of the hair being 1 mm. Processing of the raw image data with DaVis consisted of extracting the velocity field from the pictures taken by the camera. The first step was the subtraction of the background noise resulting mainly from the reflection of the laser light by surrounding objects such as the

tank or the hair support. It allowed us to keep only the flowing particles. The scale length setting of the sliding background operation was 16 pixels. For the velocity analysis, we used a cross-correlation algorithm with multiple decreasing passes. The first pass used interrogation windows of 128 pixels with and overlap of 50 % and was followed by two passes with windows of 32 pixels and 50 % overlap, all with circular windows. A mask is created around the hair, the maximum expected displacement is 10 pixel (0.3 m/s), and the spatial resolution is set to 24 pixels. After this several plots are made of the velocity to first validate if the results as good or not and then to investigate them. The quality of the plot is based on the air particles moving at the correct frequency perpendicularly to the hair shaft, without harsh noise making the displacement go oblique upwards or downwards. Figure 6.4 shows a screenshot of how the DaVis 10 software shows the flow direction around the hair.

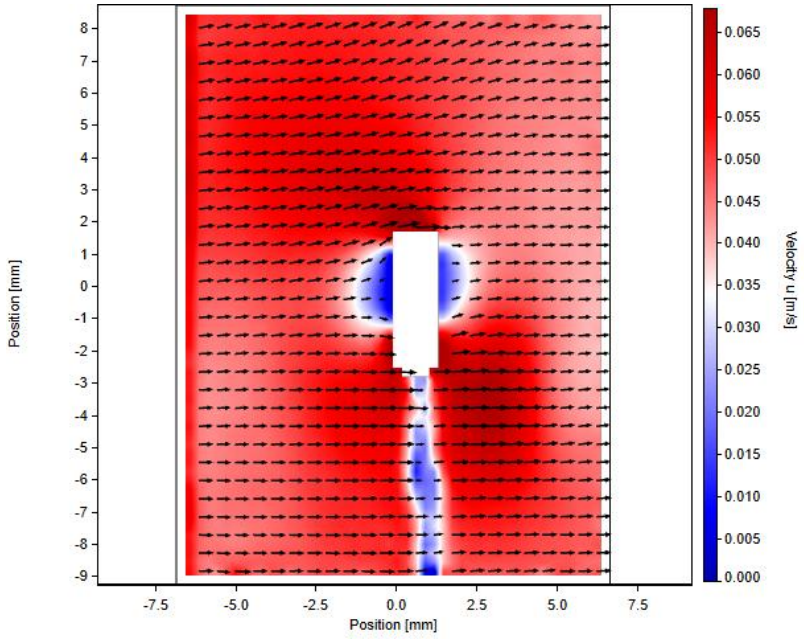

Figure 6.4: Airflow direction plot in DaVis 10 software based on data recorded with the PIV system.

From Figure 6.4 it can also be noticed one of the issues that were encountered when testing the sensor with the hair tip facing the camera, below the hair the sensor blocks the laser creating a shadowed area. Based on the sensor's location relative to the centre of the laser's light sheet this shadowing effect did not occur only below the sensor but on the sides as well. This issue

also presented itself when the sensor was facing the camera longitudinally, albeit it was not important for the bottom of the sensor, as this was blocked by the sensor's external case, it was problematic when shadowing occurred along the hair shaft. While better care in positioning the sensor reduced this issue, it is one of the problems to consider when comparing simulated and experimental results.

6.3 Comparison of COMSOL and PIV results

6.3.1 Data scaling

Given that the actual power of the speakers in the PIV system and the signal in COMSOL could not be perfectly matched scaling is required. Due to the shadowing issue explained in the previous section a scaling in the distance axis is needed as well. The following results state explicitly the scaling applied. Figure 6.5 shows an example of unscaled plot and a scaled one. The scaling of the x-axis is made by finding the location at which the velocity is 0 m/s (as this overlaps with the hair shaft location) for both COMSOL and PIV. Then the PIV data is scaled to match the COMSOL region at which the flow is zero (as COMSOL does not suffer from shadowing). In the y-axis the velocity data has been normalized to PIV range.

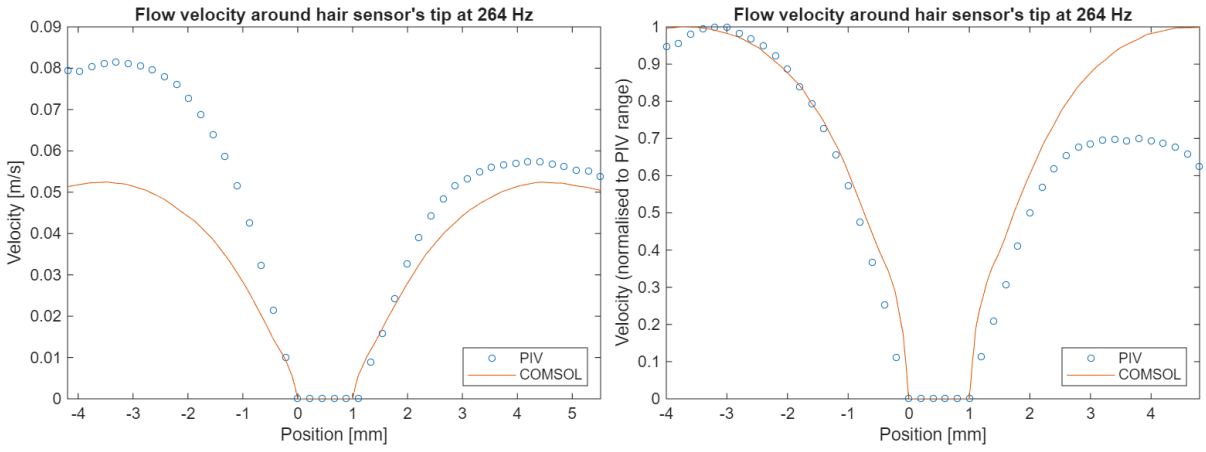

Figure 6.5: Flow velocity around the hair shaft at 264 Hz, comparison of PIV and COMSOL result. On the left the results have no scaling, one the right the results have been normalized.

One of the main issues when plotting PIV and COMSOL values is that it is hard to match the exact location at which the measurement is taken. The point where the laser sheet is, respective to the hair shaft is important, and different locations will yield different results. Moreover, the laser sheet is quite wide relative to the artificial hair size (Figure 6.3 shows this very clearly) so it is hard to compare these fixed result of the PIV to COMSOL where we can move the plane used for data extraction back and forth, even at nanometre scale. Therefore, the laser sheet was placed as close as possible to the edge of the tip when the tip was facing the camera, and as central to the hair shaft as possible when the sensor was facing the camera longitudinally. Then, the horizontal and vertical planes in COMSOL were moved slightly to try and match the data.

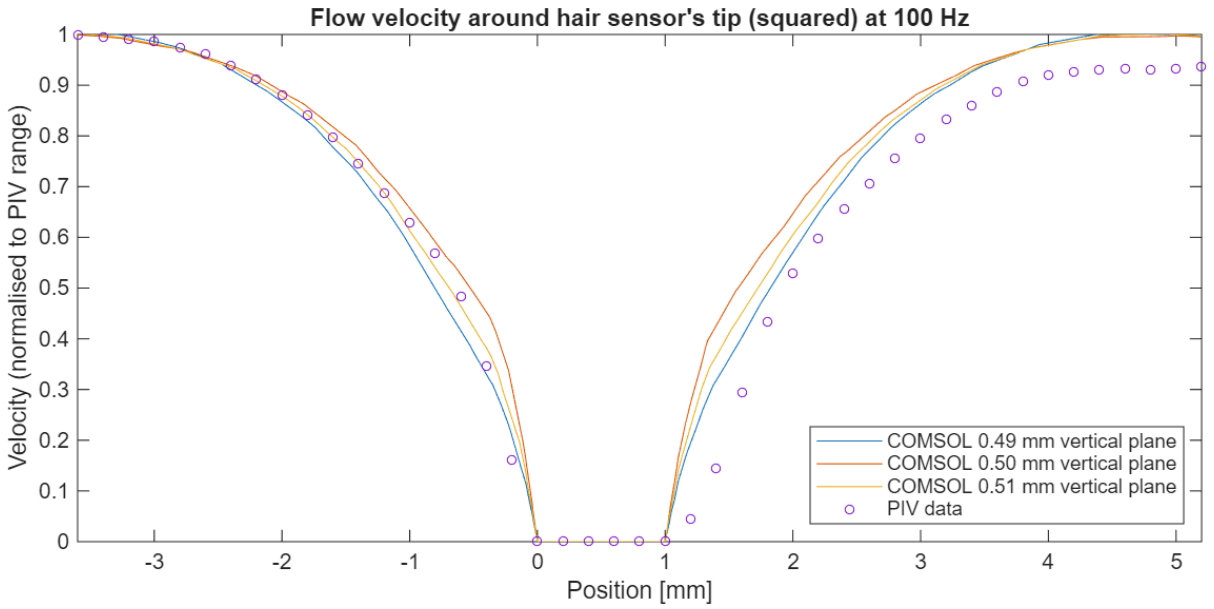

Figure 6.6: Flow velocity at the hair tip for the squared hair sensor at 100 Hz for different COMSOL data extraction vertical planes. COMSOL data for the plane positioned at 0.49 mm, at 0.5 mm, i.e., the centre of the hair shaft, and 0.51 mm.

6.3.2 Flow velocity around hair sensor's tip

Figure 6.7 shows the velocity of air around the squared artificial hair's tip for different frequencies. There seems to be a slight disagreement between COMSOL and the measured data for the size of the boundary layer and of the velocity at both sides of the boundary layer. For

the former, one of the reasons can be the fact that, as said earlier, it is hard to line up the COMSOL plane for the export of data to the same position of the PIV's laser sheet. Another reason can be that the COMSOL simulation has ideal conditions, so there might be a discrepancy in the actual set-up and the simulation. Regardless of this, the curves have almost the same shape, and the difference in boundary layer thickness is of a few micrometres, which can be deemed acceptable. They could also be due to better scaling needed in the X-axis. For the difference in velocity for both sides one of the reasons might be that the two speakers might have not been perfectly equidistant, due to a human error when positioning them at the two sides of the sensor. Another reason could include the shadowing present on the right-hand side of the hair produced by the laser sheet impairing the PIV measurements. For 100 Hz, the difference in airflow velocity is minimal, >0.005 m/s, it increases to almost 0.02 m/s at 200 Hz and 264 Hz, and then it reduces again at 300 Hz, with a difference around 0.01 m/s.

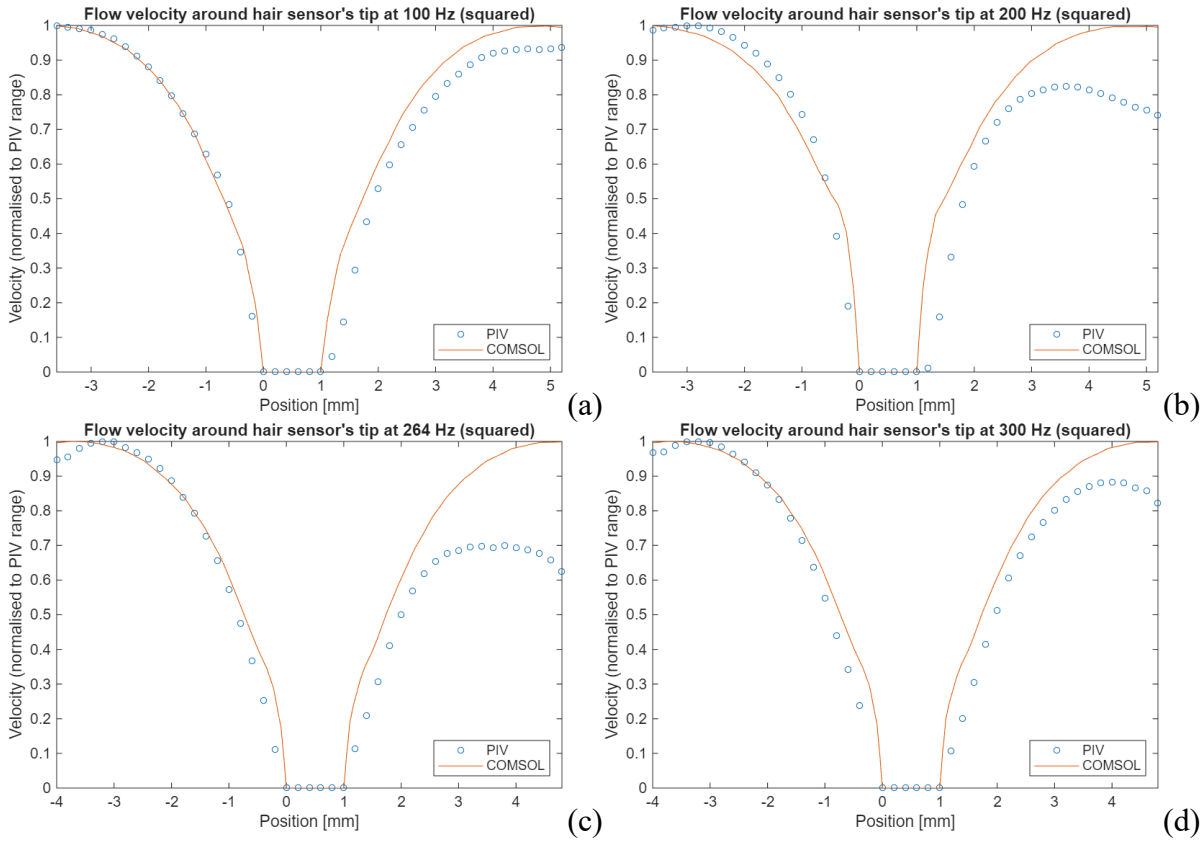

Figure 6.7: Flow velocity at the hair tip for the squared hair sensor at different frequencies, comparison between COMSOL and PIV data. Data at 100 Hz (a), 200 Hz (b), 264 Hz, i.e., the resonant frequency (c), and 300 Hz (d).

Figure 6.8 shows the velocity of air around the cylindrical artificial hair's tip for different frequencies. Similar conclusions could be raised to the ones for the squared hairs. Nevertheless, the difference in size of the boundary layer seems to be smaller for the cylindrical hair, maybe due to its cross section being circular (reducing shadowing and possible differences due to a different COMSOL plane). Even here a difference in velocity can be seen between the two sides, albeit it seems to be reduced compared to the squared artificial hair.

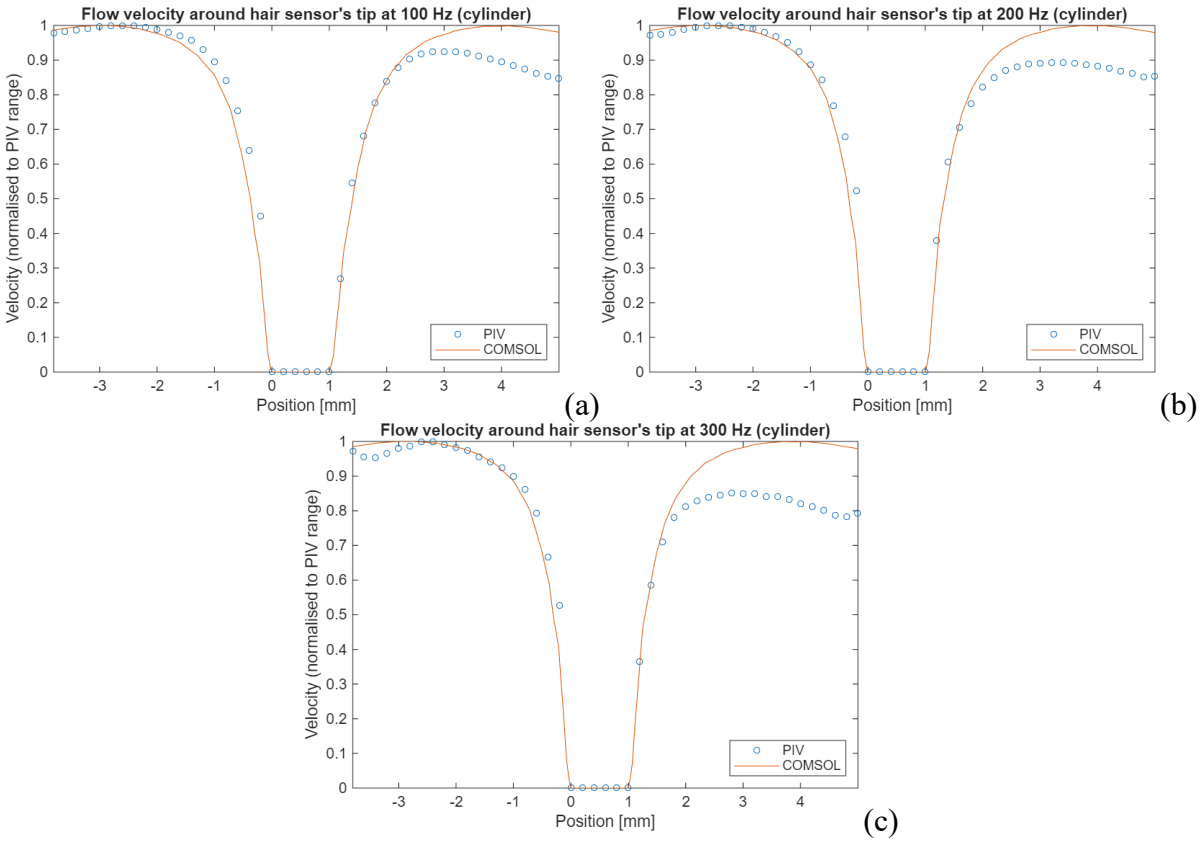

Figure 6.8: Flow velocity at the hair tip for the cylindrical hair sensor at different frequencies, comparison between COMSOL and PIV data. Data at 100 Hz (a), 200 Hz (b), and 300 Hz (c).

6.3.3 Flow velocity around hair sensor's shaft

Figure 6.9 shows the velocity of air around the squared artificial hair's shaft for different frequencies. For the hair shaft it is even harder to match the exact point to more differences between COMSOL and the PIV. In fact, these results look less precise than the hair tip. Many of the hypotheses for any differences between the two raise above still apply here. They include shadowing due to the hair shaft size, misalignments of the two speakers in the PIV set-up and discrepancies between the real-world and the ideal conditions of the simulation. Lastly, scaling issues could also present in this scenario, as well as the difficulty in exporting COMSOL data and PIV on the same plane (as already mentioned). For 100 Hz and 264 Hz there is a large discrepancy in velocity between the left-hand side and the right-hand side. Similar to the discrepancy observed for the tip.

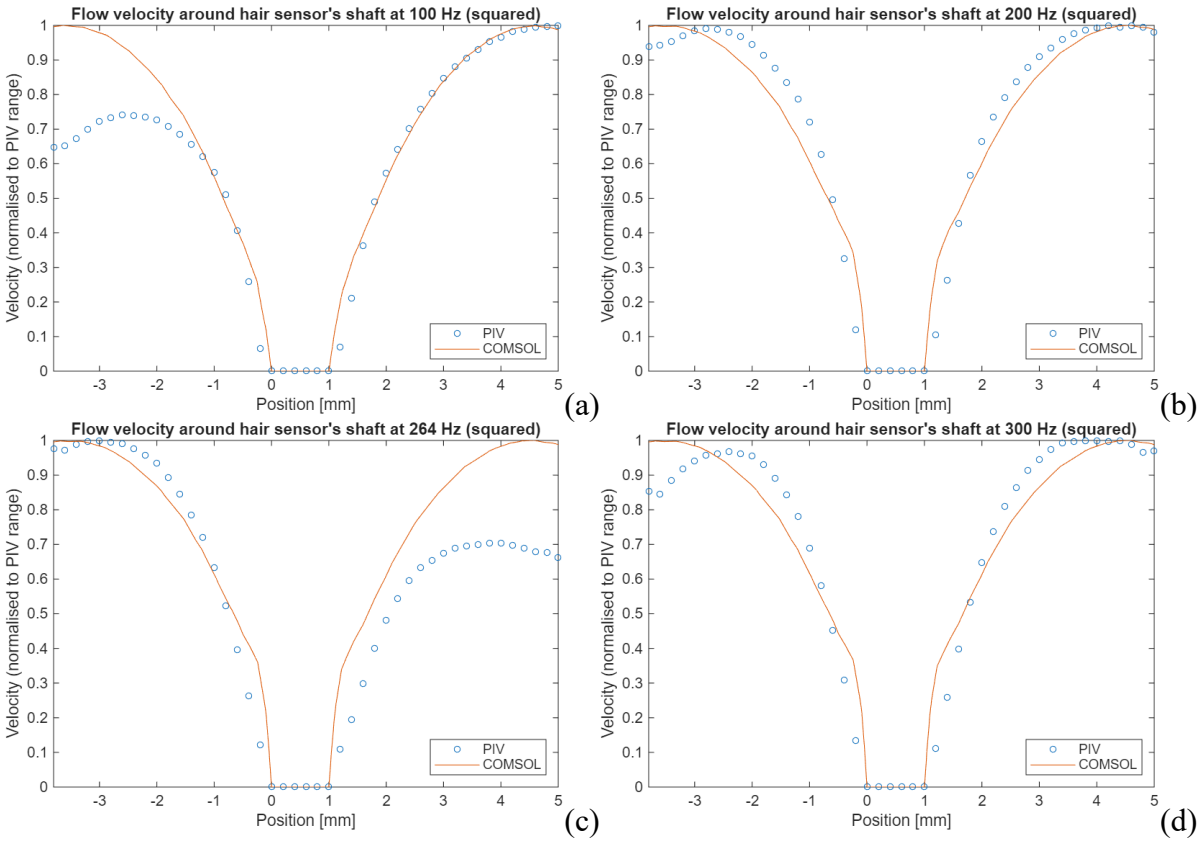

Figure 6.9: Flow velocity at the hair shaft for the squared hair sensor at different frequencies, comparison between COMSOL and PIV data. Data at 100 Hz (a), 200 Hz (b), 264 Hz, i.e., the resonant frequency (c), and 300 Hz (d).

Figure 6.10 shows the velocity of air around the cylindrical artificial hair's shaft for different frequencies. Even in this case, as with the hair's tip measurements, the agreement of the PIV data and the COMSOL simulation seems better than the squared hair one. This is likely due to the cylindrical hair having a more uniform boundary layer and therefore it is easier to align the data export plane in COMSOL with the location of the laser sheet of the PIV. Nevertheless, the results for the 300 Hz measurement are not perfect, since the right-hand size velocity is particularly lower compared to the left-hand side. There is a difference of 0.03 m/s, which is much larger than the ones measured at the tip. Further work should be conducted to understand the nature of such discrepancies.

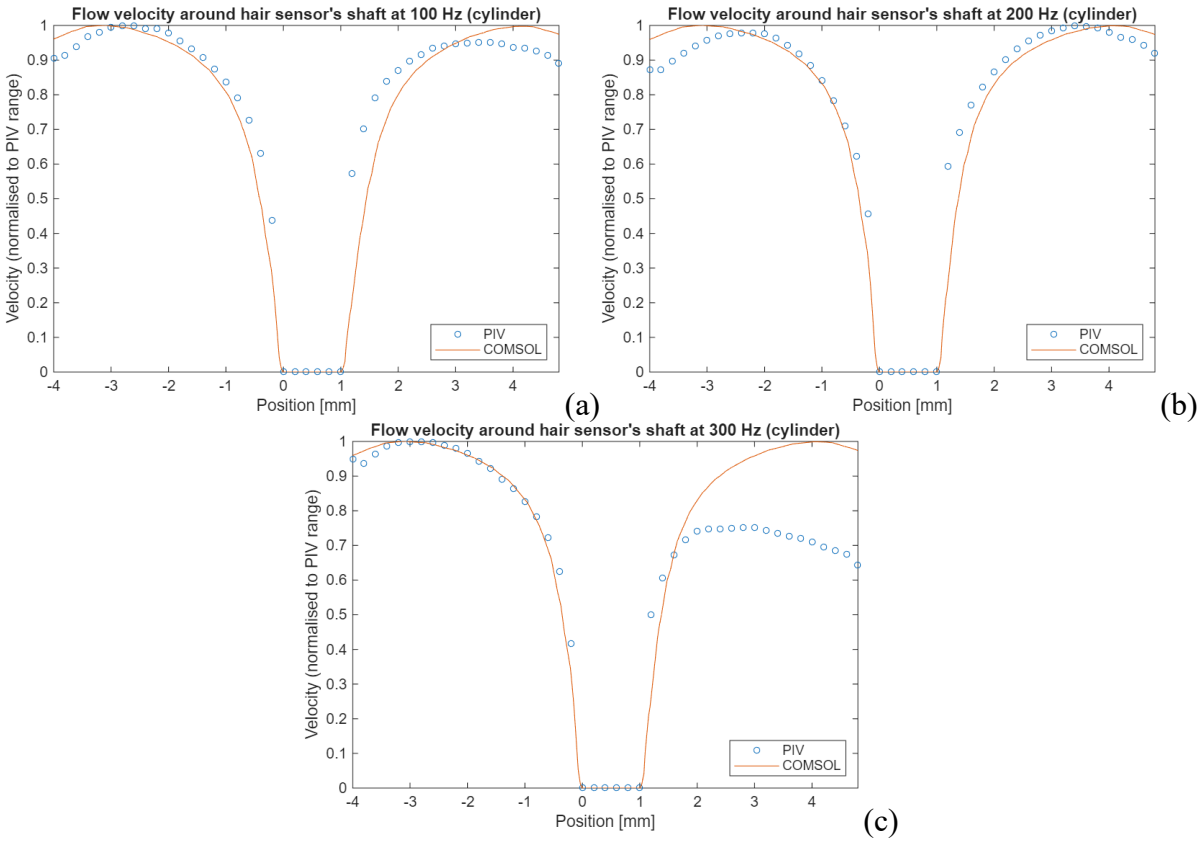

Figure 6.10: Flow velocity at the hair shaft for the cylindrical hair sensor at different frequencies, comparison between COMSOL and PIV data. Data at 100 Hz (a), 200 Hz (b), and 300 Hz (c).

6.4 Conclusions and Future Work

The results shown above show overall a good agreement, meaning that the basic COMSOL model can be used reliably to understand the boundary layer of the AHS. Experiments can produce unexpected results due to mechanism that are not modelled in simulation. This work showed that the basic laminar flow module in COMSOL can be used reliably without including extra features that would increase the simulation time and complexity of the model. Nevertheless, further work is required.

- Extending the study to the **airflow sensor** is one of the further work possible directions. The acoustic sensor has very small displacements, often in the nanometre range, therefore its effect on modifying the flow can be limited, and it cannot be detected by the PIV. On the other hand, the airflow sensor's displacement is visible to the naked eye, and therefore to a PIV system. Extending the study of the PIV, and its agreement with COMSOL results, can help in understanding better the response of the sensor.
- Extend the study to **arrays of sensors** can be used to better understand the optimal distancing and location of the several sensors in an array.
- Explore the use of the boundary layer detection in **autonomous vehicles**, as suggested by Zhang et al. [115]. The use of airflow sensors in autonomous vehicles is one of the possible applications for the airflow sensor. Proper study on this application needs to be conducted. If the sensor can be used to reliably detect the position of the flow boundary layer separation this can assist in efficient and reliable manoeuvring of autonomous vehicles. This is especially important for flying vehicles.
- Further study needs to be conducted to investigate the use of the *Pressure Acoustic Time Domain* module in COMSOL instead of the laminar flow for appropriate placement of acoustic hair sensors in array. This is particularly important because with

the increase in tested frequency there is an increase in computational power required for the simulation. Making it prohibitive for much larger frequencies. Since COMSOL version 6.3, the *Pressure Acoustic Time Domain* became the only module to support GPU-accelerated simulation [190]. Albeit this could be expanded in the future to other modules, investigating its use with a powerful GPU could cut the computation time required for acoustic artificial hair sensors. Albeit the focus of this module is different the one of laminar flow, it could still be interesting to compare the results of the two to better understand the sensor response in the time domain.

7

Conclusions and Future Work

"Human subtlety will never devise an invention more beautiful, more simple or more direct than does nature because in her inventions nothing is lacking, and nothing is superfluous."

Leonardo Da Vinci

Nature has been an inspiration for human technological advancement since the beginning of time. Even in prehistorical times, when humans observed a naturally occurring fire and then attempted to recreate it. Nature has always been a silent "muse" for humans to draw their inspiration from for the improvement of their lives. Leonardo Da Vinci was notorious for drawing inspiration from nature for his engineering and many of his inventions. And nowadays terminology like "bioinspiration" keeps trending in the research and innovation world. Eons of evolutions in insects, and more widely arthropods, perfected their sensory mechanisms to operate at a small scale. Therefore, it should not come with surprise that current researchers take these amazing animals as inspiration for the miniaturization of sensing devices. In the past century, entomologists extensively studied the hair-like mechanoreceptors of insects. As marine biologists did for similar hair-like structures in aquatic life. And at the beginning of this century engineers drew inspiration from them to create usable sensors. Several researchers took on this journey, producing the most disparate kind of sensors. Most of these were produced using conventional micro electromechanical system (MEMS) production techniques.

In 2020 Rajasekaran et al., presented the first 3D-printed hair-like sensor [20]. It made use of a technology called two-photon polymerization (2PP), probably the technique with the best printing resolution in the nanometre range. Nevertheless, this project decided to make use of Digital Light Projection (DLP). DLP compared to 2PP allows the production of multiple sensors in batches. This is because the samples are printed at the same time in the XY-axis, so what changes the time of manufacture is the sample's height (Z-axis). DLP allows for multi-material printing and is much cheaper than 2PP, however it has lower resolution (it is in the micrometre range compared to 2PP's nanometre range). The wide printing area of DLP provides the opportunity to integrate arrays of sensors within a single structure. Apart from DLP and 2PP other 3D-printing techniques exist and have been involved in producing sensors [21, 191-205]. Nevertheless, many of them, albeit generally cheaper, suffer from worse

resolution, and they share the same non-batch capabilities of 2PP. DLP offers the capability to print sensors at a small scale, and to print them in batches with no increase in time. Making it a possible competitor to conventional MEMS producing techniques.

In Chapter 4 it was proved that it is possible to print structures in arrays with acoustic sensitivity. By changing the hair structure (e.g., length or thickness), it was possible to tune the artificial hair for a different narrow frequency band. Making it possible, in theory, to acquire audio with separated frequency bands. This could prove useful in audio applications like speech recognition, where the use of the Fourier transform is the primary tool that can inform us of the frequency content of an audio signal. Nevertheless, converting the artificial hair displacement in an electric signal was not successful unfortunately. This was the biggest drawback of the entire project, and albeit some progress was made in the right direction, substantial changes are required to the structure of the sensor to make it functional for our needs. Moreover, the sensitivity of these structures was proved only for low frequencies and efforts need to be made to extend it to cover the whole audible spectrum at least.

In Chapter 5 it was shown how the structure of the acoustic sensors could be adapted to sense other phenomena, namely air flow. Unlike its acoustic counterpart, the mechanical displacements of this sensor were successfully converted into electric signals. Even though the characterization of the sensor was made challenging by the availability of tools, it was also possible to perform it under limited conditions. The full range and capabilities of this sensor need to be further studied. Having an artificial hair-like sensor that could be adapted to different sensing needs was a constant thought throughout this project; inspired by how different hair-like sensory systems could sense different phenomena in insects. Albeit not recorded, a capability of this structure to act as an acceleration-like and gyroscope-like mechanism was observed and warrants further observation.

In Chapter 6 the movement of air flow around the hair shaft was investigated during an exchange at the Université de Tours, in France. It was concluded that the results of COMSOL simulations were congruent to the flow observed thanks to a particle image velocimetry. Further investigation needs to be conducted.

Lastly, it is important to reflect on future work beyond the content of this thesis. Albeit in each chapter this has already been explored it is hereafter summarized. The most functional investigations for the improvement of these sensors are:

- Investigation of different **materials** and **sensing methodologies** should be at the base. While the acoustic hair proposed on this thesis could be used as a proof-of-concept, its feasibility as a sensor will strongly depend on different materials and sensing methods. These could also improve the fabrication process and make it less complicate, or cheaper than the use of platinum in the airflow sensor. Some of the possibilities are piezoelectric hydrogels [170, 171, 203], conductive and/or electrosensitive UV-curable resins [206], other deposition systems, optic sensing methods and laser-induced graphene [172]. Albeit 3D-printing has been introduced as an alternative to MEMS production techniques, its use to move from prototyping of these acoustic sensors to functioning sensors cannot be excluded.
- Investigate different **geometries** is also another avenue for these sensors. Especially for the acoustic ones to investigate possible alternatives to make it functional or to reach higher frequencies. For the airflow sensor different thicknesses or geometric variation of the hair will make a change on the sensor's sensitivity this needs to be of course appropriately investigated.
- Extend the **sensitivity** study. For the airflow sensor this means investigating further its directionality but also completing the characterization with stronger flows. For

the acoustic sensors albeit they were made to work mechanically no study was made on directionality, and sensitivity.

- Study their use in **arrays**. The potential to print an array of sensors has been stressed multiple times across this thesis, it needs of course further investigation into what does it mean in terms of appropriate positioning of each sensor and circuitry required. Part of the reasoning behind chapter 6 was to investigate how the flow reacts around the hair, this needs to be extended further to optimize possible arrays of sensors. Study of their use in an array includes also the computation needed to use all this data.
- Improvements on the **signal conditioning**. For the scope of this project this applied only to the airflow sensor of course. But better signal conditioning and circuitry is required to extract the best response from the sensor. A similar study would follow functioning acoustic hair sensors.

Other less direct investigations include:

- **Applications** need to be further investigated. Several possible applications for these sensors have been proposed throughout this thesis, further work needs to be conducted in each of these areas and compare this sensor to the state-of-art sensing made in those areas (e.g., biomedical respirators, meteorology, etc.). Of course, there might be possible applications that have been ignored and not proposed **in** this thesis, especially since it was heavily focused on creating the sensor rather than implementing it in a specific application. Therefore, investigating other possible applications is part of the future work needed.
- The use of appropriate coating could allow the use of this sensor **underwater** or with other fluids. This is another field of further research that could be opened for these sensors.

- Improvements on **simulation** and **numerical methods** needs to be made as these can speed up the prototyping and further development process of these sensors. They can also open the door to optimization of the sensor.
- Possible **other iterations** of this sensor to sense other phenomena should be investigated. Similarly to how different hair mechanoreceptors in insects' sense different domains, like direct touch or acceleration.
- Albeit ambitious, a possible iteration of the acoustic sensor for **neuromorphic** sensing should be investigated. These hair sensors could allow for the creation of a truly neuromorphic acoustic sensor that produces spikes at the output for different frequency bands.

A. Appendix

A.1 COMSOL method code for combining Eigenfrequency and Frequency Domain studies

For the following COMSOL method code some parameters need to be initialized. To initialize parameters right-click on *Global Definitions* and select parameters. The parameters as in Table A.1 need to be created. The value of *f_eigen* is just assigned to a random value, the real value will be calculated by the Eigenfrequency study. The values of f_*step* and *deltaFreqRange* can be changed to change the step size of the Frequency Domain study, and the range of frequencies tested by the latter.

Table A.1: Parameters needed in COMSOL to use the method code for combining Eigenfrequency and Frequency Domain studies.

Name	*Expression*	*Description*
f_eigen	110 [Hz]	Resonant frequency for cantilever-like movement. Calculated by eigenfrequency study.
f_step	1 [Hz]	Frequency step for frequency domain study.
deltaFreqRange	10 [Hz]	Plus/minus range around resonant frequency for frequency domain study.
f_max	f_eigen+deltaFreqRange	Upper end of frequency study range.
f_min	f_eigen-deltaFreqRange	Lower end of frequency study range.

The Eigenfrequency and Frequency Domain studies need to be set through COMSOL appropriately prior to using the method. The identifier of the study needs to be substituted in the following code. In my case the Eigenfrequency study was the third study in the model, and its identifier is *std3*. The Frequency Domain study was the fourth study, and its identifier is *std4*. In this study I was also performing a material sweep for different metals and a parametric

sweep for different metal layer thicknesses. Minor modifications to the method need to be performed if these are not needed.

```
// Set metal thickness in eigenfrequency study (parametric sweep)
model.study("std3").feature("param").setIndex("plistarr",
toString(metalThickness), 0);
// Run Eigenfrequency study
if (eigen) {
  message("Running eigenfrequency study...");
  model.study("std3").run();
}

// Get the results table from the eigenfrequency study, only real values are
taken
double[][] eigenResults = model.result().evaluationGroup("eg1").getReal();

// Get the number of metal thicknesses that have been tested
int numThick = metalThickness.length;
message("Number of parameters of the parametric sweep: "+toString(numThick));
// Get the number of metals that have been tested from the last column, first
row
int lastRowIndex = eigenResults.length-1;
double numMetal = eigenResults[lastRowIndex][0];
message("Number of metals tested: "+toString(numMetal));

// Create a new array for eigenfrequencies averages
double[] avgEigenFreq = new double[numThick];
// Loop through the eigenFrequencies result table every numParam places of i
for (int i = 0; i < numThick; i++) {
  // Initialize sum and count for averaging
  double sum = 0;
  int count = 0;
  // Loop through all the metals
  for (int j = 0; j < numMetal; j++) {
    // Add the values at each location if they exist
    if (i+(numThick*j) < eigenResults.length) {
```

```
        sum += eigenResults[i+(numThick*j)][2];
        count++;
      }
    }
    // Calculate the average and store it in the array
    if (count > 0) {
      avgEigenFreq[i] = sum/count;
      message("Average resonant frequency at metal thickness
"+toString(metalThickness[i])+" nm is "+toString(avgEigenFreq[i], 4)+" Hz");
    }
  }

  // New array to contain integer eigen frequencies
  int[] avgEigenFreqInt = new int[avgEigenFreq.length];
  // Round each elements of the averaged eigenfrequency results
  for (int i = 0; i < avgEigenFreq.length; i++) {
    avgEigenFreqInt[i] = (int) Math.ceil(avgEigenFreq[i]);
  }

  // Set study step and frequency range values in global definitions
  model.param().set("f_step", f_step+" [Hz]");
  model.param().set("deltaFreqRange", deltaFreqRange+" [Hz]");

  // Set parametric study of Frequency Domain to "Specified combinations"
  model.study("std4").feature("param1").set("sweeptype", "sparse");
  // Set metal thickness to the frequency domain study (parametric sweep)
  model.study("std4").feature("param1").setIndex("plistarr",
  toString(metalThickness), 0);
  // Set rounded average eigenfrequencies to the frequency domain study
  (parametric sweep)
  model.study("std4").feature("param1").setIndex("plistarr",
  toString(avgEigenFreqInt), 1);
  // Set range of frequencies for the frequency domain study, f_min and f_max are
  calculated in the global definitions
  model.study("std4").feature("freq").set("plist", "range(f_min,f_step,f_max)");
  // Run Frequency Domain study
  if (freqdom) {
```

```
  message("Running Frequency Domain study...");
  model.study("std4").run();
}
message("Simulation ended.");
```

A.2 Analytical model for cylindrical hair-like sensors

The following analytical model for cylindrical hair-like sensor is from Humphrey et al. [53]. Albeit in insects the hair-like structure is not a perfect cylinder as from the tip to the bottom the diameter varies, in this mechanical model it is approximated by a circular cylinder of diameter d and length L. The mechanical characteristics constants for a specific hair-like sensory system need dynamic experiments to be conducted for their correct evaluation. They are the torsional spring S, in some sources referred to as torsional stiffness, and damping R, relating to the pivoting joint at the base of the hair. The only mechanical property of the hair sensory system that can be calculated analytically is its moment of inertia I, which depends on the hair shaft geometry, it is calculated as in eq. (A.1) [53]. Other two moments of inertia that contribute to the hair's response are the moment of inertia relative to the fluid medium density and viscosity, I_ρ and I_μ, respectively, calculated in eqs. (A.2) and (A.3) [53]. Moreover, the damping constant of the hair associated with the fluid's viscosity, R_μ needs to be evaluated as in eq. (A.4) [53].

$$I = \frac{\pi \rho_h d^2}{48}\left(4L^3 + \frac{3}{4}d^2 L\right) \tag{A.1}$$

$$I_\rho = \frac{\pi \rho d^2 L^3}{12} \tag{A.2}$$

$$I_\mu = -\frac{\pi^2 \mu G L^3}{3g\omega} \tag{A.3}$$

$$R_\mu = \frac{4}{3}\pi \mu G L^3 \tag{A.4}$$

Where,

ρ_h hair density in kg/m^3

ρ fluid medium density (for air at 27 ˚C, it is 1.1614 kg/m^3)

μ fluid medium dynamic viscosity (for air at 27 ˚C, it is $1.85 \cdot 10^{-5}$ kg/(m·s))

ω frequency in rad/s ($\omega = 2\pi f$)

The quantities *G* and *g* are given by [53]

$$G = -\frac{g}{g^2 + \frac{\pi^2}{16}} \tag{A.5}$$

$$g = 0.577 + \ln s \tag{A.6}$$

Where *s* is the Stokes' parameter, expressed as [53]

$$s = \sqrt{\frac{d^2 \omega \rho}{16\mu}} \tag{A.7}$$

The total inertia and damping constant of the hair is therefore given by [53]

$$I_t = I + I_\rho + I_\mu \tag{A.8}$$

$$R_t = R + R_\mu \tag{A.9}$$

These variables can then be used in the general equation of angular momentum for a filiform hair, eq. (A.10) [53], which was derived by the motion of pendulums described by Stokes [207]. Humphrey et al. then proceed to derive the physically approximate but analytical exact solutions for the evaluation of the resonant frequencies based on angular displacement, eq. (A.11), and velocity, eq. (A.12) [53]. This approximative model can be applied only in cases where the angular displacement of the hair is <10˚ and that the following condition is met $2I_t S - R_t^2 > 0$ [53].

$$I_t \ddot{\theta} + R_t \dot{\theta} + S\theta = 4\pi\mu G \int_0^L V_F y dy + \left(\frac{\pi \rho d^2}{4} - \frac{\pi^2 \mu G}{g\omega}\right) \int_0^L V_F y dy \tag{A.10}$$

$$\omega_{res(\theta)} = \sqrt{\frac{S}{I_t} - \frac{R_t^2}{2I_t^2}} \tag{A.11}$$

$$\omega_{res(V)} = \sqrt{\frac{S}{I_t}} \tag{A.12}$$

Given all the hair system variables, one can use a numerical solver to solve the equation and find the resonant frequency in alternative to the eigenfrequency and frequency domain study of COMSOL. The analytical model solving eq. (A.11) has been coded in MATLAB and can be found in below in A.2.2.

A.2.1 Evaluating the sensor's stiffness in COMSOL

As previously stated, the torsional stiffness *S*, and damping *R*, of the sensor's analytical model need to be evaluated experimentally. The alternative could be the use of FEA to estimate these values. This section explains how to evaluate the torsional stiffness in COMSOL. The damping has not been evaluated in COMSOL since the analytical model was not followed.

1. Create a load group in the global definitions and create your geometry (right-click under load and constraint groups).
2. Under your 3D component's Definitions, add an integration (right click in *definitions>non-local couplings>integration*).
3. In the integration operation add the top face (as boundary) at which you will apply a prescribed rotation/displacement. Basically, apply it at the top of the tip of the hair shaft. Under *Advanced>Method*, select *Summation over nodes*.
4. Right click on Definitions and create Variables.
5. Define in variable a variable with a name of choice and the expression:

```
with(1,intop1(solid.RMx))/(1[rad]*1[mm])
```

This means that with the first load group, it will return the momentum of the solid of the integrated operation specified above. This momentum is then divided for a prescribed rotation of 1 radian, with a 1 mm x-axis of rotation, which will be defined later.

6. Add the specified material(s) and the *Solid Mechanics* physics module.
7. In *Solid Mechanics* select the interested domains. Add a fixed constraint at the point you expect the object to not move. Add a rigid connector boundary, selecting the same boundary of the integration operation from point 3.
8. In rigid connector, under prescribed rotation select By Prescribed Rotation. For the x-axis add:

   `if(root.group.lg1,1*root.group.lg1,0)`

   Basically, the if-operator specifies that, if load group 1 is selected, the prescribed rotation is applied, otherwise not (sets it to 0). For the y- and z-axis leave them at zero. Under angle of rotation set 1 rad.
9. Add a *Stationary Study*. Under study extensions select define load cases and tick the *lg1* box. Compute the study.
10. In Results, right-click on *Derived Values* and select *Global Evaluation*. In expression write the name of the variable you specified in point 5. Click on evaluate and the torsional stiffness will be shown on a table in N/rad.
11. Since the torsional stiffness in the analytical model needs to be in N·m/rad, and we prescribed a displacement of 1 mm, the value to use in the equation is the one evaluated in point 10, multiplied by 1 mm.

You can extend the study to evaluate the bending stiffness produced by a momentum on the other directions by adding two more variables in point 5 as follows and then adding them in the evaluation of point 10.

`with(1,intop1(solid.RMy))/(1[rad]*1[mm])`

```
with(1,intop1(solid.RMz))/(1[rad]*1[mm])
```

These will give the bending stiffness produced by a momentum on the direction of the axis perpendicular to the axis towards which the structure will bend. For example, for a movement/bending in the x-axis we are interested in the bending stiffness in the y-axis (the momentum *RMy*). Since COMSOL creates 3D plots showing the way the structure bends it is suggested to use the stiffness in the direction showing the bending that is expected by the sensor.

A.2.2 MATLAB code for the cylindrical hair's analytical model

For the following MATLAB code, the *Symbolic Math Toolbox* is required to be appropriately run.

```
% Frequency as a variable

syms f_0

assume(f_0, 'real')



% Density of fluid (air at 27C)

rho_air = 1.1614; % [kg/m^3]

% Viscosity of fluid (air at 27C)

mu_air = 1.85e-5; % [kg/(m*s)]

% Diameter of the hair

d_0 = 1 *1e-3; %[m]

% Length of the air

l_0 = 4 *1e-3; %[m]
```

```
% Stiffness of the hair

S_0 = 0.4506e-3; %[N*m/rad]

% Damping constant of the hair

R_0 = 01e-7; %[N*m*s/rad]

% Density of hair material

rho_0 = 1178; %[kg/m^3]



% Stokes parameter

s(f_0) = sqrt((2*pi*f_0*rho_air*d_0^2)/(16*mu_air));

% Parameters for inertia I_mu

g(f_0) = 0.577 + log(s);

G(f_0) = g/(g^2 + (pi/4)^2);

% Moment of inertias from different contributions

I = (pi*rho_0*d_0^2)/48 * (4*l_0^3 + 0.75*l_0*d_0^2);

I_rho = (pi*rho_0*d_0^2*l_0^3)/30;

I_mu(f_0) = - (pi^2*mu_air*G*l_0^3)/(3*g*2*pi*f_0);

% Total moment of inertia

I_t(f_0) = I + I_rho + I_mu;



% Damping due to fluid

R_mu(f_0) = 4/3 * pi*mu_air*G*l_0^3;

% Total damping
```

```
R_t(f_0) = R_0 - R_mu;


% Resonant frequency [Hz]
equation = S_0 == I_t*(2*pi*f_0)^2 + (R_t^2/(2*I_t));
resonant_frequency = vpasolve(equation,f_0, [-Inf Inf])
```

Bibliography

[1] Y. Ozaki, T. Ohyama, T. Yasuda, and I. Shimoyama, "An air flow sensor modeled on wind receptor hairs of insects," in *Proceedings IEEE Thirteenth Annual International Conference on Micro Electro Mechanical Systems (Cat. No.00CH36308)*, 2000: IEEE, doi: 10.1109/memsys.2000.838573.

[2] H. Ko *et al.*, "Bioinspired piezoresistive acceleration sensor using artificial filiform sensillum structure," *Sensors and Materials,* vol. 27, no. 6, pp. 437–445, 2015.

[3] M. R. Maschmann *et al.*, "Bioinspired Carbon Nanotube Fuzzy Fiber Hair Sensor for Air-Flow Detection," *Advanced Materials,* vol. 26, no. 20, pp. 3230–3234, 2014–05–01 2014, doi: 10.1002/adma.201305285.

[4] K. Slinker *et al.*, *Variable deflection response of sensitive CNT-on-fiber artificial hair sensors from CNT synthesis in high aspect ratio microcavities* (SPIE Smart Structures and Materials + Nondestructive Evaluation and Health Monitoring). SPIE, 2015.

[5] X. Shi and C.-H. Cheng, "Artificial hair cell sensors using liquid metal alloy as piezoresistors," in *The 8th Annual IEEE International Conference on Nano/Micro Engineered and Molecular Systems*, 2013–04–01 2013: IEEE, pp. 978–981, doi: 10.1109/nems.2013.6559886.

[6] J.-E. Han, D. Kim, and K.-S. Yun, "All-polymer hair structure with embedded three-dimensional piezoresistive force sensors," *Sensors and Actuators A: Physical,* vol. 188, pp. 89–94, 2012/12/01/ 2012, doi: https://doi.org/10.1016/j.sna.2012.03.045.

[7] A. Qualtieri, F. Rizzi, M. T. Todaro, A. Passaseo, R. Cingolani, and M. De Vittorio, "Stress-driven AlN cantilever-based flow sensor for fish lateral line system," *Microelectronic Engineering,* vol. 88, no. 8, pp. 2376–2378, 2011/08/01/ 2011, doi: https://doi.org/10.1016/j.mee.2011.02.091.

[8] A. Qualtieri, F. Rizzi, G. Epifani, A. Ernits, M. Kruusmaa, and M. De Vittorio, "Parylene-coated bioinspired artificial hair cell for liquid flow sensing," *Microelectronic Engineering,* vol. 98, pp. 516–519, 2012/10/01/ 2012, doi: https://doi.org/10.1016/j.mee.2012.07.072.

[9] C. Abels, A. Qualtieri, M. De Vittorio, W. M. Megill, and F. Rizzi, "A bio-inspired real-time capable artificial lateral line system for freestream flow measurements," *Bioinspir Biomim,* vol. 11, no. 3, p. 035006, Jun 3 2016, doi: 10.1088/1748-3190/11/3/035006.

[10] A. G. P. Kottapalli, M. Asadnia, J. M. Miao, G. Barbastathis, and M. S. Triantafyllou, "A flexible liquid crystal polymer MEMS pressure sensor array for fish-like underwater sensing," *Smart Materials and Structures,* vol. 21, no. 11, 2012, doi: 10.1088/0964-1726/21/11/115030.

[11] A. G. P. Kottapalli, M. Bora, M. Asadnia, J. Miao, S. S. Venkatraman, and M. Triantafyllou, "Nanofibril scaffold assisted MEMS artificial hydrogel neuromasts for enhanced sensitivity flow sensing," *Scientific Reports,* vol. 6, no. 1, p. 19336, 2016–01–14 2016, doi: 10.1038/srep19336.

[12] D. Shen *et al.*, "Bio-inspired Flexible Airflow Sensor with Self-bended 3D Hair-like Configurations," *Journal of Bionic Engineering,* vol. 19, no. 1, pp. 73–82, 2022–01–01 2022, doi: 10.1007/s42235-021-00110-y.

[13] L.-G. Tran and W.-T. Park, "Biomimetic Flow Sensor for Detecting Flow Rate and Direction as an Application for Maneuvering Autonomous Underwater Vehicle," *International Journal of Precision Engineering and Manufacturing-Green Technology,* vol. 9, no. 1, pp. 163–173, 2022–01–01 2022, doi: 10.1007/s40684-020-00282-8.

[14] G. J. M. Krijnen *et al.*, "MEMS based hair flow-sensors as model systems for acoustic perception studies," *Nanotechnology,* vol. 17, no. 4, pp. S84–S89, 2006–02–28 2006, doi: 10.1088/0957-4484/17/4/013.

[15] G. Krijnen, T. Lammerink, R. Wiegerink, and J. Casas, "Cricket Inspired Flow-Sensor Arrays," in *2007 IEEE Sensors*, 2007–01–01 2007: IEEE, doi: 10.1109/icsens.2007.4388455.

[16] R. J. Wiegerink, A. Floris, R. K. Jaganatharaja, N. Izadi, T. S. J. Lammerink, and G. J. M. Krijnen, "Biomimetic Flow-Sensor Arrays Based on the Filiform Hairs on the Cerci of Crickets," in *2007 IEEE Sensors*, 2007–01–01 2007: IEEE, doi: 10.1109/icsens.2007.4388591.

[17] N. a. J. Izadi, R. K. and Floris, J. and Krijnen, G., "Optimization of Cricket-inspired, Biomimetic Artificial Hair Sensors for Flow Sensing," 2008, doi: 10.48550/ARXIV.0802.3768.

[18] H. Herzog *et al.*, "μ-biomimetic flow-sensors—introducing light-guiding PDMS structures into MEMS," *Bioinspiration & Biomimetics,* vol. 10, no. 3, p. 036001, 2015/04/16 2015, doi: 10.1088/1748-3190/10/3/036001.

[19] Y. Li *et al.*, "An all-optical multidirectional mechano-sensor inspired by biologically mechano-sensitive hair sensilla," *Nature Communications,* vol. 15, no. 1, 2024–04–04 2024, doi: 10.1038/s41467-024-47299-0.

[20] K. Rajasekaran, H. D. Bae, S. Bergbreiter, and M. Yu, "3D Printed Bio-Inspired Hair Sensor for Directional Airflow Sensing," in *2020 IEEE/RSJ International Conference on Intelligent Robots and Systems (IROS)*, 2020–10–24 2020: IEEE, doi: 10.1109/iros45743.2020.9340711.

[21] M. R. Khosravani and T. Reinicke, "3D-printed sensors: Current progress and future challenges," *Sensors and Actuators A: Physical,* vol. 305, 2020, doi: 10.1016/j.sna.2020.111916.

[22] M. Pagac *et al.*, "A Review of Vat Photopolymerization Technology: Materials, Applications, Challenges, and Future Trends of 3D Printing," *Polymers,* vol. 13, no. 4, p. 598, 2021–02–17 2021, doi: 10.3390/polym13040598.

[23] I. Gibson *et al.*, *Additive manufacturing technologies*. Springer, 2021.

[24] P. Photinos, *The Physics of Sound Waves*, 2nd ed. Bristol, UK: IOP Publishing Ltd, 2021.

[25] M. Garstang, D. Larom, R. Raspet, and M. Lindeque, "Atmospheric controls on elephant communication.," *Journal of Experimental Biology,* vol. 198, no. 4, pp. 939–951, 1995–04–01 1995, doi: 10.1242/jeb.198.4.939.

[26] M. A. Coultas, R. H. Defran, M. L. Dixon, and S. S. Berry, "The dog audiogram," *The Journal of the Acoustical Society of America,* vol. 70, no. S1, pp. S31–S31, 1981–11–01 1981, doi: 10.1121/1.2018819.

[27] Rickye S. Heffner and H. E. Heffner, "Hearing range of the domestic cat," *Hearing Research,* vol. 19, no. 1, pp. 85–88, 1985, doi: 10.1016/0378-5955(85)90100-5.

[28] S. Maroonroge, D. C. Emanuel, and T. R. Letowski, "Basic anatomy of the hearing system," *Helmet-Mounted Displays: Sensation, Perception and Cognition Issues. Fort Rucker, Alabama: US Army Aeromedical Research Laboratory,* pp. 279–306, 2000.

[29] Charles Stangor and J. Walinga, "Chapter 5.3 Hearing," in *Introduction to Psychology - 1st Canadian Edition*. Victoria, B.C., Canada: BCcampus, 2014.

[30] J. E. Yack, "The structure and function of auditory chordotonal organs in insects," *Microscopy Research and Technique,* vol. 63, no. 6, pp. 315–337, 2004–04–15 2004, doi: 10.1002/jemt.20051.

[31] T. A. Keil, "Functional morphology of insect mechanoreceptors," *Microscopy Research and Technique,* vol. 39, no. 6, pp. 506–531, 1997, doi: 10.1002/(SICI)1097-0029(19971215)39:6<506::AID-JEMT5>3.0.CO;2-B.

[32] H. Markl and J. Tautz, "The sensitivity of hair receptors in caterpillars of Barathra brassicae L. (lepidoptera, noctuidae) to particle movement in a sound field," *Journal of Comparative Physiology,* vol. 99, no. 1, pp. 79–87, 1975–03–01 1975, doi: 10.1007/bf01464713.

[33] M. C. Göpfert and D. Robert, "Nanometre–range acoustic sensitivity in male and female mosquitoes," *Proceedings of the Royal Society of London. Series B: Biological Sciences,* vol. 267, no. 1442, pp. 453–457, 2000–03–07 2000, doi: 10.1098/rspb.2000.1021.

[34] C. S. Henry, "The Importance of Low-Frequency, Substrate-Borne Sounds in Lacewing Communication (Neuroptera: Chrysopidae)," *Annals of the Entomological Society of America,* vol. 73, no. 6, pp. 617–621, 1980, doi: 10.1093/aesa/73.6.617.

[35] L. Vilhelmsen, N. Isidoro, R. Romani, H. H. Basibuyuk, and D. L. J. Quicke, "Host location and oviposition in a basal group of parasitic wasps: the subgenual organ, ovipositor apparatus and associated structures in the Orussidae (Hymenoptera, Insecta)," *Zoomorphology,* vol. 121, no. 2, pp. 63–84, 2001–10–01 2001, doi: 10.1007/s004350100046.

[36] D. D. Yager, "Structure, development, and evolution of insect auditory systems," *Microscopy Research and Technique,* vol. 47, no. 6, pp. 380–400, 1999, doi: 10.1002/(sici)1097-0029(19991215)47:6<380::Aid-jemt3>3.0.Co;2-p.

[37] T. G. Forrest, M. P. Read, H. E. Farris, and R. R. Hoy, "A tympanal hearing organ in scarab beetles.," *Journal of Experimental Biology,* vol. 200, no. 3, pp. 601–606, 1997–02–01 1997, doi: 10.1242/jeb.200.3.601.

[38] J. E. Yack, L. D. Otero, J. W. Dawson, A. Surlykke, and J. H. Fullard, "Sound production and hearing in the blue cracker butterfly Hamadryas feronia (Lepidoptera, nymphalidae) from Venezuela," *Journal of Experimental Biology,* vol. 203, no. 24, pp. 3689–3702, 2000–12–15 2000, doi: 10.1242/jeb.203.24.3689.

[39] R. L. Rodriguez and M. D. Greenfield, "Behavioural context regulates dual function of ultrasonic hearing in lesser waxmoths: bat avoidance and pair formation," *Physiological Entomology,* vol. 29, no. 2, pp. 159–168, 2004–06–01 2004, doi: 10.1111/j.1365-3032.2004.00380.x.

[40] T. A. Keil, "Comparative morphogenesis of sensilla: A review," *International Journal of Insect Morphology and Embryology,* vol. 26, no. 3, pp. 151–160, 1997/07/01/ 1997, doi: https://doi.org/10.1016/S0020-7322(97)00017-2.

[41] K. R. Jessen, "Glial cells," *The International Journal of Biochemistry & Cell Biology,* vol. 36, no. 10, pp. 1861–1867, 2004/10/01/ 2004, doi: https://doi.org/10.1016/j.biocel.2004.02.023.

[42] T. Shimozawa, J. Murakami, and T. Kumagai, "Cricket Wind Receptors: Thermal Noise for the Highest Sensitivity Known," in *Sensors and Sensing in Biology and Engineering*, F. G. Barth, J. A. C. Humphrey, and T. W. Secomb Eds. Vienna: Springer Vienna, 2003, pp. 145–157.

[43] A. Reißland and P. Görner, "Mechanics of trichobothria in orb-weaving spiders (Agelenidae, Araneae)," *Journal of Comparative Physiology,* vol. 123, no. 1, pp. 59–69, 1978–01–01 1978, doi: 10.1007/bf00657344.

[44] K. Meßlinger, "Fine structure of scorpion trichobothria (Arachnida, Scorpiones)," *Zoomorphology,* vol. 107, no. 1, pp. 49–57, 1987–06–01 1987, doi: 10.1007/bf00312129.
[45] A. Reissland and P. Görner, "Trichobothria," in *Neurobiology of Arachnids*, F. G. Barth Ed. Berlin, Heidelberg: Springer Berlin Heidelberg, 1985, pp. 138–161.
[46] T. A. Keil and R. A. Steinbrecht, "Mechanosensitive and Olfactory Sensilla of Insects," in *Insect Ultrastructure: Volume 2*, R. C. King and H. Akai Eds. Boston, MA: Springer US, 1984, pp. 477–516.
[47] P. Görner, "A proposed transducing mechanism for a multiply-innervated mechanoreceptor (trichobothrium) in spiders," in *Cold Spring Harbor Symposia on Quantitative Biology*, 1965, vol. 30: Cold Spring Harbor Laboratory Press, pp. 69–73.
[48] C. Zhang *et al.*, "High-aspect-ratio deflection transducers inspired by the ultra-sensitive cantilever configuration of scorpion trichobothria," *Journal of Materials Chemistry C,* vol. 8, no. 18, pp. 6093–6101, 2020–01–01 2020, doi: 10.1039/d0tc00241k.
[49] B. D. Saltin, Y. Matsumura, A. Reid, J. F. Windmill, S. N. Gorb, and J. C. Jackson, "Material stiffness variation in mosquito antennae," *Journal of The Royal Society Interface,* vol. 16, no. 154, p. 20190049, 2019–05–01 2019, doi: 10.1098/rsif.2019.0049.
[50] R. Devarakonda, F. G. Barth, and J. A. C. Humphrey, "Dynamics of arthropod filiform hairs. IV. Hair motion in air and water," *Philosophical Transactions of the Royal Society B,* vol. 351, no. 1342, pp. 933–946, 29 July 1996 1996, doi: https://doi.org/10.1098/rstb.1996.0086.
[51] N. H. Fletcher, "Acoustical response of hair receptors in insects," *Journal of Comparative Physiology ? A,* vol. 127, no. 2, pp. 185–189, 1978–06–01 1978, doi: 10.1007/bf01352303.
[52] J. A. C. Humphrey, F. G. Barth, M. Reed, and A. Spak, "The Physics of Arthropod Medium-Flow Sensitive Hairs: Biological Models for Artificial Sensors," in *Sensors and Sensing in Biology and Engineering*, F. G. Barth, J. A. C. Humphrey, and T. W. Secomb Eds. Vienna: Springer Vienna, 2003, pp. 129–144.
[53] J. A. C. Humphrey, F. G. Barth, and K. Voss, "The Motion-Sensing Hairs of Arthropods: Using Physics to Understand Sensory Ecology and Adaptive Evolution," in *Ecology of Sensing*, Berlin, Heidelberg, F. G. Barth and A. Schmid, Eds., 2001// 2001: Springer Berlin Heidelberg, pp. 105–125.
[54] S. R. Hill, B. S. Hansson, and R. Ignell, "Characterization of Antennal Trichoid Sensilla from Female Southern House Mosquito, Culex quinquefasciatus Say," *Chemical Senses,* vol. 34, no. 3, pp. 231–252, 2009, doi: 10.1093/chemse/bjn080.
[55] T. Vondran, K. H. Apel, and H. Schmitz, "The infrared receptor of Melanophila acuminata De Geer (Coleoptera: Buprestidae): ultrastructural study of a unique insect thermoreceptor and its possible descent from a hair mechanoreceptor," *Tissue and Cell,* vol. 27, no. 6, pp. 645–658, 1995/12/01/ 1995, doi: https://doi.org/10.1016/S0040-8166(05)80020-5.
[56] L. K. Baxter, *Capacitive sensors : design and applications*. New York: New York : IEEE Press, 1997.
[57] "Parallel plate capacitor." Wikipedia. https://en.m.wikipedia.org/wiki/File:Parallel_plate_capacitor.svg (accessed 30/01/2025).
[58] G. Brasseur, B. Brandstatter, and H. Zangl, "State of the art of robust capacitive sensors," in *1st International Workshop on Robotic Sensing, 2003. ROSE' 03.*, 2003: IEEE, doi: 10.1109/rose.2003.1218702.

[59] X. Hu and W. Yang, "Planar capacitive sensors – designs and applications," *Sensor Review,* vol. 30, no. 1, pp. 24–39, 2010, doi: 10.1108/02602281011010772.

[60] J. C. Doll and B. L. Pruitt, *Piezoresistor Design and Applications*, 2013 ed. New York, NY: New York, NY: Springer New York, 2013.

[61] Z. Tan, H. Jiang, H. Zhang, X. Tang, H. Xin, and S. Nihtianov, "Power-Efficiency Evolution of Capacitive Sensor Interfaces," *IEEE Sensors Journal,* vol. 21, no. 11, pp. 12457–12468, 2021–06–01 2021, doi: 10.1109/jsen.2020.3035109.

[62] A. Ahmadpour Bijargah, A. Heidary, P. Torkzadeh, and S. Nihtianov, "An accurate and power-efficient period-modulator-based interface for grounded capacitive sensors," *International Journal of Circuit Theory and Applications,* 2019–05–08 2019, doi: 10.1002/cta.2642.

[63] H. Jiang, Y. Liu, L. Middelburg, B. E. Mansouri, and S. Nihtianov, "A Continuous-Time Readout IC with 0.12 aF/Hz for Capacitive Inertial Sensors," in *2021 IEEE International Conference on Integrated Circuits, Technologies and Applications (ICTA)*, 2021–11–24 2021: IEEE, doi: 10.1109/icta53157.2021.9661905.

[64] R. Nojdelov and S. Nihtianov, "Capacitive-Sensor Interface With High Accuracy and Stability," *IEEE Transactions on Instrumentation and Measurement,* vol. 58, no. 5, pp. 1633–1639, 2009–05–01 2009, doi: 10.1109/tim.2009.2012957.

[65] S.-Y. Peng, M. S. Qureshi, P. E. Hasler, A. Basu, and F. L. Degertekin, "A Charge-Based Low-Power High-SNR Capacitive Sensing Interface Circuit," *IEEE Transactions on Circuits and Systems I: Regular Papers,* vol. 55, no. 7, pp. 1863–1872, 2008–08–01 2008, doi: 10.1109/tcsi.2008.918006.

[66] D. M. G. Preethichandra and K. Shida, "A simple interface circuit to measure very small capacitance changes in capacitive sensors," *IEEE Transactions on Instrumentation and Measurement,* vol. 50, no. 6, pp. 1583–1586, 2001–01–01 2001, doi: 10.1109/19.982949.

[67] Z. Tan, S. H. Shalmany, G. C. M. Meijer, and M. A. P. Pertijs, "An Energy-Efficient 15-Bit Capacitive-Sensor Interface Based on Period Modulation," *IEEE Journal of Solid-State Circuits,* vol. 47, no. 7, pp. 1703–1711, 2012–07–01 2012, doi: 10.1109/jssc.2012.2191212.

[68] F. M. L. Van Der Goes and G. C. M. Meijer, "A novel low-cost capacitive-sensor interface," *IEEE Transactions on Instrumentation and Measurement,* vol. 45, no. 2, pp. 536–540, 1996–04–01 1996, doi: 10.1109/19.492782.

[69] Y. Yoo and B.-D. Choi, "Readout Circuits for Capacitive Sensors," *Micromachines,* vol. 12, no. 8, p. 960, 2021–08–13 2021, doi: 10.3390/mi12080960.

[70] H. Jiang, S. Amani, J. G. Vogel, S. H. Shalmany, and S. Nihtianov, "A 117DB in-Band CMRR 98.5DB SNR Capacitance-to-Digital Converter for Sub-NM Displacement Sensing with an Electrically Floating Target," in *2018 IEEE Symposium on VLSI Circuits*, 2018–06–01 2018: IEEE, doi: 10.1109/vlsic.2018.8502363.

[71] R. Nojdelov, S. Nihtianov, A. Yacoot, and D. Voigt, "Capacitance-to-Digital Converter for Accurate Displacement Measurement in the Sub-nanometre Range," in *IMEKO TC4 conference*, 2014.

[72] S. J. Rupitsch, *Piezoelectric Sensors and Actuators: Fundamentals and Applications*, 1st 2019. ed. Berlin, Heidelberg: Berlin, Heidelberg: Springer Berlin / Heidelberg, 2018.

[73] D. M. Stefanescu, *Handbook of Force Transducers: Characteristics and Applications*, 2 ed. Cham: Cham: Springer International Publishing AG, 2020.

[74] R. Domingo-Roca, A. Feeney, J. F. C. Windmill, and J. C. Jackson-Camargo, "Directionally Sensitive Active Helmholtz Resonator Metamaterials Enabled

Through 3D-Printing," in *2024 IEEE SENSORS*, 20–23 Oct. 2024 2024, pp. 1–4, doi: 10.1109/SENSORS60989.2024.10784726.

[75] W. Thomson, "XIX. On the electro-dynamic qualities of metals:—Effects of magnetization on the electric conductivity of nickel and of iron," *Proceedings of the Royal Society of London,* vol. 8, no. 0, pp. 546–550, 1857–12–31 1857, doi: 10.1098/rspl.1856.0144.

[76] H. Tomlinson and W. G. Adams, "I. The influence of stress and strain on the action of physical forces," *Philosophical Transactions of the Royal Society of London,* vol. 174, pp. 1–172, 1883, doi: doi:10.1098/rstl.1883.0001.

[77] H. Tomlinson and W. G. Adams, "II. On the increase in resistance to the passage of an electric current produced on wires by stretching," *Proceedings of the Royal Society of London,* vol. 25, no. 171-178, pp. 451–453, 1877, doi: doi:10.1098/rspl.1876.0066.

[78] J. W. Cookson, "Theory of the Piezo-Resistive Effect," *Physical Review,* vol. 47, no. 2, pp. 194–195, 01/15/ 1935, doi: 10.1103/PhysRev.47.194.2.

[79] J. Bardeen and W. Shockley, "Deformation Potentials and Mobilities in Non-Polar Crystals," *Physical Review,* vol. 80, no. 1, pp. 72–80, 10/01/ 1950, doi: 10.1103/PhysRev.80.72.

[80] S. H. Christie, "Experimental Determination of the Laws of Magneto-Electric Induction in Different Masses of the Same Metal, and of Its Intensity in Different Metals," *Philosophical Transactions of the Royal Society of London,* vol. 123, pp. 95–142, 1833. [Online]. Available: http://www.jstor.org/stable/107990.

[81] C. Wheatstone, "An account of several new instruments and processes for determining the constants of a voltaic circuit," *Abstracts of the Papers Printed in the Philosophical Transactions of the Royal Society of London,* vol. 4, pp. 469–471, 1843, doi: doi:10.1098/rspl.1837.0240.

[82] S. Ekelof, "The genesis of the Wheatstone bridge," *Engineering science and education journal.,* vol. 10, pp. 37–40, 2001, doi: 10.1049/esej:20010106.

[83] Z. Han *et al.*, "Artificial Hair-Like Sensors Inspired from Nature: A Review," *Journal of Bionic Engineering,* vol. 15, no. 3, pp. 409–434, 2018–05–01 2018, doi: 10.1007/s42235-018-0033-9.

[84] E. Commission and C. R. a. D. I. S. (CORDIS). "Cricket Inspired Perception and Autonomous Decision Automata (CICADA)." https://cordis.europa.eu/project/id/IST-2001-34718 (accessed 24 Apr. 2025).

[85] E. Commission and C. R. a. D. I. S. (CORDIS). "Customized Intelligent Life-Inspired Arrays (CILIA)." https://cordis.europa.eu/project/id/016039 (accessed 24 Apr. 2025).

[86] A. Dagamseh, C. Bruinink, M. Kolster, R. Wiegerink, T. Lammerink, and G. Krijnen, "Array of biomimetic hair sensor dedicated for flow pattern recognition," in *2010 Symposium on Design Test Integration and Packaging of MEMS/MOEMS (DTIP)*, 5–7 May 2010 2010, pp. 48–50.

[87] A. M. K. Dagamseh, T. S. J. Lammerink, M. L. Kolster, C. M. Bruinink, R. J. Wiegerink, and G. J. M. Krijnen, "Dipole-source localization using biomimetic flow-sensor arrays positioned as lateral-line system," *Sensors and Actuators A: Physical,* vol. 162, no. 2, pp. 355–360, 2010/08/01/ 2010, doi: https://doi.org/10.1016/j.sna.2010.02.016.

[88] A. M. K. Dagamseh, R. J. Wiegerink, T. S. J. Lammerink, and G. J. M. Krijnen, "Towards a high-resolution flow camera using artificial hair sensor arrays for flow pattern observations," *Bioinspiration & Biomimetics,* vol. 7, no. 4, p. 046009, 2012/09/06 2012, doi: 10.1088/1748-3182/7/4/046009.

[89] N. Izadi, M. J. de Boer, J. W. Berenschot, and G. J. M. Krijnen, "Fabrication of superficial neuromast inspired capacitive flow sensors," *Journal of Micromechanics and Microengineering,* vol. 20, no. 8, p. 085041, 2010/07/28 2010, doi: 10.1088/0960-1317/20/8/085041.

[90] H. Droogendijk, C. M. Bruinink, R. G. P. Sanders, A. M. K. Dagamseh, R. J. Wiegerink, and G. J. M. Krijnen, "Improving the performance of biomimetic hair-flow sensors by electrostatic spring softening," *Journal of Micromechanics and Microengineering,* vol. 22, no. 6, p. 065026, 2012/05/22 2012, doi: 10.1088/0960-1317/22/6/065026.

[91] H. Droogendijk, C. Bruinink, R. Sanders, and G. Krijnen, "Tunable Sensor Response by Voltage-Control in Biomimetic Hair Flow Sensors," *Micromachines,* vol. 4, no. 1, pp. 116–127, 2013–03–19 2013, doi: 10.3390/mi4010116.

[92] H. Droogendijk, M. J. De Boer, R. G. P. Sanders, and G. J. M. Krijnen, "Advantages of Electrostatic Spring Hardening in Biomimetic Hair Flow Sensors," *Journal of Microelectromechanical Systems,* vol. 24, no. 5, pp. 1415–1425, 2015–10–01 2015, doi: 10.1109/jmems.2015.2409134.

[93] A. M. K. Dagamseh, "Estimation of squeeze film damping in artificial hair-sensor towards the detection-limit of crickets' hairs," *Microsystem Technologies,* vol. 20, no. 4-5, pp. 963–970, 2014–04–01 2014, doi: 10.1007/s00542-014-2099-6.

[94] H. Droogendijk, M. J. De Boer, R. G. P. Sanders, and G. J. M. Krijnen, "A biomimetic accelerometer inspired by the cricket's clavate hair," *Journal of The Royal Society Interface,* vol. 11, no. 97, p. 20140438, 2014–08–06 2014, doi: 10.1098/rsif.2014.0438.

[95] H. Droogendijk, R. A. Brookhuis, M. J. De Boer, R. G. P. Sanders, and G. J. M. Krijnen, "Towards a biomimetic gyroscope inspired by the fly's haltere using microelectromechanical systems technology," *Journal of The Royal Society Interface,* vol. 11, no. 99, p. 20140573, 2014–10–06 2014, doi: 10.1098/rsif.2014.0573.

[96] H. Droogendijk, M. J. De Boer, R. G. P. Sanders, and G. J. M. Krijnen, "Bio-inspired hair-based inertial sensors," in *Biomimetic Technologies*: Elsevier, 2015, pp. 93–119.

[97] F. Zhifang, C. Jack, Z. Jun, B. David, L. Chang, and D. Fred, "Design and fabrication of artificial lateral line flow sensors," *Journal of Micromechanics and Microengineering,* vol. 12, no. 5, p. 655, 2002/06/24 2002, doi: 10.1088/0960-1317/12/5/322.

[98] J. Chen, Z. Fan, J. Zou, J. Engel, and C. Liu, "Two-Dimensional Micromachined Flow Sensor Array for Fluid Mechanics Studies," *Journal of Aerospace Engineering,* vol. 16, no. 2, pp. 85–97, 2003, doi: doi:10.1061/(ASCE)0893-1321(2003)16:2(85).

[99] N. Chen, C. Tucker, J. M. Engel, Y. Yang, S. Pandya, and C. Liu, "Design and Characterization of Artificial Haircell Sensor for Flow Sensing With Ultrahigh Velocity and Angular Sensitivity," *Journal of Microelectromechanical Systems,* vol. 16, no. 5, pp. 999–1014, 2007–10–01 2007, doi: 10.1109/jmems.2007.902436.

[100] Y. Yang, N. Chen, C. Tucker, J. Engel, S. Pandya, and C. Liu, "From artificial hair cell sensor to artificial lateral line system: Development and application," in *2007 IEEE 20th International Conference on Micro Electro Mechanical Systems (MEMS)*, 2007–01–01 2007: IEEE, pp. 577–580, doi: 10.1109/memsys.2007.4432986.

[101] C. Xue, S. Chen, W. Zhang, B. Zhang, G. Zhang, and H. Qiao, "Design, fabrication, and preliminary characterization of a novel MEMS bionic vector hydrophone,"

Microelectronics Journal, vol. 38, no. 10, pp. 1021–1026, 2007/10/01/ 2007, doi: https://doi.org/10.1016/j.mejo.2007.09.008.

[102] A. T. Abdulsadda and X. Tan, "An artificial lateral line system using IPMC sensor arrays," *International Journal of Smart and Nano Materials,* vol. 3, no. 3, pp. 226–242, 2012–09–01 2012, doi: 10.1080/19475411.2011.650233.

[103] Y. Bian, J. Qiu, X. Wang, H. Ji, and K. Zhu, "The constitutive equations of half coated metal core piezoelectric fiber," *International Journal of Applied Electromagnetics and Mechanics,* vol. 29, no. 1, pp. 47–64, 2009, doi: 10.3233/jae-2009-1005.

[104] Y. Bian, R. Liu, and S. Hui, "Fabrication of a polyvinylidene difluoride fiber with a metal core and its application as directional air flow sensor," *Functional Materials Letters,* vol. 09, no. 01, 2016, doi: 10.1142/s1793604716500016.

[105] Y. Bian, Y. Zhang, and X. Xia, "Design and Fabrication of a Multi-electrode Metal-core Piezoelectric Fiber and Its Application as an Airflow Sensor," *Journal of Bionic Engineering,* vol. 13, no. 3, pp. 416–425, 2016–09–01 2016, doi: 10.1016/s1672-6529(16)60314-1.

[106] M. Asadnia, A. G. P. Kottapalli, Z. Shen, J. Miao, and M. Triantafyllou, "Flexible and Surface-Mountable Piezoelectric Sensor Arrays for Underwater Sensing in Marine Vehicles," *IEEE Sensors Journal,* vol. 13, no. 10, pp. 3918–3925, 2013–10–01 2013, doi: 10.1109/jsen.2013.2259227.

[107] M. Asadnia, A. G. P. Kottapalli, J. Miao, M. E. Warkiani, and M. S. Triantafyllou, "Artificial fish skin of self-powered micro-electromechanical systems hair cells for sensing hydrodynamic flow phenomena," *Journal of The Royal Society Interface,* vol. 12, no. 111, p. 20150322, 2015–10–01 2015, doi: 10.1098/rsif.2015.0322.

[108] J. Fu, Y. Jiang, and D. Zhang, "PVDF based artificial canal lateral line for underwater detection," in *2015 IEEE SENSORS*, 1–4 Nov. 2015 2015, pp. 1–4, doi: 10.1109/ICSENS.2015.7370613.

[109] B. Jin *et al.*, "Flexible Hair-Like Piezoelectric Acoustic Particle Velocity Sensor with Enhanced Sensitivity for Speaker Recognition," *Advanced Functional Materials,* 2024–10–28 2024, doi: 10.1002/adfm.202417164.

[110] Y. Wang, J. Zhao, Y. Xia, and P. Liu, "Configuration optimization of bionic piezoelectric hair sensor for acoustic/tactile detection," *Bioinspiration & Biomimetics,* vol. 15, no. 5, p. 056015, 2020–08–12 2020, doi: 10.1088/1748-3190/ab8f6c.

[111] A. Alfadhel, B. Li, A. Zaher, O. Yassine, and J. Kosel, "A magnetic nanocomposite for biomimetic flow sensing," *Lab Chip,* vol. 14, no. 22, pp. 4362–4369, 2014–01–01 2014, doi: 10.1039/c4lc00821a.

[112] A. Alfadhel and J. Kosel, "Magnetic micropillar sensors for force sensing," in *2015 IEEE Sensors Applications Symposium (SAS)*, 2015–04–01 2015: IEEE, pp. 1–4, doi: 10.1109/sas.2015.7133654.

[113] A. Alfadhel and J. Kosel, "Magnetic Nanocomposite Cilia Tactile Sensor," *Advanced Materials,* vol. 27, no. 47, pp. 7888–7892, 2015–12–01 2015, doi: 10.1002/adma.201504015.

[114] A. Alfadhel, M. Khan, S. Cardoso, D. Leitao, and J. Kosel, "A Magnetoresistive Tactile Sensor for Harsh Environment Applications," *Sensors,* vol. 16, no. 5, p. 650, 2016–05–07 2016, doi: 10.3390/s16050650.

[115] L. Zhang, Z. Hang, and H. Hu, "Toward Large-scale Application of a Bio-Inspired MEMS Optical Hair Flow Sensor Array," in *2024 IEEE SENSORS*, 20–23 Oct. 2024 2024, pp. 01–04, doi: 10.1109/SENSORS60989.2024.10784825.

[116] D. H. Kang *et al.*, "A Self-Powered, Highly Sensitive, and Frequency-Tunable Triboelectric Acoustic Sensor Inspired by the Human Cochlea," *Advanced*

Functional Materials, vol. 34, no. 48, 2024–11–01 2024, doi: 10.1002/adfm.202408344.
[117] M. Sarcar, K. M. Rao, and K. L. Narayan, *Computer aided design and manufacturing*. PHI Learning Pvt. Ltd., 2008.
[118] R. W. Clough, "The Finite Element Method in Plane Stress Analysis," 1960.
[119] S. S. S. Unnikrishnan Nair, *Introduction to Finite Element Analysis, A Textbook for Engineering Students*, 1 ed. Singapore: Springer Singapore (in English), 2023, p. 409.
[120] COMSOL. "The Solid Mechanics Interface." https://doc.comsol.com/6.1/doc/com.comsol.help.sme/sme_ug_solid.07.002.html (accessed 24th Sep. 2025).
[121] COMSOL. "The Pressure Acoustics, Frequency Domain Interface." https://doc.comsol.com/5.5/doc/com.comsol.help.aco/aco_ug_pressure.05.002.html (accessed 24th Sep. 2025).
[122] COMSOL. "The Electrostatics Interface." https://doc.comsol.com/5.6/doc/com.comsol.help.comsol/comsol_ref_acdc.22.28.html (accessed 24th Sep. 2025).
[123] COMSOL. "The Electric Currents Interface." https://doc.comsol.com/6.3/doc/com.comsol.help.comsol/comsol_ref_acdc.26.52.html (accessed 24th Sep. 2025).
[124] COMSOL. "Solid–Thin Structure Connection." https://doc.comsol.com/6.3/doc/com.comsol.help.sme/sme_ug_multiphysics.18.74.html (accessed 24th Sep. 2025).
[125] J. R. Martins and A. Ning, *Engineering design optimization*. Cambridge University Press, 2021.
[126] A. R. Parkinson, R. Balling, and J. D. Hedengren, "Optimization methods for engineering design," *Brigham Young University,* vol. 5, no. 11, 2013.
[127] *ISO/ASTM 52900:2021*, ISO and ASTM, 2021. [Online]. Available: https://www.iso.org/obp/ui/#iso:std:iso-astm:52900:ed-2:v1:en
[128] M. Ziaee and N. B. Crane, "Binder jetting: A review of process, materials, and methods," *Additive Manufacturing,* vol. 28, pp. 781–801, 2019/08/01/ 2019, doi: https://doi.org/10.1016/j.addma.2019.05.031.
[129] I. Gibson, D. Rosen, and B. Stucker, "Directed Energy Deposition Processes," in *Additive Manufacturing Technologies: 3D Printing, Rapid Prototyping, and Direct Digital Manufacturing*, I. Gibson, D. Rosen, and B. Stucker Eds. New York, NY: Springer New York, 2015, pp. 245–268.
[130] I. Gibson, D. Rosen, B. Stucker, and M. Khorasani, "Material Extrusion," in *Additive Manufacturing Technologies*, I. Gibson, D. Rosen, B. Stucker, and M. Khorasani Eds. Cham: Springer International Publishing, 2021, pp. 171–201.
[131] I. Gibson, D. Rosen, B. Stucker, and M. Khorasani, "Material Jetting," in *Additive Manufacturing Technologies*: Springer International Publishing, 2021, pp. 203–235.
[132] I. Gibson, D. Rosen, B. Stucker, and M. Khorasani, "Powder Bed Fusion," in *Additive Manufacturing Technologies*: Springer International Publishing, 2021, pp. 125–170.
[133] I. Gibson, D. Rosen, B. Stucker, and M. Khorasani, "Sheet Lamination," in *Additive Manufacturing Technologies*: Springer International Publishing, 2021, pp. 253–283.
[134] R. Phillips, "Photopolymerization," *Journal of Photochemistry,* vol. 25, no. 1, pp. 79–82, 1984/05/01/ 1984, doi: https://doi.org/10.1016/0047-2670(84)85016-9.

[135] K. Sertoglu, "Carbon launches its new M3 and M3 Max 3D printers – technical specifications and pricing," vol. 2025, ed: 3D Printing Industry, 2022.
[136] Asiga, "Max X," Max X27 datasheet.
[137] "Asiga MAX User Guide," ed: Asiga, 2019.
[138] O. H. Nam *et al.*, "Influence of postprinting cleaning methods on the cleaning efficiency and surface and mechanical properties of three-dimensionally printed resins," *The Journal of Prosthetic Dentistry,* vol. 132, no. 4, pp. 838.e1–838.e9, 2024/10/01/ 2024, doi: https://doi.org/10.1016/j.prosdent.2024.02.026.
[139] S. M. Rossnagel, "Thin film deposition with physical vapor deposition and related technologies," *Journal of Vacuum Science & Technology A: Vacuum, Surfaces, and Films,* vol. 21, no. 5, pp. S74–S87, 2003–09–01 2003, doi: 10.1116/1.1600450.
[140] A. Scientific, "Automatic Sputter Coater," AGB7341 datasheet, Jul. 2021.
[141] S. S. Azim, A. Satheesh, K. K. Ramu, S. Ramu, and G. Venkatachari, "Studies on graphite based conductive paint coatings," *Progress in Organic Coatings,* vol. 55, no. 1, pp. 1–4, 2006/01/01/ 2006, doi: https://doi.org/10.1016/j.porgcoat.2005.09.001.
[142] M. N. H. Jamaluddin, M. H. M. Salleh, and M. Z. Zulkifli, "Investigation of strain measurement on paper-based strain sensor using carbon electrical conductive paint," in *AIP Conference Proceedings*, 2023–01–01 2023, vol. 2758: AIP Publishing, p. 030001, doi: 10.1063/5.0123965.
[143] S. M. El-Sawy, F. A. Abdel-Mohdy, and I. M. Morsi, "Silver electric conductive paints," *Pigment & Resin Technology,* vol. 15, no. 1, pp. 8–9, 1986–01–01 1986, doi: 10.1108/eb042191.
[144] A. C. Christopoulos and G. J. Tsamasphyros, "Strain Measurements Using Electrically Conductive Silver Paint," *Sensor Letters,* vol. 12, pp. 1530–1533, 2014, doi: 10.1166/sl.2014.3343.
[145] A. Scientific, "Agar Quick drying silver paint," AGG302 datasheet, Jun. 2021.
[146] Ossila, "Spin Coater User Manual," L2001A3 datasheet, Nov. 2021.
[147] M. D. Tyona, "A theoritical study on spin coating technique," *Advances in materials Research,* vol. 2, no. 4, pp. 195–208, 2013–12–25 2013, doi: 10.12989/amr.2013.2.4.195.
[148] Ossila. "Spin Coating: Complete Guide to Theory and Techniques." https://www.ossila.com/pages/spin-coating (accessed 19/11/2024).
[149] E. L. Ritman, "Current Status of Developments and Applications of Micro-CT," *Annual Review of Biomedical Engineering,* vol. 13, no. Volume 13, 2011, pp. 531–552, 2011, doi: https://doi.org/10.1146/annurev-bioeng-071910-124717.
[150] L. Marques, C. Appoloni, and C. Fernandes, "Porosity study of synthetic sandstones by non-destructive nuclear techniques," *Materials Research,* vol. 14, pp. 394–402, 08/05 2011, doi: 10.1590/S1516-14392011005000048.
[151] M. H. McKetty, "The AAPM/RSNA physics tutorial for residents. X-ray attenuation," *RadioGraphics,* vol. 18, no. 1, pp. 151–163, 1998, doi: 10.1148/radiographics.18.1.9460114.
[152] S. Puvanasunthararajah, D. Fontanarosa, M. L. Wille, and S. M. Camps, "The application of metal artifact reduction methods on computed tomography scans for radiotherapy applications: A literature review," *Journal of Applied Clinical Medical Physics,* vol. 22, no. 6, pp. 198–223, 2021–06–01 2021, doi: 10.1002/acm2.13255.
[153] B. J. Schwarz and M. H. Richardson, "Experimental modal analysis," *CSI Reliability week,* vol. 35, no. 1, pp. 1–12, 1999.
[154] Y. Yeh and H. Z. Cummins, "Localized fluid flow measurements with an HeNe laser spectrometer," *Applied Physics Letters,* Article vol. 4, no. 10, pp. 176–178, 1964, doi: 10.1063/1.1753925.

[155] S. J. Rothberg *et al.*, "An international review of laser Doppler vibrometry: Making light work of vibration measurement," *Optics and Lasers in Engineering,* vol. 99, pp. 11–22, 2017–12–01 2017, doi: 10.1016/j.optlaseng.2016.10.023.
[156] Jerome Eichenberger and J. Sauer, "Validating Complex Models Accurately and Without Contact Using Scanning Laser Doppler Vibrometry (SLDV)," *Rotating Machinery, Optical Methods & Scanning LDV Methods. Conference Proceedings of the Society for Experimental Mechanics Series,* vol. 6, 2021, doi: https://doi.org/10.1007/978-3-030-76335-0_11.
[157] P. Castellini, M. Martarelli, and E. P. Tomasini, "Laser Doppler Vibrometry: Development of advanced solutions answering to technology's needs," *Mechanical Systems and Signal Processing,* vol. 20, no. 6, pp. 1265–1285, 2006/08/01/ 2006, doi: https://doi.org/10.1016/j.ymssp.2005.11.015.
[158] Polytec GmbH. *MSA-100-3D Micro System Analyzer - Product brochure.* (2019). Waldbronn, Germany. Accessed: 19/02/2024. [Online]. Available: https://www.polytec.com/us/vibrometry/products/microscope-based-vibrometers/msa-100-3d-micro-system-analyzer
[159] P. GmbH, "3D vibration measurement for MEMS & microsystems," MSA-100-3D datasheet, May 2019.
[160] R. J. Adrian, "Twenty years of particle image velocimetry," *Experiments in Fluids,* vol. 39, no. 2, pp. 159–169, 2005–08–01 2005, doi: 10.1007/s00348-005-0991-7.
[161] Phantom, "Phantom® Miro® LAB-, LC- and R-Series Cameras," Miro 310 datasheet, Apr. 2016.
[162] I. Suomi and T. Vihma, "Wind Gust Measurement Techniques—From Traditional Anemometry to New Possibilities," *Sensors,* vol. 18, no. 4, p. 1300, 2018–04–23 2018, doi: 10.3390/s18041300.
[163] G. Comte-Bellot, "Hot-Wire Anemometry," *Annual Review of Fluid Mechanics,* vol. 8, no. 1, pp. 209–231, 1976–01–01 1976, doi: 10.1146/annurev.fl.08.010176.001233.
[164] Sauermann, "Hotwire Thermo-anemometer Data Sheet," Si-VH3 datasheet, Jul. 2023.
[165] Sauermann, "Hotwire Thermo-anemometer User Manual," Si-VH3 datasheet, Nov. 2021.
[166] S. Martinelli, A. Reid, R. Domingo-Roca, and J. F. C. Windmill, "Additive Manufacturing of an Insect Bio-Inspired Hair Acoustic Sensor," in *2023 IEEE SENSORS*, 29 Oct.–1 Nov. 2023 2023, pp. 1–4, doi: 10.1109/SENSORS56945.2023.10324858.
[167] A. Vitale, M. G. Hennessy, O. K. Matar, and J. T. Cabral, "A Unified Approach for Patterning via Frontal Photopolymerization," *Advanced Materials,* vol. 27, no. 40, pp. 6118–6124, 2015–10–01 2015, doi: 10.1002/adma.201502607.
[168] Formlabs, "General Purpose Resins," FLGPGR04 datasheet, Sept. 2016 [Revised Aug. 2023].
[169] Formlabs, "Elastic 50A," FLELCL01 datasheet, Jul. 2020.
[170] X. Ding, R. Jia, Z. Gan, Y. Du, D. Wang, and X. Xu, "Tough and conductive polymer hydrogel based on double network for photo-curing 3D printing," *Materials Research Express,* vol. 7, no. 5, p. 055304, 2020/05/11 2020, doi: 10.1088/2053-1591/ab8cfb.
[171] C. Zhang, S. H. Kwon, and L. Dong, "Piezoelectric Hydrogels: Hybrid Material Design, Properties, and Biomedical Applications," *Small,* vol. 20, no. 28, 2024–07–01 2024, doi: 10.1002/smll.202310110.
[172] S. Aftab *et al.*, "Laser-Induced Graphene for Advanced Sensing: Comprehensive Review of Applications," *ACS Sensors,* vol. 9, no. 9, pp. 4536–4554, 2024/09/27 2024, doi: 10.1021/acssensors.4c01717.

[173] K. R. Ryan, M. P. Down, N. J. Hurst, E. M. Keefe, and C. E. Banks, "Additive manufacturing (3D printing) of electrically conductive polymers and polymer nanocomposites and their applications," *eScience,* vol. 2, no. 4, pp. 365–381, 2022/07/01/ 2022, doi: https://doi.org/10.1016/j.esci.2022.07.003.
[174] A. T. Cullen and A. D. Price, "Digital light processing for the fabrication of 3D intrinsically conductive polymer structures," *Synthetic Metals,* vol. 235, pp. 34–41, 2018/01/01/ 2018, doi: https://doi.org/10.1016/j.synthmet.2017.11.003.
[175] B. Zhu, J. M. F. Guerreiro, Y. Zhang, B. P. Tiller, and J. F. C. Windmill, "Additive Manufacturing (AM) Capacitive Acoustic and Ultrasonic Transducers Using a Commercial Direct Light Processing (DLP) Printer," *IEEE Sensors Journal,* vol. 20, no. 4, pp. 1770–1777, 2020–02–15 2020, doi: 10.1109/jsen.2019.2950089.
[176] S. Pagliano *et al.*, "Micro 3D printing of a functional MEMS accelerometer," *Microsystems & Nanoengineering,* vol. 8, no. 1, 2022–09–19 2022, doi: 10.1038/s41378-022-00440-9.
[177] A. Vanarse, "A Review of Current Neuromorphic Approaches for Vision, Auditory, and Olfactory Sensors," 2016.
[178] L. S. Smith, "Toward a neuromorphic microphone," 2015.
[179] T. J. Koickal *et al.*, "Design of a spike event coded RGT microphone for neuromorphic auditory systems," 2011.
[180] V. Gubbi, T. Ivanov, K. Ved, C. Lenk, and M. Ziegler, "Bio-inspired acoustic MEMS sensor with tunable resonance frequency," *Sensors and Actuators A: Physical,* vol. 387, p. 116369, 2025/06/01/ 2025, doi: https://doi.org/10.1016/j.sna.2025.116369.
[181] E. Times. "Artificial Hearing: From Ear Drums to Tuning Forks." in "EE Times Current." G. D'Angelo, S. Bains, and C. Lenk, 2025 https://www.eetimes.com/podcasts/artificial-hearing-from-ear-drums-to-tuning-forks/
[182] S. Martinelli, A. Reid, and J. F. C. Windmill, "Additive Manufacturing of an Airflow Sensor Inspired by the Flat Trichobothria of Scorpions," in *2025 IEEE International Conference on Flexible and Printable Sensors and Systems (FLEPS)*, 2025–06–22 2025: IEEE, pp. 1–4, doi: 10.1109/fleps65444.2025.11105673.
[183] S. Martinelli, A. Reid, and J. F. C. Windmill, "3D-Printed Airflow Hair Sensor Inspired by the Buthus occitanus Scorpion's flat Trichobothria," *IEEE Sensors Journal,* vol. 2026, no. 2, pp. 1428 – 1435, 15 Jan. 2026 2026, doi: 10.1109/JSEN.2025.3635869.
[184] B. L. Pruitt and T. W. Kenny, "Piezoresistive cantilevers and measurement system for characterizing low force electrical contacts," *Sensors and Actuators A: Physical,* vol. 104, no. 1, pp. 68–77, 2003/03/15/ 2003, doi: https://doi.org/10.1016/S0924-4247(02)00485-5.
[185] Asiga. "Asiga Material Library." https://www.asiga.com/open-material-library/ (accessed 12/09/2025).
[186] R. Domingo-Roca, L. Asciak, J. F. C. Windmill, H. Mulvana, and J. C. Jackson-Camargo, "Non-destructive Analysis of the Mechanical Properties of 3D-Printed Materials," *Journal of Nondestructive Evaluation,* vol. 41, no. 1, 2022–03–01 2022, doi: 10.1007/s10921-022-00854-5.
[187] T. Instruments, "INAx126 MicroPower Instrumentation Amplifiers," INA126 datasheet, Sep. 2000 [Revised Jan. 2022].
[188] COMSOL. "The Laminar Flow Interface." https://doc.comsol.com/5.4/doc/com.comsol.help.comsol/comsol_ref_fluidflow.20.21.html (accessed 03 Nov. 2025).

[189] K. Photonics, "LD Pumped All-Solid-State Green Laser," MGL-F-532-2000-5 datasheet.
[190] COMSOL. "Setting Up GPU-Accelerated Computing Within COMSOL Multiphysics®." https://www.comsol.com/support/learning-center/article/92461 (accessed 31st Oct. 2025).
[191] X. Bao, J. Meng, Z. Tan, C. Zhang, L. Li, and T. Liu, "Direct-ink-write 3D printing of highly-stretchable polyaniline gel with hierarchical conducting network for customized wearable strain sensors," *Chemical Engineering Journal,* vol. 491, p. 151918, 2024/07/01/ 2024, doi: https://doi.org/10.1016/j.cej.2024.151918.
[192] D. Lo Presti *et al.*, "Optimization and characterization of a 3D-printed wearable strain sensor for respiration and heartbeat measurements," *Measurement,* vol. 228, p. 114377, 2024/03/31/ 2024, doi: https://doi.org/10.1016/j.measurement.2024.114377.
[193] X. Luo, H. Cheng, K. Chen, L. Gu, S. Liu, and X. Wu, "Multi-walled carbon nanotube-enhanced polyurethane composite materials and the application in high-performance 3D printed flexible strain sensors," *Composites Science and Technology,* vol. 257, p. 110818, 2024/10/20/ 2024, doi: https://doi.org/10.1016/j.compscitech.2024.110818.
[194] X. Xia *et al.*, "Structural Design and DLP 3D Printing Preparation of High Strain Stable Flexible Pressure Sensors," *Advanced Science,* vol. 11, no. 37, 2024–10–01 2024, doi: 10.1002/advs.202304409.
[195] J. Zhu *et al.*, "Photocuring 3D printable flexible strain sensor enhanced by in situ grown silk fibroin nanoparticles," *Chemical Engineering Journal,* vol. 497, p. 154762, 2024/10/01/ 2024, doi: https://doi.org/10.1016/j.cej.2024.154762.
[196] L. Cui *et al.*, "Recent progress of 3D-printed polymeric gel sensors for flexible electronics," *Materials Horizons,* vol. 12, no. 21, pp. 8802–8831, 2025–01–01 2025, doi: 10.1039/d5mh00381d.
[197] M. I. Farid, W. Wu, G. Li, F. Zhang, and X. Zhu, "High-Performance 3D Printed Thermoplastic Polyurethane Composite Resistive Flexible Strain Sensor," *Journal of Applied Polymer Science,* vol. 142, no. 19, p. e56859, 2025–05–15 2025, doi: 10.1002/app.56859.
[198] B. Han, Y. Wang, C. Liu, Z. Liu, and Q. Zhang, "3D printed continuous carbon fiber reinforced TPU metamaterials for flexible multifunctional sensors," *Chemical Engineering Journal,* vol. 513, p. 162767, 2025/06/01/ 2025, doi: https://doi.org/10.1016/j.cej.2025.162767.
[199] S. Imranuddin, A. Pratap Singh, G. Stano, S. M. Al Islam Ovy, G. Percoco, and Y. Tadesse, "Enhancing 3-D-Printed Piezoresistive Sensors: An Investigation Into Process Parameters, Sensor Geometries and Materials Selection," *IEEE Sensors Journal,* vol. 25, no. 8, pp. 13063–13072, 2025–04–15 2025, doi: 10.1109/jsen.2025.3546641.
[200] W. Lina *et al.*, "All 3D-printed high-sensitivity adaptive hydrogel strain sensor for accurate plant growth monitoring," *Soft Science,* vol. 5, no. 1, p. 2, 2025, doi: 10.20517/ss.2024.38.
[201] L. J. S. Santos *et al.*, "3D-printed metal-free thermal sensor based on PLA coated with PLA/CNTs nanocomposite ink," *Sensors and Actuators A: Physical,* vol. 384, p. 116279, 2025/04/01/ 2025, doi: https://doi.org/10.1016/j.sna.2025.116279.
[202] K. A. Tiston, C. Tipachan, T. Yimnoi, R. Cheacharoen, V. P. Hoven, and B. Narupai, "3D Printing of Ultrastretchable and Tough Double-Network Hydrogel for Strain Sensor," *Advanced Materials Technologies,* vol. 10, no. 3, 2025–02–01 2025, doi: 10.1002/admt.202400751.

[203] D. Wang *et al.*, "3D-printable polyacrylamide/quaternary chitosan-based multifunctional hydrogel flexible sensors," *Reactive and Functional Polymers,* vol. 214, p. 106308, 2025/09/01/ 2025, doi: https://doi.org/10.1016/j.reactfunctpolym.2025.106308.
[204] F. Xiao, Z. Wei, Z. Xu, H. Wang, J. Li, and J. Zhu, "Fully 3D-Printed Soft Capacitive Sensor of High Toughness and Large Measurement Range," *Advanced Science,* vol. 12, no. 8, 2025–02–01 2025, doi: 10.1002/advs.202410284.
[205] J. Yi, S. Yang, L. Yue, and I. M. Lei, "Digital light processing 3D printing of flexible devices: actuators, sensors and energy devices," *Microsystems & Nanoengineering,* vol. 11, no. 1, p. 51, 2025–03–19 2025, doi: 10.1038/s41378-025-00885-8.
[206] B. Zhu, "Additive Manufacturing (3D Print) of Air-coupled Diaphragm Ultrasonic Transducers," Doctor of Philosophy, Electronic and Electrical Engineering, University of Strathclyde, Glasgow, UK, 2019.
[207] G. G. Stokes, "On the effect of the internal friction of fluids on the motion of pendulums," 1851.